

Thèse de doctorat  
de l'Université Sorbonne Paris Cité  
Préparée à l'Université Paris Diderot  
**École Doctorale N°564 Physique en Île-de-France**  
*Institut de Physique Théorique du CEA Saclay*  
*Laboratoire de Physique des Solides de l'Université Paris-Sud*

# Spin polarisation and topological properties of Yu-Shiba-Rusinov states

Par **Vardan Kaladzhyan**

Thèse de doctorat de physique

Dirigée par Cristina Bena et Pascal Simon

**Thèse présentée et soutenue à Saclay, le 15 septembre 2017.**

**Composition du Jury :**

Président du jury : Dr. Benoît Douçot, CNRS Université Pierre et Marie Curie  
Rapporteurs : Prof. Lars Fritz, Universiteit Utrecht  
Prof. Felix von Oppen, Freie Universität Berlin  
Examineurs : Prof. Vincent Repain, Université Paris Diderot  
Dr. Ramón Aguado, Instituto de Ciencia de Materiales de Madrid, CSIC  
Directeur de thèse : Dr. Cristina Bena, Institut de Physique Théorique du CEA Saclay  
Co-directeur de thèse : Prof. Pascal Simon, Université Paris Sud



*To my loving parents and little sister.*



## Acknowledgements

I would like to start by acknowledging the contribution of the members of my PhD defense jury, Felix von Oppen, Lars Fritz, Ramón Aguado, Vincent Repain and Benoît Douçot, for all their valuable comments, questions and corrections concerning my PhD thesis, as well as for insightful discussions during the defense. I should also thank Felix von Oppen and Lars Fritz for their wonderful referee reports.

I thank all my teachers and professors, especially those who taught me maths, physics, foreign languages and music – subjects that brought me this far and helped me to achieve everything I have got today.

I am sincerely grateful to my first scientific supervisor, Sergey Artemenko, whose amazing sense of humour along with a deep knowledge of both scientific and non-scientific matters determined my desire to continue my studies in the Academia. If it was not for him I would have never dared to apply for PhD positions abroad.

It is hard to overestimate the role of Natasha Kirova in my recent achievements, and I am forever grateful to her for leaving my CV on Pascal's and Cristina's desks at the right moment and for giving her recommendations, as well as for being ready to help me whenever I was in need.

I also acknowledge the help of Stéphane Nonnenmacher for spending his valuable time on preparing with me the scholarship-winning talk I gave for the École Doctorale, as well as for leading me through my first steps in doing all the necessary paperwork at Université Paris 7.

To Alexei Grinbaum I am very grateful for introducing me to the cultural life of Paris, for sharing with me all the life hacks and subtleties of living in France, as well as for his support and all the lunches, suppers and concerts we shared together during these three years.

I would like also to thank Ipsita Mandal, Julien Despres, Clément Dutreix, Silas Hoffman, Joel Röntynen, Teemu Ojanen, Nicholas Sedlmayr, Pavel Aseev and Mircea Trif for fruitful collaborations and discussions.

To amazing secretaries, Véronique Thieulart, Sylvie Zaffanella and Joëlle Taïeb, I am thankful for simplifying my life and leaving me more time for doing research. I would love also to thank

François Gelis and Sylvie Hénon for always responding quickly and helping me with my personal administrative issues.

To all the LPS people I am grateful for long tea and lunch breaks during which I was motivated to improve my French in order to participate and contribute, as well as for being patient about all my grammar questions. I would like to thank especially Mircea, Fred and Oscar for raising controversial subjects, Oliver and Mark for all the dirty jokes, Sébastien and Olesia for forcing us to take breaks, Nicolas for being himself, Manali for delivering and sharing all the fresh gossip from the plateau and beyond, as well as for her inexhaustible sense of humour and for being the heart of the group, and of course Sergueï, for always inquiring about my weekends, sharing with me both the sad and the happy moments of my PhD, and for believing in me.

To all the IPhT people I am thankful for amazing working conditions and nice debates in the coffee room. I would like to note especially all the conversations with Valerio, Valentina, Hanna, Luca, Steven, Christian, Pierre, Corentin and all the others. I was thoroughly enjoying lunches with the string theory group, especially the interesting discussions and advices of Iosif Bena.

I am thankful to all my officemates (Oliver, Hanna, Rémy, Christian, Quentin, Valerio, Valentina and Andrej) for standing my unbearable morning self as well as for listening patiently to all my endless complaints.

I am immensely grateful to Roger Balian for inspiring and insightful discussions around a cup of coffee in IPhT, and for helping me to achieve what I could have never achieved without him.

Thanks to my cousin Anna, whose sarcastic jokes and brilliant knowledge of both French language and bureaucracy allowed me to stay sane and survive these three years. I will always remember those long tea sessions during the weekends I spent in Coulommiers.

To Cristina and Pascal, my gorgeous supervisors without whom this thesis would have never existed, I am grateful for amazing projects, insightful discussions and for all the time they spent on teaching me patiently and sharing their knowledge and experience in both condensed matter physics and beyond. With them I've always felt guided and cared for.

For all the non-verbal and verbal support I am grateful to my Russian friends: I would like to start by acknowledging the hilarious 'Le Petit Tousai' chat sessions, and continue by thanking the MIPT troop Ilya, Danila, Alexander and of course Anya for keeping the spirit of our dorm

room n°419 alive both in the Internet and in real life. I cannot forget all the laughable Skype sessions we had with Li, Lu and Di as well as the rare but helpful conversations with Marina Prozorova and Roza Gelman. I am more than grateful to both Anyas for keeping me sane. And finally, for numerous soul-saving conversations I thank my sour milk brother Azim, whose support and care mean the world to me.

Last but not least I would like to thank my fantastic family for always being there for me.

## Abstract

Titre : Polarisation en spin et propriétés topologiques des états de Yu-Shiba-Rusinov

Résumé : Dans ce manuscrit de thèse, nous revisitons d'abord la physique des états de Yu-Shiba-Rusinov, en nous concentrant sur leur polarisation en spin. Nous commençons par montrer théoriquement que nous pouvons extraire beaucoup d'informations sur le supraconducteur hôte, en analysant la densité locale d'états électroniques liée à la présence d'impuretés magnétiques. Tout d'abord, nous démontrons que le couplage spin-orbite peut être lu directement et sans ambiguïté par la spectroscopie par effet tunnel résolu en spin dans les systèmes bidimensionnels et unidimensionnels, qu'ils soient supraconducteurs ou métalliques. Nous analysons les oscillations induites par les impuretés dans la densité d'états électroniques. En particulier, nous nous concentrons sur la transformation de Fourier (TF) des oscillations de Friedel et nous notons que les caractéristiques à haute intensité apparaissent pour un vecteur d'onde donné par deux fois la longueur inverse du spin-orbite. Ensuite, nous montrons qu'il est possible de déterminer le mécanisme d'appariement dominant, qu'il soit en ondes s ou en ondes p, dans les supraconducteurs non conventionnels en analysant la structure spectrale résolue en spin des états liés de Yu-Shiba-Rusinov. De manière frappante, nous démontrons qu'une analyse minutieuse de la densité d'états électroniques polarisée en spin ne permet pas seulement de caractériser sans équivoque le degré d'appariement de type triplet, mais également son orientation, a.k.a. le vecteur  $\mathbf{d}$ .

Enfin, nous proposons et discutons deux approches différentes d'ingénierie et de contrôle des phases topologiques à l'aide d'impuretés scalaires et magnétiques. Nous commençons par fournir une théorie microscopique des réseaux d'impuretés scalaires sur les supraconducteurs chiraux. Nous montrons que pour un supraconducteur topologique de type chiral, les impuretés scalaires donnent lieu à une hiérarchie complexe de phases non triviales distinctes avec des nombres de Chern élevés. Deuxièmement, nous proposons et étudions théoriquement une nouvelle plateforme prometteuse que nous appelons la chaine dynamique de Shiba, c'est-à-dire une chaine d'impuretés magnétiques classiques dans un supraconducteur en ondes s avec des spins qui précèdent. Nous montrons que cette approche peut être utilisée non seulement pour créer une phase supraconductrice topologique, mais surtout pour contrôler les transitions de phase

topologiques au moyen de la dynamique de la texture de la magnétisation.

Ce manuscrit est organisé comme suit. Dans la première partie, les informations d'introduction essentielles sur la supraconductivité, les oscillations de Friedel et les états de Yu-Shiba-Rusinov sont fournies. La deuxième partie est consacrée à la polarisation en spin des états Yu-Shiba-Rusinov et aux propriétés qui pourraient être extraites au moyen de la microscopie par effet tunnel résolu en spin. Dans la dernière partie, deux configurations proposées pour l'ingénierie de phases topologiques, basées sur les états induits par les impuretés, sont présentées, suivies de conclusions, d'un bref résumé des réalisations de cette thèse et enfin d'une discussion de possibles directions futures.

Mots clés : physique de la matière condensée, physique des solides, supraconductivité, impuretés, états liés

Title: Spin polarisation and topological properties of Yu-Shiba-Rusinov states

Abstract: In this manuscript we first revisit the physics of Yu-Shiba-Rusinov subgap states, focusing on their spin polarisation. We start by showing theoretically that we can extract a considerable amount of information about the host superconductor, by analysing spin-polarised local density of states related to the presence of magnetic impurities. First, we demonstrate that the spin-orbit coupling in two-dimensional and one-dimensional systems, both superconducting and metallic, can be read-off directly and unambiguously via spin-resolved STM. We analyse the impurity-induced oscillations in the local density of states. In particular, we focus on the Fourier transform (FT) of the Friedel oscillations and we note that high-intensity FT features appear at a wave vector given by twice the inverse spin-orbit length. Second, in unconventional superconductors with both s-wave and p-wave pairing, by analysing the spin-resolved spectral structure of the Yu-Shiba-Rusinov states it is possible to determine the dominating pairing mechanism. Most strikingly, we demonstrate that a careful analysis of spin-polarised density of states allows not only to unambiguously characterise the degree of triplet pairing, but also to define the orientation of the triplet pairing vector, also known as the d-vector.

Finally, we discuss two different ways of engineering and controlling topological phases with both scalar and magnetic impurities. We start with providing a microscopic theory of scalar impurity structures on chiral superconductors. We show that given a non-trivial chiral superconductor, the scalar impurities give rise to a complex hierarchy of distinct non-trivial phases with high Chern numbers. Second, we propose and study theoretically a new promising platform that we call 'dynamical Shiba chain', i.e. a chain of classical magnetic impurities in an s-wave superconductor with precessing spins. We have shown that it can be employed not only for engineering a topological superconducting phase, but most remarkably for controlling topological phase transitions by means of magnetisation texture dynamics.

This manuscript is organised as follows. In the first part, the essential introductory information on superconductivity, Friedel oscillations and Yu-Shiba-Rusinov states is provided. The second part is dedicated to spin polarisation of Yu-Shiba-Rusinov states and the properties that could be extracted by means of spin-resolved STM measurements. In the last part, two setups pro-

posed for topological phase engineering based on impurity-induced states are presented, followed by conclusions with a brief summary of the thesis achievements and further directions to pursue.

Keywords: condensed matter physics, solid state physics, superconductivity, impurities, bound states



# Contents

<b>Acknowledgements</b>	<b>i</b>
<b>Abstract</b>	<b>vi</b>
<b>I Introduction</b>	<b>1</b>
<b>1 Superconductivity</b>	<b>3</b>
1.1 Experimental discovery . . . . .	3
1.2 Phenomenological and microscopic theories . . . . .	4
1.3 Bardeen–Cooper–Schrieffer theory . . . . .	4
1.4 Bogoliubov–de Gennes Hamiltonian . . . . .	6
1.5 Cooper pairs beyond the BdG Hamiltonian . . . . .	8
<b>2 Friedel oscillations</b>	<b>12</b>
2.1 Explanation in a nutshell . . . . .	12
2.2 State of the art . . . . .	14

<b>3 Yu-Shiba-Rusinov states</b>	<b>16</b>
3.1 Theoretical prediction and discovery . . . . .	16
3.2 Underlying mechanism and properties . . . . .	17
<b>II Spin polarisation of Yu-Shiba-Rusinov states as a probe of the host superconductors</b>	<b>21</b>
<b>4 General model and methods</b>	<b>23</b>
4.1 Generalised BdG Hamiltonian . . . . .	23
4.2 T-matrix approach . . . . .	23
4.3 Analytical approach . . . . .	26
4.4 Example of a 2D s-wave superconductor . . . . .	28
<b>5 Extracting spin-orbit coupling</b>	<b>32</b>
5.1 Model and techniques . . . . .	37
5.2 Results for two-dimensional systems . . . . .	39
5.3 Results for one-dimensional systems . . . . .	48
5.4 Discussion . . . . .	51
<b>6 Extracting triplet pairing type</b>	<b>54</b>
6.1 Model and techniques . . . . .	56
6.2 Results . . . . .	58
6.3 Discussion . . . . .	72

---

<b>III</b>	<b>Engineering topological superconductors with impurities</b>	<b>74</b>
<b>7</b>	<b>Chern mosaic in a p-wave superconductor</b>	<b>78</b>
7.1	Chiral p-wave superconductors . . . . .	80
7.2	Topological properties . . . . .	82
7.3	Physical realisations . . . . .	84
7.4	Discussion . . . . .	85
<b>8</b>	<b>Dynamical Shiba chain</b>	<b>87</b>
8.1	Model . . . . .	89
8.2	Effective band structure . . . . .	91
8.3	Quasi-spectrum and topology . . . . .	92
8.4	Detection and physical implementations . . . . .	95
8.5	Discussion . . . . .	96
	<b>Conclusions</b>	<b>97</b>
	<b>Appendixes</b>	<b>105</b>
<b>A</b>	<b>Analytical calculation of the Shiba states wave functions</b>	<b>105</b>
A.1	s-wave superconductors with Rashba SOC . . . . .	106
A.2	p-wave superconductors . . . . .	118
<b>B</b>	<b>Metallic systems with Rashba SOC in the presence of magnetic impurities</b>	<b>140</b>

<b>C Engineering with scalar impurities in a p-wave SC</b>	<b>150</b>
C.1 Spinless p-wave case . . . . .	150
C.2 Single scalar impurity bound states . . . . .	151
C.3 Lattice of scalar impurities . . . . .	152
C.4 $H$ as a topological Hamiltonian . . . . .	153
C.5 Including spin . . . . .	154
C.6 Effect of a non-localised potential . . . . .	155
C.7 Spectrum of an infinite strip . . . . .	157
<b>D Dynamical Shiba chain</b>	<b>159</b>
D.1 Derivation of the effective two-band model . . . . .	159
D.2 Winding number calculation . . . . .	166
D.3 Frequency domain description of the Shiba bands . . . . .	166
D.4 Shiba band gap at $E=B$ . . . . .	170
D.5 Circuit implementation of a precessing helical texture . . . . .	171
<b>E Asymptotic expansions</b>	<b>174</b>
<b>Annex</b>	<b>177</b>
<b>Bibliography</b>	<b>198</b>
<b>List of Publications</b>	<b>218</b>

# Part I

## Introduction

New ideas and theories developing around the turn of the XX century shaped modern theoretical physics. One of those theories – quantum mechanics – became thereupon an irreplaceable milestone for various research fields such as e.g. high-energy and condensed matter physics. Derived from Latin, the word 'quantum' means 'how great' or 'how many'. So how great quantum mechanics really is? How many different phenomena can be accurately circumscribed only within the scope of quantum theory?

Triumphant and irrefutable explanation of discrete atomic spectra by newborn quantum theory was followed by development of band structure theory enabling us to describe solid state physics. The latter led to remarkable technological advancements, allowing humanity to enter a new, digital era, and significantly augmented the pace of progress. One of the most promising applications of quantum mechanics nowadays are e.g. the rapidly developing fields of quantum computation and quantum chemistry. Today, condensed matter physics and quantum chemistry are becoming intertwined for two conspicuous reasons. First of all, all the devices in the experiments are becoming more complicated, and thus require sophisticated chemical engineering techniques. Second, it is important to be able to design new materials and structures with predetermined physical properties.

Despite all the pre-eminent success of quantum mechanics, not all the quantum phenomena were explained immediately after their discovery. Furthermore, certain theories, such as for example general relativity, appeared to be incompatible with quantum mechanics, giving rise to inevitable scepticism in the scientific community. Notably, it took decades to develop reasonable theories circumscribing superconductivity and providing at least a basic notion of the subject, by making very strong assumptions and leaving behind certain details and controversial issues. In spite of the aforementioned difficulties, it is hard to deny that a vast variety of phenomena is successfully described within the scope of the quantum mechanical approach.

In the chapters below I first give a very concise introduction into the phenomenon of superconductivity, providing the insight necessary to understand the rest of the manuscript. Second, a brief description of Friedel oscillations is conveyed, as well as their possible applications and the main motivations to study them. I finalise the introductory part by presenting the physics of impurity-induced in-gap states in superconductors, also known as Yu-Shiba-Rusinov states.

# Chapter 1

## Superconductivity

### 1.1 Experimental discovery

Like many other physical phenomena, superconductivity was first observed experimentally and then explained theoretically. The story of superconductivity began in 1911 when Dutch physicist Kamerlingh Onnes discovered that the resistance of mercury cooled down to critical temperature  $T_c = 4.2$  K dropped abruptly to zero [1]. In subsequent years more and more superconducting materials were being discovered, with different structures and critical temperatures, and more experiments were being carried out.

Two remarkable experimental discoveries played a key role in understanding the challenging phenomenon of superconductivity. First, in 1933 Meissner and Ochsenfeld found out that superconductors expelled applied magnetic fields [2], thus providing an oblique evidence of spin of electrons being one of the essential ingredients to attain superconducting state. Second, in 1950 Maxwell and Reynolds *et al.*, drawing upon experimentally measured critical temperatures of different isotopes of mercury, noted a strong dependence on the isotropic mass of the constituent element [3,4]. Today, their data can be interpreted in the following way: first, not only electrons are responsible for superconductivity. Second, since masses of ions are explicitly affecting superconducting phase transition temperatures, we conclude that vibrations of crystal lattices – phonons – should be taken into account to provide a consistent explanation.

## 1.2 Phenomenological and microscopic theories

Employing all the previously collected experimental data described above, two groundbreaking fundamental theories of superconductivity were developed by Ginzburg and Landau in 1950 and Bardeen, Cooper and Schrieffer in 1957. The former was initially formulated as a phenomenological theory [5], whereas the latter provided a complete microscopic description [6] sought for decades after the discovery of superconductors in 1911. Both aforementioned works were awarded with Nobel Prizes, due to their unquestionable significance and undeniable colossal impact on the condensed matter community.

Despite its phenomenological formulation, Ginzburg-Landau theory was exploited to explain and predict numerous macroscopic properties of superconductors. For instance, the type-I and type-II classification, associated with the presence of Abrikosov vortices, can be described within the scope of the aforementioned phenomenological approach. However, in 1959 Lev Gor'kov demonstrated that Bardeen–Cooper–Schrieffer theory (hereinafter referred to as the BCS theory) reduced to Ginzburg-Landau theory in the vicinity of the critical temperature [7]. Furthermore, it was proven that all the phenomenological parameters introduced by Ginzburg and Landau could be expressed in terms of microscopic parameters of the BCS theory. For the sake of simplicity, I restrict myself in what follows to speak only in terms of the latter.

## 1.3 Bardeen–Cooper–Schrieffer theory

One of the most important concepts lying at the core of superconductivity is electron-phonon interaction. At the first glance it seems ridiculous – how can electrons interact with phonons? Phonons do not carry any electric charge, therefore Coulomb interaction does not play a role. What are we left with?

Before going into the details of the BCS theory, I would like to start with a simple experiment that will elucidate the origins of electron-phonon interaction. Imagine a large square elastic piece of fabric held by its corners as it is shown in Fig. 1.1 with a metallic ball lying on its surface. It is clear without any calculations that the ball bends the surface creating a 'potential well' in the middle of the square. What will happen if one now adds another ball, exactly like the first one? The answer is obvious even without carrying out the experiment – the second

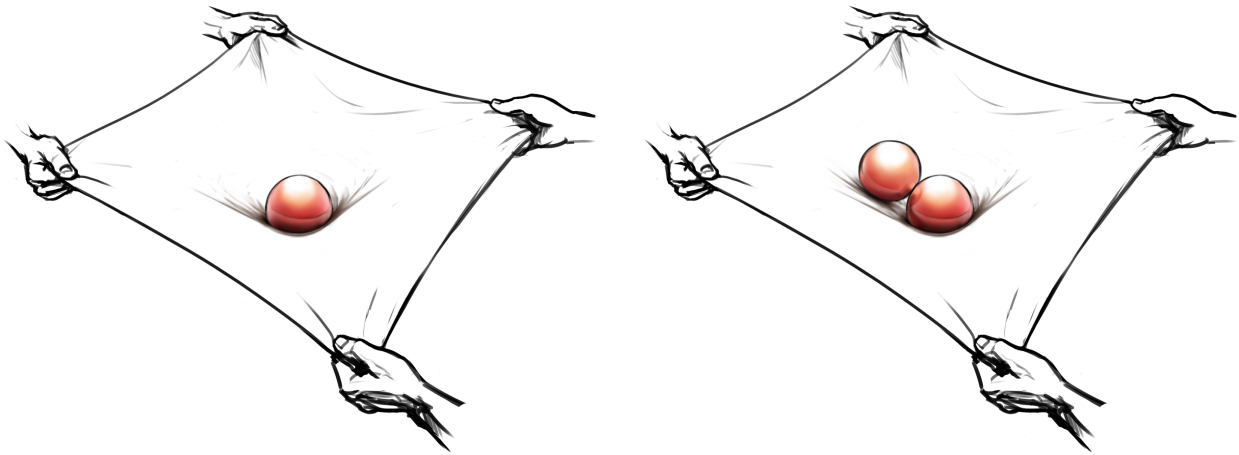


Figure 1.1: Thought experiment providing an analogy for electrons (red balls) moving through a crystal lattice (piece of elastic fabric). A single electron interacts with positively charged ions of the lattice, deforming it. If the temperature of the system is low enough, this deformation may result in an effective attractive interaction between electrons, enabling them to form pairs. (Image by I. Tetin)

ball, wherever we put it on the surface, will tend to minimise its energy, and thus eventually will stick to the first ball, as it is demonstrated in Fig. 1.1. Imagine now that those balls were both carrying some negative charge, what would happen in that case? It is clear that a new energy scale – Coulomb interaction – is thereby introduced into the system, and hence the resulting state depends now on which energy scale dominates. Let us restrict ourselves to the situation when the Coulomb energy is smaller than the potential energy acquired by the balls. In this particular case we will end up having a situation similar to the first experiment, where the balls did not care any electric charge. Therefore, effectively these balls will be again attracted to each other – that is what an experimentalist will observe. And finally, one should say that if for some reason the corners of the fabric are constantly shaken with sufficiently large amplitudes, the picture with two balls sticking to each other will never occur.

The logic described above can be applied to electrons moving in the electric field of positive ions constituting the crystal lattice of a given solid. The only difference is that in the thought experiment in Fig. 1.1 the mass of the balls was the reason of surface bending, whereas here it is the negative charge of electron responsible for it. Therefore, electrons moving through a crystal lattice of positively charged ions can deform the lattice, and these deformations can result in effective attraction of electrons, even though we know that Coulomb repulsion tends to keep them apart. Hence it is energetically favourable for electrons to move closer to each other, i.e. form pairs. The last remark about shaking the corners of the fabric is a direct analogue

of temperature. The higher the temperature, the more the lattice is shaken, and therefore the effect described above is less pronounced or even absent. This is one of the reasons why superconductivity mainly occurs at low temperatures.

These pairs of electrons are called Cooper pairs, one of the most salient building blocks of the BCS theory of superconductivity. Of course, the explanation above is an explanation in a nutshell, however it gives us the flavour of the phenomenon. As soon as the Cooper pairs are formed, instead of a gas of fermions we are dealing with a gas of bosons. Which brings us to the second milestone of the BCS theory, namely the fact that superconductivity within this framework is a macroscopic effect of Bose condensation of Cooper pairs.

Despite the fact that numerous superconducting phenomena can be circumscribed in terms of the aforementioned theories, for calculations carried out in this manuscript it is more practical to use the Bogoliubov–de Gennes Hamiltonian derived within the scope of mean-field approach to the BCS theory.

## 1.4 Bogoliubov–de Gennes Hamiltonian

We start by writing a Hamiltonian of a system of pairwise interacting fermions:

$$\hat{H}_{micr} = \sum_{\mathbf{p},\sigma} \left( \frac{p^2}{2m} - \mu \right) \hat{c}_{\mathbf{p},\sigma}^\dagger \hat{c}_{\mathbf{p},\sigma} + \frac{1}{2} \sum_{\mathbf{p}_i,\sigma,\mathbf{p}'_i,\sigma'} \langle \mathbf{p}'_1\sigma \mathbf{p}'_2\sigma' | U | \mathbf{p}_1\sigma \mathbf{p}_2\sigma' \rangle \hat{c}_{\mathbf{p}'_1,\sigma}^\dagger \hat{c}_{\mathbf{p}'_2,\sigma'}^\dagger \hat{c}_{\mathbf{p}_2,\sigma'} \hat{c}_{\mathbf{p}_1,\sigma}, \quad (1.1)$$

where  $\hat{c}_{\mathbf{p},\sigma}^\dagger$  ( $\hat{c}_{\mathbf{p},\sigma}$ ) are creation (annihilation) fermionic operators of particles with momentum  $\mathbf{p}$  and spin  $\sigma$ . Electron-phonon interaction is denoted by  $U$ ,  $\mu$  is the chemical potential. In what follows we apply all the possible simplifications to the equation above.

First of all, it is worth mentioning that in the second summation in Eq. (1.1) we must take into account momentum conservation, i.e.  $\mathbf{p}'_1 + \mathbf{p}'_2 = \mathbf{p}_1 + \mathbf{p}_2$ . To simplify the following discussion, we also assume that electron-phonon interaction is purely local, and thus the matrix element of the second term can be replaced

$$\langle \mathbf{p}'_1\uparrow \mathbf{p}'_2\downarrow | U | \mathbf{p}_1\uparrow \mathbf{p}_2\downarrow \rangle \rightarrow \langle 00 | U | 00 \rangle \equiv U_0/V.$$

Note also that the assumption of locality ensures that only fermions with opposite spins can be

created or annihilated on the same site in accordance with the Pauli exclusion principle, and therefore, only the matrix elements corresponding to interaction without subsequent spin flip survive. After all these assumptions we get:

$$\hat{H}_{micr} = \sum_{\mathbf{p},\sigma} \left( \frac{p^2}{2m} - \mu \right) \hat{c}_{\mathbf{p},\sigma}^\dagger \hat{c}_{\mathbf{p},\sigma} + \frac{U_0}{2V} \sum_{\mathbf{p}_i,\sigma,\mathbf{p}'_i} \hat{c}_{\mathbf{p}'_i,\sigma}^\dagger \hat{c}_{\mathbf{p}'_i,-\sigma}^\dagger \hat{c}_{\mathbf{p}_2,-\sigma} \hat{c}_{\mathbf{p}_1,\sigma}. \quad (1.2)$$

Further simplifications can be made if one counts the number of interacting pairs with resulting momentum  $\mathbf{p} = \mathbf{p}_1 + \mathbf{p}_2$ . We hence find out that the number of pairs with  $\mathbf{p} = \mathbf{0}$  is much larger than the number of pairs with  $\mathbf{p} \neq \mathbf{0}$ , and therefore the latter can be neglected. Finally we have

$$\hat{H}_{micr} \approx \sum_{\mathbf{p},\sigma} \left( \frac{p^2}{2m} - \mu \right) \hat{c}_{\mathbf{p},\sigma}^\dagger \hat{c}_{\mathbf{p},\sigma} + \frac{U_0}{V} \sum_{\mathbf{p},\mathbf{p}'} \hat{c}_{\mathbf{p}\uparrow}^\dagger \hat{c}_{-\mathbf{p}\downarrow}^\dagger \hat{c}_{-\mathbf{p}'\downarrow} \hat{c}_{\mathbf{p}'\uparrow}. \quad (1.3)$$

Diagonalising the Hamiltonian above is quite complex, and therefore we make one last simplifying step using the mean-field approach. We denote

$$\Delta_s = \langle \hat{c}_{-\mathbf{p}\downarrow} \hat{c}_{\mathbf{p}\uparrow} \rangle \quad (1.4)$$

which is an anomalous non-zero average for a superconducting state (complex parameter in the general case), and we rewrite Eq. (1.3) in the following form:

$$\hat{H} = \sum_{\mathbf{p},\sigma} \xi_p \hat{c}_{\mathbf{p},\sigma}^\dagger \hat{c}_{\mathbf{p},\sigma} + \sum_{\mathbf{p}} \left[ \Delta_s^* \hat{c}_{-\mathbf{p}\downarrow} \hat{c}_{\mathbf{p}\uparrow} + \Delta_s \hat{c}_{-\mathbf{p}\downarrow}^\dagger \hat{c}_{\mathbf{p}\uparrow}^\dagger \right] + \text{const}, \quad (1.5)$$

where  $\xi_p \equiv p^2/2m - \mu$ . Finally, we introduce a basis consisting of both particle-hole and spin degrees of freedom, the so-called Nambu basis  $\Psi_{\mathbf{p}} \equiv \left\{ c_{\mathbf{p}\uparrow}, c_{\mathbf{p}\downarrow}, c_{-\mathbf{p}\downarrow}^\dagger, -c_{-\mathbf{p}\uparrow}^\dagger \right\}^T$ , and Eq. (1.5) thus reads

$$\hat{H} = \frac{1}{2} \sum_{\mathbf{p}} \Psi_{\mathbf{p}}^\dagger H_{\text{BdG}}(\mathbf{p}) \Psi_{\mathbf{p}} + \text{const},$$

where the Bogoliubov–de Gennes Hamiltonian (hereinafter referred to as BdG)  $H_{\text{BdG}}$  written in the Nambu basis takes the form:

$$H_{\text{BdG}}(\mathbf{p}) = \begin{pmatrix} \xi_p & 0 & \Delta_s & 0 \\ 0 & \xi_p & 0 & \Delta_s \\ \Delta_s & 0 & -\xi_p & 0 \\ 0 & \Delta_s & 0 & -\xi_p \end{pmatrix} \equiv \xi_p \sigma_0 \otimes \tau_z + \Delta_s \sigma_0 \otimes \tau_x. \quad (1.6)$$

Above we have used the tensor product  $\otimes$ , namely the matrix  $\sigma_0$  acting in spin subspace as identity matrix and  $\tau_z, \tau_x$  acting in particle-hole subspace as the corresponding Pauli matrices. Depending on the context, in what follows I will employ both tensor product notation and four by four matrices. The foregoing discussion implies that we stay within the frame of the mean-field approach, and parameter  $\Delta_s$ , which is nothing but the superconducting gap or, equivalently, superconducting pairing, must be found self-consistently employing its definition in terms of the anomalous average. I would like to mention also that the Hamiltonian defined in Eq. (1.6) respects particle-hole symmetry (PHS), and the description I chose is 'particle-hole redundant'. It implies that for any eigenstate corresponding to energy  $E$  there is always a particle-hole partner with energy  $-E$ , embedded by construction. It is therefore important to be careful while calculating observables in order to avoid counting the same thing twice.

Throughout the derivation of Eq. (1.6) we made several strong assumptions, some of them being not necessary to attain a superconducting state. E.g. we have used the fact that the only Cooper pairs forming are those of electrons of opposite spins, which is not necessarily the case. Fortunately, there is a possibility to extend the BdG Hamiltonian to other types of pairing, which brings us to the next section.

## 1.5 Cooper pairs beyond the BdG Hamiltonian

Even though the BdG Hamiltonian does not describe properly the whole range of observed superconducting phenomena, its extensions were proven to be applicable. One of the possible extensions is to consider pairing different from the conventional pairing described in the previous section. When two electrons form a Cooper pair, there are two degrees of freedom, or equivalently, two quantum numbers to 'play with': the spin quantum number and the orbital quantum number. Depending on whether spins of electrons compensate each other or not, one can have a singlet with  $S = 0$  or a triplet with  $S = 1$ . Note that in the previous section we considered only singlet pairing. The orbital quantum number can take all the non-negative integer values, i.e.  $L = 0, 1, 2$ , etc. However, these numbers cannot be chosen independently since the wave function of a fermionic system must be antisymmetric in accordance with the Pauli exclusion principle. Spin and orbital degrees of freedom are not coupled, ergo the wave function can be written as a product of orbital and spin parts. A product of two functions is an-

tisymmetric if and only if one of the functions is symmetric and the other one is antisymmetric. Therefore, we must choose  $S$  and  $L$  such that

$$(-1)^L \cdot (-1)^{S+1} = -1.$$

Hence there are two possibilities for the wave function of a Cooper pair: symmetric orbital part ( $L \in 2\mathbb{Z}_+$ ) and antisymmetric spin part ( $S = 0$ ), or vice versa, i.e. antisymmetric orbital part ( $L \in 1+2\mathbb{Z}_+$ ) and symmetric spin part ( $S = 1$ ). The former corresponds to an s-wave superconductor ( $L = 0, S = 0$ ), a d-wave superconductor ( $L = 2, S = 0$ ), etc., whereas the latter refers to a p-wave superconductor ( $L = 1, S = 1$ ), an f-wave superconductor ( $L = 3, S = 1$ ) and so forth. It is now clear that the BdG Hamiltonian given by Eq. (1.6) describes an s-wave superconductor, also known as a *conventional* superconductor. Any other type of superconductivity distinct from conventional is usually referred to as *unconventional* superconductivity.

In my thesis I am going to use conventional superconductors, as well as one type of unconventional ones – p-wave superconductors, restricting myself to 2D or 1D cases. To extend the description given by Eq. (1.6), henceforward I will employ the so-called  $\mathbf{d}$ -vector notation developed by R. Balian and N.R. Werthamer in Ref. [8]. In the most general case one can write the superconducting pairing function as a  $2 \times 2$  matrix in spin subspace:

$$\Delta(\mathbf{p}) = \begin{pmatrix} \Delta_{\uparrow\downarrow}(\mathbf{p}) & -\Delta_{\uparrow\uparrow}(\mathbf{p}) \\ \Delta_{\downarrow\downarrow}(\mathbf{p}) & -\Delta_{\downarrow\uparrow}(\mathbf{p}) \end{pmatrix}$$

To connect this pairing function to that considered before, we must set  $-\Delta_{\uparrow\uparrow} = \Delta_{\downarrow\downarrow} = 0$ , and simultaneously  $\Delta_{\uparrow\downarrow} = -\Delta_{\downarrow\uparrow} = \Delta_s = \text{const}$ . One can always rewrite any  $2 \times 2$  matrix in the basis of Pauli matrices  $\sigma_0$  (unity matrix) and  $\boldsymbol{\sigma} = \{\sigma_x, \sigma_y, \sigma_z\}$ . Thus we decompose

$$\Delta(\mathbf{p}) = d_0(\mathbf{p})\sigma_0 + \mathbf{d}(\mathbf{p}) \cdot \boldsymbol{\sigma},$$

where we define

$$d_0(\mathbf{p}) \equiv \frac{\Delta_{\uparrow\downarrow} - \Delta_{\downarrow\uparrow}}{2}, \quad d_x(\mathbf{p}) \equiv \frac{\Delta_{\downarrow\downarrow} - \Delta_{\uparrow\uparrow}}{2}, \quad d_y(\mathbf{p}) \equiv \frac{\Delta_{\downarrow\downarrow} + \Delta_{\uparrow\uparrow}}{2i}, \quad d_z(\mathbf{p}) \equiv \frac{\Delta_{\uparrow\downarrow} + \Delta_{\downarrow\uparrow}}{2}. \quad (1.7)$$

To understand the connection of  $d_0, \mathbf{d}$  to pairing types introduced above, we first reconsider the case of a purely singlet pairing. Due to the fact that the orbital part must be symmetric

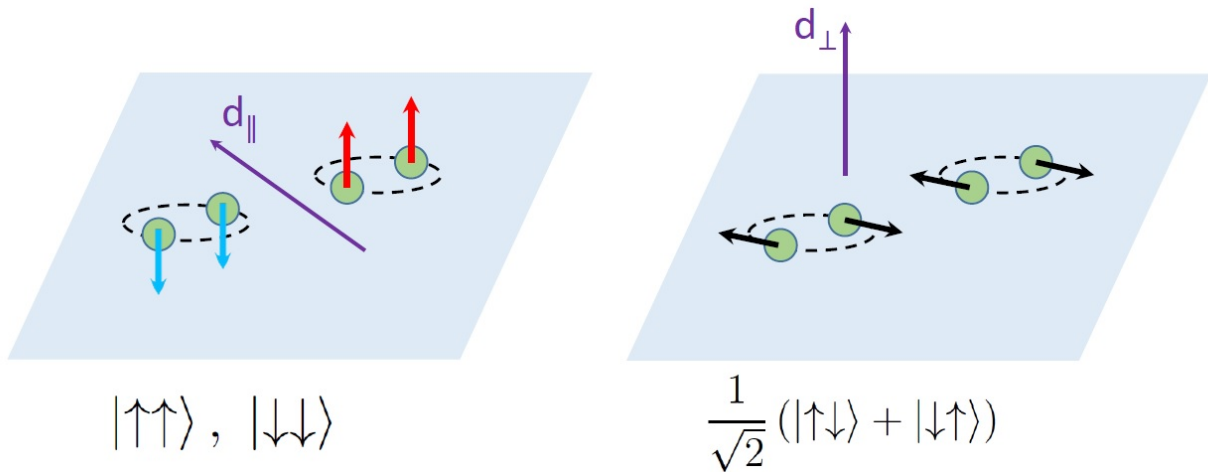


Figure 1.2: Left: helical p-wave with  $\mathbf{d}_{\parallel}(\mathbf{p}) = (p_y, -p_x, 0)$ ; Right: chiral p-wave with  $\mathbf{d}_{\perp}(\mathbf{p}) = (0, 0, p_x + ip_y)$ . In the helical p-wave there are Cooper pairs with spins perpendicular to the plane of the superconductor, either both up or both down, whereas in the chiral p-wave Cooper pair condensate consists of pairs with opposite spins lying in the plane, as the direction of the  $\mathbf{d}$ -vector dictates. Note that despite the fact that the pair contains electrons with antiparallel spins, the spin part of the wave function is symmetric, since the combination is even (unlike the case of an s-wave).

we have  $d_0(-\mathbf{p}) = d_0(\mathbf{p})$ ,  $\mathbf{d} = \mathbf{0}$ , and in particular  $d_0 = \Delta_s$  in case of an s-wave superconductor. Second, we turn to the case of a purely triplet pairing. As argued above, the orbital part of a triplet pairing function must be antisymmetric, therefore in order to achieve purely triplet pairing we set  $d_0 = 0$ , and we require  $\mathbf{d}(-\mathbf{p}) = -\mathbf{d}(\mathbf{p})$ .

It is also worth discussing the physical meaning of the  $\mathbf{d}$ -vector. It points in a direction perpendicular to the plane in which the spins of Cooper pairs lie. Throughout this manuscript I consider two types of p-wave superconductors, both being gapped for all the values of momentum  $\mathbf{p}$ . The first type respecting time-reversal symmetry (TRS) will be called in what follows 'helical p-wave', whereas the second type breaking TRS will be referred to as 'chiral p-wave'. The helical p-wave can be described by the following choice of the  $\mathbf{d}$ -vector:  $\mathbf{d}_{\parallel}(\mathbf{p}) = (p_y, -p_x, 0)$ , whereas the chiral p-wave is given by  $\mathbf{d}_{\perp}(\mathbf{p}) = (0, 0, p_x + ip_y)$ . To show explicitly what types of Cooper pairs we have in these cases, I refer the reader to Fig. 1.2.

Finally, to extend the BdG Hamiltonian to the cases of both s-wave and p-wave pairing, we rewrite Eq. (1.6) utilising the  $\mathbf{d}$ -vector notation developed above:

$$H_{\text{BdG}}(\mathbf{p}) = \begin{pmatrix} \xi_p \sigma_0 & \Delta(\mathbf{p}) \\ \Delta^\dagger(\mathbf{p}) & -\xi_p \sigma_0 \end{pmatrix}, \quad (1.8)$$

where  $\Delta(\mathbf{p}) = d_0(\mathbf{p})\sigma_0 + \mathbf{d}(\mathbf{p}) \cdot \boldsymbol{\sigma}$ , and  $\sigma$ -matrices act in spin subspace. The Hamiltonian defined by Eq. (1.8) will be used hereinafter to describe various superconductors with both s-wave and p-wave pairing.

# Chapter 2

## Friedel oscillations

Unlike the phenomenon of superconductivity, Friedel oscillations were first predicted theoretically by J. Friedel in 1958 [9], and thereafter observed experimentally. He considered the problem of electrons in a metal scattered by a single localised scalar impurity and showed that such scattering resulted in oscillations in local density of states of the underlying metal.

It was not until 1993 that these oscillations were observed utilising a recently developed powerful experimental tool – scanning tunnelling microscopy (STM) [10, 11]. The main idea behind this method is to move a conducting tip applied over the surface of a studied material, and to measure the tunnelling conductance that is proportional to the local density of states. In case of Friedel oscillations the observed conductance has peaks and dips depending on the position of the tip with respect to the position of the impurity. Hence the STM image resembles concentric circular ripples created by a stone dropped into water (see Fig. 2.1).

The significance of this discovery is hard to overestimate since it became the second most explicit way to show the quantum nature of microscopic objects (electrons in case of Friedel oscillations), after the famous Young’s double-slit experiment in 1801.

### 2.1 Explanation in a nutshell

It appears that virtual bound states form due to interference of incident and outgoing electronic waves, or in other words, quasiparticle states with finite lifetime. One of the reasons for that is

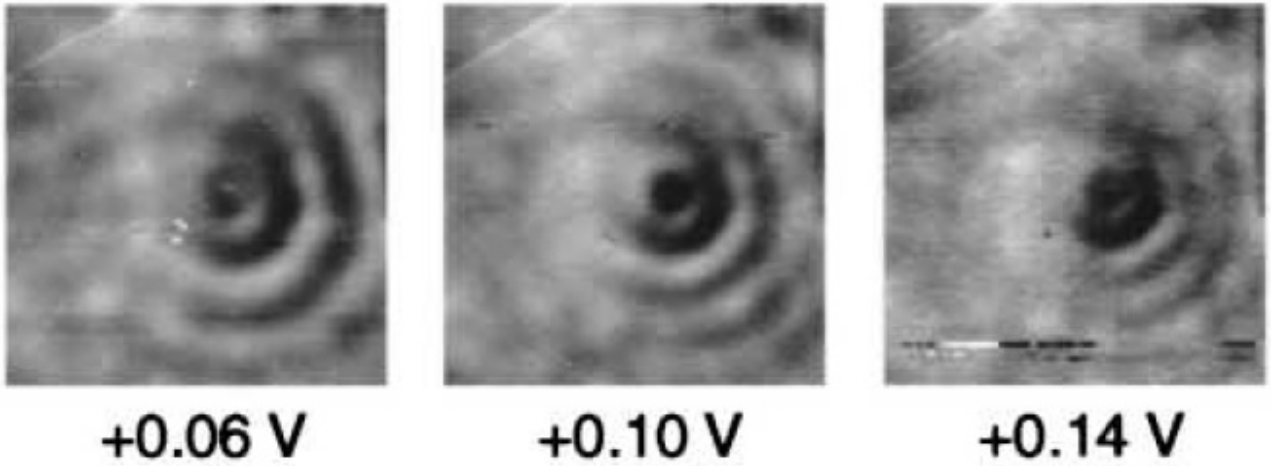


Figure 2.1: STM images of Friedel oscillations taken at different tip voltages. Higher values of the tip voltage correspond to higher energies of electrons. Image is taken from Ref. [12].

the fact that they are plunged into the continuum of bulk states, or mathematically speaking, the quasiparticle Green's function pole contains a non-zero imaginary component responsible for the exchange with the bulk.

The first step to understand the phenomenon of Friedel oscillations is to use a well-known one-dimensional example of a particle scattering on a wall, playing the role of an impurity. An incident right-moving plane wave with momentum  $k_0$  is fully reflected by an infinite wall, and thus becomes an outgoing left-moving wave with momentum  $-k_0$ . The resulting picture is shown in Fig. 2.2: incident and reflected waves interfere forming a standing wave with wavelength  $\lambda = 2\pi/2k_0 = \pi/k_0$ . Despite being oversimplified, this analogy allows to taste the flavour of this phenomenon.

In what follows I turn to a more complicated case of electrons with parabolic spectrum  $E(\mathbf{k}) = \frac{\mathbf{k}^2}{2m}$  scattering on a localised impurity. At a given energy  $E_0$  electrons live on circular contours defined by  $E_0 = \frac{\mathbf{k}^2}{2m}$ . Elastic scattering of these electrons by point-like impurities can change their momenta between all the points on the circle. Therefore, the resulting state is a superposition of all the stationary waves with all the possible momenta, the dominating ones being those with wavelength  $\lambda_E = \pi/k(E)$ . These waves correspond to scattering between two diametrically opposite points on circular contours with momentum  $2k(E)$ . Hence the resulting picture will contain standing concentric waves centred at the position of the impurity. Averaged over all the energies, the local density of states of a 3D metal in the presence of a localised

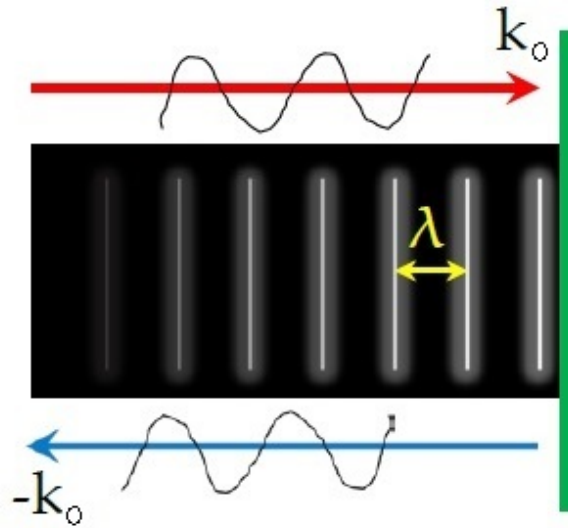


Figure 2.2: A schematic picture of standing waves with  $\lambda = \pi/k_0$  forming due to interference of incident (red arrow) and outgoing (blue arrow) waves scattered by an infinite wall (green vertical line).

impurity can be written as

$$\delta\rho(r) \sim \frac{\cos 2k_F r}{r^2} \quad (2.1)$$

The power-law decay changes as a function of dimensionality of the problem, being  $1/r$  in 2D and absent in 1D, as well as a function of lattice symmetries. For instance, in graphene, Friedel oscillations are expected to have the conventional  $1/r$  behaviour characteristic for a 2D system, however accidental cancellations due to additional symmetries of the honeycomb lattice lead to a  $1/r^2$  dependence of the local density of states (for details see Ref. [13]).

## 2.2 State of the art

Friedel oscillations were measured in various systems in 3D, as well as in low-dimensional systems, both 2D and 1D, where longer coherence lengths of electrons in comparison with the 3D case facilitate experimental observation. Despite being discovered more than fifty years ago, they still attract a lot of attention amongst condensed matter physicists [13–17].

One of the convenient experimental tools to study Friedel oscillations is to take the Fourier transform of the ripples in real space, obtained with STM. The resulting picture in momentum space contains sharp features corresponding to those wave vectors that are present in the

oscillatory terms in real space. That enables one to extract the dominant scattering processes. This experimental technique, also known as Fourier-transform scanning tunnelling microscopy (FT-STM), is a well-developed and versatile tool widely used nowadays [18–20].

To give an illustration I use Eq. (2.1) and perform the Fourier transform

$$\int d\mathbf{r} \frac{\cos 2k_F r}{r^2} e^{-i\mathbf{k}\mathbf{r}} = \frac{\pi^2}{k} [1 + \text{sgn}(k - 2k_F)], \quad \text{where } k = |\mathbf{k}|. \quad (2.2)$$

It is clear that the Fourier-transformed Friedel oscillations have a discontinuity at  $k = 2k_F$ , hence we expect to see a sharp feature appearing at that point.

One of the most fascinating things about Friedel oscillations is that we are capable of extracting some information about the underlying material by analysing the effects of disorder. It is somewhat counter-intuitive, since common knowledge dictates 'the purer the better' and that in the presence of impurities one is not able to study the desired properties of a sample. Notably, the original STM experiments on Friedel oscillations gave access to measuring the Fermi momentum by Fourier-transforming the real space data and looking at the  $\mathbf{k}$ -space features. Further examples provided in the next part of the manuscript are supporting this claim.

So far we got acquainted with the phenomena of superconductivity and Friedel oscillations in conducting systems. Having two physical phenomena of different nature at our disposal, it is often compelling to consider their interplay. It brings me to the final chord of the introductory part – are there any impurity-induced oscillations in superconductors?

# Chapter 3

## Yu-Shiba-Rusinov states

### 3.1 Theoretical prediction and discovery

It all started in 1959 when Anderson published his famous article about BCS superconductors with scalar disorder [21]. He argued that 'the B.C.S. theory in its original form, assuming a constant interaction, will be more nearly correct in the dirty superconductor region than it will be for pure superconductors'. This statement is referred to as 'Anderson's theorem', and it is worth noting that it holds only if, first of all, disorder is not breaking time-reversal symmetry (TRS), and second, we are dealing with a conventional BCS superconductor. The first condition breaks down e.g. for TRS-breaking magnetic disorder, which was proven to be destructive for the phenomenon of superconductivity [22]. The second condition does not hold for any unconventional superconductor.

Almost a decade later in three independent pioneering theoretical papers it was described how the superconducting order was suppressed in the presence of a single localised magnetic impurity [23–25]. It was found that a pair of bound states appeared in the superconducting gap (see Fig. 3.1). These states are called 'Yu-Shiba-Rusinov states', or simply 'Shiba bound states'. I refer to them in plural, however it is important to point out that there are two of them only due to the particle-hole redundancy of the Bogoliubov-de Gennes Hamiltonian. Therefore, it would be more accurate to think of them as of a single bound state with electron and hole parts.

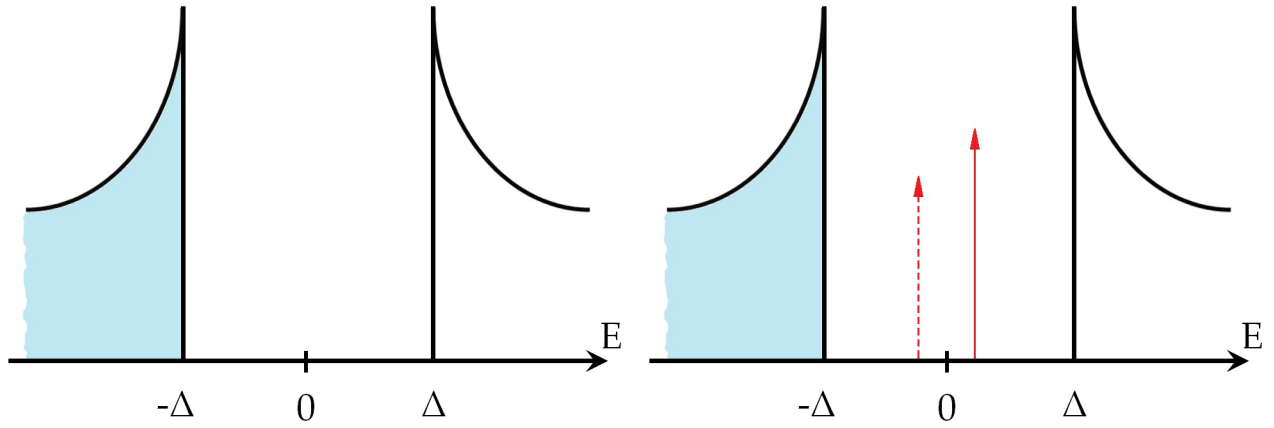


Figure 3.1: Left: Density of states of a conventional superconductor. All the states below the gap ( $E < -\Delta$ ) are filled (shown in turquoise) whereas there are no states in the gap ( $|E| < \Delta$ ) and above the gap ( $E > \Delta$ ). Right: Density of states of a conventional superconductor in the presence of a localised magnetic impurity. There is a pair of in-gap states (Shiba bound states) appearing at opposite energies (shown as red arrows), the dashed arrow stands for the negative-energy state.

It was not until the turn of the century when these states were observed experimentally with STM [26] for a 3D superconductor. Later, in 2015 they were also detected in a 2D superconductor, where their coherence lengths were larger than in 3D [27].

## 3.2 Underlying mechanism and properties

In this section I provide only qualitative explanations and demonstrations, leaving all the detailed derivations and formulae to the next part of my thesis.

Roughly speaking, Shiba bound states are an analogue of Friedel oscillations for superconducting systems, however there are important differences. To unveil the mechanism of formation of Shiba bound states we should keep in mind that, first of all, since we are dealing with a superconductor we should think in terms of Cooper pairs, not electrons. Second, a magnetic impurity creates a local magnetic field acting on spins of electrons, whereas in case of Friedel oscillations we were dealing with a localised scalar potential. In addition, we note that only classical spins of impurities are considered, therefore there is no Kondo physics in the discussion below.

In a nutshell, Cooper pairs are broken by a local classical magnetic field induced by an impurity (see the left column of Fig. 3.2). Afterwards, one of the electrons forming the pair couples to

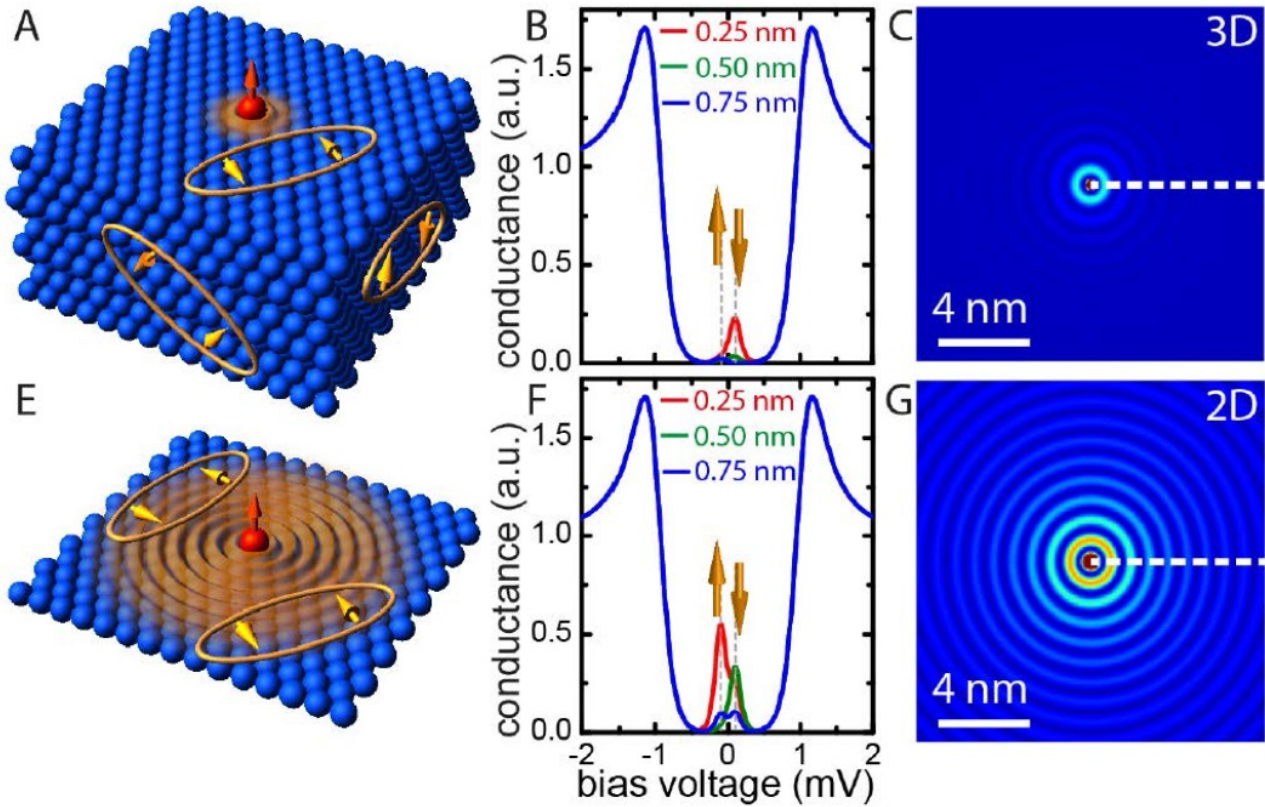


Figure 3.2: Shiba states in 3D (first row) and 3D (second row) superconductors. Left column: schematic pictures of superconductors with magnetic impurities (red spheres with arrows) and Cooper pairs (two yellow encircled arrows). Middle: Density of states of a superconductor with a localised magnetic impurity, measured with STM. Red and green peaks appearing at opposite energies correspond to Shiba states. Right: Spatial dependence of Shiba states given by STM measurements at energies of Shiba peaks in the middle column (cf. Fig. 2.1). Image is taken from Ref. [27].

the impurity, whereas the other one forms a subgap bound state. Similar to the case of Friedel oscillations, an STM measurement detects ripples of local density of states in real space (see the right column of Fig. 3.2). The drastic difference is that Shiba states are well-defined bound states forming at a *specific* energy value in the superconducting gap, whereas Friedel oscillations are given by virtual bound states forming at all the possible energy values, as described in the previous chapter. In other words, to detect Shiba states we must perform an STM measurement at a fixed energy value of the bound state (see Fig. 3.2), contrary to Friedel oscillations.

Note that Shiba states have opposite spin polarisation, which is in agreement with the explanation above. Indeed, one of the electrons of a Cooper pair couples to the impurity spin. In order to minimise the energy this coupling polarises the corresponding pair. And hence the outcome is a bound state polarised along the spin of the impurity.

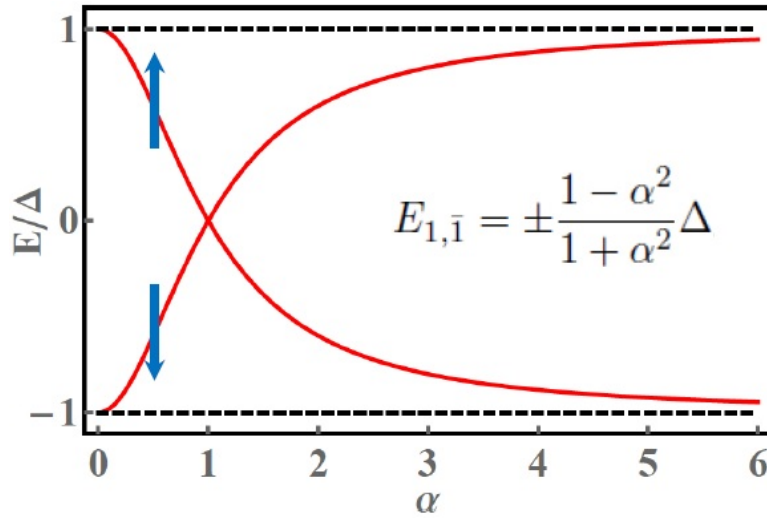


Figure 3.3: Energies of Shiba states as a function of the dimensionless impurity strength  $\alpha = \pi\nu JS$ , where  $\nu$  is the normal-phase density of states,  $J$  denotes the exchange coupling constant, and  $S$  is the spin of the impurity. Black dashed lines mark the superconducting gap, and blue arrows depict the spin polarisation of a corresponding state. The crossing point at  $\alpha = 1$  is associated with change of the ground state parity.

Let us now take a closer look at how the energies of Shiba states depend on the parameters of the system. In Fig. 3.3 I plot the energies of Shiba states as a function of the dimensionless impurity strength  $\alpha = \pi\nu JS$ , expressed in terms of the normal-phase density of states  $\nu$ , the exchange coupling constant between magnetic impurity and electrons  $J$ , and the spin of the impurity  $S$ . The corresponding formula

$$E_{1, \bar{1}} = \pm \frac{1 - \alpha^2}{1 + \alpha^2} \Delta \quad (3.1)$$

will be derived in the next part of my thesis, however, several comments should be made at this point.

Notably, the formula given by Eq. (3.1) becomes invalid for  $\alpha \gg 1$  due to breakdown of the mean-field theory approach. For large values of  $\alpha$ , the impurity is strong enough to modify crucially the superconducting order parameter, which hence cannot be set to a constant any more and must be defined self-consistently (for further details consider e.g. Ref. [28]). In this respect it is worth mentioning that in the majority of STM measurements Shiba states form at points closer to  $\alpha \sim 1$ , which justifies the validity of the mean-field approach. A qualitative criterion for the breakdown of the mean-field theory would be to have a renormalised superconducting gap in a region comparable to the coherence length of the bound states – in

that case the gap renormalisation cannot be ignored any longer.

Another 'dangerous' limit of Eq. (3.1) is the weak impurity regime, i.e.  $\alpha \ll 1$ . It is possible to treat the impurity spin classically and hence to avoid Kondo physics whilst the Kondo temperature  $T_K \sim \exp[-1/\nu JS]$  is smaller than the superconducting gap. As long as that condition holds Eq. (3.1) remains valid.

And finally, the peculiar crossing at  $\alpha = 1$  corresponds physically to the point where the impurity effectively binds an electron, thereby changing the superconducting ground state parity from even to odd.

Another point worth mentioning is that throughout this dissertation the spin of impurities is always treated classically, assuming that  $S \gg \hbar$ , and therefore it does not make too much sense to keep it in all the formulae below. Hence hereinafter I omit it in all the expressions by including it into the exchange coupling constant. In other words, I replace everywhere  $JS \rightarrow J$  and keep that in mind.

Further details and properties of Shiba states, as well as their possible applications, will be discussed in the next parts of this dissertation.

Hereinafter we set  $\hbar = 1$ .

## Part II

# Spin polarisation of Yu-Shiba-Rusinov states as a probe of the host superconductors

---

This isn't right. This isn't even wrong.

*Wolfgang Pauli*

In 1922 Otto Stern and Walther Gerlach conducted their famous experiment proving that angular momentum was quantised [29–31]. Silver atoms travelling in a non-uniform magnetic field were caught by a detector screen, which showed a discrete set of points, thus revealing the quantum nature of spin or, in other words, the so-called intrinsic angular momentum. Spin-related phenomena are widely used in everyday life. Nuclear magnetic resonance (NMR) and electron spin resonance are employed for spectroscopy in physics and chemistry, as well as in medicine.

Since the pioneering works of Yu, Shiba and Rusinov [23–25] it was known that magnetic impurity bound states in conventional superconductors were spin-polarised (see Fig. 3.3). It was not until 1997 when STM enabled to observe Yu-Shiba-Rusinov states [26], leaving behind, however, their spin polarisation. In order to detect the latter it is necessary to utilise the so-called spin-polarised STM. Created by Roland Wiesendanger in the early nineties [32], it is currently a well-established experimental technique accessible in many different laboratories. The main idea behind SP STM is to use a magnetised tip instead of an ordinary metallic one. Such a tip favours only tunnelling of electrons with spins parallel to that of electrons in the tip, thus allowing to study spin-related properties of electrons.

It is worth noting that spin-resolved spectra of Shiba states induced by Mn impurities in  $\text{MnB}_2$  were analysed theoretically in Ref. [33]. The authors paid particular attention to scattering from non-local impurity potentials and related Shiba peaks, proposing to distinguish those from the bulk states by employing SP STM spectroscopy.

Motivated by the aforementioned findings, in what follows below I focus on the spin polarisation of Yu-Shiba-Rusinov states giving access to various properties of underlying superconductors, both conventional and unconventional. This part is organised as follows: in the next chapter I describe in detail the model and the methods we have used in our work. The next two chapters are dedicated to determining the spin-orbit coupling constant and discriminating between s-wave and p-wave pairing by analysing the spin polarisation of Shiba states, as well as determining the type of p-wave pairing.

# Chapter 4

## General model and methods

### 4.1 Generalised BdG Hamiltonian

We consider a low-dimensional superconductor (2D or 1D) within the scope of a generalised Bogoliubov-de Gennes Hamiltonian. Written in the Nambu basis  $\Psi_{\mathbf{p}} = (\psi_{\uparrow\mathbf{p}}, \psi_{\downarrow\mathbf{p}}, \psi_{\downarrow-\mathbf{p}}^\dagger, -\psi_{\uparrow-\mathbf{p}}^\dagger)^\text{T}$  it reads

$$\mathcal{H}_0 = \begin{pmatrix} \xi_{\mathbf{p}}\sigma_0 + \lambda(p_y\sigma_x - p_x\sigma_y) & \Delta(\mathbf{p}) \\ \Delta^\dagger(\mathbf{p}) & -\xi_{\mathbf{p}}\sigma_0 - \lambda(p_y\sigma_x - p_x\sigma_y) \end{pmatrix}, \quad (4.1)$$

where  $\Delta(\mathbf{p}) = \Delta_s\sigma_0 + \varkappa \mathbf{d}(\mathbf{p}) \cdot \boldsymbol{\sigma}$  is a mixed s-wave and p-wave pairing, and  $\xi_{\mathbf{p}} = \mathbf{p}^2/2m - \varepsilon_F$  is the spectrum of free electrons with Fermi energy  $\varepsilon_F$ .  $\lambda$  is the Rashba spin-orbit coupling constant. To describe a 2D superconductor we set momentum  $\mathbf{p} \equiv (p_x, p_y)$ , whereas in the 1D case we take  $\mathbf{p} \equiv p_x$  and  $p_y \rightarrow 0$ . Note that the concept of  $\mathbf{d}$ -vector is not vernacular in 1D systems, however we can still exploit it *formally*. The operator  $\psi_{\sigma\mathbf{p}}^\dagger$  creates a particle of spin  $\sigma = \uparrow, \downarrow$  and momentum  $\mathbf{p}$ . The system is considered to lay in the  $(x, y)$  plane. Pauli matrices  $\boldsymbol{\sigma} = (\sigma_x, \sigma_y, \sigma_z)$  act in spin subspace.

### 4.2 T-matrix approach

In what follows in this part of the manuscript we study what happens when a point-like single impurity is introduced into a system described by Eq. (4.1). We consider impurities that have

both a scalar potential component  $U$  and a magnetic potential component  $\mathbf{J} = (J_x, J_y, J_z)$ , and are described by the following Hamiltonian:

$$\mathcal{H}_{imp} = V\delta(\mathbf{r}) \equiv \begin{pmatrix} U\sigma_0 + \mathbf{J} \cdot \boldsymbol{\sigma} & 0 \\ 0 & -U\sigma_0 + \mathbf{J} \cdot \boldsymbol{\sigma} \end{pmatrix} \delta(\mathbf{r}), \quad (4.2)$$

where  $U$  and  $\mathbf{J}$  are the scalar and magnetic strengths respectively. Hereafter we treat these impurities perturbatively without taking into account the superconducting gap renormalisation [28] occurring at very small distances compared to the coherence length of both the superconductor and the bound states. It is also worth mentioning that we consider only scattering in the  $s$ -channel, which is equivalent to taking a  $\delta$ -like potential. A plausible justification for such an approximation is provided e.g. in Appendix C.6.

We solve the problem of finding and studying the properties of subgap states induced by impurities given by Eq. (4.2) in low-dimensional superconductors defined by Eq. (4.1). In what follows we use two different approaches that eventually converge towards the same results (qualitatively, not quantitatively). Our goal is to find the spin polarisation of impurity-induced subgap states. First, we tackle the problem with the help of the so-called T-matrix that is described e.g. in Ref. [34]. Second, we exploit an approach described in detail in Ref. [35], allowing to find the wave functions of impurity-induced states. For the sake of brevity, I am omitting the formulae for the 1D case, since they can be straightforwardly obtained from those for the 2D case.

We start by defining the unperturbed (bare) retarded Green's function in momentum space

$$G_0(E, \mathbf{p}) = [(E + i0)\mathbb{I}_4 - \mathcal{H}_0(\mathbf{p})]^{-1} \quad (4.3)$$

and in real space as the Fourier transform of Eq. (4.3)

$$G_0(E, \mathbf{r}) = \int \frac{d\mathbf{p}}{(2\pi)^2} G_0(E, \mathbf{p}) e^{i\mathbf{p}\mathbf{r}}. \quad (4.4)$$

The small positive imaginary shift  $+i0$  ensures that we consider the retarded Green's function and allows to avoid singularities while inverting the corresponding matrix. To find the perturbed retarded Green's function in the presence of a localised impurity we use the perturbation series given by Eq. (3.15) from Ref. [34], where we replace the Fourier-transformed  $\hat{U}_{\mathbf{k}\mathbf{k}'}$  by  $V$  defined

in Eq. (4.2):

$$G_0(\mathbf{p}, \mathbf{p}') = G_0(\mathbf{p}) + G_0(\mathbf{p})V G_0(\mathbf{p}') + G_0(\mathbf{p})V \sum_{\mathbf{p}''} G_0(\mathbf{p}'')V G_0(\mathbf{p}') + \dots \equiv G_0(\mathbf{p}) + G_0(\mathbf{p})T(E)G_0(\mathbf{p}'),$$

where

$$T(E) \equiv V + V \sum_{\mathbf{p}''} G_0(\mathbf{p}'')V + \dots = V + V \sum_{\mathbf{p}''} G_0(\mathbf{p}'')T(E).$$

Thus, for a localised impurity potential the perturbed retarded Green's function can be expressed in terms of a T-matrix that depends solely on energy, and can be found as follows

$$T(E) = \left[ \mathbb{I}_4 - V \sum_{\mathbf{p}''} G_0(\mathbf{p}'') \right]^{-1} V \quad (4.5)$$

It is worth noting that the T-matrix contains all the information about the perturbed system. Mathematically speaking, the poles of the T-matrix correspond to the energies of impurity-induced states. The real-space perturbed Green's function can be written in terms of bare Green's functions in real space and the T-matrix:

$$\Delta G(E, \mathbf{r}) \equiv G_0(E, -\mathbf{r})T(E)G_0(E, \mathbf{r}). \quad (4.6)$$

Now we can express the non-polarised,  $\delta\rho(\mathbf{r}, E)$ , and spin-polarised local density of states (SP LDOS),  $S_{\hat{n}}(\mathbf{r}, E)$ , with  $\hat{n} = x, y, z$  in terms of Eqs. (4.5,4.6)

$$S_x(\mathbf{r}, E) = -\frac{1}{\pi} \text{Im} [\Delta G_{12}(E, \mathbf{r}) + \Delta G_{21}(E, \mathbf{r})], \quad (4.7)$$

$$S_y(\mathbf{r}, E) = -\frac{1}{\pi} \text{Re} [\Delta G_{12}(E, \mathbf{r}) - \Delta G_{21}(E, \mathbf{r})], \quad (4.8)$$

$$S_z(\mathbf{r}, E) = -\frac{1}{\pi} \text{Im} [\Delta G_{11}(E, \mathbf{r}) - \Delta G_{22}(E, \mathbf{r})], \quad (4.9)$$

$$\delta\rho(\mathbf{r}, E) = -\frac{1}{\pi} \text{Im} [\Delta G_{11}(E, \mathbf{r}) + \Delta G_{22}(E, \mathbf{r})], \quad (4.10)$$

where  $\Delta G_{ij}$  denotes the  $ij$ -th component of the matrix  $\Delta G$ . The FT of the SP LDOS components in momentum space,  $S_{\hat{n}}(\mathbf{p}, E) = \int d\mathbf{r} S_{\hat{n}}(\mathbf{r}, E)e^{-i\mathbf{p}\mathbf{r}}$ , with  $\hat{n} = x, y, z$ , as well as the FT

of the non-polarised LDOS,  $\delta\rho(\mathbf{p}, E) = \int d\mathbf{r} \delta\rho(\mathbf{r}, E)e^{-i\mathbf{p}\mathbf{r}}$  are given by

$$S_x(\mathbf{p}, E) = \frac{i}{2\pi} \int \frac{d\mathbf{q}}{(2\pi)^2} [\tilde{g}_{12}(E, \mathbf{q}, \mathbf{p}) + \tilde{g}_{21}(E, \mathbf{q}, \mathbf{p})], \quad (4.11)$$

$$S_y(\mathbf{p}, E) = \frac{1}{2\pi} \int \frac{d\mathbf{q}}{(2\pi)^2} [g_{21}(E, \mathbf{q}, \mathbf{p}) - g_{12}(E, \mathbf{q}, \mathbf{p})], \quad (4.12)$$

$$S_z(\mathbf{p}, E) = \frac{i}{2\pi} \int \frac{d\mathbf{q}}{(2\pi)^2} [\tilde{g}_{11}(E, \mathbf{q}, \mathbf{p}) - \tilde{g}_{22}(E, \mathbf{q}, \mathbf{p})], \quad (4.13)$$

$$\delta\rho(\mathbf{p}, E) = \frac{i}{2\pi} \int \frac{d\mathbf{q}}{(2\pi)^2} [\tilde{g}_{11}(E, \mathbf{q}, \mathbf{p}) + \tilde{g}_{22}(E, \mathbf{q}, \mathbf{p})], \quad (4.14)$$

where  $d\mathbf{q} \equiv dq_x dq_y$ ,

$$g(E, \mathbf{q}, \mathbf{p}) = G_0(E, \mathbf{q})T(E)G_0(E, \mathbf{p} + \mathbf{q}) + G_0^*(E, \mathbf{p} + \mathbf{q})T^*(E)G_0^*(E, \mathbf{q}),$$

$$\tilde{g}(E, \mathbf{q}, \mathbf{p}) = G_0(E, \mathbf{q})T(E)G_0(E, \mathbf{p} + \mathbf{q}) - G_0^*(E, \mathbf{p} + \mathbf{q})T^*(E)G_0^*(E, \mathbf{q}),$$

and  $g_{ij}$ ,  $\tilde{g}_{ij}$  denote the corresponding components of the matrices  $g$  and  $\tilde{g}$ .

Several remarks should be made about the method above. First of all, the above-mentioned T-matrix method becomes very handy in numerical calculations. The integrals over momenta in Eqs. (4.11-4.14) are performed over the first Brillouin zone. The energies  $E$  specified in those equations are the energies of the impurity-induced states. In the approach described above they can be found as poles of the T-matrix situated in the superconducting gap. Second, to avoid singularities in the definition of the bare retarded Green's function in Eq. (4.3) we will replace it with a finite  $+i\delta$  in all the numerical calculations, keeping in mind its physical meaning – quasiparticle lifetime. In all the realistic systems it is finite since there is always some temperature broadening, as well as coupling to an external bath (occurring e.g. in STM measurements) or any other source of decoherence.

### 4.3 Analytical approach

An alternative approach to studying the problem allows to extract the wave functions of the impurity-induced states and study their behaviour. Furthermore, having found the wave functions we can find different observables, such as e.g. LDOS and SP LDOS. We start by writing

the Schrödinger equation

$$[\mathcal{H}_0 + \mathcal{H}_{imp}] \Phi(\mathbf{r}) \equiv [\mathcal{H}_0 + V\delta(\mathbf{r})] \Phi(\mathbf{r}) = E\Phi(\mathbf{r}),$$

where the Hamiltonians on the left side are defined in Eqs. (4.1,4.2). After the Fourier transform we get in the momentum space

$$(E - \mathcal{H}_0)\Phi(\mathbf{p}) = V\Phi(\mathbf{r} = \mathbf{0}).$$

Employing the definition of the bare retarded Green's function, we express the wave function in momentum space in terms of its value at the origin  $\mathbf{r} = \mathbf{0}$ :

$$\Phi(\mathbf{p}) = G_0(E, \mathbf{p})V\Phi(\mathbf{r} = \mathbf{0}).$$

To return to the real space we perform the FT again:

$$\Phi(\mathbf{r}) = G_0(E, \mathbf{r})V\Phi(\mathbf{r} = \mathbf{0}). \quad (4.15)$$

Substituting  $\mathbf{r} = \mathbf{0}$ , we first define self-consistently the wave function at the origin and the corresponding energy value from

$$[\mathbb{I}_4 - G_0(E, \mathbf{r} = \mathbf{0})V] \Phi(\mathbf{0}) = 0 \quad (4.16)$$

by utilising the non-triviality condition  $\det [\mathbb{I}_4 - G_0(E, \mathbf{r} = \mathbf{0})V] = 0$ . Inserting the energies and corresponding Nambu spinors  $\Phi(\mathbf{0})$  back into Eq. (4.15) enables us to determine the spatial dependence of the Shiba state wave function. Finally, we define the non-polarised and the SP LDOS

$$\rho(E, \mathbf{r}) = \Phi^\dagger(\mathbf{r}) \begin{pmatrix} \sigma_0 & 0 \\ 0 & 0 \end{pmatrix} \Phi(\mathbf{r}), \quad (4.17)$$

and

$$\mathbf{S}(E, \mathbf{r}) = \Phi^\dagger(\mathbf{r}) \begin{pmatrix} \boldsymbol{\sigma} & 0 \\ 0 & 0 \end{pmatrix} \Phi(\mathbf{r}), \quad (4.18)$$

where we take into account only the electron components of the wave function, and not the hole ones. This is because the physical observables are related to only one of the two components,

for example in a STM measurement one injects an electron at a given energy and thus have access to the allowed number of electronic states, not to both the electronic and hole states simultaneously. The Bogoliubov-de Gennes Hamiltonian contains the so-called particle-hole redundancy, and the electron and the hole components can be simply recovered from each other by overall changes of sign, and/or changing the sign of the energy.

In the next section I demonstrate the power of the analytical approach above for a magnetic impurity in an s-wave superconductor. More complicated cases will be considered in the following chapters.

## 4.4 Example of a 2D s-wave superconductor

I begin by considering the pure s-wave pairing case, i.e.  $\varkappa = 0$  and  $\lambda = 0$  in Eq. (4.1), with a single localised magnetic impurity, in other words  $U = 0$  in Eq. (4.2). As mentioned above, this situation has already been addressed in previous works such as Ref. [35]. However, I am revisiting this limit here in order to compute the spin-polarised LDOS defined in the previous section, as well as to derive Eq. (3.1) for the sake of completeness.

In order to obtain the real space form of the retarded Green's functions we need to integrate the bare momentum space Green's function over all momenta. For this we need first to perform the following two integrals:

$$X_0(\mathbf{0}) = - \int \frac{d\mathbf{p}}{(2\pi)^2} \frac{1}{\xi_{\mathbf{p}}^2 + \omega^2}, \quad X_1(\mathbf{0}) = - \text{p.v.} \int \frac{d\mathbf{p}}{(2\pi)^2} \frac{\xi_{\mathbf{p}}}{\xi_{\mathbf{p}}^2 + \omega^2}, \quad (4.19)$$

where  $\omega^2 \equiv \Delta_s^2 - E^2$ . Using the principal value (abbreviated as p.v.) for the second integral is fully equivalent to performing the calculation with a natural ultraviolet energy cut-off, such as the Debye frequency  $\omega_D$ , and then taking the limit of  $\omega_D \rightarrow \infty$ . We rewrite  $\int \frac{d\mathbf{p}}{(2\pi)^2} = \nu \int d\xi_{\mathbf{p}}$ , where  $\nu = \frac{m}{2\pi}$ , and we find

$$X_0(\mathbf{0}) = -\pi\nu \frac{1}{\omega}, \quad X_1(\mathbf{0}) = 0. \quad (4.20)$$

Therefore, the bare Green's function is given by

$$G_0(E, \mathbf{r} = \mathbf{0}) = -\frac{\pi\nu}{\omega} \sigma_0 \otimes \begin{pmatrix} E & \Delta_s \\ \Delta_s & E \end{pmatrix}. \quad (4.21)$$

Using (4.16) it is easy to show that, consistent with the Anderson theorem, there are no subgap states forming for a purely scalar impurity ( $\mathbf{J} = \mathbf{0}$ ) in Eq. (4.2); while in the case of a purely magnetic impurity ( $U = 0$ ) we obtain two energy levels independent of the direction of  $\mathbf{J}$ :

$$E_{1,\bar{1}} = \pm \frac{1 - \alpha^2}{1 + \alpha^2} \Delta_s, \quad \text{where } \alpha = \pi\nu J. \quad (4.22)$$

The presence of two symmetric energy levels is a direct consequence of the imposed particle-hole symmetry of the Bogoliubov-de-Gennes Hamiltonian. The value  $\alpha = 1$  corresponds to a change in the ground state parity.

The corresponding eigenvectors at the origin are given by

$$\Phi_{\bar{1}}(\mathbf{0}) = \begin{pmatrix} 1 & 0 & -1 & 0 \end{pmatrix}^T, \quad \Phi_1(\mathbf{0}) = \begin{pmatrix} 0 & 1 & 0 & 1 \end{pmatrix}^T$$

for an impurity along the *z*-axis and

$$\Phi_{\bar{1}}(\mathbf{0}) = \begin{pmatrix} 1 & 1 & -1 & -1 \end{pmatrix}^T, \quad \Phi_1(\mathbf{0}) = \begin{pmatrix} 1 & -1 & 1 & -1 \end{pmatrix}^T$$

for an impurity along the *x*-axis. To find the coordinate dependence and the asymptotic behaviour of the Shiba states we perform the Fourier transforms:

$$X_0(\mathbf{r}) = - \int \frac{d\mathbf{p}}{(2\pi)^2} \frac{e^{i\mathbf{p}\mathbf{r}}}{\xi_{\mathbf{p}}^2 + \omega^2}, \quad X_1(\mathbf{r}) = - \int \frac{d\mathbf{p}}{(2\pi)^2} \frac{\xi_{\mathbf{p}} e^{i\mathbf{p}\mathbf{r}}}{\xi_{\mathbf{p}}^2 + \omega^2}.$$

We detail this calculation in Appendix A and here we only give the final results:

$$X_0(r) = -2\nu \cdot \frac{1}{\omega} \cdot \text{Im} K_0[-i(1 + i\Omega)p_F r], \quad X_1(r) = -2\nu \cdot \text{Re} K_0[-i(1 + i\Omega)p_F r], \quad (4.23)$$

where  $\Omega \equiv \omega/v_F p_F$  and  $K_0$  denotes the modified Bessel function of the second kind. It is worth noting that these functions diverge at  $r = 0$ , but this divergence can be disregarded as it occurs only at the point where the impurity is localised and, therefore, the Schrödinger equation is not

well-defined. However, this problem can be always avoided by introducing an infrared cut-off if needed. Since these functions have spherical symmetry we can write down the unperturbed Green's function as

$$G_0(E, r) = \sigma_0 \otimes \begin{pmatrix} [EX_0(r) + X_1(r)] & \Delta_s X_0(r) \\ \Delta_s X_0(r) & [EX_0(r) - X_1(r)] \end{pmatrix},$$

where  $r = |\mathbf{r}|$ . Using Eq. (4.15) we find for an impurity along the  $z$ -axis:

$$\Phi_{\bar{1}}(r) = +J_z \begin{pmatrix} (E_{\bar{1}} - \Delta_s)X_0(r) + X_1(r) \\ 0 \\ -(E_{\bar{1}} - \Delta_s)X_0(r) + X_1(r) \\ 0 \end{pmatrix}, \quad \Phi_1(r) = -J_z \begin{pmatrix} 0 \\ (E_1 + \Delta_s)X_0(r) + X_1(r) \\ 0 \\ (E_1 + \Delta_s)X_0(r) - X_1(r) \end{pmatrix}.$$

The formation of Shiba states implies the breaking of Cooper pairs, and subsequently the coupling of the electrons to the spin of the impurity. Therefore, there is no physical reason for the Shiba states to be polarised in any other direction than the direction of the impurity spin. Thus we expect intuitively that  $S_{1,\bar{1}}^x(r) = S_{1,\bar{1}}^y(r) = 0$  for both  $\Phi_1, \Phi_{\bar{1}}$  and this is indeed the case. Moreover, utilising Eqs. (4.17) and (4.18) we have

$$S_{\bar{1}}^z(r) = +\rho_{\bar{1}}(r) = +J_z^2 [(E_{\bar{1}} - \Delta_s)X_0(r) + X_1(r)]^2, \\ S_1^z(r) = -\rho_1(r) = -J_z^2 [(E_1 + \Delta_s)X_0(r) + X_1(r)]^2.$$

Similarly, for an impurity along the  $x$ -axis we have

$$\Phi_{\bar{1}}(\mathbf{r}) = +J_x \begin{pmatrix} (E_{\bar{1}} - \Delta_s)X_0(r) + X_1(r) \\ (E_{\bar{1}} - \Delta_s)X_0(r) + X_1(r) \\ -(E_{\bar{1}} - \Delta_s)X_0(r) + X_1(r) \\ -(E_{\bar{1}} - \Delta_s)X_0(r) + X_1(r) \end{pmatrix}, \quad \Phi_1(\mathbf{r}) = -J_x \begin{pmatrix} (E_1 + \Delta_s)X_0(r) + X_1(r) \\ -(E_1 + \Delta_s)X_0(r) - X_1(r) \\ (E_1 + \Delta_s)X_0(r) - X_1(r) \\ -(E_1 + \Delta_s)X_0(r) + X_1(r) \end{pmatrix}.$$

For the same reasons as before, we have  $S_{1,\bar{1}}^y(r) = S_{1,\bar{1}}^z(r) = 0$ , and

$$S_{\bar{1}}^x(r) = +\rho_{\bar{1}}(r) = +2J_x^2 [(E_{\bar{1}} - \Delta_s)X_0(r) + X_1(r)]^2, \\ S_1^x(r) = -\rho_1(r) = -2J_x^2 [(E_1 + \Delta_s)X_0(r) + X_1(r)]^2.$$

Note that all the functions given above are not normalised. This choice is made for the sake of simplicity; furthermore, since we are only interested in the form of the spatial dependence, the overall normalisation constant is not relevant for our analysis.

The asymptotic forms of the functions  $X_0$  and  $X_1$  for  $r \rightarrow \infty$  are derived in Appendix E, and are given by

$$X_0(r) \sim -\sqrt{2\pi} \nu \cdot \frac{1}{\omega} \frac{\sin(p_F r + \pi/4)}{\sqrt{p_F r}} e^{-p_S r}, \quad X_1(r) \sim -\sqrt{2\pi} \nu \cdot \frac{\cos(p_F r + \pi/4)}{\sqrt{p_F r}} e^{-p_S r},$$

where  $p_S = \Omega p_F = \omega/v_F$  is the inverse superconducting decay length, and the impurity-induced oscillations have a period corresponding to the Fermi momentum  $p_F$ , as expected for Friedel oscillations at Fermi energy.

In the rest of this part of the manuscript calculations are performed along similar lines.

# Chapter 5

## Extracting spin-orbit coupling

Spin-orbit (SO) interaction or spin-orbit coupling was known since the dawn of quantum mechanics. Naïvely, one can think of it as an interaction between the spin of a given particle and the magnetic field induced by its motion. The most known manifestations of SO can be found in atoms, notably the energy levels of electrons acquire finite shifts and splittings (cf. Zeeman effect) due to the fact that electrons interact with the intrinsic magnetic field induced by its orbital motion.

A rigorous derivation of spin-orbit interaction requires using the Dirac equation. However, to understand the basics it is sufficient to deduce it semiclassically, considering an electron moving with velocity  $\mathbf{v}$  in a radial electric field  $\mathbf{E} = -\nabla V(r)$  of an atom. In its rest frame the electron is subject to a magnetic field  $\mathbf{B} = -\mathbf{v} \times \mathbf{E}/c$ , where  $c$  is the speed of light. We note that we neglect the higher order terms in  $v/c$ . Having a non-zero magnetic moment, the electron interacts with this magnetic field, and the corresponding energy is given by

$$E_{\text{int}}^{\text{L}} = -\boldsymbol{\mu}_e \cdot \mathbf{B}.$$

The magnetic moment  $\boldsymbol{\mu}_e$  is proportional to the spin of the electron and can be written as  $\boldsymbol{\mu}_e = -\frac{g\mu_B}{2}\boldsymbol{\sigma}$ , where  $g$  is the electron spin g-factor,  $\mu_B$  is the Bohr magneton, and  $\boldsymbol{\sigma}$  is a vector consisting of the Pauli matrices  $\sigma_x, \sigma_y, \sigma_z$ . The resulting interaction energy up to a constant can be expressed as

$$E_{\text{int}}^{\text{L}} \propto \boldsymbol{\sigma} \cdot \mathbf{p} \times \nabla V.$$

The energy we have calculated above is called 'Larmor interaction energy'. The spin-orbit interaction has, however, another contribution, originating from the Thomas precession. Luckily, the Thomas interaction energy has exactly the same dependence on spin, momentum and gradient of the potential  $V$  [36]. Therefore, the spin-orbit interaction is written as

$$E_{\text{SO}} = E_{\text{int}}^{\text{L}} + E_{\text{int}}^{\text{T}} \propto \boldsymbol{\sigma} \cdot \mathbf{p} \times \nabla V.$$

In solid state physics there are numerous phenomena related to SO coupling. In general it can be taken into account by writing down complicated effective multiband Hamiltonians, circumscribing realistic systems. However, for qualitative discussions it is sufficient to utilise a simple model such as the Rashba SO interaction [37]. The following two-band Hamiltonian

$$\mathcal{H} = \left( \frac{k^2}{2m} - \varepsilon_F \right) \sigma_0 + \lambda_R (k_y \sigma_x - k_x \sigma_y)$$

describes a two-dimensional electron gas with the Rashba SO coupling constant  $\lambda_R$  and  $\boldsymbol{\sigma}$ -matrices acting in spin space. On the left panel in Fig. 5.1 it is shown how the Rashba term affects the conventional spin-degenerate parabolic spectrum, lifting the spin degeneracy and shifting the bands.

There are several conventional ways of measuring the SO coupling constant, principal ones being ARPES (or spin-resolved ARPES) and magneto-transport measurements [38]. On the right panel in Fig. 5.1 exemplary ARPES data are presented.

In what follows below, we study the spin-resolved spectral properties of the impurity states associated to the presence of magnetic impurities in two-dimensional, as well as one-dimensional systems with Rashba spin-orbit coupling. We focus on Shiba bound states in superconducting materials, as well as on impurity states in metallic systems. Using a combination of a numerical T-matrix approximation and a direct analytical calculation of the bound state wave function, we compute the local density of states together with its Fourier transform. We find that the FT of the spin-polarised LDOS, a quantity accessible via spin-polarised STM, allows to accurately extract the strength of the spin-orbit coupling. Also we confirm that the presence of magnetic impurities is strictly necessary for such measurement, and that non-spin-polarised experiments cannot have access to the value of the spin-orbit coupling.

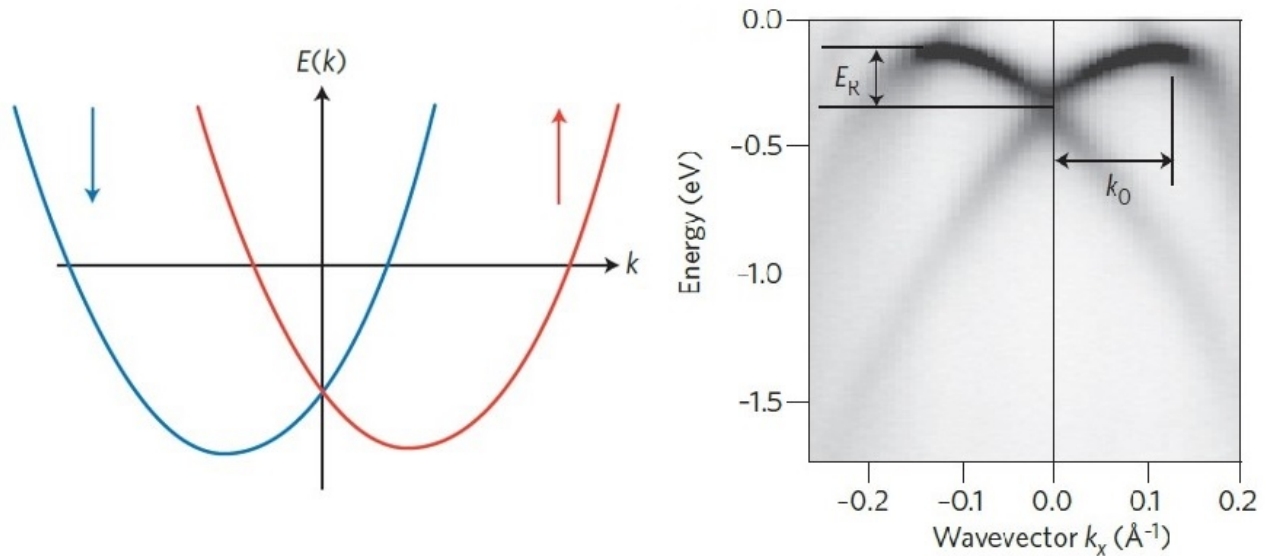


Figure 5.1: Left: a parabolic band split by the Rashba spin-orbit coupling. The spin degeneracy inherent for metallic spectra in the absence of SO is lifted. Right: ARPES image of a spin-split parabolic dispersion (borrowed from Ref. [38]). The energy shift is denoted  $E_R$ , whereas  $k_0$  is the momentum offset due to spin-orbit interaction.

The electronic bands of materials that lack an inversion centre are split by the spin-orbit coupling. A strong SO coupling implies that the spin of the electron is tied to the direction of its momentum. Materials with strong SO coupling have been receiving a considerable attention in the past decade partly because SO is playing an important role for the discovery of new topological classes of materials [39, 40]. Two-dimensional topological insulators, first predicted in graphene [41], have been discovered in HgTe/CdTe heterostructures [42] following a theoretical prediction by Bernevig *et al.* [43]. They are characterised by one-dimensional helical edge states where the spin is locked to the direction of propagation due to the strong SO coupling. Similar features occur for the surface states of 3D topological insulators which also have a strong bulk SO coupling [39]. The spin-to-momentum locking was directly observed by angle-resolved photoemission spectroscopy (ARPES) experiments [44, 45].

Topological superconductors share many properties with topological insulators. They possess exotic edge states called Majorana fermions, particles which are their own antiparticles [39]. Topological superconductivity can be either induced by the proximity with a standard s-wave superconductor or be intrinsic. In the former case, Majorana states have thus been proposed to form in one-dimensional [46, 47] and two-dimensional semiconductors [48, 49] with strong SO coupling when proximitised with a s-wave superconductor, and in the presence of a Zeeman field. Following this strategy, many experiments have reported signatures of Majorana fermions

through transport spectroscopy in one dimensional topological wires [50–54]. However, there are presently only a few material candidates such as strontium ruthenate [55], certain heavy fermion superconductors [56], or some doped topological insulators such as  $\text{Cu}_x\text{Bi}_2\text{Se}_3$  [57], that may host intrinsic topological superconductivity.

Although SO coupling has been playing an essential role in the discovery of new topological materials, it is also of crucial importance in the physics of spin Hall effect [58], in spintronics [59] and quantum (spin) computation since it allows to electrically detect and manipulate spin currents in confined nanostructures (see Ref. [38] for a recent review).

Based on the prominent role played by SO in the past decades, it is thus of great interest to be able to evaluate the SO coupling value in a given material accurately, though in general this is a very difficult task. Inferences can be made from ARPES measurements [60–62]; in particular spin-polarised ARPES measurements have been used to evaluate the SO coupling in various materials [63–69]. Other possibilities involve magneto-transport measurements in confined nanostructures: this technique has been used to measure the SO coupling in clean carbon nanotubes [70] or in InAs nanowires [71].

Here we propose a method to measure the magnitude of the SO coupling directly using spin-polarised scanning tunnelling microscopy (STM) [32], and the Fourier transform (FT) of the local density of states (LDOS) near magnetic impurities (FT-STM). The FT-STM technique has been used in the past in metals, where it helped in mapping the band structure and the shape and the properties of the Fermi surface [10, 11, 18–20, 72–74], as well as in extracting information about the spin properties of the quasiparticles [75]. More spectacularly, it was used successfully in high-temperature SCs to map with high resolution the particular d-wave structure of the Fermi surface, as well as to investigate the properties of the pseudogap [76–78].

In what follows, on one hand, we calculate the Fourier transform of the spin-polarised local density of states (SP LDOS) of the so-called Shiba bound state [23–25, 34] associated with a magnetic impurity in a superconductor. Shiba bound states have been measured experimentally by STM [26, 79, 80] and it has actually been shown that the extent of the Shiba wave function can reach tens of nanometres in 2D superconductors, which allows one to measure the spatial dependence of the LDOS of such states with high resolution [27]. We consider both one-dimensional and two-dimensional superconductors with SO coupling. While two-dimensional systems such as e.g.  $\text{Sr}_2\text{RuO}_4$ , [55] or  $\text{NbSe}_2$  [27, 81] become superconducting when brought

at low temperature, one-dimensional wires such as InAs and InSb are not superconducting at low temperature. In order to see the formation of Shiba states one would need to proximitise them by a SC substrate. The formation of Shiba states in such systems [82, 83], as well as in p-wave superconductors [84, 85], has been recently touched upon, but the effect of the SO coupling on the FT of the SP LDOS in the presence of magnetic impurities has not previously been analysed.

On the other hand we focus on the effects of the spin-orbit coupling on the impurity states of a classical magnetic impurity in one-dimensional and two-dimensional metallic systems such as Pb [86] and Bi, as well as InAs and InSb semiconducting wires that can be also modelled as metals in the energy range that we consider. We should note that for these systems no bound state forms at a specific energy, but the impurity is affecting equally the entire energy spectrum.

By studying the two classes of systems described above we show that the SO coupling can directly be read-off from the FT features of the SP LDOS in the vicinity of the magnetic impurity. We note that such a signature appears only for magnetic impurities, and only when the system is investigated using spin-polarised STM measurements, the non-spin-polarised measurements do not provide information on the SO, as it has also been previously noted [87]. The main difference between the SC and metallic systems, beyond the existence of a bound state in the former case, is that the spin-polarised Friedel oscillations around the impurity have additional features in the SC phase, the most important one being the existence of oscillations with a wavelength exactly equal to the SO coupling length scale; such oscillations are not present in the metallic phase. Another difference is the broadening of the FT features in the superconducting phase compared to the non-SC phase in which the sole broadening is due to the quasiparticle lifetime.

We focus on Rashba SO coupling as assumed to be the most relevant for the systems considered, but we have checked that our conclusion holds for other types of SO. To obtain the SP LDOS we use a T-matrix approximation [20, 88, 89], and we present both numerical and analytical results which allow us to obtain a full understanding of the observed features, of the splittings due to the SO, as well as of the spin-polarisation of the impurity states and of the symmetry of the FT features.

Below we first present the model for two-dimensional and one-dimensional cases and the basics of the techniques employed. In Section 5.2 we show our results for the spin-polarised LDOS,

calculated both numerically and analytically, for 2D systems, both in the SC and metallic phase. Section 5.3 is devoted to spin-polarised LDOS of impurity-induced states in one-dimensional systems. Concluding remarks and discussion of the results can be found in the last section of this chapter. We left the details of the analytical calculations to the corresponding Appendixes.

## 5.1 Model and techniques

The model we utilise in this chapter is a particular case of the general model given by Eq. (4.1), where we set the triplet pairing constant  $\varkappa = 0$ . Thus we consider an s-wave superconductor with s-wave pairing  $\Delta_s$ , and Rashba SO coupling  $\lambda$ , for which the Hamiltonian, written in the Nambu basis  $\Psi_{\mathbf{p}} = (\psi_{\uparrow\mathbf{p}}, \psi_{\downarrow\mathbf{p}}, \psi_{\downarrow-\mathbf{p}}^\dagger, -\psi_{\uparrow-\mathbf{p}}^\dagger)^\text{T}$ , is given by:

$$\mathcal{H}_0 = \sigma_0 \otimes (\xi_{\mathbf{p}}\tau_z + \Delta_s\tau_x) + \mathcal{H}_{SO}. \quad (5.1)$$

The energy spectrum is  $\xi_{\mathbf{p}} \equiv \frac{\mathbf{p}^2}{2m} - \varepsilon_F$ , where  $\varepsilon_F$  is the Fermi energy. The operator  $\psi_{\sigma\mathbf{p}}^\dagger$  creates a particle of spin  $\sigma = \uparrow, \downarrow$  of momentum  $\mathbf{p} \equiv (p_x, p_y)$  in 2D and  $\mathbf{p} \equiv p_x$  in 1D. The system is considered to lay in the  $(x, y)$  plane in 2D case, whereas in 1D case we set  $p_y$  to zero in the expressions above, and we consider a system lying along the  $x$ -axis. The metallic limit is recovered by setting  $\Delta_s = 0$ . The Rashba Hamiltonian can be written as

$$\mathcal{H}_{SO} = \lambda(p_y\sigma_x - p_x\sigma_y) \otimes \tau_z, \quad (5.2)$$

in 2D and simply as  $\mathcal{H}_{SO} = \lambda p_x\sigma_y \otimes \tau_z$  in 1D. We have introduced  $\boldsymbol{\sigma} = (\sigma_x, \sigma_y, \sigma_z)$  and  $\boldsymbol{\tau} = (\tau_x, \tau_y, \tau_z)$ , the Pauli matrices acting respectively in the spin and the particle-hole subspaces.

In what follows we study what happens when a single localised impurity is introduced in this system. We consider magnetic impurities of spin  $\mathbf{J} = (J_x, J_y, J_z)$  described by the following Hamiltonian:

$$\mathcal{H}_{imp} = \mathbf{J} \cdot \boldsymbol{\sigma} \otimes \tau_0 \cdot \delta(\mathbf{r}) \equiv V \cdot \delta(\mathbf{r}), \quad (5.3)$$

where  $\mathbf{J}$  is the magnetic strength. We only consider here classical impurities oriented either along the  $z$ -axis,  $\mathbf{J} = (0, 0, J_z)$ , or along the  $x$ -axis,  $\mathbf{J} = (J_x, 0, 0)$ . This is justified provided the Kondo temperature is much smaller than the superconducting gap [34].

To find the impurity states in the model described above we use the T-matrix approximation described in [34,88,89] and [20], and revised in Chapter 4. We also neglect the renormalisation of the superconducting gap because it is mainly local [28,34] and therefore only introduces minor effects for our purposes. Since the impurity is localised, the T-matrix is simply given by Eq. (4.5).

To find the real-space dependence of the non-polarised,  $\delta\rho(\mathbf{r}, E)$ , and SP LDOS,  $S_{\hat{n}}(\mathbf{r}, E)$ , with  $\hat{n} = x, y, z$ , as well as their components in momentum space we utilise Eqs. (4.7-4.10) and Eqs. (4.11-4.14) respectively. Note that while the non-polarised and the SP LDOS are of course real functions when evaluated in position space, their Fourier transforms need not be. Sometimes we get either or both real and imaginary components for the FT, depending on their corresponding symmetries. In the figures we shall indicate each time if we plot the real or the imaginary component of the FT.

To obtain the FT of the non-polarised and the SP LDOS, we first evaluate the momentum integrals in Eqs. (4.5),(4.11-4.14) numerically. For this we use a square lattice version of the Hamiltonians (5.1) and (5.2), where we replace the continuum spectrum  $\xi_{\mathbf{p}}$  by the tight-binding spectrum  $\Xi_{\mathbf{p}} \equiv \mu - 2t(\cos p_x + \cos p_y)$  with chemical potential  $\mu$  and hopping parameter  $t$ . For clarity we set the lattice constant to unity. It is also worth noting that all the numerical integrations are performed over the first Brillouin zone and that we use dimensionless units by setting  $t = 1$ .

Alternatively, as detailed in Chapter 4, we find the exact form for the non-polarised and SP LDOS in the continuum limit by performing the integrals in the FT of the Green's functions analytically. Moreover, when considering the SC systems, the energies  $E$  of the Shiba states together with the corresponding eigenstates for the Shiba wave functions  $\Phi$  at the origin can be obtained from Eqs. (4.16) and (4.15) correspondingly. The latter allow to find the non-polarised and SP LDOS by means of Eqs. (4.17) and (4.18) respectively. To avoid overburdening this discussion, we leave all the further details of the aforementioned calculations to Appendixes A.1 and B.

## 5.2 Results for two-dimensional systems

### Real and momentum space dependence of the 2D Shiba bound states

For a 2D superconductor with SO coupling in the presence of a magnetic impurity one expects the formation of a single pair of Shiba states [82,83]. The energies of the particle-hole symmetric Shiba states<sup>1</sup> are given by (independent of the direction of the impurity):

$$E_{1,\bar{1}} = \pm \frac{1 - \alpha^2}{1 + \alpha^2} \Delta_s,$$

where  $\alpha = \pi\nu J$  is the dimensionless impurity strength and  $\nu = \frac{m}{2\pi}$  is the normal-phase density of states. (See Appendix A for details of how the energies of the Shiba states are calculated.) Up to the critical value  $\alpha_c = 1$  these energies are ordered the following way:  $E_1 > E_{\bar{1}}$ . As soon as  $\alpha > \alpha_c$ , energy levels  $E_1$  and  $E_{\bar{1}}$  exchange places, making the order the following:  $E_{\bar{1}} > E_1$ . When  $\alpha = \alpha_c = 1$  the impurity effectively binds an electron, and thus it corresponds to a change of the ground state parity [34,90,91]. For  $\alpha \gg 1$  the subgap states approach the gap edge and eventually merge with the continuum. For the type of impurities considered here, there is no dependence of these energies on the SO coupling in the low-energy approximation, though a weak dependence is introduced when one takes into account the non-linear form of the spectrum. The dependence of energy of the Shiba states on the impurity strength  $J$  is depicted in Fig. 5.2 where we plot the total spin of the impurity state  $S(\mathbf{p} = 0)$  as a function of energy and impurity strength. Note that the two opposite-energy Shiba states have opposite spins.

We are interested in studying the spatial structure of the Shiba states in the presence of magnetic impurities oriented both perpendicular to the plane, and in the plane. This can be done both in real space and momentum space by calculating the Fourier transform of the spin-polarised LDOS using the T-matrix technique detailed in Chapter 4. We focus on the positive-energy Shiba state, noting that its negative energy counterpart exhibits a qualitatively similar behaviour. In Fig. 5.3 we show the real-space dependence of the non-polarised and SP LDOS. Each of the panels corresponds to the interference patterns originating from different types of scattering. Note that the spin-orbit value cannot be accurately extracted from these type of

---

<sup>1</sup>We often use the plural when referring to Shiba states in order to facilitate the discussion. However, it should be kept in mind that for a given localised magnetic impurity, there is a single Shiba state with particle and hole components whose real space wave function can actually behave differently.

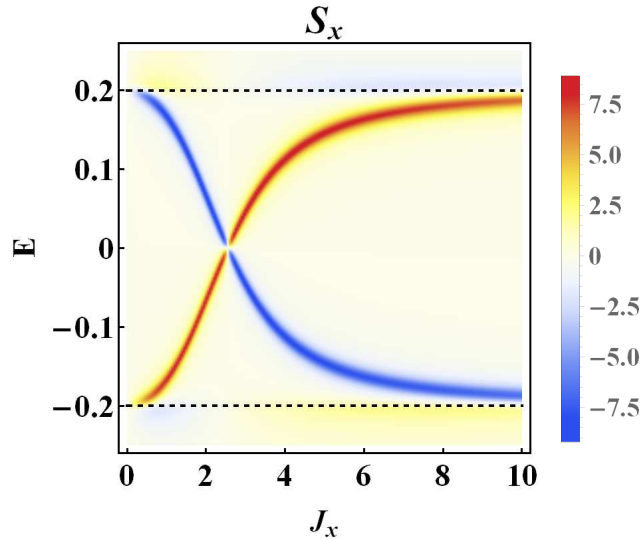


Figure 5.2: The averaged SP LDOS induced by an impurity as a function of the impurity strength for an in-plane magnetic impurity. The dashed line shows the superconducting gap. A similar result is obtained when the impurity spin is perpendicular to the plane. Note that the two Shiba states with opposite energies have opposite spin. We set  $t = 1$ ,  $\mu = 3$ ,  $\delta = 0.01$ ,  $\lambda = 0.5$ ,  $\Delta_s = 0.2$ .

measures, since the system contains oscillations with many different superposing wave vectors. To overcome this problem we focus on the FT of these features, as it is often done in spatially resolved STM experiments, which allow for a more accurate separation of the different wave vectors [10, 11, 18–20, 72–74]. Thus in Fig. 5.4 we focus on the FT of the SP LDOS for two types of impurities with spin oriented along  $z$  and  $x$  axes respectively.

Note that the SO introduces non-zero spin components in the directions different from that of the impurity spin. These components exhibit either two-fold or four-fold symmetric patterns. Also the SO is affecting strongly the spin component parallel to the impurity, in particular when the impurity is in-plane, in which case the structure of the SP LDOS around the impurity is no longer radially symmetric. However, as can be seen in the bottom panel of Fig. 5.4, the non-spin-polarised LDOS is not affected by the presence of SO, preserving a radially symmetric shape quasi-identical to that obtained in the absence of SO. Thus the SO coupling can be measured only via the spin-polarised components of the LDOS, and not the non-polarised LDOS.

These results, which are obtained using a numerical integration of the T-matrix equations, are also supported by analytical calculations which help to understand the fine structure of the FT of the SP LDOS (see Appendix A.1 for details). These calculations yield for the SP LDOS

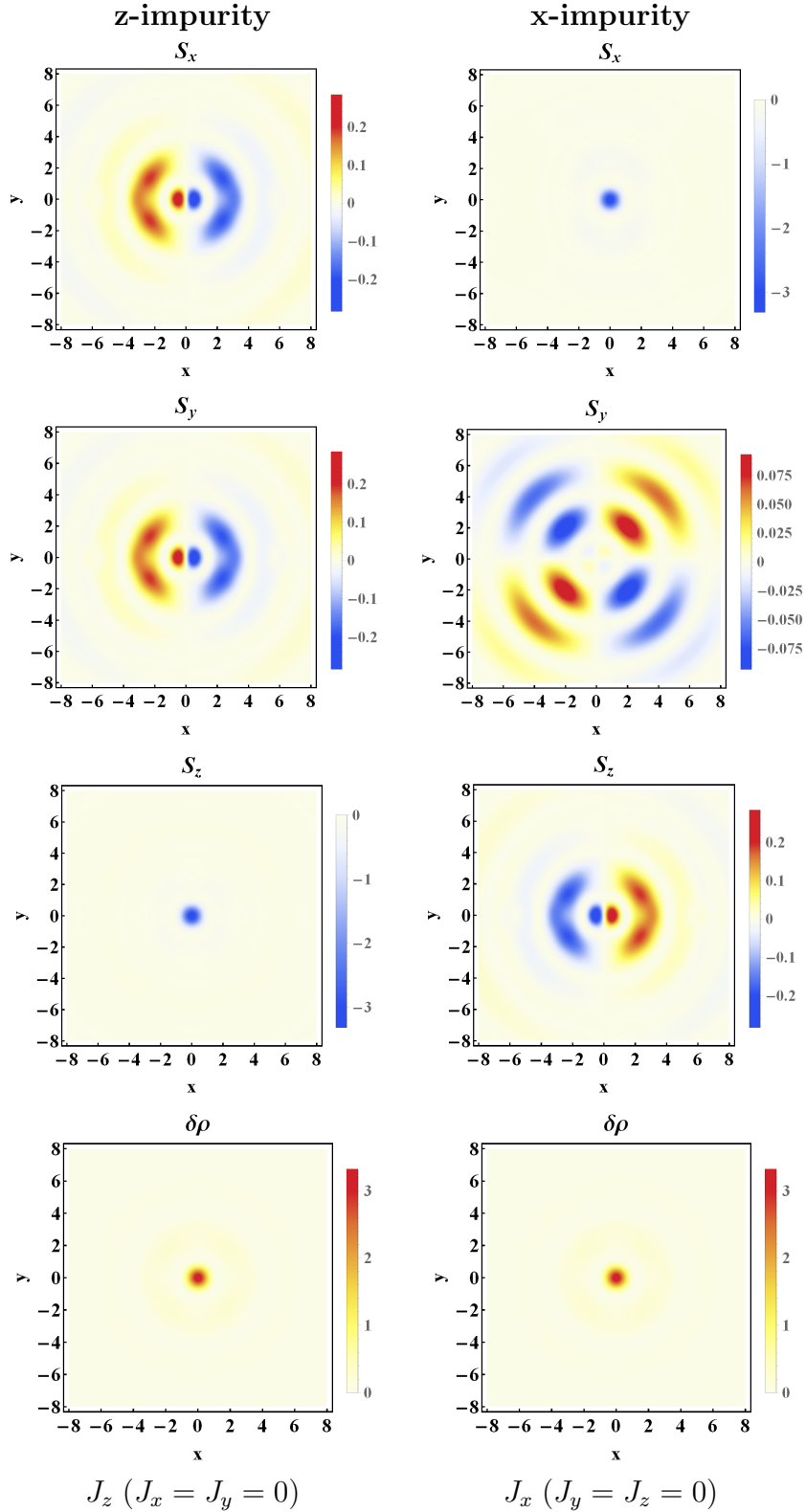


Figure 5.3: The real-space dependence of the non-polarised (bottom row) as well as of the SP LDOS components (the first three rows) for the positive energy Shiba state, for a magnetic impurity with  $J_z = 2$  (left column), and  $J_x = 2$  (right column). We take  $t = 1, \mu = 3, \delta = 0.01, \lambda = 0.5, \Delta_s = 0.2$ .

generated by a magnetic impurity perpendicular to the plane

$$\begin{aligned}
S_x(\mathbf{r}) &= +J_z^2 \left(1 + \frac{1}{\alpha^2}\right) \frac{e^{-2p_s r}}{r} \cos \phi_{\mathbf{r}} \times \left\{ \sum_{\sigma} \frac{\sigma \nu_{\sigma}^2}{p_F^{\sigma}} \cos(2p_F^{\sigma} r - \theta) + \gamma \sin p_{\lambda} r \right\}, \\
S_y(\mathbf{r}) &= +J_z^2 \left(1 + \frac{1}{\alpha^2}\right) \frac{e^{-2p_s r}}{r} \sin \phi_{\mathbf{r}} \times \left\{ \sum_{\sigma} \frac{\sigma \nu_{\sigma}^2}{p_F^{\sigma}} \cos(2p_F^{\sigma} r - \theta) + \gamma \sin p_{\lambda} r \right\}, \\
S_z(r) &= -J_z^2 \left(1 + \frac{1}{\alpha^2}\right) \frac{e^{-2p_s r}}{r} \times \left\{ \sum_{\sigma} \frac{\nu_{\sigma}^2}{p_F^{\sigma}} \sin(2p_F^{\sigma} r - \theta) - \gamma \cos p_{\lambda} r \right\}, \\
\rho(r) &= +J_z^2 \left(1 + \frac{1}{\alpha^2}\right) \frac{e^{-2p_s r}}{r} \times \left\{ 2 \frac{\nu^2}{mv} + \gamma \sin(2mvr - \theta) \right\},
\end{aligned}$$

with  $\gamma \equiv 2\nu^2 \frac{v_F^2}{v^2 p_F}$  and

$$\theta = \begin{cases} \arctg \frac{2\alpha}{1-\alpha^2}, & \text{if } \alpha \neq 1 \\ \frac{\pi}{2}, & \text{if } \alpha = 1 \end{cases}.$$

We have introduced  $e^{i\phi_{\mathbf{r}}} = \frac{x+iy}{r}$ , and  $p_F^{\sigma} = -\sigma m\lambda + mv$ ,  $p_{\lambda} = 2m\lambda$ ,  $p_s = \sqrt{\Delta_s^2 - E_1^2}/v$ , with  $v = \sqrt{v_F^2 + \lambda^2}$ , and  $v_F = \sqrt{2\varepsilon_F/m}$ . Here  $p_F^{\sigma}$ ,  $p_{\lambda}$  and  $p_s$  are the different momenta which can be read off from the SP LDOS. For an in-plane magnetic impurity we have

$$\begin{aligned}
S_x^s(r) &= -J_x^2 \left(1 + \frac{1}{\alpha^2}\right) \left\{ \sum_{\sigma} \frac{\nu_{\sigma}^2}{p_F^{\sigma}} [1 + \sin(2p_F^{\sigma} r - 2\beta)] + \gamma [\cos p_{\lambda} r + \sin(2mvr - 2\beta)] \right\} \frac{e^{-2p_s r}}{r} \\
S_x^a(\mathbf{r}) &= J_x^2 \left(1 + \frac{1}{\alpha^2}\right) \left\{ \sum_{\sigma} \frac{\nu_{\sigma}^2}{p_F^{\sigma}} [1 - \sin(2p_F^{\sigma} r - 2\beta)] - \gamma [\cos p_{\lambda} r + \sin(2mvr - 2\beta)] \right\} \frac{e^{-2p_s r}}{r} \cos 2\phi_{\mathbf{r}}, \\
S_y(\mathbf{r}) &= J_x^2 \left(1 + \frac{1}{\alpha^2}\right) \left\{ \sum_{\sigma} \frac{\nu_{\sigma}^2}{p_F^{\sigma}} [1 - \sin(2p_F^{\sigma} r - 2\beta)] - \gamma [\cos p_{\lambda} r - \sin(2mvr - \theta)] \right\} \frac{e^{-2p_s r}}{r} \sin 2\phi_{\mathbf{r}}, \\
S_z(\mathbf{r}) &= -J_x^2 \left(1 + \frac{1}{\alpha^2}\right) \left\{ 2 \sum_{\sigma} \frac{\sigma \nu_{\sigma}^2}{p_F^{\sigma}} \cos(2p_F^{\sigma} r - \theta) + 2\gamma \sin p_{\lambda} r \right\} \frac{e^{-2p_s r}}{r} \cos \phi_{\mathbf{r}}, \\
\rho(r) &= +J_x^2 \left(1 + \frac{1}{\alpha^2}\right) \left\{ 4 \frac{\nu^2}{mv} + 2\gamma \sin(2mvr - \theta) \right\} \frac{e^{-2p_s r}}{r},
\end{aligned}$$

with  $\tan \beta = \alpha$ . The  $S_x$  component is the sum of symmetric part  $S_x^s$  and an asymmetric part  $S_x^a$ . Note that the features observed in the FT of the SP LDOS plots are well captured by the analytical calculations. In particular we note that the oscillations in the SP LDOS are dominated by the following four wave vectors:

$$2p_F^{\pm}, \quad p_F^+ + p_F^- = 2mv, \quad \text{and} \quad p_F^- - p_F^+ = p_{\lambda} \equiv 2m\lambda,$$

which should give rise in the FT to high-intensity features at these wave vectors (the red arrows in Fig. 5.4). Indeed, we note in the numerical results for the FT of the SP LDOS the existence of four rings, corresponding to  $2p_F^\pm$ ,  $p_F^+ + p_F^- = 2mv$  and  $p_F^- - p_F^+ = p_\lambda$ , having the proper two-fold or four-fold symmetries, consistent with the  $\cos / \sin \phi_r$  and  $\cos / \sin 2\phi_r$  dependence of the SP LDOS obtained analytically. For example, in the  $x$  component of the SP LDOS induced by an  $x$  impurity, the  $2p_F^+$ ,  $2p_F^-$  and  $p_\lambda$  rings have a maximum along  $x$  and a minimum along  $y$ , while the  $2mv$  ring has a symmetry corresponding to a rotation by 90 degrees. The  $y$  component of the FT of the SP LDOS has a four-fold symmetry in which we can again identify the same wave vectors, while the  $S_z$  component has a two-fold symmetry, and the  $2mv$  vector is absent. Similarly, for the  $S_x$  and the  $S_y$  components of the SP LDOS induced by a  $z$  impurity (these components should be zero in the absence of the SO coupling) only the  $2p_F^\pm$  and  $p_\lambda$  wave vectors are present, with similar symmetries, while the  $S_z$  component is symmetric. Note also the central peak at  $p_x = p_y = 0$  which is due to the terms independent of position in the SP LDOS.

The most important observation is that all the components of the FT of the SP LDOS exhibit a strong feature at wave vector  $p_\lambda$ . Thus an experimental observation of this feature via spin-polarised STM would allow one to read-off directly the value of the SO coupling. The spin orbit can also be read-off from the distance between the  $2p_+$  and  $2p_-$  peaks, though the intensity of these features is not as strong. This appears clearly in Fig. 5.5, in which we plot a horizontal cut through two of the FT – SP LDOS above as a function of the SO coupling  $\lambda$ .

Note that the only wave vector present in the non-polarised LDOS is  $2mv$ , which has only a very weak dependence on  $\lambda$  for not too large values of the SO with respect to the Fermi velocity, thus it is quasi-impossible to determine the SO coupling from a measurement without spin resolution. Note also the typical two-dimensional  $1/r$  decay of the Friedel oscillations is overlapping in this case with an exponential decay with wave vector  $p_s$ .

## Comparison to the metallic phase

A similar analysis can be performed for impurity states forming in the vicinity of a magnetic impurity in a metallic system. Here the classical magnetic impurity does not lead to any localised bound states at a specific energy (cf. Friedel oscillations), and the intensity of the

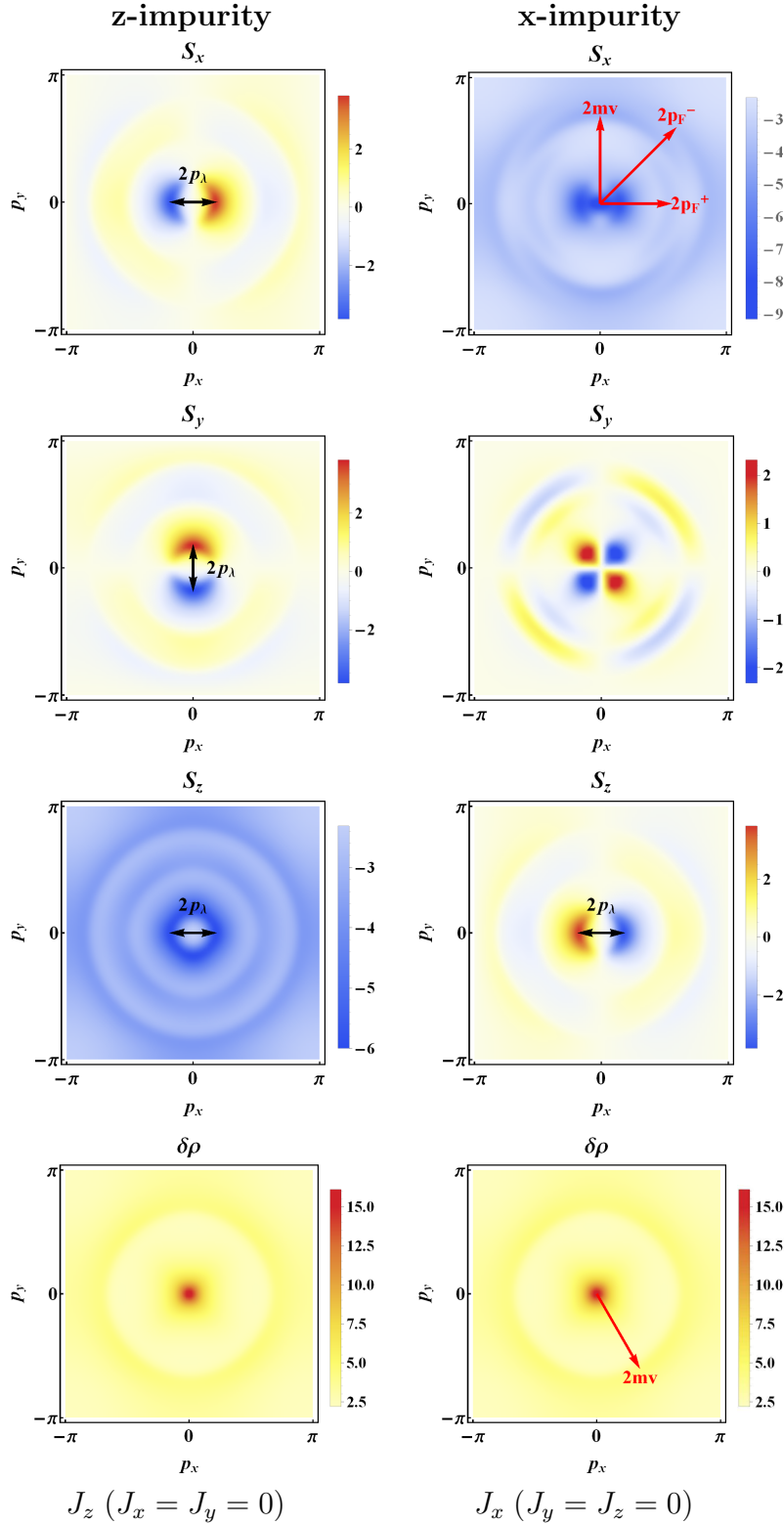


Figure 5.4: The FT of the non-polarised (bottom row) as well as of the SP LDOS components (the first three rows) for the positive energy Shiba state as a function of momentum, for a magnetic impurity with  $J_z = 2$  (left column), and  $J_x = 2$  (right column). We take  $t = 1, \mu = 3, \delta = 0.01, \lambda = 0.5, \Delta_s = 0.2$ . For a  $z$ -impurity we depict the real part of the FT for  $\delta\rho$  and for  $S_z$ , and the imaginary part for  $S_x$  and  $S_y$ , whereas for an  $x$ -impurity we take the imaginary part only for the  $S_z$  component. Black two-headed arrows correspond to the value of  $2p_\lambda \equiv 4m\lambda$  (see the analytical results) and thus allow to extract the SO coupling constant directly from these strong features in momentum space. The other arrows correspond to the other important wave vectors that can be observed in these FTs, as identified with the help of the analytical results.

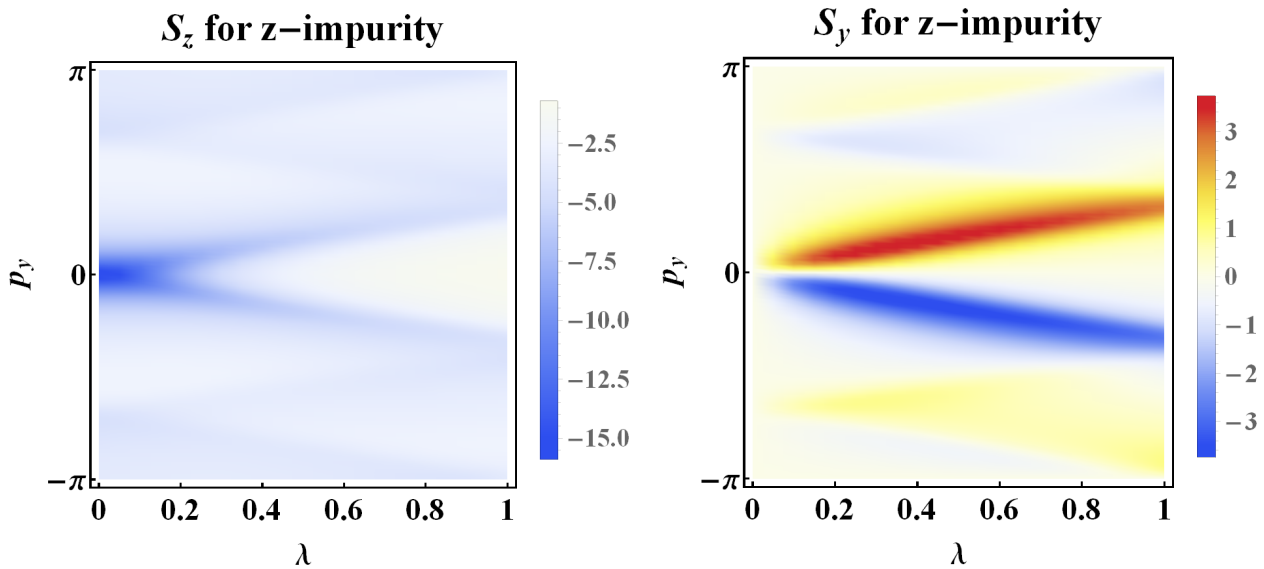


Figure 5.5: The FT of various SP LDOS component for a Shiba state as a function of the SO coupling  $\lambda$  and of  $p_y$  (for  $p_x = 0$  - vertical cut). We take  $t = 1, \mu = 3, \delta = 0.01, \Delta_s = 0.2, J_z = 2$ .

impurity contribution is roughly independent of energy.

Thus in Fig. 5.6 we plot the FT of the impurity contribution to the LDOS and SP LDOS at a fixed energy  $E = 0.1$ . We note that we have similar features to those observed in the SC regime, with the main differences being that the long-wavelength central features are now absent, and that the FT peaks are much sharper than in the SC regime. This behaviour can be explained from the analytical expressions of the non-polarised and SP LDOS, whose derivation is presented in Appendix B. The results are presented below for an out-of-plane spin impurity:

$$\begin{aligned}
 S_x(\mathbf{r}) &\sim +\frac{J}{1+\alpha^2} \frac{\cos \phi_{\mathbf{r}}}{r} \sum_{\sigma} \sigma \frac{\nu_{\sigma}^2}{p_{\sigma}} \sin 2p_{\sigma} r, \\
 S_y(\mathbf{r}) &\sim +\frac{J}{1+\alpha^2} \frac{\sin \phi_{\mathbf{r}}}{r} \sum_{\sigma} \sigma \frac{\nu_{\sigma}^2}{p_{\sigma}} \sin 2p_{\sigma} r, \\
 S_z(r) &\sim -\frac{J}{1+\alpha^2} \frac{2}{r} \sum_{\sigma} \frac{\nu_{\sigma}^2}{p_{\sigma}} \cos 2p_{\sigma} r, \\
 \rho(r) &\sim -\frac{J}{1+\alpha^2} 4\alpha v^2 \frac{v_F^2}{v^2} \frac{1}{\sqrt{p_F^2 + 2mE + E^2/v^2}} \cdot \frac{\sin p_{\varepsilon} r}{r},
 \end{aligned}$$

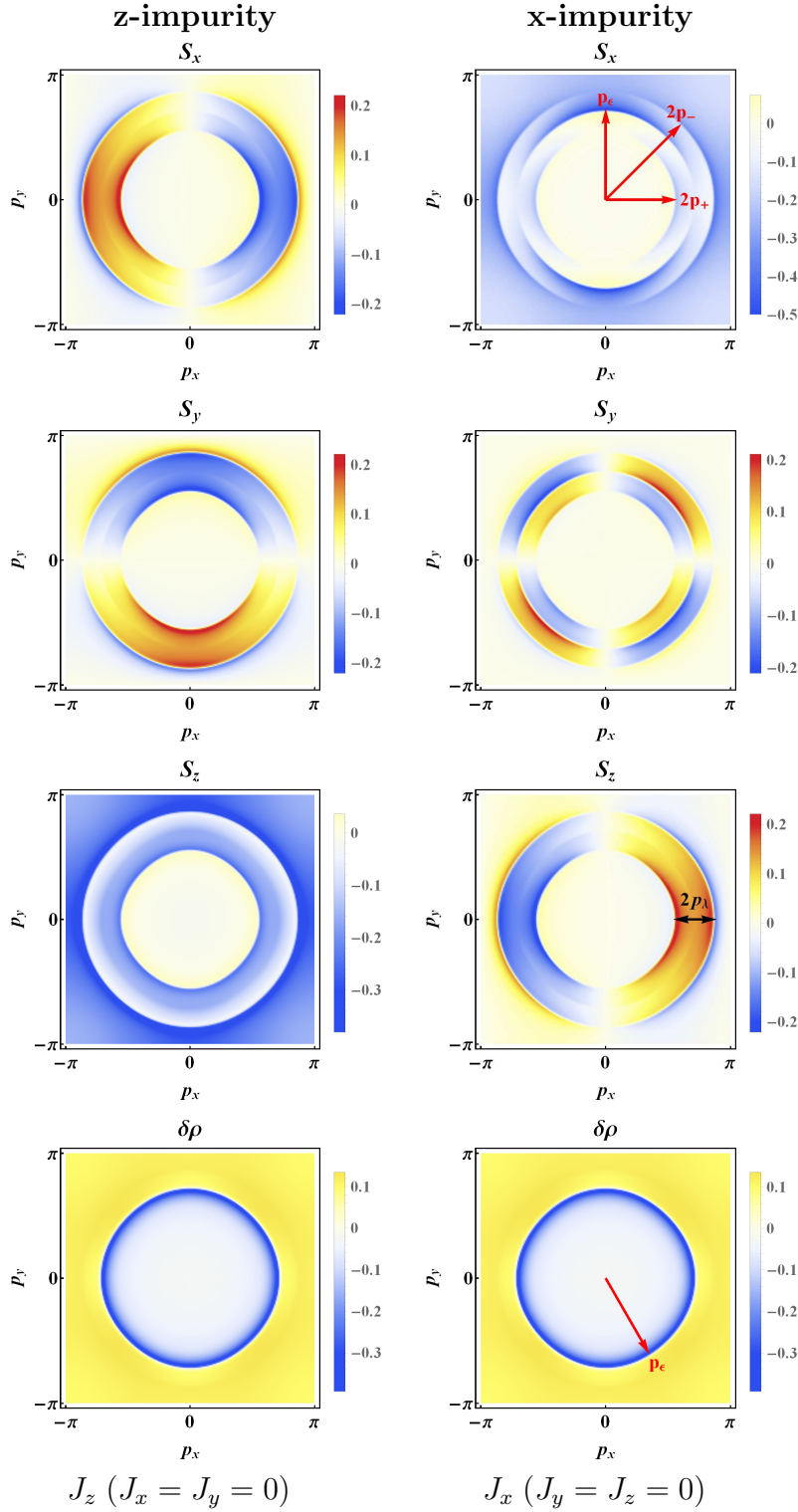


Figure 5.6: The FT of the impurity contributions to the non-polarised and SP LDOS for an energy  $E = 0.1$  and for a magnetic impurity with  $J_z = 2$  (left column), and  $J_x = 2$  (right column). We take the inverse quasiparticle lifetime  $\delta = 0.03$  and we set  $t = 1, \mu = 3, \lambda = 0.5, \Delta_s = 0$ . For a  $z$ -impurity we depict the real part of the FT for  $\delta\rho$  and for  $S_z$ , and the imaginary part for  $S_x$  and  $S_y$ , whereas for an  $x$ -impurity we take the imaginary part only for the  $S_z$  component. Unlike in the SC case, the strong peaks appearing in the centre and at  $p_\lambda$  are absent here. The arrows denote the wave vectors of the observed features as identified from the analytical calculations.

while for an  $x$  directed impurity (in-plane):

$$\begin{aligned}
S_x(\mathbf{r}) &\sim -\frac{J}{1+\alpha^2} \left\{ 2\nu^2 \frac{v_F^2}{v^2} \frac{1-\cos 2\phi_r}{r} \frac{\cos p_\varepsilon r}{\sqrt{p_F^2 + 2mE + E^2/v^2}} + \sum_\sigma \frac{\nu_\sigma^2}{p_\sigma} \frac{1+\cos 2\phi_r}{r} \cos 2p_\sigma r \right\}, \\
S_y(\mathbf{r}) &\sim -\frac{J}{1+\alpha^2} \frac{\sin 2\phi_r}{r} \left[ -2\nu^2 \frac{v_F^2}{v^2} \frac{\cos p_\varepsilon r}{\sqrt{p_F^2 + 2mE + E^2/v^2}} + \sum_\sigma \frac{\nu_\sigma^2}{p_\sigma} \cos 2p_\sigma r \right], \\
S_z(\mathbf{r}) &\sim -\frac{J}{1+\alpha^2} \frac{\cos \phi_r}{r} \sum_\sigma \sigma \frac{\nu_\sigma^2}{p_\sigma} \sin 2p_\sigma r, \\
\rho(r) &\sim -\frac{J}{1+\alpha^2} \cdot \frac{\alpha}{r} \cdot 4\nu^2 \frac{v_F^2}{v^2} \frac{\sin p_\varepsilon r}{\sqrt{p_F^2 + 2mE + E^2/v^2}},
\end{aligned}$$

with  $p_F = mv_F$ ,  $p_\sigma = p_F^\sigma + E/v \neq 0$ ,  $p_\varepsilon \equiv p_+ + p_- = 2(mv + E/v)$  and  $\nu_\sigma = \nu [1 - \sigma \frac{\lambda}{v}]$ .

Note that these expressions are very similar to those obtained in the SC regime, except that the wave vectors of the oscillations now do not include  $p_\lambda$ . However, this could still be read-off experimentally from the difference between  $p_-$  and  $p_+$ . Another important difference between the SC and non-SC regimes is the presence of the exponentially decaying term in the expressions describing the LDOS dependence for the Shiba states in the SC regime. The Shiba states have an exponential decay for distances larger than the superconducting coherence length, while the impurity states in the non-SC regime only decay algebraically as  $1/r$ . In the Fourier space this is translated into a much larger broadening of the features corresponding to the Shiba states in the SC regime with respect to that of the features corresponding to the impurity contributions in metals. The width of the peaks in the latter is solely controlled by the inverse quasiparticle lifetime  $\delta$  and is generally quite small.

Note also that in both regimes one needs to use the spin-polarised LDOS and magnetic impurities to be able to extract the value of the SO coupling, while the non-polarised LDOS is not sensitive to this wave vector. Last but not least, the LDOS perturbations induced by a non-magnetic impurity do not show any direct signature of the SO coupling (the only contributing wave vector is  $2mv$  in the metallic regime, while in the SC regime no Shiba state form for a non-magnetic impurity), thus the only manner to have access to the SO coupling is via spin-polarised STM in the presence of magnetic impurities.

### 5.3 Results for one-dimensional systems

While in one-dimensional systems superconductivity is not intrinsic, a superconducting gap can be opened via proximitising them with a superconducting substrate. For such systems it is thus particularly interesting to study the FT of the SP LDOS for both the superconducting and non-superconducting regimes, as both these regimes can be achieved experimentally at low temperature for the same materials.

We consider the Hamiltonian given by Eqs. (5.1-5.3), where we set  $p_y \rightarrow 0$ , and we perform a T-matrix analysis similar to that described in the previous section for both the SC and non-SC phases, for different directions of the magnetic impurity. The wire is considered to be oriented along the  $x$  direction, and the SO coupling is oriented along  $y$  [46,47]. We thus expect a similar and more exotic behaviour for impurities directed along  $x$  and  $z$ , and a more classical behaviour for impurities with the spin parallel to the direction of the SO, thus oriented along  $y$ .

The energies and wave functions of the Shiba states can be found using the same procedure as for the two-dimensional systems (see Appendix A). This yields for the energies of the states:

$$E_{1,\bar{1}} = \pm \frac{1 - \alpha^2}{1 + \alpha^2} \Delta_s, \text{ where } \alpha = J/v.$$

The FT of the positive energy state as a function of momentum and the SO coupling is presented in Fig. 5.7 for a SC (left column) and non-SC state (right column), for an impurity directed along  $z$ . For this situation the spin of the Shiba state has two non-zero components, one parallel to the wire, and one parallel to the impurity spin, and these two components are depicted in Fig. 5.7. Note that, similar to the two-dimensional case, there is a split of the FT features increasing linearly with the SO coupling strength. Also note that in the non-SC phase the central feature, whose wave vector is given by  $p_\lambda$ , is absent, and that the FT features are broadened in the SC regime with respect to the non-SC one. Furthermore, same as in the two-dimensional case, the SO affects the spin-polarised components but almost do not change the non-polarised LDOS, as it can be seen in Fig. 5.7 where it appears that the non-polarised LDOS FT features do not evolve with the SO coupling.

These results are confirmed by analytical calculations. Below we give the spin components and the LDOS in the SC state for an impurity directed along  $z$  obtained analytically (see Appendix

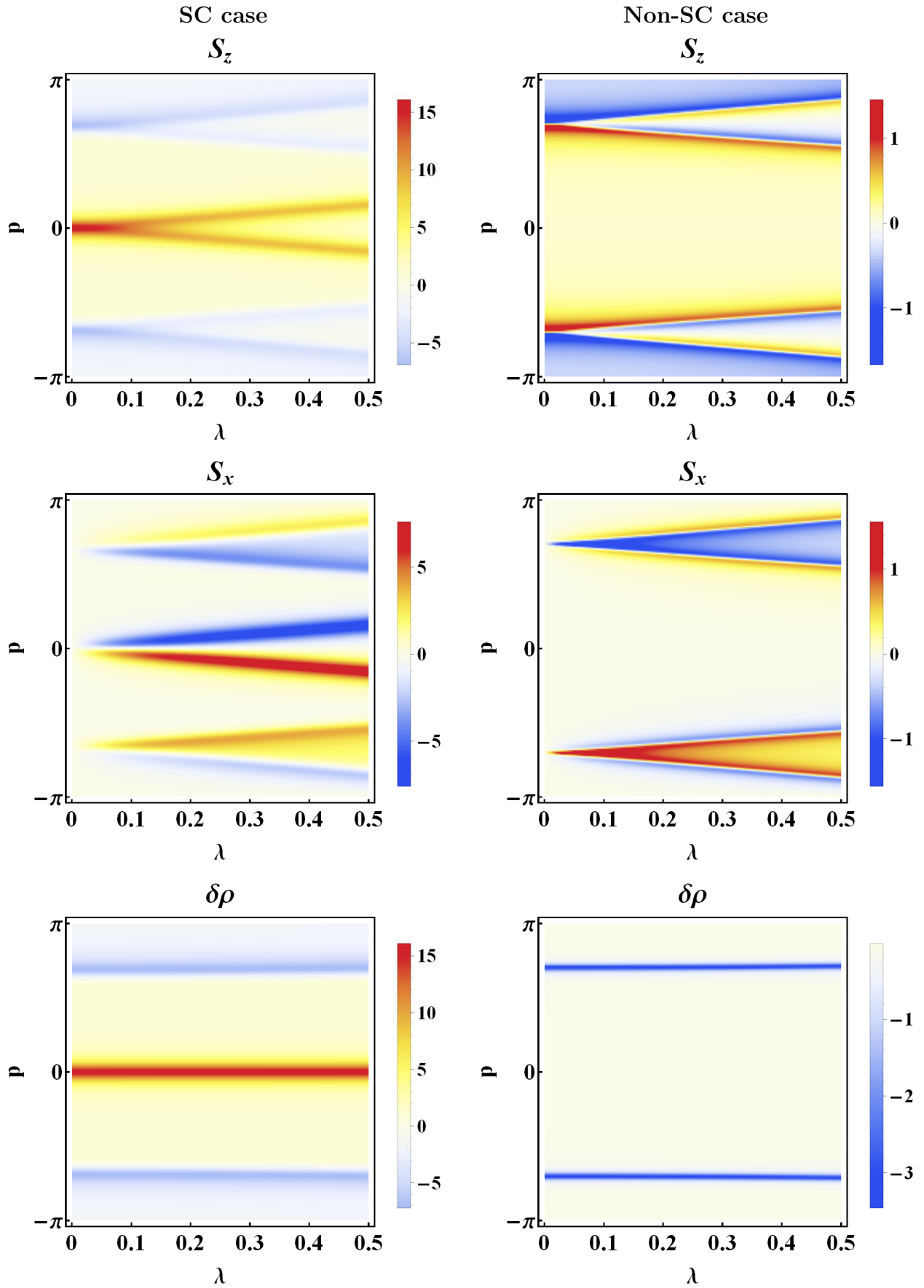


Figure 5.7: The FT of various SP LDOS component for a Shiba state (left column), and for an impurity state at  $E = 0.1$  (right column), as a function of the SO coupling  $\lambda$  and of momentum  $p$ , for an impurity perpendicular to the wire and directed along  $z$ . We set  $t = 1, \mu = 1$ . We take  $\Delta_s = 0.2, J_z = 4, \delta = 0.01$  in the SC case and  $\Delta_s = 0, J_z = 2, \delta = 0.05$  in the non-SC case.

A.1), for the positive energy Shiba state:

$$\begin{aligned}
S_x(x) &= \frac{1 + \alpha^2}{4} [2 \sin p_\lambda x + \sin(2mv|x| + p_\lambda x - 2\theta) - \sin(2mv|x| - p_\lambda x - 2\theta)] \cdot e^{-2\omega|x|/v} \\
S_y(x) &= 0 \\
S_z(x) &= -\frac{1 + \alpha^2}{4} [2 \cos p_\lambda x + \cos(2mv|x| + p_\lambda x - 2\theta) + \cos(2mv|x| - p_\lambda x - 2\theta)] \cdot e^{-2\omega|x|/v} \\
\rho(x) &= \frac{1 + \alpha^2}{2} [1 + \cos(2mv|x| - 2\theta)] \cdot e^{-2\omega|x|/v}
\end{aligned}$$

where  $\tan \theta = \alpha$ . We also present the FT of the SP LDOS for the non-SC phase for the impurity contribution corresponding to the energy  $E$  (see Appendix B):

$$\begin{aligned}
S_x(x) &= +\frac{\alpha}{1 + \alpha^2} \cdot \frac{1}{\pi v} [\cos(p_\varepsilon|x| - p_\lambda x) - \cos(p_\varepsilon|x| + p_\lambda x)] \\
S_y(x) &= 0 \\
S_z(x) &= +\frac{\alpha}{1 + \alpha^2} \cdot \frac{1}{\pi v} [\sin(p_\varepsilon|x| - p_\lambda x) + \sin(p_\varepsilon|x| + p_\lambda x)] \\
\rho(x) &= -\frac{2\alpha^2}{1 + \alpha^2} \cdot \frac{1}{\pi v} \cos p_\varepsilon x
\end{aligned}$$

As before, in the expressions above  $p_\varepsilon = 2(mv + E/v)$ ,  $p_\lambda = 2m\lambda$ .

Indeed these calculations confirm our observations, in the SC state the dominant wave vectors are  $2p_F^\pm = 2mv \pm p_\lambda$ ,  $2mv$  and  $p_\lambda$ , while in the non-SC phase only  $p_\varepsilon \pm p_\lambda$ , and  $2mv$ .

Similar results are obtained if the impurity is oriented along  $x$ , with the only difference that the  $x$  and  $z$  components will be interchanged, up to an overall sign change (see Appendixes A.1 and B). For impurities parallel to  $y$ , and thus to the SO vector, we expect the SP LDOS to be less exotic, and indeed in this case the only non-zero component of the impurity SP LDOS is  $S_y$ . In the SC regime we thus find

$$\begin{aligned}
S_x(x) &= 0 \\
S_y(x) &= -(1 + \alpha^2)[1 + \cos(2mv|x| - 2\theta)] \cdot e^{-2\omega|x|/v} \\
S_z(x) &= 0 \\
\rho(x) &= +(1 + \alpha^2)[1 + \cos(2mv|x| - 2\theta)] \cdot e^{-2\omega|x|/v}
\end{aligned}$$

while in the non-SC regime we have

$$\begin{aligned}
 S_x(x) &= 0 \\
 S_y(x) &= +\frac{2\alpha}{1+\alpha^2} \cdot \frac{1}{\pi v} \sin p_\epsilon |x| \\
 S_z(x) &= 0 \\
 \rho(x) &= -\frac{2\alpha^2}{1+\alpha^2} \cdot \frac{1}{\pi v} \cos p_\epsilon x
 \end{aligned}$$

We see that  $S_y$  exhibits features only at the  $2mv$  and correspondingly at the  $p_\epsilon$  wave vectors, same as the non-polarised LDOS, thus not allowing for the detection of the SO coupling.

For intermediate directions of the impurity spin, all three components will be present, with the  $x$  and  $z$  exhibiting all the wave vectors, while the  $y$  component solely the  $2mv$ , and with relative intensities given by the relative components of the impurity spin.

Thus, we conclude that, same as in the 2D case, the SO can be measured using spin-polarised STM and magnetic impurities; moreover, in the 1D case one needs to consider impurities that have a non-zero component perpendicular to the direction of the SO.

## 5.4 Discussion

We have analysed the formation of Shiba states and impurity states in 1D and 2D superconducting and metallic systems with Rashba SO coupling. In particular we have studied the Fourier transform of the local density of states of Shiba states in SCs and of the impurity states in metals, both non-polarised and spin-polarised. We have shown that the spin-polarised density of states contains information that allows one to extract experimentally the strength of the SO coupling. In particular, the features observed in the FT of the SP LDOS split with a magnitude proportional to the SO coupling strength. Moreover, the Friedel oscillations in the SP LDOS in the SC regime show a combination of wavelengths, out of which the SO length can be read off directly and non-ambiguously. We note that these signatures are only visible in the spin-polarised quantities and in the presence of magnetic impurities. For non-spin-polarised measurements, no such splitting is present and the wave vectors observed in the FT of the SP LDOS basically do not depend on the SO coupling. When comparing the results for the SC

Shiba states to the impurity contribution in the metallic state and we find a few interesting differences, such as a broadening of the FT features corresponding to a spatial exponential decay of the Shiba states compared to the non-SC case. Moreover, the FT of the SP LDOS in the SC regime exhibits extra features with a wavelength equal to the SO length which are not present in the non-SC phase. It would be interesting to generalise our results to more realistic calculations which may include some specific lattice characteristics, more realistic material-dependent tight-binding parameters for the band structure and the SO coupling values. However, we should note that our results have a fully general characteristic, independent of the band structure or other material characteristics, and that the features in the FT of the non-polarised LDOS will correspond to split features in the spin-polarised LDOS, and thus the spin-orbit can be measured unequivocally from the split obtained from the comparison between the non-polarised and spin-polarised measurements. We have checked that up to a rotation in the spin space our results hold also for other types of SO coupling such as Dresselhaus [92].

According to our knowledge, the FT-STM is a well-established experimental technique which does not deal with large systematic errors [10, 11, 18–20, 72–74]. The experimental data presented e.g. in Ref. [20] shows that the resolution in the Fourier space (momentum space) reaches  $0.05 \text{ \AA}^{-1}$ , whereas a typical value of spin-orbit coupling wave vector  $p_\lambda \sim 0.15 \text{ \AA}^{-1}$  (see e.g. Ref. [38]), and thus it is sufficient to resolve the features originating from the spin-orbit coupling. Moreover, we would like to point that the exponent  $e^{-2p_s r}$  defines in the real space how far the impurity-induced states are extended, and it manifests in the momentum space as the widening of the ring-like features appearing at particular momenta. The condition of resolving the spin-orbit is thus  $2p_s < p_\lambda$ , otherwise the widening is large enough to blur the spin-orbit feature. This condition can be rewritten in a more explicit way, namely

$$\frac{1}{\sqrt{1 + (\lambda/v_F)^2}} \cdot \frac{\alpha}{1 + \alpha^2} \cdot \frac{\Delta_s}{\varepsilon_F} < \frac{\lambda}{v_F}$$

For any realistic parameters the first two factors on the left side are of the order of unity, and  $\Delta_s/\varepsilon_F \sim 10^{-3}$  for superconductors. However, for realistic values of the spin-orbit coupling  $\lambda$ , this inequality holds and therefore there should not be any technical problem with resolving those features.

The results of this Chapter can be tested using for example materials such as Pb, Bi, NbSe<sub>2</sub> or InAs and InSb wires, which are known to have a strong SO coupling, using spin-polarised

STM which is nowadays becoming more and more available [32].

# Chapter 6

## Extracting triplet pairing type

In the early eighties it became clear that the theory of conventional superconductivity with s-wave pairing was not sufficient to describe certain compounds. Notably,  $\text{CeCu}_2\text{Si}_2$  reported by Steglich *et al.* in 1979 was believed to be a singlet d-wave superconductor [93] until 2014, when its superconducting properties were revisited by Kittaka *et al.* [94]. Later on, a plethora of unconventional superconductors was discovered, including the best known examples of triplet pairing –  $^3\text{He}$  superfluid reported by A. Leggett and J. Wheatley in 1975 [95,96], as well as the first triplet organic superconductor  $(\text{TMTSF})_2\text{PF}_6$  [97]. The discovery of high-temperature SC  $\text{LaBaCuO}_4$  by Bednorz and Müller in 1986 [98] was an important breakthrough that attracted even more attention to the physics of unconventional SCs.

Typical ways to discriminate experimentally conventional SCs from unconventional ones are to analyse either the power-law dependence of the nuclear magnetic resonance relaxation rate and/or the specific heat capacity dependence on temperature. Despite significant progress in material science, to date no solid state compound has been proven to be a p-wave superconductor. One of the most promising candidates is strontium ruthenate first described in the group of Maeno in 1994 [99]. However, the subject remains controversial and to date there is no agreement in the scientific community [100].

In what follows we study the magnetic properties of the impurity bound states in superconductors with p-wave pairing and find striking signatures in their spin polarisation which allow to unambiguously discriminate a non-topological superconducting phase from a topological one. Moreover, we show how these properties, which could be measured using spin-polarised scanning

tunnelling microscopy (STM), also enable to determine the direction of the spin-triplet pairing vector of the host material and thus to distinguish between different types of unconventional pairing.

Ever since the discovery of strontium ruthenate as one the first unconventional superconductors (SCs) more than thirty years ago [55], the search for the symmetry of Cooper pairs [101, 102] has been among the most important tasks to be addressed in order to characterise new superconducting materials. In the past decade, many new SCs with broken inversion symmetry have been discovered. These SCs are expected to display unconventional pairing due to the strong spin-orbit coupling. Indeed, in these materials, the twofold spin degeneracy is lifted by spin-orbit interaction, and the Cooper pairs exhibit a mixture of singlet and triplet pairing [103, 104]. Examples of such systems can be found in non-centrosymmetric SCs [102, 105] and doped topological insulators [57]. Other materials with unconventional pairing can also be uncovered within two-dimensional (2D) or quasi-2D superconductors which necessarily break the 3D inversion symmetry, such as the surface states of topological insulators in the proximity of s-wave superconductors [106], 2D materials with strong spin-orbit coupling proximitised by s-wave superconductivity [48, 49], monolayer or few-layer transition metal dichalcogenides [107, 108], etc.

The fact that the surface states of non-centrosymmetric SCs with mixed singlet and triplet pairing are predicted to support spin-polarised currents [109, 110] suggests that such 2D unconventional superconductors may exhibit a non-trivial spin response to local magnetic fields and magnetic impurities. In s-wave SCs, magnetic impurities lead to so-called intra-gap Shiba bound states (SBSs) [23–25] (see [34] for a review) which have experimentally been probed using STM [26, 27, 79, 80].

While a point-like scalar impurity does not induce a SBS in s-wave SCs [34], it gives rise to one SBS in p-wave dominant SCs [83, 111–113]. More interestingly, a point-like magnetic impurity leads to the formation of one SBS in the s-dominant regime and of two SBSs in the p-dominant regime, although as we show here, not all of them are always subgap states. This may suggest to use the number of SBSs as a natural criterion to discriminate between s-wave and p-wave SCs. However, we note that this quantity depends on the number of impurity orbitals which hybridise with the SC as well as the impurity shape. Recently it has also been shown that Shiba states in p-wave SCs have a non-trivial spectral dependence with respect to the spin-

orbit coupling (SOC) or with the direction of the magnetic moment [83], compared to the s-wave SCs. However, the former parameter (SOC) is usually given while the latter is not so easy to handle experimentally with magnetic fields.

In this Chapter, we propose to determine the degree of triplet pairing together with the orientation with respect to the sample plane of the spin-triplet pairing vector (the so-called  $\mathbf{d}$ -vector [101,102]) using spin-polarised STM measurements of the integrated spin-polarised local density of states (SP LDOS) of the SBSs, as well as its Fourier transform (FT), for the Shiba states associated with magnetic impurities. We find that for an impurity with a spin orthogonal to the  $\mathbf{d}$ -vector, the particle and hole component of the SBSs closest to mid-gap have spins of the same sign in the p-dominant regime, and of opposite sign in the s-dominant regime. Furthermore, when both the  $\mathbf{d}$ -vector and the impurity spin are in-plane, we find a spectacular cancellation of half of the in-plane spin components of the SBSs which can be traced back to the orbital pairing nature of the host SC. Therefore, the relative sign of the spin for these two states can serve as a probe to test experimentally the degree of p-wave pairing via spin-polarised STM measurements or using spin-polarised transport experiments. Moreover, by studying the Fourier transform (FT) of the electronic SP LDOS of these states, we find distinct features, the most striking being that the FT of the SP LDOS acquires a four-fold-symmetry, characteristic for the orbital p-wave pairing, in the topological p-wave dominant regime when both the  $\mathbf{d}$ -vector and the impurity spin are in the plane.

## 6.1 Model and techniques

We consider a 2D SC with both s-wave SC pairing  $\Delta_s$  and p-wave SC pairing  $\varkappa$ . The corresponding Hamiltonian is that of Eq. (4.1), where we set the Rashba SO constant  $\lambda = 0$ . Thus in the Nambu basis  $\Psi_{\mathbf{p}} = (\psi_{\uparrow\mathbf{p}}, \psi_{\downarrow\mathbf{p}}, \psi_{\downarrow-\mathbf{p}}^\dagger, -\psi_{\uparrow-\mathbf{p}}^\dagger)^\text{T}$  we have

$$\mathcal{H}_0 = \begin{pmatrix} \xi_{\mathbf{p}}\sigma_0 & \Delta(\mathbf{p}) \\ \Delta^\dagger(\mathbf{p}) & -\xi_{\mathbf{p}}\sigma_0 \end{pmatrix}. \quad (6.1)$$

where  $\Delta(\mathbf{p}) = \Delta_s\sigma_0 + \varkappa\mathbf{d}(\mathbf{p}) \cdot \boldsymbol{\sigma}$  is the mixed s-wave and p-wave pairing function. In order to simplify the discussion, we assume in what follows that  $\Delta_s$  and  $\varkappa$  are real and positive. The symbol  $\boldsymbol{\sigma}$  denotes the Pauli matrices acting in the spin subspace. The operator  $\psi_{\sigma\mathbf{p}}^\dagger$  creates

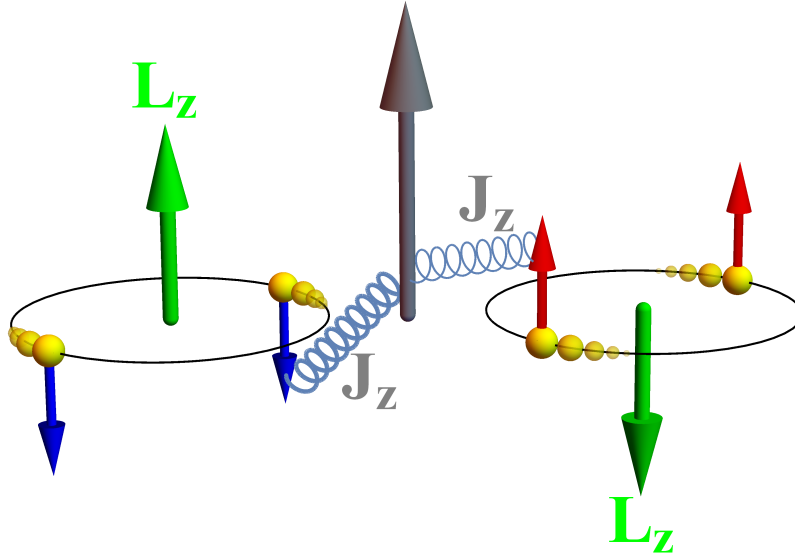


Figure 6.1: Sketch of an out-of-plane magnetic impurity in a p-wave TRS superconductor with an in-plane  $\mathbf{d}$ -vector. In this case, electrons forming Cooper pairs have always some out-of-plane spin components (blue and red arrows) [55]. Furthermore, due to TRS, Cooper pairs have either an angular momentum (green arrow) with  $L_z = +1$  and are composed of electrons with spins  $S_z = -1/2$  or the opposite [55]. TRS is locally broken by a magnetic impurity. For antiferromagnetic exchange interactions,  $J_z > 0$ , breaking Cooper pairs with electron spins  $S_z = -1/2$  (blue arrows) is energetically favoured compared to Cooper pairs with spins  $S_z = 1/2$  (red arrows), hence two non-degenerate in-gap bound states are expected.

a particle of spin  $\sigma = \uparrow, \downarrow$  of momentum  $\mathbf{p} = (p_x, p_y)$ . The system is considered to lay in the  $(x, y)$  plane. The energy dispersion in the normal state is embodied by  $\xi_{\mathbf{p}}$ . Since our main message is barely modified by the presence of the spin-orbit coupling term, we leave the discussion of its effect to Appendix A.2, whereas its effect on the spin polarisation of SBSs in superconductors with purely singlet pairing is discussed in detail in Chapter 5, as well as in Ref. [85]. The vector  $\mathbf{d}(\mathbf{p})$  parametrises the odd-parity triplet pairing term. We consider two cases: a TRS in-plane  $\mathbf{d}$ -vector,  $\mathbf{d}_{\parallel}(\mathbf{p}) = (p_y, -p_x, 0)$ , and a TRS breaking out-of-plane  $\mathbf{d}$ -vector,  $\mathbf{d}_{\perp}(\mathbf{p}) = (0, 0, p_x + ip_y)$ . The latter case has been introduced to describe the superconducting phase of  $\text{Sr}_2\text{RuO}_4$  [55]. We have studied other  $\mathbf{d}$ -vectors giving rise to unitary states and found out that these two choices are generic enough to describe 2D anomalous SCs. For the  $\mathbf{d}_{\parallel}$  case, we have checked that the total angular momentum operator  $M_{\parallel}^z = L_z + \sigma_z/2$  commutes with the Hamiltonian  $\mathcal{H}_0$  while for the  $\mathbf{d}_{\perp}$  case, the operators  $M_{\perp}^z = L_z - \tau_z/2$  and  $\sigma_z$  commutes with  $\mathcal{H}_0$ . Here,  $\mathbf{L} = \mathbf{r} \times \mathbf{p}$  denotes the orbital momentum operator and  $\tau_z$  is the Pauli matrix acting in particle-hole subspace.

In what follows we study what happens when a point-like magnetic impurity is introduced in the anomalous SC (see Fig. 6.1 for a sketch of a magnetic impurity immersed in a p-wave SC with an in-plane  $\mathbf{d}$ -vector). The impurities we consider have both a scalar component  $U$  and a magnetic component  $\mathbf{J} = (J_x, J_y, J_z)$ , and are described by Eq. (4.2). We assume that the  $s$ -channel is dominating over all the other scattering channels, since the impurity is described by delta-potential. We only consider here classical impurities oriented either along the  $z$ -axis,  $\mathbf{J} = (0, 0, J_z)$ , or along the  $x$ -axis,  $\mathbf{J} = (J_x, 0, 0)$ . These two directions are enough to make a point in the case of a 2D superconductor.

In order to analyse the spin structure of these Shiba states, we resort to the general T-matrix approximation scheme circumscribed in detail in Chapter 4 and in Ref. [34]. Even though for some limiting cases the T-matrix can be obtained analytically, below we use a more general numerical approach to find it and express the desired physical quantities.

## 6.2 Results

Before turning to the spin polarisation of SBS, it is worth making several remarks regarding certain peculiarities of the band structure in case of mixed s-wave and p-wave pairings, as well as the number and behaviour of the Yu-Shiba-Rusinov states.

### Band structure

The energy spectrum of the Hamiltonian in Eq. (6.1) is given by  $|\mathcal{E}| = \sqrt{\xi_{\mathbf{p}}^2 + (\Delta_s \pm \varkappa|\mathbf{p}|)^2}$ , and the effective superconducting gap reads  $\Delta_{eff} = |\Delta_s - \varkappa p_F|/\sqrt{1 + \tilde{\varkappa}^2}$  (see the derivation e.g. in Appendix A.2). We plot in Fig. 6.2 the spin-resolved band structure (the spin-polarised spectral function) as a function of energy and momentum for the model in Eq. (6.1) for an in-plane  $\mathbf{d}$ -vector,  $\mathbf{d} = \mathbf{d}_{\parallel}$ . We note that the bands acquire opposite spin polarisations reflecting the helical nature of the superconductor. Notably, the gaps in the two bands are different due to the presence of both s-wave and p-wave couplings. If the s-wave and p-wave coupling become equal, one of the gaps is closing, and the system becomes gapless [114, 115]: this point marks the transition between an s-dominant and p-dominant regime, or in other words, between a trivial and a topological superconductor.

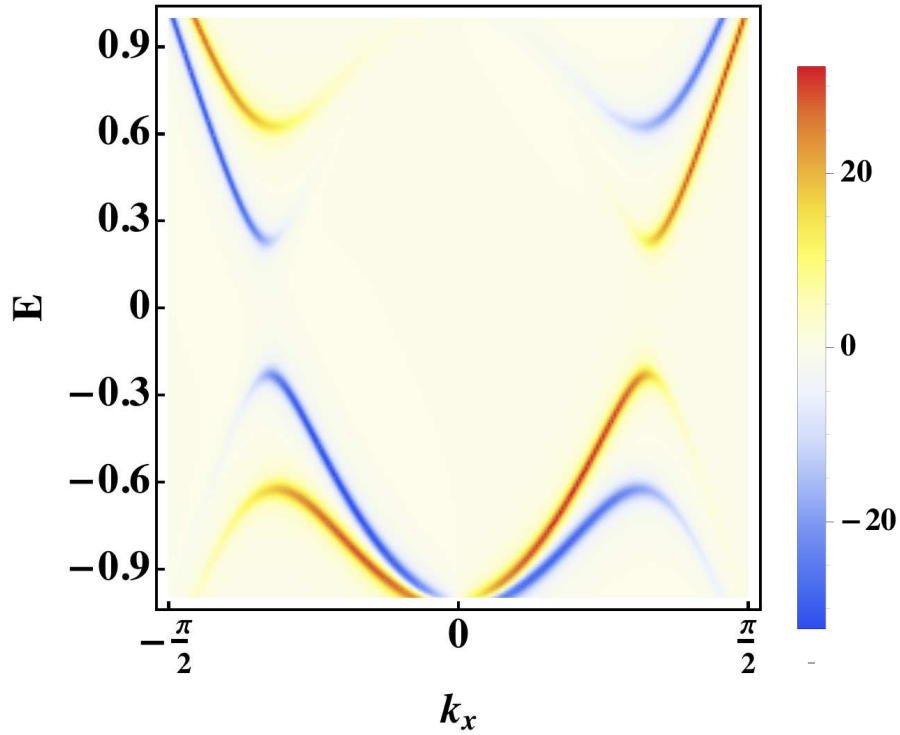


Figure 6.2: Spin-resolved band structure: We plot the  $x$  component of the spin-polarised spectral function as a function of energy and  $k_x$ . We consider a lattice model with dispersion  $\xi_{\mathbf{k}} = -2t \cos k_x - 2t \cos k_y - \mu$  with  $t$  the hopping amplitude and  $\mu$  the chemical potential. We take  $t = 1$ ,  $\mu = -3$ ,  $\Delta_s = 0.2$ ,  $\tilde{\varkappa} = 0.5$  and an inverse quasiparticle lifetime  $\delta = 0.03$ .

## Shiba bound states

Before we discuss the SBS in superconductors with p-wave pairing, we need to revisit the case of pure s-wave pairing. In case of the latter we set  $\lambda = 0$ ,  $\varkappa = 0$  in Eq. (4.1), and we notice that

$$\Theta \mathcal{H}_{s\text{-wave}}(\mathbf{p}) \Theta^{-1} = \mathcal{H}_{s\text{-wave}}(-\mathbf{p}),$$

where  $\Theta = i\sigma_y \otimes \tau_0 \cdot \mathcal{K}$ , with  $\mathcal{K}$  denoting the complex conjugation, is the time-reversal symmetry operator. Thus, the Hamiltonian for an s-wave SC respects time-reversal symmetry, and a localised impurity, which does not violate TRS, cannot affect the local density of states. The last statement is a corollary fact of the Anderson theorem [21], that implies that neither the critical temperature,  $T_c$ , nor the density of states are affected by the non-magnetic impurity scattering. Consequently, there are no impurity-induced states forming around a localised non-magnetic impurity in an s-wave SC.

The situation is drastically different when we turn to unconventional SCs, and p-wave SCs in particular. The latter break inversion symmetry and/or TRS, and the Anderson theorem

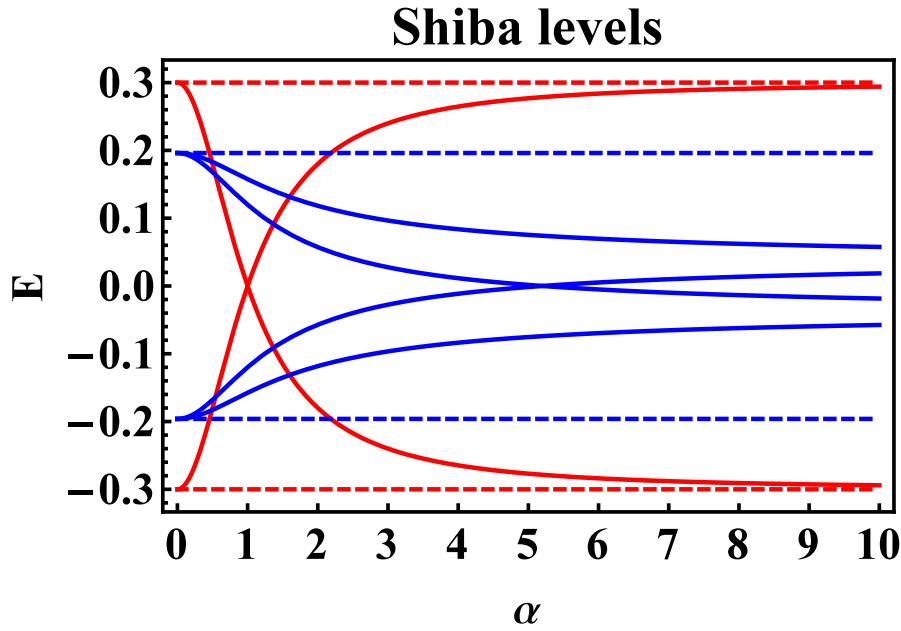


Figure 6.3: The energies of the Shiba states (in arbitrary units) for a s-wave SC (red lines) and a p-wave SC (blue lines) as function of the dimensionless impurity strength  $\alpha = \pi\nu J$  (the scalar potential is absent). The red and blue dashed lines denote the s-wave and p-wave SC gaps correspondingly. We set  $k_F = 1$ ,  $\Delta_s = 0.3$ ,  $\tilde{\kappa} = 0.2$ .

becomes inapplicable. The spectrum of the Shiba states can be found analytically as detailed in Appendix A.2. We generically found a pair of SBS for a point-like impurity. The SBS energies for a localised impurity with both scalar and magnetic components  $U$  and  $\mathbf{J}$  are given by:

$$|E_{\pm}| = \frac{-\gamma\beta_{\pm}^2 \operatorname{sgn} \beta_{\pm} + \sqrt{1 + \beta_{\pm}^2(1 - \gamma^2)}}{1 + \beta_{\pm}^2} \Delta_t, \quad (6.2)$$

where  $\beta_{\pm} = \frac{\pi\nu(U \pm |\mathbf{J}|)}{\sqrt{1 + \tilde{\kappa}^2}}$  is the dimensionless impurity strength,  $\gamma = \frac{\tilde{\kappa}}{\sqrt{1 + \tilde{\kappa}^2}}$ , and  $\Delta_t = \frac{\tilde{\kappa}k_F}{\sqrt{1 + \tilde{\kappa}^2}}$  is the effective p-wave gap. For a non-magnetic impurity, the two SBS are degenerate while this degeneracy is lifted for a magnetic impurity. Unlike s-wave SCs, non-magnetic disorder gives rise to impurity-induced states, similarly to what happens in a d-wave SC. Nonetheless, the important discrepancy is that in the latter Shiba states are not well-defined in the sense that they acquire a finite lifetime. Mathematically speaking, the poles of the perturbed retarded Green's function attain a non-zero imaginary part [34]. Contrary to that, in fully gapped p-wave SCs considered in this manuscript there is no broadening of the impurity bound states.

The behaviour of these energy levels is qualitatively different in s-wave SCs than in p-wave SCs. First of all, when increasing the impurity strength, the Shiba states in an s-wave SC approach the gap and eventually merge with the continuum, whereas in the p-wave case they

remain in the gap and asymptotically approach  $\pm\gamma\Delta_t$  (see Fig. 6.3). Second, the crossing point in the s-wave case is always at  $\alpha = 1$  independent of the singlet pairing  $\Delta_s$ , while for p-wave SCs the crossing point appears at  $\alpha = 1/\gamma \gg 1$  and thus depends on the value of the triplet pairing  $\tilde{\kappa}$ . Some realistic values of  $\alpha$  can be extracted from experimental data given e.g. in [27] for an s-wave SC: the superconducting gap is about 1 meV and the Shiba state appears at 0.1 meV, therefore  $\alpha \approx 0.9$  (close to the crossing point in Fig. 6.3). Since no p-wave superconductor has been unambiguously discovered so far (there are only some candidates like  $\text{Sr}_2\text{RuO}_4$  [55]), there is no experimental data available. However, taking comparable impurity strengths, we therefore expect the experiments to be in the regime much before the crossing point (see Fig. 6.3). We believe that it is unlikely to observe that point experimentally, because the dimensionless impurity strength must be too large ( $\alpha \sim 10$  since  $\gamma \ll 1$ ). Furthermore, in this regime the gap is renormalised (or even utterly suppressed), and the problem requires a self-consistent approach leading to a qualitatively different result, namely, the Shiba states might transform into the Andreev bound states (see [28] for further details). Also note that the physical meaning of the crossing point is the change in the ground state parity for both types of pairing.

In what follows we show how the degeneracy is lifted in the case of an impurity with both scalar and magnetic potentials. A scalar impurity in a pure p-wave SC has two degenerate Shiba states. For the in-plane  $\mathbf{d}$ -vector case which is TRS, the two SBS form Kramers pairs with total angular momentum  $M_z = M_{\parallel}^z = \pm 1/2$  (for an out-of-plane  $\mathbf{d}$ -vector, the Shiba states can be labelled with  $S_z = \pm 1/2$ ). When a small growing magnetic moment is introduced in the impurity potential, this degeneracy is lifted and the two levels split. For a magnetic impurity along the z-axis,  $M_z = \pm 1/2$  is conserved and the SBS with  $M_z = -1/2$  has a lower energy due to antiferromagnetic interactions (see Fig. 6.4 for a sketch of the energy levels of Shiba bound states). Note that an in-gap quasi-particle excitation with  $M_z = -1/2$  is *a priori* a coherent superposition of states with  $(L_z = 0, S_z = -1/2)$  and  $(L_z = -1, S_z = 1/2)$ , the former being more electron-like, the latter being more hole-like. Since the impurity potential is point-like, only the  $(L_z = 0, S_z = \pm 1/2)$  components are affected by the impurity which explains the labelling used in Fig. 6.4. It is easy to compute this splitting using a series representation for

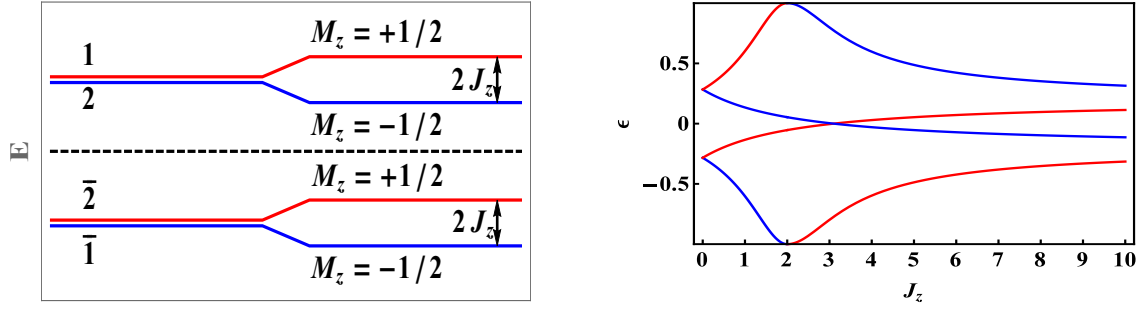


Figure 6.4: Left: Sketch of the energy levels obtained by perturbation theory in impurity strength  $J_z$ . The colours stand for the angular momentum: red for  $+1/2$  and blue for  $-1/2$ . Right: Energy levels as a function of impurity strength  $J_z$  obtained analytically. We set  $\tilde{\kappa} = 0.2$  and used the same colour code.

$\eta = J_z/U \ll 1$ . We find

$$\delta\epsilon = \epsilon_2 - \epsilon_1 \approx \frac{2\beta^2}{(1 + \beta^2)^2} \left[ 1 + \frac{\eta}{\sqrt{1 + \beta^2(1 - \eta^2)}} \right] \eta,$$

where  $\beta = \frac{\pi\nu U}{\sqrt{1 + \tilde{\kappa}^2}}$ . We plot the energy levels using the analytical expressions in Eq. (6.2). The evolution of the energy levels as a function of the dimensionless magnetic impurity strength is plotted in Fig. 6.4.

## Spin polarisation of Shiba states

We begin by plotting the spatially averaged LDOS and SP LDOS as functions of energy. Note that when performing the T-matrix calculations we consider a discretised version of the Hamiltonian in Eq. (6.1) and we perform all the momentum integrals over the first Brillouin zone (see e.g. the caption in Fig. 6.2). The impurity states appear as resonances overlapping with a background which corresponds to the DOS in the absence of impurities. Since the unperturbed DOS is not spin-polarised, this background is non-zero only for the averaged LDOS, and the SP DOS contains only impurity-induced contributions. The unperturbed retarded Green's function, the T-matrix and the FT of the SP LDOS components,  $S_{\hat{n}}(\mathbf{p}, E)$ , with  $\hat{n} = x, y, z$ , as well as the FT of the LDOS,  $\delta\rho(\mathbf{p}, E)$ , are given by Eqs. (4.5) and (4.11-4.14). The average DOS and SP DOS are given respectively by

$$\begin{aligned} \rho(E) &= \rho_0(E) + \mathcal{N}\delta\rho(\mathbf{p} = 0, E) \\ S_{\hat{n}}(E) &= S_{\hat{n}}(\mathbf{p} = 0, E), \end{aligned}$$

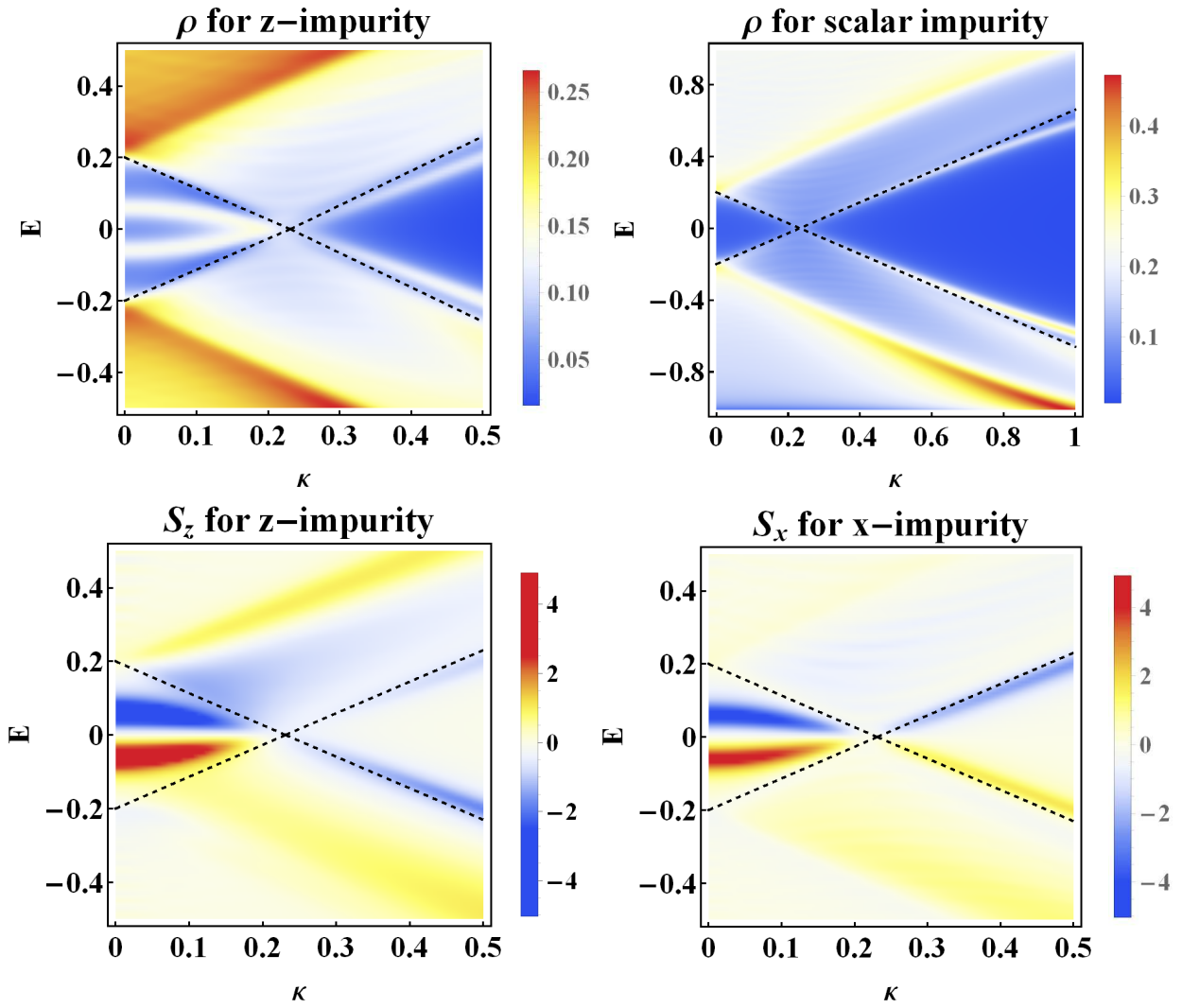


Figure 6.5: Average LDOS (first row) and SP LDOS (second row) (in arbitrary units) as functions of energy and the p-wave pairing,  $\tilde{\kappa}$ , for an in-plane  $\mathbf{d}$ -vector. We consider a scalar impurity with  $U = 6$  in the upper right panel, and magnetic impurities with an impurity strength of  $J_z = 2$  (left column) and with  $J_x = 2$  (lower right panel). We set  $\Delta_s = 0.2$ , and  $\delta = 0.03$ . The gap of the system is denoted by the dashed line.

for  $\hat{n} = x, y, z$ . Here  $\mathcal{N}$  denotes the impurity concentration. The energy  $E$  corresponds to energies of Shiba states. Hereafter, we consider the dilute impurity limit and thus we take in what follows a concentration of impurities of  $\mathcal{N} = 2\%$ .

In Figs. 6.5, 6.6, 6.7 and 6.8 we focus on how the impurity states are affected by the value of  $\kappa$ , the p-wave order parameter, as well as by the impurity strength  $\mathbf{J}$ . Note that an impurity with magnetic moment along a direction specified by a unit vector  $\hat{n}$ , gives rise to a total (averaged along the entire space) non-zero polarisation *only* along  $\hat{n}$ , even if it would give rise to a non-zero spatial spin structure in more than one spin components.

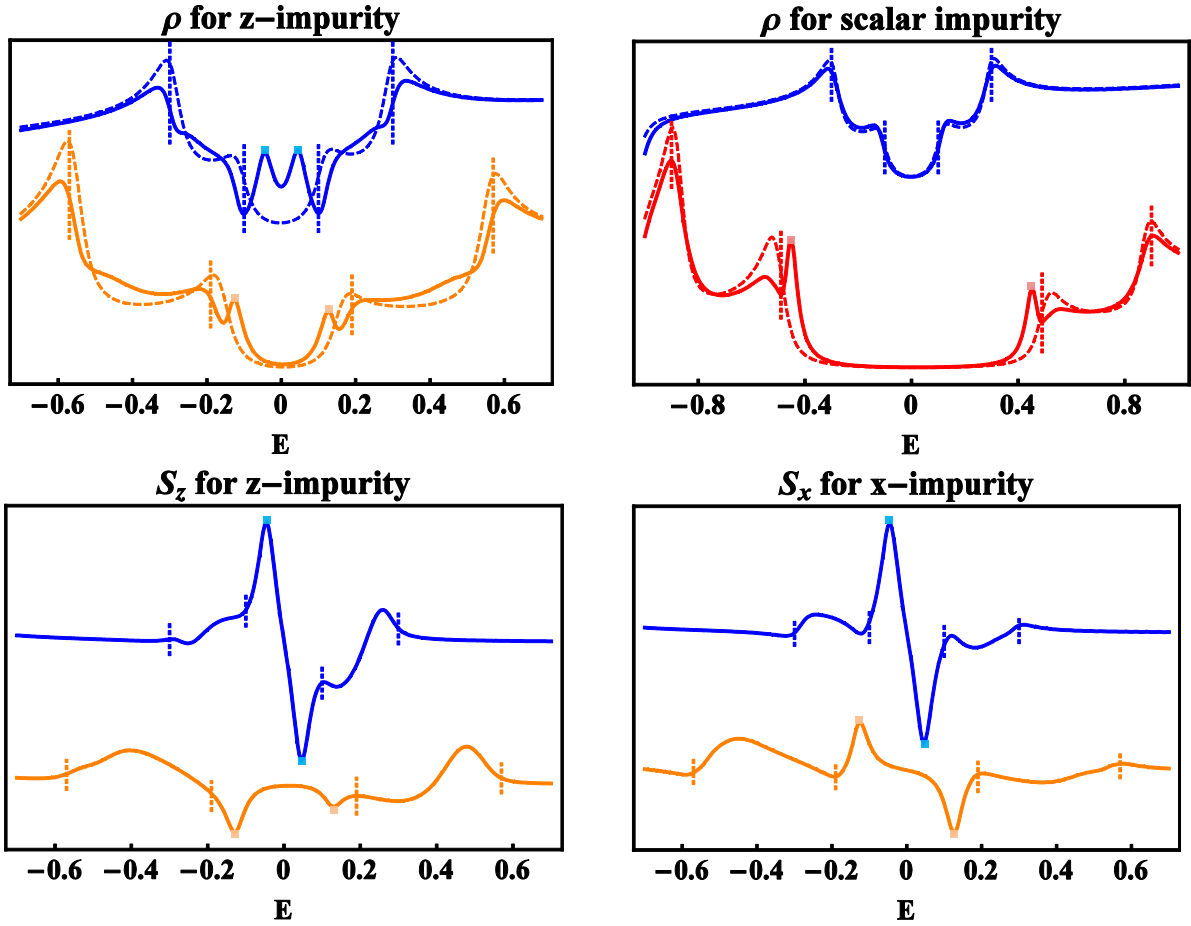


Figure 6.6: Upper panel: Average LDOS (in arbitrary units) as functions of energy for an in-plane  $\mathbf{d}$ -vector for different values of the p-wave pairing,  $\tilde{\kappa}$ : blue stands for  $\tilde{\kappa} = 0.1$ , orange for  $\tilde{\kappa} = 0.4$  and red for  $\tilde{\kappa} = 0.8$ . The dashed lines correspond to the averaged LDOS in the absence of impurities while the plain lines show the LDOS in presence of impurities. We can thus disentangle the spectral features due to the impurity bound states from the gap edges. Lower panel: same as the upper panel but for the SP LDOS. The vertical dashed lines correspond to the two gap edges denoted in the main text by  $\Delta_{eff}^{\pm}$ . The subgap Shiba states peaks are marked by filled squares. The other parameters are the same as in Fig. 6.5.

### Number of Shiba bound states

The number of Shiba states depends on the type of impurity, as well as on the two competing SC order parameters. Therefore, there is no in-gap SBS in the non-topological s-dominant regime for a scalar impurity, and a double-degenerate SBS in the topological p-dominant regime [34,83] (see also [116] and Appendix A.2). As shown in Figs. 6.5 and 6.6, these states tend to stay close to the gap edge for not too large p-wave couplings. For a magnetic impurity, one SBS forms in the s-dominant regime, and two in the p-dominant regime (see Figs. 6.5, 6.6 and 6.7). Out of the two, in most cases one is a subgap state, while the other is dissolved in the continuum. When the impurity strength increases this 'bulk' SBS approaches the gap edge and becomes

more visible (see Fig. 6.8 and also Appendix A.2). However, this is not a generic feature. All impurity states can be in-gap states, as it does occur for a pure p-wave SC (see Fig. 6.8), as well as for a small s-wave coupling (see Fig. A.3 in Appendix A.2). When increasing the impurity strength the energy of the inner BS decreases to zero and there is a level crossing corresponding to a change of the ground state parity [34, 90] (see Figs. 6.7 and 6.8). As can be seen from these two figures the pure p-wave and the dominant p-wave regime are very similar, the main difference being the position of the outer SBS with respect to the band edge.

### Local density of states

In the upper panel of Fig. 6.5, we plot the average LDOS as a function of the triplet pairing parameter  $\varkappa$  and energy. This allows us to visualise the subgap states together with the edges of the gap. In order to illustrate the spectral features of the averaged LDOS, we plot in the upper panel of Fig. 6.6 vertical cuts of the density plots shown in Fig. 6.5. The dashed lines mark the unperturbed averaged LDOS. In the presence of both s-wave and p-wave pairing, there exist two effective values giving the gap edges (for derivation see Appendix A.2):

$$\Delta_{eff}^{\pm} = \frac{|\Delta_s \pm \varkappa p_F|}{\sqrt{1 + \varkappa^2}}. \quad (6.3)$$

It is clear that some of the noticeable out-of-the-gap features appearing in Fig. 6.5 can be traced back to the gap edges (denoted by the dashed lines) slightly modified by the presence of the impurity that affects all the energies in the continuum. Besides we can identify features corresponding to the localised impurity, which we identify by filled squares. The subgap Shiba states peaks are identified by filled triangles. Note that the asymmetry in the averaged LDOS between positive and negative energy  $E$ , is a direct consequence of the fact that we plot only the electronic parts of the Green's function to circumvent the particle-hole redundancy of the BdG description. Moreover, there is no contradiction with the particle-hole symmetry (PHS) since the peaks appear at opposite energies as expected, whereas values of the spectral function we plot might differ.

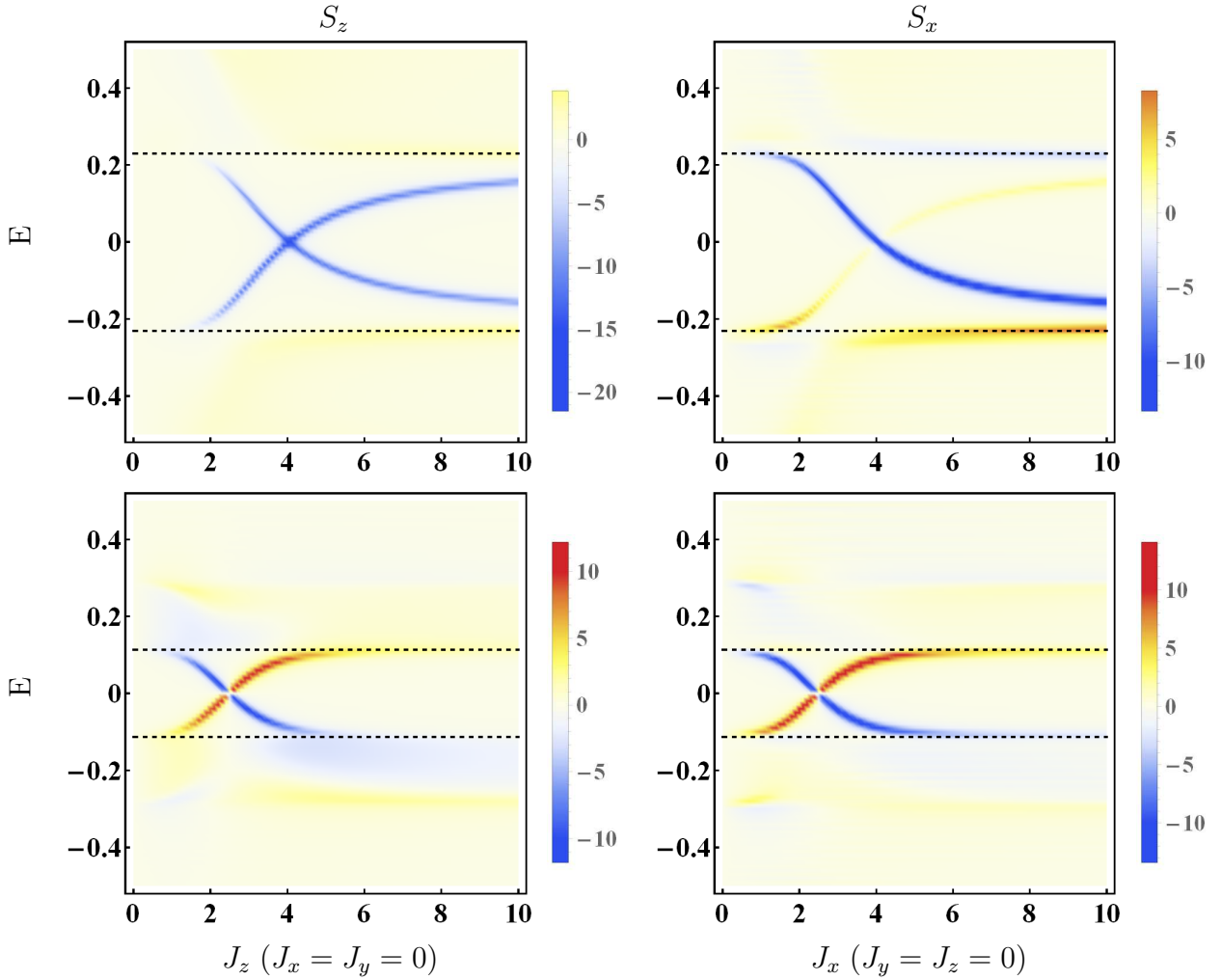


Figure 6.7: Average SP LDOS as a function of energy and impurity strength for magnetic impurities with spin along  $z$  (left column) and  $x$  (right column) for an in-plane  $\mathbf{d}$ -vector. We set  $\delta = 0.01$  and we focus on the dominant p-wave case ( $\tilde{\kappa} = 0.5$ ,  $\Delta_s = 0.2$ , first row), and the dominant s-wave case ( $\tilde{\kappa} = 0.1$ ,  $\Delta_s = 0.2$ , second row). The gap is denoted by the dashed line.

### Spin-polarised local density of states

As a first striking result, we find that for the 'orthogonal' configurations (either an in-plane  $\mathbf{d}$ -vector and an out-of-plane impurity spin, or the reverse situation), both particle and hole components of the SBSs closest to mid-gap have electronic spins with the same spin orientation in the p-dominant regime, and of opposite orientation in the s-dominant regime. This is also shown in the upper left panel of Figs. 6.7 and 6.8 for the former case (see also Fig. A.4 in Appendix A.2 for the latter case). This is a direct signature of the triplet nature of the Cooper pair and of the  $\mathbf{d}$ -vector orientation. Indeed, the spins of the paired electrons live in the plane orthogonal to the  $\mathbf{d}$ -vector (see Fig. 6.1). For an in-plane  $\mathbf{d}$ -vector, the paired electrons have, therefore, always a non-zero spin component along the  $z$  direction. Because of

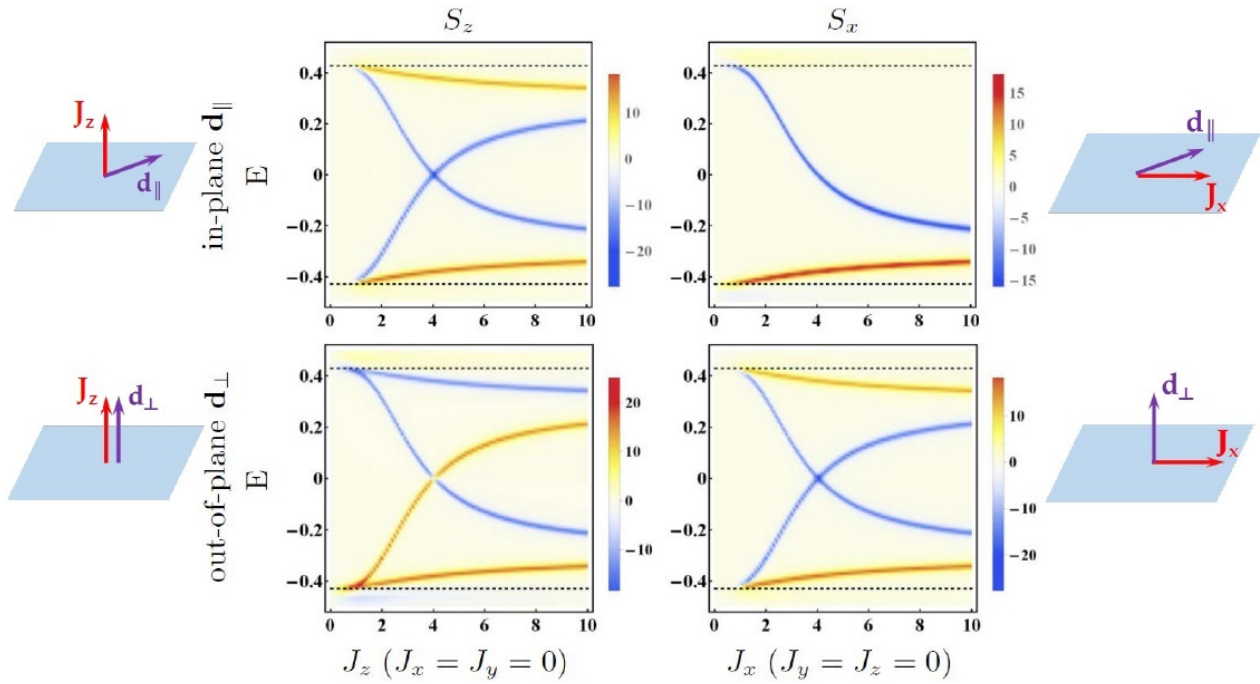


Figure 6.8: Average SP LDOS as a function of energy and impurity strength for magnetic impurities with spin along  $z$  (second column) and along  $x$  (third column). The sketches on the left and on the right are showing the relative position of the  $\mathbf{d}$ -vector and impurity spin  $J_{z,x}$ . We take  $\delta = 0.01$  and we focus on the pure p-wave  $\tilde{\kappa} = 0.5$ ,  $\Delta_s = 0$  with in-plane  $\mathbf{d}_{\parallel}$  (first row) and out-of-plane  $\mathbf{d}_{\perp}$  (second row). The gap is denoted by the dashed line.

the antiferromagnetic exchange coupling, it thus costs less energy to break Cooper pairs with spins pointing in the direction opposite to the impurity spin. Note that in the latter case  $M_{\parallel}^z$  commutes with the full Hamiltonian  $\mathcal{H}_0 + \mathcal{H}_{imp}$  which allows to attribute a well defined angular momentum  $M_{\parallel}^z = \pm 1/2$  to the Shiba states. By analogy with the local susceptibility of triplet SCs [102] this explains the spin sensitivity of the SBS to a local impurity spin pointing along the  $z$  axis. On the other hand, when the  $\mathbf{d}$ -vector and the impurity spin are both in-plane (Fig. 6.5 lower right panel) or both out-of-plane (lower left panel of Fig. 6.8, and also Fig. A.4 in Appendix A.2), the opposite-energy SBS closest to mid-gap have spins of opposite sign for both the s-wave and p-wave dominant regimes as expected from the previous argument based on the spin orientation of the paired electrons.

Our second important result is that the magnitude of the average SP LDOS of the particle and hole component of the SBSs are generically different. Most strikingly, when both the  $\mathbf{d}$ -vector and the impurity spin are in-plane (in this case  $M_{\parallel}^z$  is no longer a conserved quantity) only two of the four states remain spin-polarised while the spin polarisation of the other two goes to zero (see Fig. 6.8) in the extreme case of a pure p-wave SC. This cancellation can be

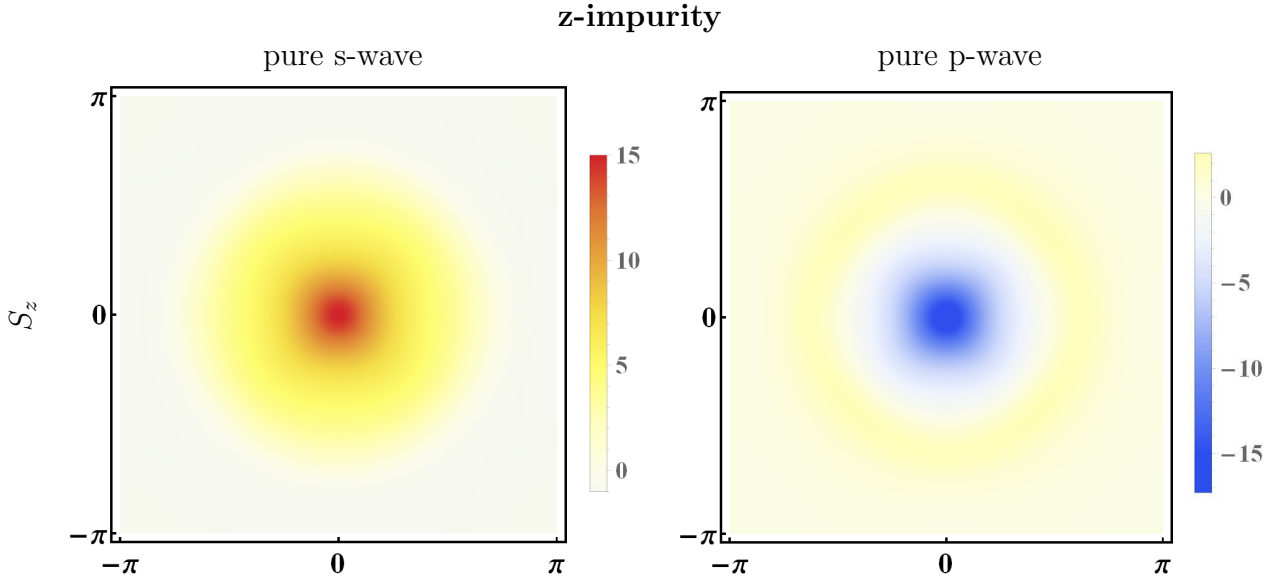


Figure 6.9: The real part of the FT of the  $S_z$  SP LDOS component for the hole component of a Shiba BS as a function of momentum ( $p_x, p_y$ ) for a magnetic impurity with  $J_z = 2$  and an in-plane  $\mathbf{d}$ -vector. We take  $\Delta_s = 0.2, \tilde{\kappa} = 0$  for a pure s-wave SC, and  $\Delta_s = 0, \tilde{\kappa} = 0.5$  for a pure p-wave SC.

directly traced back to the orbital nature of the p-wave order parameter which entails that  $S_x(\mathbf{p} = \mathbf{0}) = S_y(\mathbf{p} = \mathbf{0}) = 0$  for this particular SBS components (see the first row in Fig. 6.10 as well as Fig. 6.11). Results obtained with the analytical approach confirm the numerical ones. For further details I refer the reader to Appendix A.2 as well as to Ref. [85]. Despite the fact that this exact cancellation would disappear with the inclusion of the SOC, a strong asymmetry between the SP DOS of the particle and hole components of the SBSs largely survives (see Fig. A.7 in Appendix A.2).

We now focus on the FT of the SP LDOS associated with SBSs. As shown above, the most dramatic situation corresponds to an in-plane  $\mathbf{d}$ -vector. For a z-impurity, the SP LDOS of the positive energy state (the electron component of the SBS) does not change sign when undergoing the topological transition, while the spin polarisation of the negative energy state (the hole component) does (see lower left panel of Fig. 6.5). We thus focus on the latter.

In Fig. 6.9 we plot the FT of  $S_z(\mathbf{p}, E)$  (the only non-zero component of the SP LDOS) for the pure s-wave (left panel) and pure p-wave (right panel) regimes. Although they have similar shapes, as expected by rotational symmetry along the z-axis, they show qualitative different behaviours: in the former case, one obtains a central peak and a ring with the same sign, while for the latter case they have opposite signs, corresponding to a spin flip of the average spin

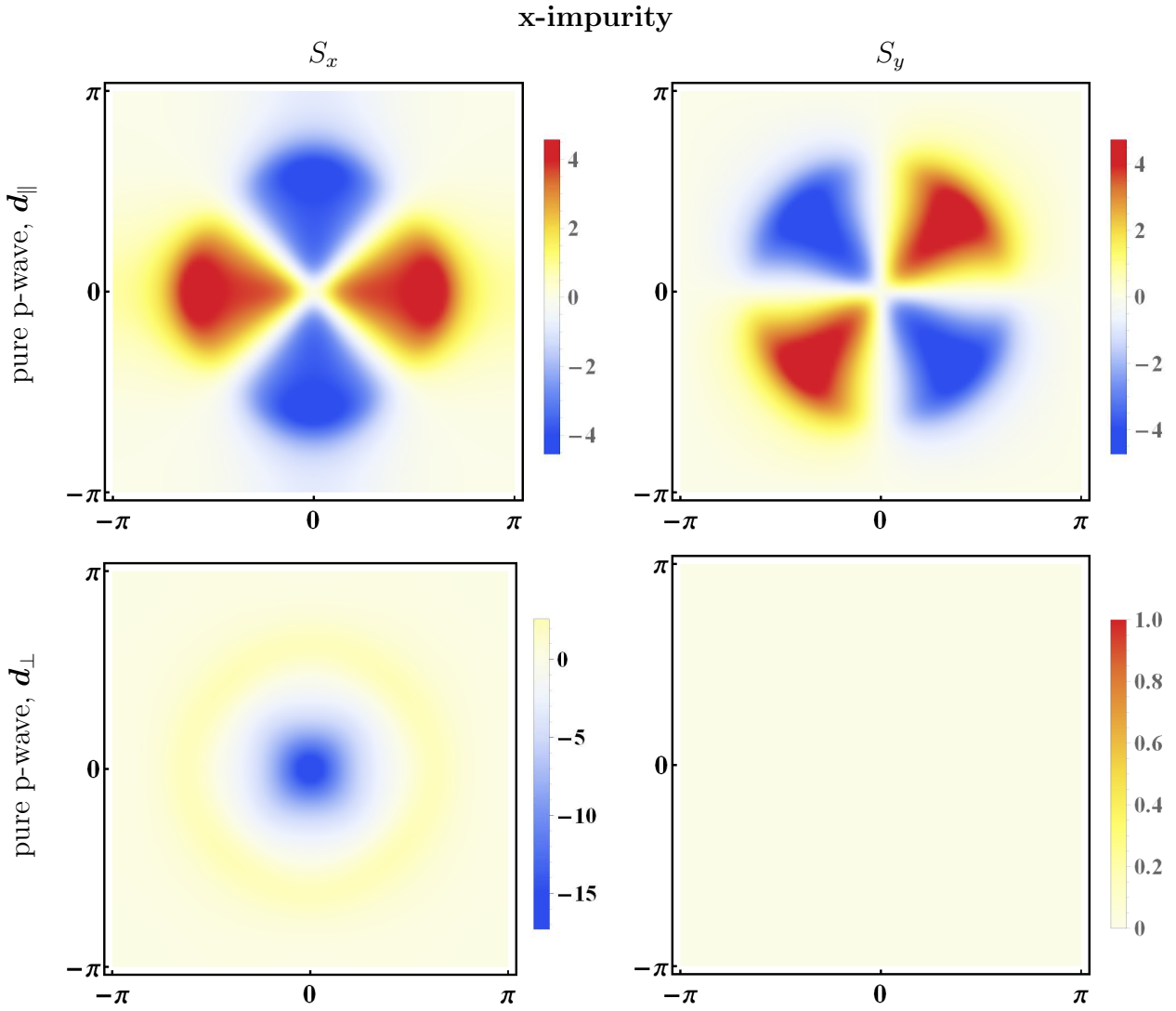


Figure 6.10: The real part of the FT of the  $S_x$  and  $S_y$  components of SP LDOS in arbitrary units for the hole component of a Shiba state as a function of momentum  $(p_x, p_y)$ , for a magnetic impurity with  $J_x = 2$ . We take  $\tilde{\kappa} = 0.5$  for the pure p-wave SC with  $\mathbf{d}$  in plane (first row) and  $\mathbf{d}$  perpendicular to the plane (second row).

polarisation between the dominant s-wave and dominant p-wave regimes.

Finally, we focus on the FT of the SP LDOS for a state whose total spin polarisation goes to zero in the pure p-wave case, as described in Fig. 6.8 for both in-plane  $\mathbf{d}$ -vector and spin impurity ( $J_x = 2$ ). While for the pure s-wave case (not shown) the  $S_x$  observable would exhibit the same qualitative features as those described in the left panel of Fig. 6.9, for the pure p-wave SC both  $S_x$  and  $S_y$  are non-zero (first row of Fig. 6.10), and most strikingly exhibit characteristic four-fold symmetries. For an in-plane  $\mathbf{d}$ -vector,  $\mathcal{H}_{imp}$  no longer commutes with  $\mathcal{H}_0$  and therefore an in-plane impurity is sensitive to the orbital part of the triplet Cooper pairs. Due to this four-fold symmetry we have also  $S_{x/y}(\mathbf{r} = \mathbf{0}) = 0$ , in agreement with analytical solutions (see

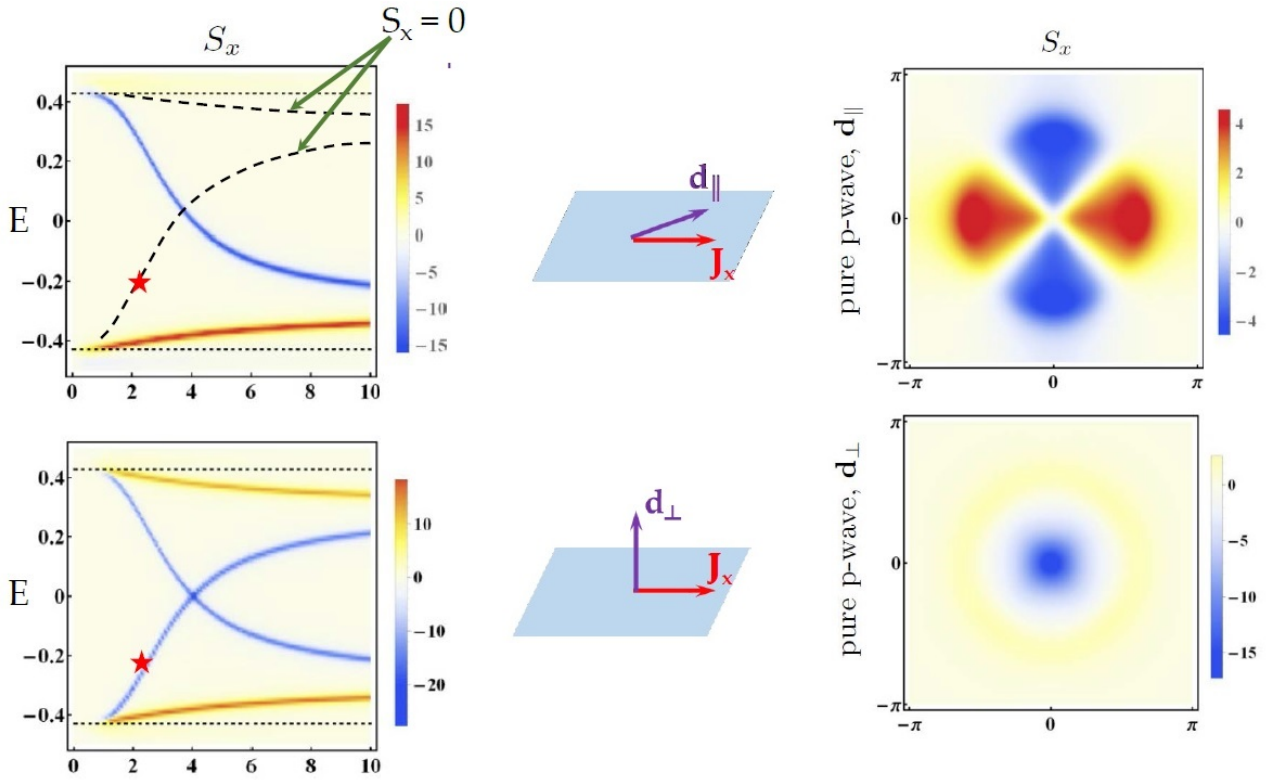


Figure 6.11: Left: the second column of Fig. 6.8. Middle: relative positions of the  $\mathbf{d}$ -vector and impurity spin. Right: the first column of Fig. 6.10. The red stars mark the values of energy and impurity strength at which we computed the FT LDOS in the right column. Black dashed lines show the Shiba states with zero spin polarisation along  $x$  direction. In the first row the accidental spin cancellation occurs due to the four-fold symmetry of the p-wave, whereas in the second row the spin polarisation of the Shiba state is negative, and can be traced back to the value of the FT LDOS at  $\mathbf{p} = \mathbf{0}$ .

Appendix A.2). Note that this is a very unique feature. For comparison we consider also a pure p-wave state with a  $\mathbf{d}_\perp$  vector perpendicular to the plane (second row of Fig. 6.10) and we find that in this case only the  $S_x$  component of the SP LDOS is non-zero and moreover has a radial structure as expected by rotational symmetry around the  $z$  axis. Therefore such characteristic spin anisotropy, if detected in spin-polarised STM, can be used as a signature of the transition into a topological p-dominant regime, as well as an indicator of the direction of the  $\mathbf{d}$ -vector.

In order to show explicitly the difference between the  $\mathbf{d}_\parallel$  and  $\mathbf{d}_\perp$ , we combine in Fig. 6.11 the second column of Fig. 6.8. and the first column of Fig. 6.10. Since the latter shows the FT of LDOS, we specify with a red star at which energy and impurity strength value we compute it.

We should note that the previous two results are qualitatively unchanged when comparing s-wave and p-wave dominant SCs instead of pure s-wave and p-wave (see Appendix A.2) for a detailed description of the mixed case), though small differences arise such as non-zero values

for all the components of the FT of the SP LDOS. Moreover, the results presented above qualitatively hold in the presence of Rashba SOC although the cancellation present in Fig. 6.8 becomes only partial (see Fig. A.8 in Appendix A.2).

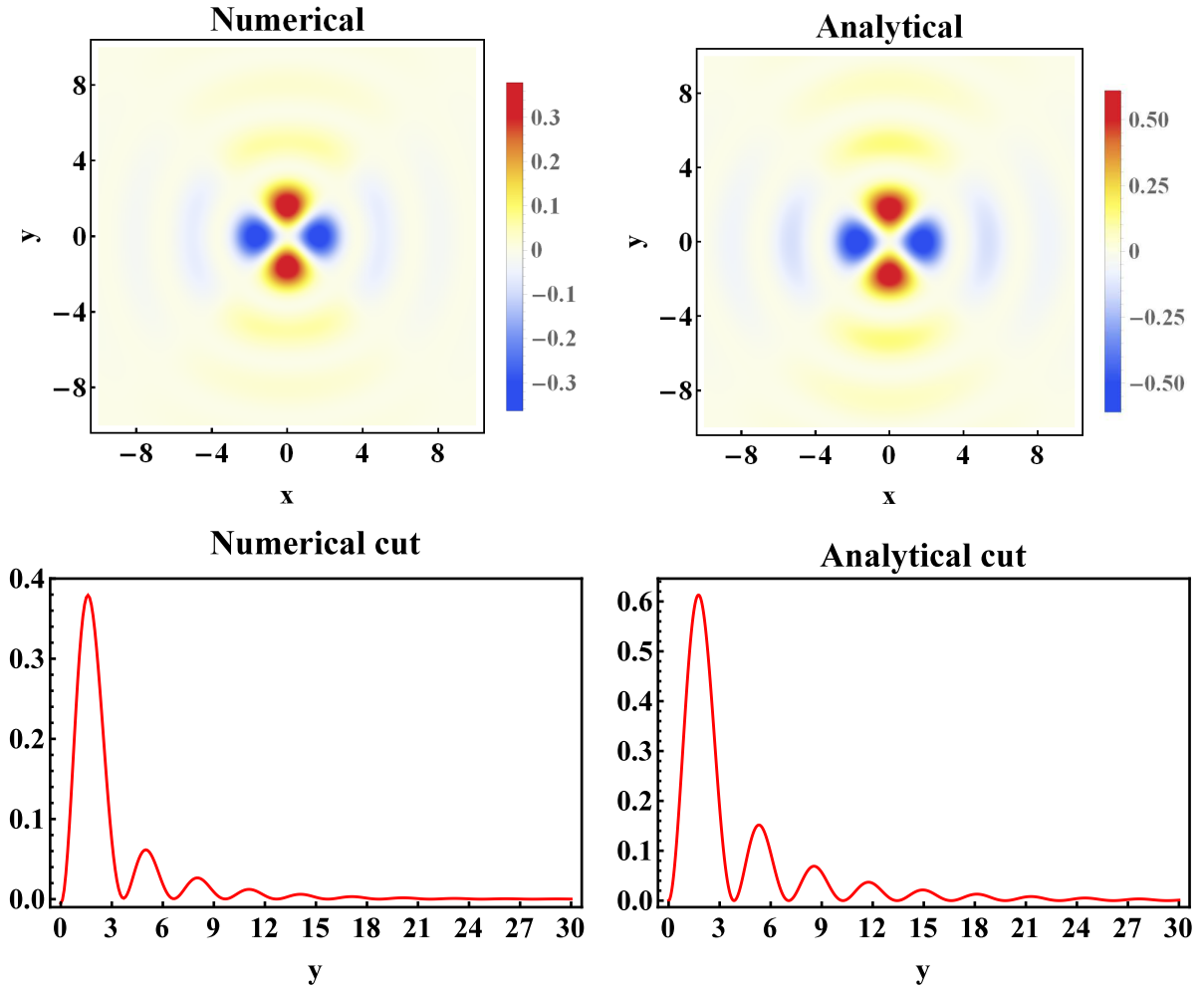


Figure 6.12:  $S_x$  for  $x$ -impurity (in arbitrary units) in coordinate space, for an in-plane  $\mathbf{d}$ -vector, and for the negative inner energy. In the left two panels we show the numerical simulations on a square lattice with spectrum  $\Xi_k = \mu - 2t(\cos k_x + \cos k_y)$ , where we take  $\mu = 3$ ,  $t = 1$  and the lattice constant is set to unity (for more details see Ref. [84]). In the right two panels we plot analytical results derived in this manuscript. To match the spectrum on a lattice we take  $\nu = 1/4\pi$ ,  $v_F = 2$ ,  $k_F = 1$ . The triplet pairing  $\tilde{\chi} = 0.2$  and the impurity strength  $J_x = 2$  for both panels. The two lower panels correspond to 1D cuts of the upper two panels at  $x = 0$ . It is clear that both plots reflect the characteristic p-wave four-fold symmetry and qualitatively agree except at very short distance as expected.

Note also that the results remain valid if the direction of the impurity spin is arbitrary. As it has already been pointed out in the article, an impurity with magnetic moment along a direction specified by a unit vector  $\hat{n}$ , gives rise to a total (averaged along the entire space) non-zero polarisation only along  $\hat{n}$ , even if it would give rise to a non-zero spatial spin structure in more than one spin components. Thus, instead of having one non-zero spin-polarised DOS

component in a particular direction ( $x$ ,  $y$  or  $z$ ), one has all three of them if all three  $J_x$ ,  $J_y$  and  $J_z$  present. We have checked that the average spin structure along a given direction in this case is exactly similar to that corresponding to the impurity spin pointing along this particular direction. For the FT of the SPDOS a particular example is presented in the Appendix A.2.

Finally, in Fig. 6.12 we present a qualitative comparison of these analytical results with the previously obtained numerical simulations on a square lattice by calculating  $S_x$  for a  $x$ -impurity (in arbitrary units) in coordinate space. The two approaches agree very well except at small distances from the impurity. This is expected since the analytical model is a low-energy approximation for the square-lattice model introduced in this part, and thus it is expected to give accurate results at small energies and large distances. We also note that the wave functions we calculated analytically are non-normalised ones. Therefore, the overall amplitude of the results cannot be compared (and hence the different scales). Note there is a small discrepancy between the periods of the oscillations obtained using analytical and numerical tools, which can be traced back to the difference of the energies of the Shiba states between the two models. Overall, the qualitative agreement between the numerical and analytical results is remarkably good, especially at large distances, as expected.

### 6.3 Discussion

All the aforementioned numerical data are confirmed by analytical calculations of the spatial structure and the asymptotic expansions of the wave functions for the SBS in 2D superconductors (see Appendix A.2). We believe that our results can be used for studying the topological phases of matter that can be engineered with impurities in different types of p-wave superconductors, in particular the exact analytical form of the Shiba wave functions, are useful for computing the Chern numbers in such emergent topological superconductors.

We have analysed the formation of Shiba states in 2D SCs with broken inversion symmetry with an admixture of s-wave and p-wave superconductivity. We have found that the number, the energy and especially the spin polarisation of the Shiba states depend strongly on the ratio between the values of the s-wave and p-wave coupling. We propose to test experimentally the presence of the p-wave coupling, as well as the direction of the  $\mathbf{d}$ -vector with respect to the sample plane by measuring the spin polarisation and energy of the Shiba bound states via spin-

polarised STM or transport. We note that these signatures are only visible in the spin-polarised quantities and in the presence of magnetic impurities.

Our results can be tested using quasi-2D SCs such as  $\text{Sr}_2\text{RuO}_4$  described by realistic multiband models that can be found e.g. in Refs. [117–120]. One of the possible extensions of these findings could be to generalise these results for higher order triplet pairing SCs, such as an f-wave SC.

## Part III

# Engineering topological superconductors with impurities

---

In allem Chaos ist Kosmos und in aller  
Unordnung geheime Ordnung.

---

*Carl Gustav Jung*

Atoms are the building blocks of condensed matter physics. Each of them is a quantum mechanical system with a discrete electronic spectrum. Solids consist of atoms organised into lattices, and their electronic spectra disperse forming a 'solid state band structure' schematically shown in Fig. 6.13. Nature provided us with more than a hundred different atoms (not to count their isotopes), and a huge variety of possible ways to combine and arrange them. Physical properties of a given solid are inherited from the atoms constituting it, and can be sometimes traced back to their energy spectra. Therefore, experimentalists were highly motivated to engineer solids with desired properties utilising single atoms as 'LEGO' pieces. It was not until 1989 when Eigler and Schweizer made a revolutionary breakthrough – they managed to position individual xenon atoms on a single-crystal nickel surface, and succeeded in arranging 35 atoms as letters 'I', 'B' and 'M', standing for the IBM logo [121].

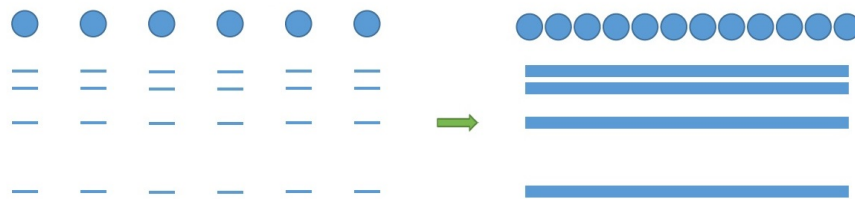


Figure 6.13: Left: atoms situated far away from each other have discrete spectra. Right: organised in lattices atoms form solids, where due to wave function overlap discrete atomic energy levels broaden into solid state bands.

Further development of the STM technique resulted in observation of impurity-induced in-gap states in superconductors [26] predicted by Yu, Shiba and Rusinov in the sixties [23–25]. It took more than two decades to realise that Yu-Shiba-Rusinov states could be used for engineering topological phases of matter. The motivation for such an idea is the following: magnetic impurities in superconductors, being far from each other, give rise to discrete impurity-induced energy levels, as shown on the left panel of Fig. 6.14. Physically such a situation corresponds to exponentially small overlaps between wave functions of Shiba states localised at different impurities. In other words, the distance between impurities  $d$  is larger than the coherence length  $\xi$  of the impurity-induced states. Notably, this picture changes drastically when  $d < \xi$ , namely when the wave functions of in-gap states start to overlap, thus giving rise to dispersive Shiba bands instead of discrete levels, which is schematically shown on the right panel of

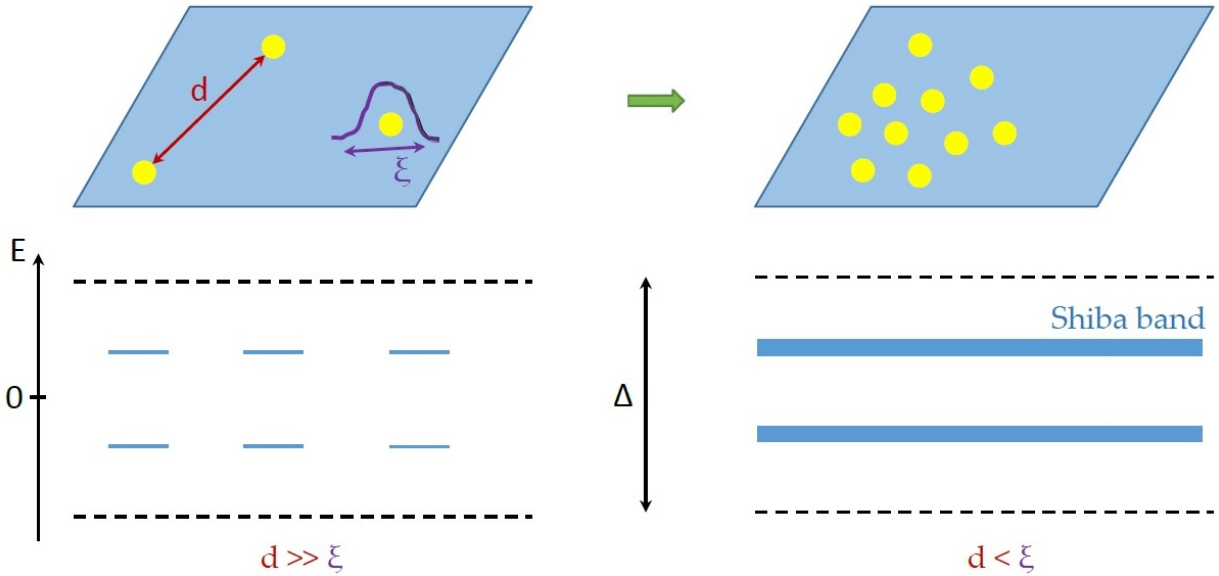


Figure 6.14: Left: impurities immersed into a superconductor are giving rise to discrete in-gap energy levels due to the fact that the distance  $d$  between them is larger than the coherence length  $\xi$  of the impurity-induced states. Right: wave functions of Shiba states have a substantial overlap since  $d < \xi$ , and thus a Shiba band arises.

Fig. 6.14. Such a situation is somewhat analogous to discrete spectra of atoms broadening into solid state bands, discussed above. The possible topological character of Shiba bands is the main topic of the last two Chapters of this manuscript.

The first Shiba-based proposal to engineer a topological phase was made by Pientka et al. in 2013 [35]. The idea was to deposit a helical chain of magnetic impurities on top of an s-wave superconductor (see Fig. 6.15) and study the topological properties of the arising Shiba band. 'Helicity' in this context referred to the fact that the spins of those impurities were organised in a helical pattern, namely their polar angle being constant and azimuthal angle changing in equal steps while moving along the chain. By deriving an effective model for the Shiba band it was shown that it could enter either a topological phase hosting Majorana bound states at the edges of the chain, or a trivial phase, depending on the parameters of the system. This work was followed by many other theoretical proposals, that will be mentioned below. Furthermore, in 2014 a chain of ferromagnetic atoms was deposited on top of a superconductor experimentally, and the arising Shiba band was proven to be in a topological phase by showing zero-energy peaks at the edges of the chain [122]. Further progress in this field will be discussed below for more specific setups.

Inspired by the aforementioned ideas, in what follows below I focus on engineering topological

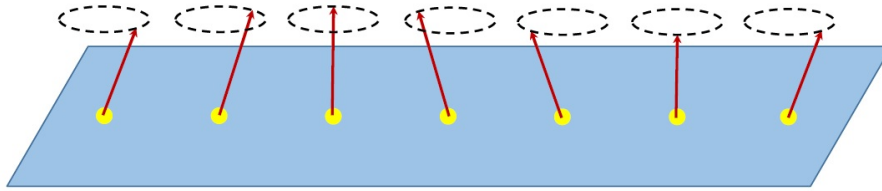


Figure 6.15: A helical chain of magnetic impurities embedded on an s-wave superconductor. The red arrows are showing the directions of spins of impurities, organised as a helix, namely as we move from one impurity to its neighbour we change the azimuthal angle (phase), whereas the polar angle stays constant. The phase differences as well as the impurity spacing are constant as we move along the chain.

phases with different types of impurities in both conventional and unconventional superconductors. The remaining part of the manuscript is organised as follows. In the next Chapter we consider the influence of scalar impurities deposited on top of two-dimensional chiral superconductors. As discovered recently, magnetic impurity lattices on an s-wave superconductor may give rise to a rich topological phase diagram. We show that similar mechanism takes place in chiral superconductors decorated by non-magnetic impurities, thus avoiding the delicate issue of magnetic ordering of adatoms. We illustrate the method by presenting the theory of scalar impurity lattices embedded on chiral p-wave superconductors. While a prerequisite for the topological state engineering is a chiral superconductor, the proposed procedure results in vistas of non-trivial descendant phases with different Chern numbers. And finally, in the last Chapter we study theoretically a chain of classical magnetic impurities with precessing spins in an s-wave superconductor. Utilising a rotating wave description, we derive an effective Hamiltonian that describes the emergent Shiba band. We find that this Hamiltonian shows non-trivial topological properties, and we obtain the corresponding topological phase diagrams both numerically and analytically. We show that changing the precession frequency offers control over the topological phase transitions and the emergence of Majorana bound states.

# Chapter 7

## Chern mosaic in a p-wave superconductor

Engineering novel quantum phases of matter with exotic properties is a rapidly growing trend in contemporary physics. The main goal is to employ simpler and well-understood ingredients and methods to create more complex structures with desirable properties. Recent promising efforts to realise [50, 52, 54] topological superconductivity in nanowire systems [46, 47] demonstrate the power of the approach. While it seems unlikely that Nature directly provides us with Majorana quasiparticles that could be employed in quantum information applications [123], it is increasingly probable that those can be achieved in laboratory. In the spirit of engineering novel controllable states of matter, we show how to realise a complex hierarchy of topological phases with scalar impurity superstructures adsorbed on chiral superconductors.

Magnetic atoms on *s*-wave superconductors give rise to Yu-Shiba-Rusinov subgap states [23–25, 34] which have been probed experimentally by scanning tunnelling microscopy (STM) [26, 27, 79, 80]. Superstructures fabricated from magnetic atoms are currently under active experimental [122, 124, 125] and theoretical research [35, 82, 126–139]. Intriguing properties of these systems include possibility for various one dimensional (1D) topological superconducting phases with Majorana bound states and rich 2D topological phases [140–143]. Topologically non-trivial phase is known to arise in 1D ferromagnetic arrays when the underlying superconductor has a strong Rashba spin-orbit coupling or in arrays with helical magnetic textures. In 1D structures there are theoretical arguments why magnetic self-tuning could result in a non-trivial ground

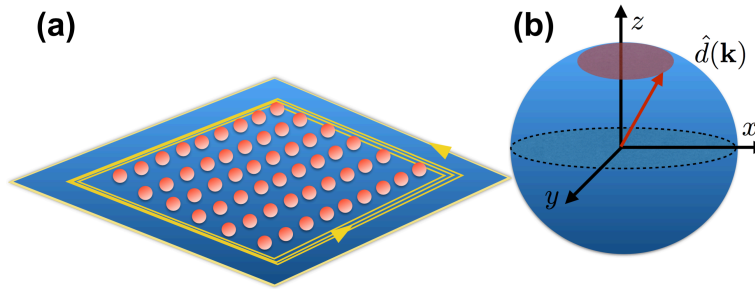


Figure 7.1: (a) Schematic representation of the studied system, consisting of scalar scatterers deposited on top of a chiral superconductor. The topological phase on the impurity lattice can be widely modified from that of the underlying compound. (b) In two-band models the Chern number can be illustrated through the motion of the  $\hat{d}(\mathbf{k})$  vector on the unit sphere. A long-range hopping translates to high Chern numbers through rapid rotation of  $\hat{d}(\mathbf{k})$ .

state [128–130, 135, 138, 144], though in real systems there are number of complications. In particular, in 2D structures the nature and tunability of magnetic textures is a delicate and largely unsolved question.

Very recently it was proposed that scalar impurities could be utilised to realise interesting topological states in 1D structures [145] and 2D toy models [146]. The procedure requires a non-s-wave superconductor host material with chiral or helical pairing components but circumvents the need for specific magnetic textures of adatoms. In the present work we provide a microscopic theory of scalar impurity structures on chiral superconductors. We show that given a non-trivial chiral superconductor, the scalar impurities give rise to a complex hierarchy of distinct non-trivial phases. The Chern number of the phase can be structurally designed by employing different impurities and varying the impurity lattice constant. We illustrate the procedure with a chiral p-wave superconductor. However, our results are not restricted to chiral p-wave systems and also apply to time-reversal breaking s+p-mixtures, higher chiral superconductors and the artificial p-wave model realised in sandwich structures of a 2D semiconductor proximity coupled to an s-wave superconductor and a ferromagnetic insulator.

## 7.1 Chiral p-wave superconductors

Here we formulate the theory describing the system in Fig. 7.1 a). The bulk electrons in a 2D spinless  $p_x + ip_y$  superconductor are described by a Bogoliubov-de Gennes (BdG) Hamiltonian

$$\mathcal{H}_{\mathbf{p}}^{\text{bulk}} = \xi_{\mathbf{p}} \tau_z + \kappa (p_x \tau_x - p_y \tau_y),$$

expressed in the Nambu basis  $(\psi_{\mathbf{p}}, \psi_{-\mathbf{p}}^\dagger)^T$ . Here the single-particle energy is  $\xi_{\mathbf{p}} = \frac{p^2}{2m} - \epsilon_F$  with the Fermi energy  $\epsilon_F$ , and  $\kappa$  is the superconducting p-wave pairing amplitude which is taken as real and positive. The Pauli matrices  $\tau_i$  operate in the particle-hole space. The collection of adatoms act as local potentials described by

$$\mathcal{H}^{(\text{imp})}(\mathbf{r}) = U \tau_z \sum_n \delta(\mathbf{r} - \mathbf{r}_n),$$

where  $\mathbf{R}_n$  are the positions of the atoms and  $U$  is the impurity strength. Our treatment is also valid if we consider impurities of a finite size (see Appendix C.6 for details). The total Hamiltonian consists of the sum  $\mathcal{H} = \mathcal{H}^{(\text{bulk})} + \mathcal{H}^{(\text{imp})}$ .

Each scalar impurity atom binds a single physical subgap state [84], which in the BdG formalism is represented by a pair of states at energies  $\epsilon = \pm \frac{\gamma\beta^2 - \sqrt{1+\beta^2(1-\gamma^2)}}{1+\beta^2} \Delta_t$  for repulsive potential  $\beta > 0$ . For attractive potential  $\beta < 0$  the solutions are otherwise the same with the exception of a minus sign in front of the square root (see Appendix C.2). Here we have defined quantities  $\beta = \pi\nu U$ ,  $\gamma = \frac{\tilde{\kappa}}{\sqrt{1+\tilde{\kappa}^2}}$ ,  $\tilde{\kappa} = \frac{\kappa}{v_F}$  and  $\Delta_t = \frac{\kappa k_F}{\sqrt{1+\tilde{\kappa}^2}}$ , where  $v_F$  is the Fermi velocity and  $\nu$  the density of states in the bulk <sup>1</sup>.

The parameter  $\Delta_t$  represents the p-wave bulk gap determining the coherence length  $\xi^{-1} = \frac{\Delta_t}{v_F}$  and  $\beta$  is a dimensionless impurity strength. Strong impurities with  $\beta \gg 1$  give rise to deep-lying subgap states close to the Fermi level while weak impurity states reside near the gap edge. Analogous to the Shiba states in 2D systems [27], the scalar impurity wave functions have asymptotic form  $e^{ik_F r - r/\xi_E} / \sqrt{k_F r}$  away from the impurity where the decay length is given by  $\xi_E = \xi / \sqrt{1 - (E/\Delta_t)^2}$  [85].

When impurity atoms are arranged into a regular array with a lattice constant  $a < \xi$ , the impurity states bound to a particular atom are hybridised with several nearest neighbours.

<sup>1</sup>These results are derived by linearising the dispersion relation around the Fermi momentum (see [84]).

This leads to the formation of subgap energy bands which support rich topological properties. To study the topological properties of the subgap bands, we formulate effective low-energy theory valid in the deep-dilute impurity regime  $\beta \gg 1$ ,  $\sqrt{k_F a} \gg 1$  in the vicinity of the Fermi level. However, as we discussed below, the effective theory yields an exact topological phase diagram which is valid also outside the deep-dilute regime. As outlined in Appendix C.3, a similar procedure that was applied in the Shiba systems [35, 82, 131, 140] results in a description of the impurity lattice in terms of the tight-binding Hamiltonian

$$H_{mn} = \begin{pmatrix} h_{mn} & \Delta_{mn} \\ \Delta_{mn}^\dagger & -h_{mn}^* \end{pmatrix}. \quad (7.1)$$

The effective Hamiltonian has an  $N \times N$  BdG block structure, where  $N$  is the number of impurity atoms. The BdG blocks are given by

$$h_{mn} = \begin{cases} \epsilon_0, & m = n \\ A(r_{mn}), & m \neq n \end{cases} \quad \Delta_{mn} = \begin{cases} 0, & m = n \\ \frac{x_{mn} + iy_{mn}}{r_{mn}} B(r_{mn}), & m \neq n \end{cases} \quad (7.2)$$

where the onsite term  $\epsilon_0 = \Delta_t(\gamma - \beta^{-1})$  arises from the decoupled impurity energy,  $r_{mn} = |\mathbf{R}_m - \mathbf{R}_n|$  is the distance between two impurity lattice sites and  $x_{mn} = x_m - x_n$ ,  $y_{mn} = y_m - y_n$ .

The matrix elements depend on the functions

$$A(r) = -\frac{2\Delta_t}{\pi} \text{Re} \left\{ \eta K_0[-i\eta k_F r] \right\}, \quad B(r) = -i \frac{2\Delta_t}{\pi} \text{Re} \left\{ \eta K_1[-i\eta k_F r] \right\},$$

where  $K_j(x)$  stands for the modified Bessel function of the second kind with index  $j$  and  $\eta = 1 + i\tilde{z}$ . The block matrices in Eq. (7.2) define a hopping model where the amplitudes satisfy asymptotic behaviour  $\Delta_{mn}, h_{mn} \sim \frac{e^{-r_{mn}/\xi}}{\sqrt{r_{mn}}}$  at long distances. The model (7.1) with entries (7.2) is a lattice discretised chiral superconductor with rich topological properties discussed below.

## 7.2 Topological properties

The topological phase diagram of the effective model (7.2) is conveniently extracted in momentum space. For any Bravais lattice we can define Fourier transforms

$$d_x(\mathbf{k}) = \text{Re} \sum_{\mathbf{R}} e^{i\mathbf{k}\cdot\mathbf{R}} \Delta_{\mathbf{R}}, \quad d_y(\mathbf{k}) = -\text{Im} \sum_{\mathbf{R}} e^{i\mathbf{k}\cdot\mathbf{R}} \Delta_{\mathbf{R}}, \quad d_z(\mathbf{k}) = \sum_{\mathbf{R}} e^{i\mathbf{k}\cdot\mathbf{R}} h_{\mathbf{R}},$$

where the sum is over all the lattice vectors  $\mathbf{R} = (x_{mn}, y_{mn})$ . The Hamiltonian can then be written in a simple form  $H(\mathbf{k}) = \mathbf{d}(\mathbf{k}) \cdot \boldsymbol{\sigma}$  with energies  $E(\mathbf{k}) = \pm|\mathbf{d}(\mathbf{k})|$ . The effective Hamiltonian  $H(\mathbf{k})$  describes gapped two-band model satisfying the particle-hole symmetry  $\mathcal{C}H(\mathbf{k})^*\mathcal{C}^{-1} = -H(-\mathbf{k})$ , where  $\mathcal{C} = \sigma_x \mathcal{K}$  and  $\mathcal{K}$  denotes complex conjugation. The studied model belongs to the Altland-Zirnbauer class  $D$ , admitting a  $\mathbb{Z}$ -valued classification by Chern numbers [147, 148]. For two-band models the Chern number is found by evaluating the expression

$$C = \frac{1}{4\pi} \int_{\text{BZ}} d^2k \frac{\mathbf{d}}{|\mathbf{d}|^3} \cdot \left( \frac{\partial \mathbf{d}}{\partial k_x} \times \frac{\partial \mathbf{d}}{\partial k_y} \right), \quad (7.3)$$

which yields integers. The integer value of the Chern number can be visualised through construction depicted in Fig. 7.1 (b). The Hamiltonian defines a unit vector  $\hat{\mathbf{d}}(\mathbf{k}) = \mathbf{d}(\mathbf{k})/|\mathbf{d}(\mathbf{k})|$  which can be depicted as a point on the surface of a unit sphere. Absolute value of the Chern number measures how many times  $\hat{\mathbf{d}}(\mathbf{k})$  covers the sphere when  $\mathbf{k} = (k_x, k_y)$  covers the Brillouin zone of the impurity lattice. The long-range hopping gives rise to rapidly rotating components of  $\mathbf{d}$  vector and thus may lead to chiral states with Chern numbers much larger than unity.

As pointed out in Appendix C.4, the effective description (7.1), derived under assumptions of a deep and dilute impurity configuration  $\beta \gg 1$ ,  $\sqrt{k_F a} \gg 1$ , actually acts as a topological Hamiltonian yielding the *exact* phase diagram which is also valid outside the deep-dilute regime. This happens because at the topological phase transition, accompanied by the energy gap closing, the effective model (7.1) becomes exact irrespectively of the values of  $\beta$  and  $k_F a$ .

In Fig. 7.2 we have plotted the topological phase diagram and the energy gap diagram for square lattices. It is clearly evident that the system possesses multiple phases which can be tuned by the separation and strength of the impurities. For higher values of the hybridisation parameter  $k_F a$  the hopping is highly oscillatory, thus leading to more rapid alternation of Figs. 7.3 and 7.4. The generic features of the phase diagrams seem to be in line with the Chern mosaic

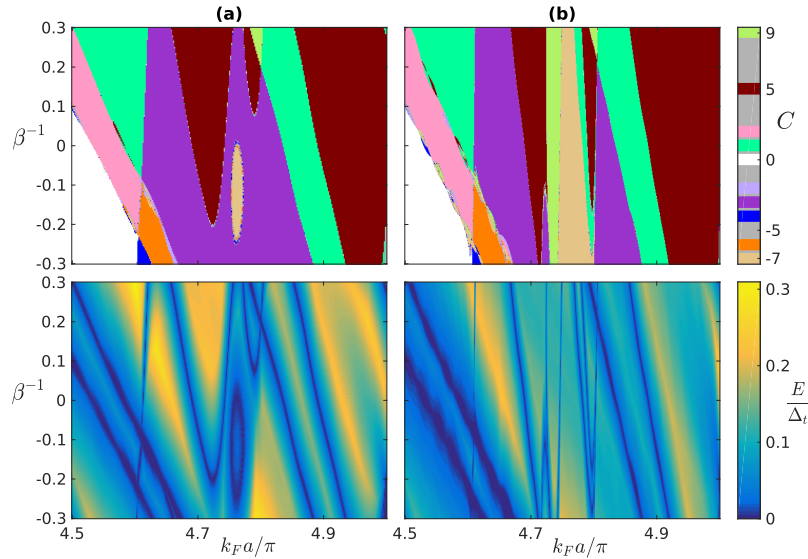


Figure 7.2: (a): Chern number (above) and energy gap (below) diagrams for a square lattice of impurities with lattice constant  $a$  and coherence length  $\xi/a = 5$ . The quantity  $\beta^{-1}$  in the vertical axis controls the strengths of the impurity. The  $\beta^{-1} = 0$  line, corresponding to infinite impurity potential  $|U| = \infty$ , divides the repulsive and attractive impurity regions. The horizontal axis  $k_F a$  controls the hybridisation between the bound states centred at different impurity sites. (b): Same as (a) but for coherence length  $\xi/a = 10$ .

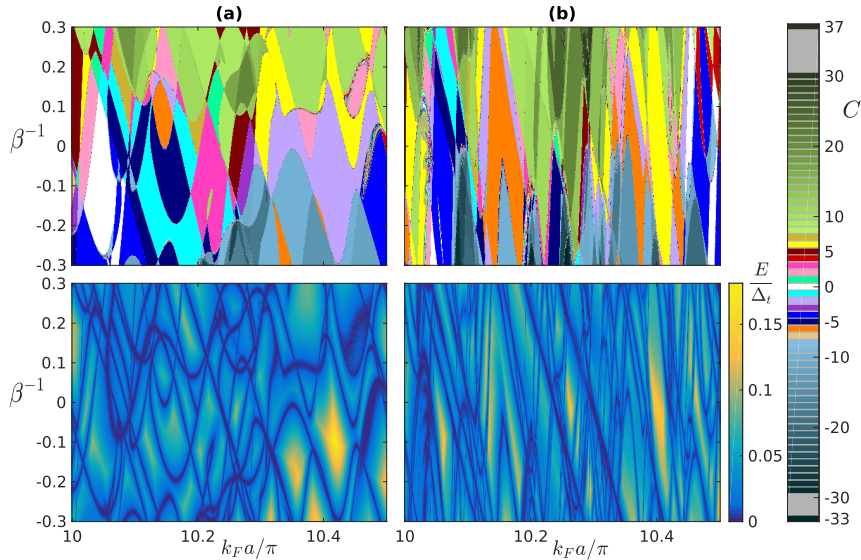


Figure 7.3: The same quantities as in Fig. 7.2 but for larger values of the hybridisation parameter  $k_F a$ .

behaviour discovered in magnetic lattices [140,141]. For robust states the energy gaps are of the order of  $0.1 - 0.2\Delta_t$ . Probably larger gaps can be obtained, but studying those would require more elaborate theory as the employed approximations become unreliable. Scalar impurity superstructures clearly allow remarkable possibilities for topological state engineering in the

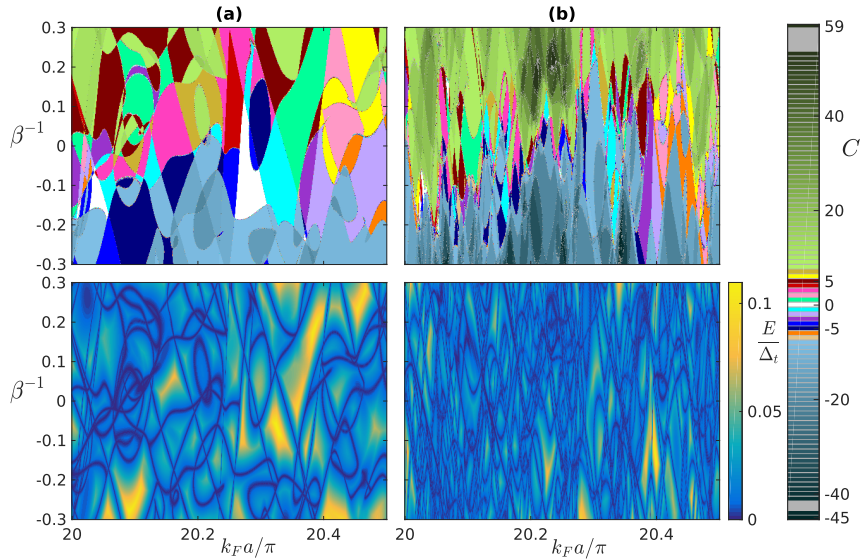


Figure 7.4: The same quantities as in Fig. 7.2 but for larger values of the hybridisation parameter  $k_F a$ .

studied system without uncertainty associated to the magnetic textures.

We have also diagonalised the system on an infinite strip geometry, where the topological edge modes show up as states traversing the bulk gap. These results are discussed in more detail in Appendix C.7.

### 7.3 Physical realisations

In the above we have considered scalar impurities in spinless chiral p-wave superconductors. Our theory can be straightforwardly generalised to the candidate state of  $\text{Sr}_2\text{RuO}_4$  where the opposite spins pair to form  $L_z = 1$  Cooper pairs. Since scalar impurities do not mix spin, the  $4 \times 4$  model with spin leads to two identical but decoupled  $2 \times 2$  blocks of form Eq. (7.1) as shown in Appendix C.5. The Chern number can be evaluated for each block separately, leading to doubling of the Chern number and the edge modes compared to the spinless case.

However, there are various other candidates for the host materials. The requirements for topological state engineering by scalar impurities are rather general and met in a variety of other systems as well. The basic ingredient is that localised potentials must bind subgap bound states in the host material. These bound states in chiral superconductors are generic since Anderson's theorem which guarantees the robustness of s-wave superconductors to scalar disorder [34] is

not operational in time-reversal breaking systems. The second requirement is the phase winding structure  $\Delta_0 e^{in\phi_{\mathbf{k}}}$ , where  $\text{tg } \phi_{\mathbf{k}} = k_y/k_x$ , of the gap function of the unperturbed bulk. This will translate to a type of  $(x_{ij} \pm iy_{ij})^n/r_{ij}$  phase structure of the gap function  $\Delta_{ij}$  in the effective low-energy BdG Hamiltonian (7.2), indicating topologically non-trivial superconductivity. In addition, algebraically decaying hopping up to the coherence length is also a universal feature of gapped states. Thus any 2D chiral ( $p$ -,  $d$ -,  $f$ ...-wave) superconductor satisfies the general requirements and exhibits the characteristic features of the studied chiral  $p$ -wave model. We note that different crystal structures of the bulk give rise to distinct lattice regulations of chiral gap functions. Also, for a continuum expression  $\Delta(\mathbf{k}) \sim (k_x + ik_y)^n$ , corresponding to Chern number  $n$ , there exists many different lattice versions. However, in the case where the impurity lattice constant is much larger than that of the underlying superconductor, the continuum approximation should prove sufficient.

Dominantly  $p$ -wave superconductors with  $s$ -wave pairing amplitude, having a gap structure  $\Delta_s + \Delta_p e^{i\phi_{\mathbf{k}}}$ , is also a sufficient starting point for topological state engineering when  $\Delta_p > \Delta_s$ . In this case scalar-impurity-induced bound states exist [84] and phase winding is inherited to the effective low-energy model. Such  $s+p$ -wave structure is satisfied in the artificial chiral superconductor realised in 2D Rashba-coupled semiconductors sandwiched by an  $s$ -wave superconductor and a ferromagnetic insulator [48] at sufficiently strong magnetisation. Patterning the semiconductor layer with scalar impurities or otherwise realising the scalar lattice by applying an external structured potential gate would enable fabrication of non-trivial topological states far beyond Chern number  $|C| = 1$ .

Chiral and time-reversal breaking superconductors have also been predicted in various other low-dimensional systems. While these have not been observed in experiments so far, it is plausible that some will be realised in the future. At that point a large number of other chiral states will immediately become accessible through topological state engineering by scalar superstructures.

## 7.4 Discussion

The bulk topology in a topologically non-trivial state is reflected on its boundary properties. This property could be employed in experimental identification of non-trivial bulk states. The

subgap density of states in chiral superconductors arises due to the chiral edge modes as illustrated in Fig. 7.1 (a). Probing the local density of states by Scanning Tunnelling Microscopy (STM) reveals that the subgap modes are localised on the boundary of the impurity lattice [140]. This method can be employed to show that the impurity lattice is in a different topological phase than the underlying chiral superconductor. Experimental extraction of specific value of the Chern number of a superconductor, while in principle possible, is an unsolved issue at present. However, by fabricating interfaces between lattices of, say, different lattice constants it is possible to compare whether the two adjacent structures belong to the same topological phase. If the structures belong to different phases, there must exist pronounced subgap local density of states at the boundary due to topological edge modes.

The circulating Majorana edge modes, depicted in Fig. 7.1 (a), carry heat in otherwise gapped systems and could find applications in the future electronics as chiral heat guides. These waveguides could be designed on top of the superconductor by employing different impurity lattice structures. The Chern number of lattice yields the number of parallel thermal edge channels, so high Chern number states are generally more effective thermal conductors compared to low Chern number states. Also, Majorana bound states trapped in lattice defects could also be interesting from quantum information point of view. While the applications of chiral superconductors are still emerging, our work points to a conceptually simple method to obtain them in nanofabricated structures.

To conclude, in this work we proposed a method to engineer topological states by scalar impurities deposited on 2D chiral superconductors. In particular, we presented a microscopic theory of chiral *p*-wave superconductors with impurity lattices. This allowed us to calculate the topological phase diagram for general impurity strengths and hybridisation. Our results have remarkable conceptual and practical consequences: given a 2D chiral superconductor, it is possible to fabricate a large number of non-trivial descendant states by a straightforward procedure. Because scalar-induced subgap states are generic in time-reversal breaking superconductors and superfluids, our results have universal appeal irrespective of the platform and microscopic details of the chiral state.

# Chapter 8

## Dynamical Shiba chain

The search for topological phases of matter during the last decade has led to remarkable advancements in engineering systems with preassigned exotic excitations such as the Dirac, Weyl, or Majorana fermions. The latter have been pursued in numerous condensed matter setups [149], as they have been suggested as promising candidates for fault-tolerant topological quantum computing [150].

Ubiquitous and destructive by its nature for other phenomena, disorder has become one of the most interesting and reliable tools to build the sought-for topological systems. Discovered more than half a century ago [23–25,90] impurity-induced bound states in superconductors have been recently brought to life in the experiments [26,27]. The latter, along with the rise of topological phases of matter, initiated a series of works, both theoretical [35, 82, 126–132, 134, 137, 138, 140, 143–146, 151–155] and experimental [122, 124, 125, 156], proposing to use Shiba states as promising building blocks for desired Majorana-supporting systems. The underlying mechanism is reminiscent of that of electronic bands appearing in solids: being brought together discrete Shiba levels originating from different impurities hybridise and form Shiba bands, with electrons filling them according to the Pauli principle. The resulting band structure corresponds to that of a p-wave, or topological superconductor, that can exhibit Majorana edge modes depending on the parameters of the system under consideration. The drawback of such an implementation, however, is that system parameters are typically fixed, and one cannot explore easily the full phase diagram.

Despite significant progress in designing topological phases with impurity-induced states, there

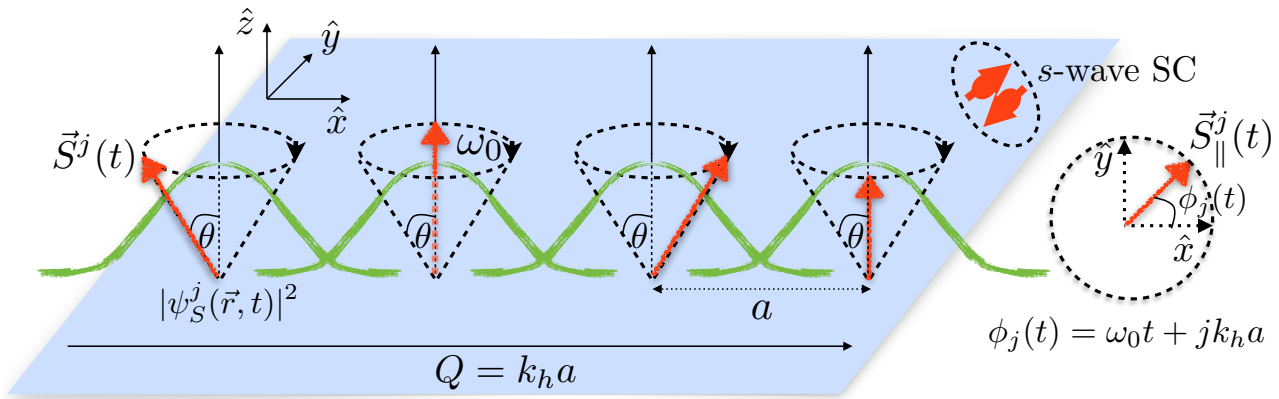


Figure 8.1: Sketch of the precessing spin helix in a two dimensional s-wave superconductor (the blue plane). The classical spins (red arrows) are separated by a distance  $a$  and precess around the  $z$  axis with a frequency  $\omega_0$  at a polar angle  $\theta$ . The precession azimuthal angle  $\phi_j(t) = \omega_0 t + k_h j a$ , with  $k_h$  the step of the helix and  $j$  the position of the spin in the chain. In green it is shown the local dynamical Shiba states wave-functions which overlap to give eventually a dynamical Shiba band.

are few systems in which topological phase transitions are controlled by tunable parameters, such as quantum spin Hall edges, channels on the surfaces of topological insulators, semiconductor nanowires, in strong magnetic fields. It is thus of great importance to propose new versatile methods of creating controllable topological phases of matter.

In this Chapter, motivated by the recent progress in the so called dynamical, or Floquet topological insulators [157, 158], we present a new promising setup not only for engineering a topological superconducting phase, but most remarkably for *controlling* topological phase transition by means of magnetisation texture dynamics. We consider theoretically a 'dynamical Shiba chain', that pertains to a set of classical magnetic impurities with precessing spins deposited on top of a 2D s-wave superconductor (see Fig. 8.1). We find that such a dynamical magnetic texture can give rise to a non-trivial Shiba band which can be controlled by tuning the precession frequency. Such features are different from previous time-dependent Floquet superconducting systems see, for example, Refs. [159–166]], in that the band is not manipulated directly by external fields, but indirectly, by the dynamics of the magnetic texture that stirs the underneath superconductor and cause the appearance of such a band. This is inherently a strong coupling regime, as the magnetic texture is the reason for such band to occur in the first place.

## 8.1 Model

The Hamiltonian describing our dynamical systems reads [127]:

$$H_{\text{tot}}(t) = H_0 + H_{\text{imp}}(t), \quad (8.1)$$

where

$$H_0 = \xi_k \tau_z + \Delta_s \tau_x, \quad (8.2)$$

$$H_{\text{imp}}(t) = \sum_j \mathbf{J}_j(t) \cdot \boldsymbol{\sigma} \delta(\mathbf{r} - \mathbf{r}_j) \quad (8.3)$$

being the sum of the Bogoliubov-De Gennes Hamiltonian for the superconductor and its coupling to the magnetic impurities, respectively. Here,  $H_0$  is written in the four-component Nambu basis  $\Psi_{\mathbf{p}} = (\psi_{\uparrow\mathbf{p}}, \psi_{\downarrow\mathbf{p}}, \psi_{\downarrow-\mathbf{p}}^\dagger, -\psi_{\uparrow-\mathbf{p}}^\dagger)^\text{T}$ , with  $\boldsymbol{\sigma} = (\sigma_x, \sigma_y, \sigma_z)$  and  $\boldsymbol{\tau} = (\tau_x, \tau_y, \tau_z)$  matrices acting in spin and particle-hole subspaces respectively. The superconducting order parameter is denoted by  $\Delta_s$ , the spectrum of free electrons is defined as  $\xi_k \equiv k^2/2m - \varepsilon_F$ , where  $\varepsilon_F$  is the Fermi energy. For the periodically driven magnetic chain we assume that the impurities are localised at positions  $\mathbf{r}_j$ , and have precessing spins that are defined as  $\mathbf{J}_j(t) \equiv J [\sin \theta \cos(\omega_0 t + \phi_j), \sin \theta \sin(\omega_0 t + \phi_j), \cos \theta]$  with precession frequency  $\omega_0$ , polar angle  $\theta$  as shown in Fig. 8.1, and equidistant individual phase shifts  $\phi_j \equiv k_h a j$ ,  $j \in \mathbb{Z}$ . In the latter  $a$  denotes the spacing between impurities, and  $k_h$  is the so-called helix step.

The time-dependent Schrödinger equation reads  $i\partial_t \Psi(\mathbf{r}, t) = H_{\text{tot}} \Psi(\mathbf{r}, t)$ . This Hamiltonian is periodic,  $H_{\text{tot}}(t + T) = H_{\text{tot}}(t)$ , with  $T = 2\pi/\omega_0$  and, moreover, the symmetry of the problem allows us to perform a time-dependent unitary transformation that makes the problem fully static. We can write  $\Psi(\mathbf{r}, t) = U(t)\Phi(\mathbf{r})e^{-iEt}$ , with  $U(t) = e^{-i\omega_0 t \sigma_z/2}$  so that we obtain the stationary Schrödinger equation:

$$[H_{\text{tot}}(0) - B\sigma_z] \Phi(\mathbf{r}) = E\Phi(\mathbf{r}), \quad (8.4)$$

where the fictitious magnetic field  $B \equiv \omega_0/2$  is perpendicular to the plane of the superconductor, which will be referred to as 'driving frequency' hereinafter, and  $E$  is the quasi-energy defined modulo  $\omega_0/2$ . Let us make now a more concise connection with the usual stroboscopic, or Floquet description of periodically driven systems. The full evolution operator for the driven

chain can be written as:

$$U_{\text{tot}}(t) = e^{-iB\sigma_z t} e^{-i\mathcal{H}_F t}, \quad (8.5)$$

with  $\mathcal{H}_F \equiv H_{\text{tot}}(0) - B\sigma_z$ . After one period  $T$ , the evolution operator can be written  $U_{\text{tot}}(T) = \exp(-i\mathcal{H}_F T)$  (up to a sign), with  $\mathcal{H}_F$  identifying as the Floquet Hamiltonian describing the evolution of the system at  $t = nT$ , with  $n \in \mathbb{N}$  (stroboscopically). The Hamiltonian  $\mathcal{H}_F$  gives rise to a quasi-energy spectrum defined up to integer multiples of  $2B$  and, as in the static case, can result in non-trivial topological properties which in an open system are identified with the appearance of edge states. However, it does not fully characterise the topological structure and the entire spectrum of edge states of the driven system. Such a complete description was developed recently in several works, where they showed that in order to fully describe that, one needs the evolution operator at all times  $t$ , not only at  $t = T$ . However, for our situation of circular spin texture precession, it turns out that  $\mathcal{H}_F$  describes fully the topological structure of the driven system, and thus we focus on that aspect only in the following.

As discussed in Ref. [167] a single magnetic impurity with a periodically driven spin gives rise to a pair of Shiba states residing in the effective gap  $\Delta_s^{\text{eff}} = \Delta_s - B$ , provided the driving frequency  $B$  is smaller than the superconducting gap  $\Delta_s$ . This condition is essential to have a gapful system and well-defined impurity-induced subgap states. The energies of these states in the deep-dilute regime ( $\alpha \sim 1$ ) are given by  $\pm\epsilon_0(B)$ , where

$$\epsilon_0(B) \equiv \left[ \left( 1 - \frac{1}{\alpha} \right) \Delta_s - B \cos \theta \right], \quad (8.6)$$

and  $\alpha \equiv \pi\nu_0 J$  is the dimensionless impurity strength parameter written in terms of normal-phase density of states  $\nu_0$ . It has been shown in Refs. [35, 131] that a static helical chain of magnetic impurities produces a  $4 \times 4$  Shiba band structure with non-trivial topological properties. Moreover, for  $\alpha \approx 1$  one can project the resulting  $4 \times 4$  Hamiltonian onto an effective  $2 \times 2$  that fully characterise the low-energy spectrum (the energy separation between the bands is of order  $\Delta_s$ ).

Hereafter we use Eq. (8.4) and, following the procedure described in Ref. [35], we derive the effective  $2 \times 2$  Hamiltonian for the emerging Shiba band. The details of this derivation are given in Appendix D.1.

## 8.2 Effective band structure

The effective Hamiltonian describing the Shiba band in the rotating frame in both aforementioned cases can be written exploiting the  $\mathbf{d}$ -vector notation as

$$\mathcal{H}_S(k) = d_0(k) + \mathbf{d}(k) \cdot \boldsymbol{\Sigma}, \quad (8.7)$$

with

$$\begin{aligned} d_0(k) &= [\Delta_s \cos \theta - B(1 - \alpha \sin^2 \theta)] F_0(B, ka, k_F a), \\ d_x(k) &= (\Delta_s - \alpha B \cos \theta) F_x(B, ka, k_F a) \sin \theta, \\ d_z(k) &= -\epsilon_0(B) + (\Delta_s - B \cos \theta) F_z(B, ka, k_F a), \end{aligned} \quad (8.8)$$

and  $d_y(k) \equiv 0$ . Eqs (8.8) represent one of our main results. Here  $\boldsymbol{\Sigma} = (\Sigma_x, \Sigma_y, \Sigma_z)$  represents a resulting Nambu space which, however, is a complicated admixture of  $\boldsymbol{\sigma}$  and  $\boldsymbol{\tau}$ . The form of the functions  $F_{0,x,z}(B, ka, k_F a)$  is in general too complicated to be displayed. However, there are various limiting cases where analytical progress is possible. In what follows we focus on two limiting cases that can be studied both analytically and numerically, i.e. the short and the long coherence length, respectively. The first case corresponds to a chain with only nearest neighbour hopping, in other words, the case of a small coherence length  $\xi \ll a$ , where  $\xi \equiv v_F / \sqrt{\Delta_s^2 - B^2}$ . In this limit, we need to set in Eq. (8.8) the following functions:

$$F_{0,x}(B, ka, k_F a) \equiv \tilde{X}_{0,1}(a) \sin \frac{k_h a}{2} \sin ka, \quad F_z(B, ka, k_F a) \equiv \tilde{X}_0(a) \cos \frac{k_h a}{2} \cos ka, \quad (8.9)$$

where

$$\tilde{X}_0(a) \equiv -\frac{2}{\pi} \text{Im} K_0 \left[ -i \left( 1 + i \frac{1}{k_F \xi} \right) k_F a \right], \quad \tilde{X}_1(a) \equiv -\frac{2}{\pi} \text{Re} K_0 \left[ -i \left( 1 + i \frac{1}{k_F \xi} \right) k_F a \right]$$

with  $k_F$  being the Fermi momentum and  $K_0$  denoting the zeroth modified Bessel function of the second kind (for further details see Appendix D.1 as well as [85]). Note that the functions  $\tilde{X}_{0,1}$  depend at least quadratically on the fictitious magnetic field  $B$ , and for  $B \ll \Delta_s$  we can neglect such dependence in leading order .

The second limiting case describes a chain with very extended Shiba states, i.e. with large

coherence length compared to the impurity spacing,  $\xi \gg a$ . Contrary to the small coherence length regime, here all the higher order hopping processes become possible. In this regime we obtain the following expressions for the functions  $F_{0,x,z}$  in Eq. (8.7)  $F_{0,x} \equiv [F_{0,1}^-(k) - F_{0,1}^+(k)]/2$  and  $F_z \equiv [F_0^-(k) + F_0^+(k)]/2$ , where we defined

$$F_0^s(k) \equiv \sqrt{\frac{2}{\pi k_F a}} \operatorname{Im} f_s(k), \quad F_1^s(k) \equiv \sqrt{\frac{2}{\pi k_F a}} \operatorname{Re} f_s(k)$$

with  $s = \pm$  and

$$f_s(k) = e^{-i\frac{\pi}{4}} \left[ \operatorname{Li}_{\frac{1}{2}} \left( e^{i(k+sk_h/2-k_F)a} \right) + \operatorname{Li}_{\frac{1}{2}} \left( e^{-i(k+sk_h/2+k_F)a} \right) \right], \quad (8.10)$$

expressed in terms of the polylogarithm function  $\operatorname{Li}(x)$ .

Note that  $d_x(k)$  in the expressions given above plays the role of the gap parameter  $\Delta_k$  from Ref. [35], which, in the limit of  $B \ll \Delta_s$  is only slightly reduced by the fictitious field. On the other hand,  $d_z(k)$  is strongly affected by the driving, as it results in a shift of the alignment of the Shiba bands, and eventually their topology. While  $d_0(k)$  does not change the topology of the bands, it does affect their overlap (the absolute gap), and it can also depend strongly on  $B$  for  $\theta \rightarrow \pi/2$  (planar helix). In fact, in such a case, the entire dependence on the magnetic field arises through this term in leading order which, however, is small for  $\alpha \sim 1$ .

### 8.3 Quasi-spectrum and topology

In what follows we study the topological properties of the Hamiltonian in Eq. (8.7) in the short and long coherence length regimes introduced above. The spectrum can be found easily as  $E(k) = d_0(k) \pm \sqrt{d_z^2(k) + d_x^2(k)}$  which, because of the periodic drive, is uniquely defined only up to an integer multiple of  $B$ . Thus, we need to fold the resulting spectrum into the first quasi-energy Brillouin zone,  $E(k) \in [-B, B]$ . The resulting one-dimensional Hamiltonian is real, and thus it belongs to the BDI symmetry class [168]. In this case the number of Majorana states emerging at one end in the case of open boundary conditions is given not by a  $\mathbb{Z}_2$ , but by a  $\mathbb{Z}$  invariant [169], which reads:

$$\mathcal{W} = \frac{1}{2\pi} \int_{-\pi}^{\pi} d\vartheta(k), \quad (8.11)$$

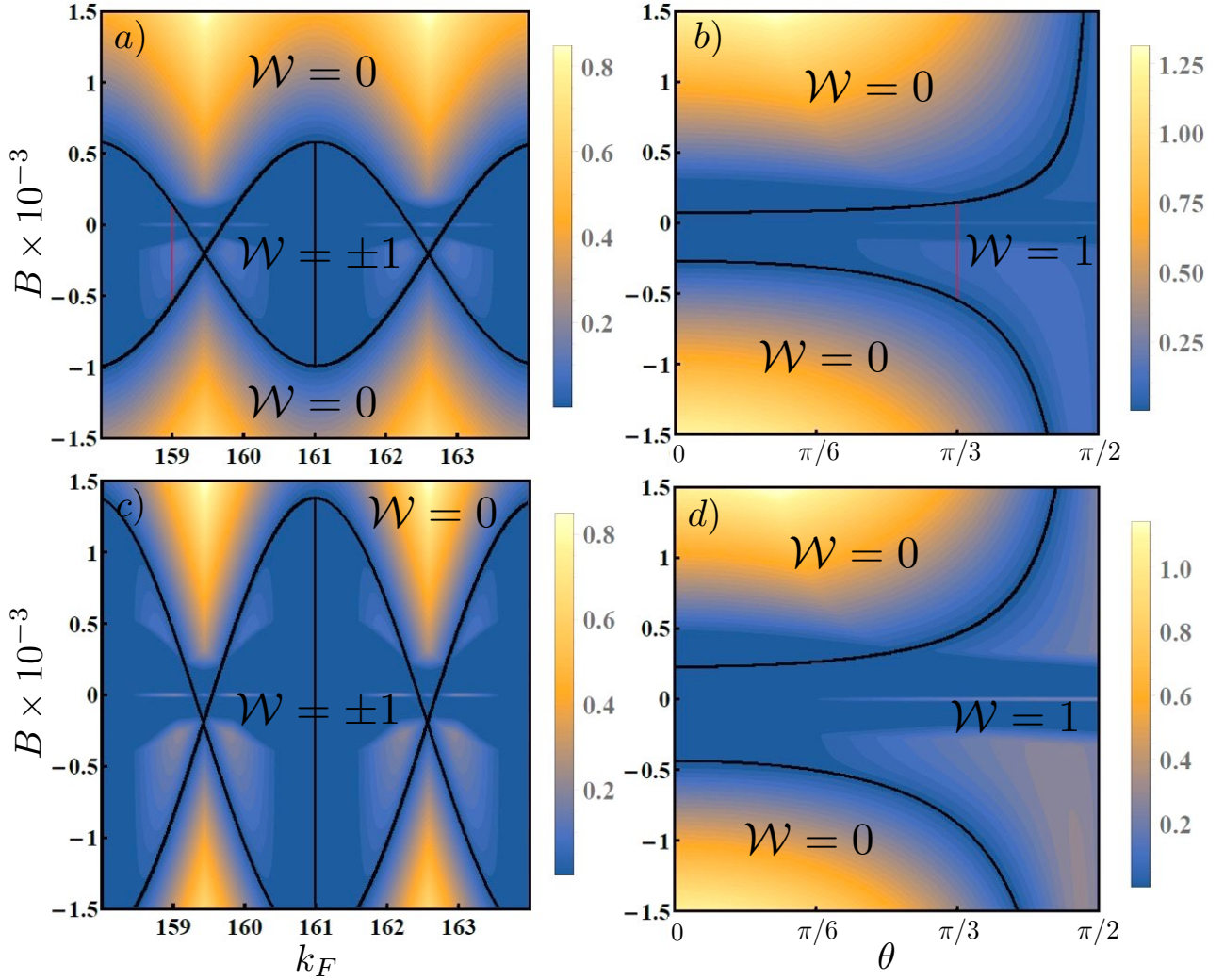


Figure 8.2: The gap around quasienergy  $E = 0$  and the winding number of the Shiba band for the small and large coherence length regimes (first and second rows respectively), plotted as functions of the driving frequency  $B$  and the Fermi momentum  $k_F$  (precession angle  $\theta$ ) in the left (right) column. The continuous black lines separate regions with different winding numbers  $\mathcal{W}$  which are well defined even for the gapless regions. The vertical red lines highlight the existence of localised Majorana end states in an open system [see Fig. 8.3 for details]. We set  $k_h = \pi/4$ ,  $v_F = 0.2$ ,  $\Delta_s = 1$ ,  $a = 1$ ,  $\alpha = 0.9999$ . The polar angle  $\theta = \pi/3$  and  $k_F = 159$  in the left and right columns correspondingly.

with  $\vartheta(k) = \text{Arg}[d_x(k) + id_z(k)]$ . This winding number characterises the number of edge states. However, it does not indicate the presence of an absolute gap in the system, meaning that it can be well defined even if the system is gapless. We depict such surprising features in Fig. 8.2, where we plot the absolute gap between the Shiba bands, as well as the corresponding winding number, as functions of the driving frequency  $B$  against the Fermi momentum  $k_F$  (angle  $\theta$ ) in the left (right) column. Both the driving frequency and the precession angles are tunable parameters and, most strikingly, this shows that the system can undergo a topological phase transition by changing the driving frequency.

We note that for the small coherence length regime (top row) the winding number can be calculated analytically (see Appendix D.2), whereas for the large coherence length (bottom row) we restrict ourselves to computing the integral in Eq. (8.11) only numerically<sup>1</sup>. A few more comments are in order. As expected for  $\theta = 0$  (corresponding to a ferromagnetic arrangement of the impurity spins) the gap is absent and the system is in a gapless trivial phase with zero winding number. Conversely, when  $\theta = \pi/2$  the spin helix is planar. This in turn means that the fictitious magnetic field  $B$  appearing in the rotating frame (see Eq. (8.4)) does not couple to the chain, which explains why no change of phase occurs while changing the driving frequency for  $\theta = \pi/2$ . Therefore, the system always enters a topological superconducting phase.

One of the most important signatures of topological systems are topological edge states. In Fig. 8.3 we show the quasi-spectrum for a dynamical chain with open boundary conditions and for the case of a short coherence length. We see that Majorana bound states (MBS) emerges at zero energy (red line), and that their existence range is in perfect agreement with the bulk winding number calculation. Moreover, we found that the MBS even exist in regions where the system is gapless, albeit they are not protected any more by the gap and any impurities could easily mix them with the bulk (extended) states. While for a region of the parameter space we found gaps at both  $E = 0$  and  $E = B$  (see Fig. 8.3), only the modes at the former are emerging for the circular driving utilised in this setup. However, such a conclusion should not hold for more general drivings of the magnetic texture.

Notably, there are two ways to approach the setup considered in this Chapter, and depending on which one we choose, we should solve the problem differently. First, we could consider this

---

<sup>1</sup>It is worth mentioning that the topologically non-trivial regions in Fig. 8.2 can be also determined by utilizing Pfaffian invariants reflecting parity of the winding number  $\mathcal{W}$ , as well as by employing the so-called 'singular points technique' developed in the Annex of this manuscript or, equivalently, in Ref. [170]

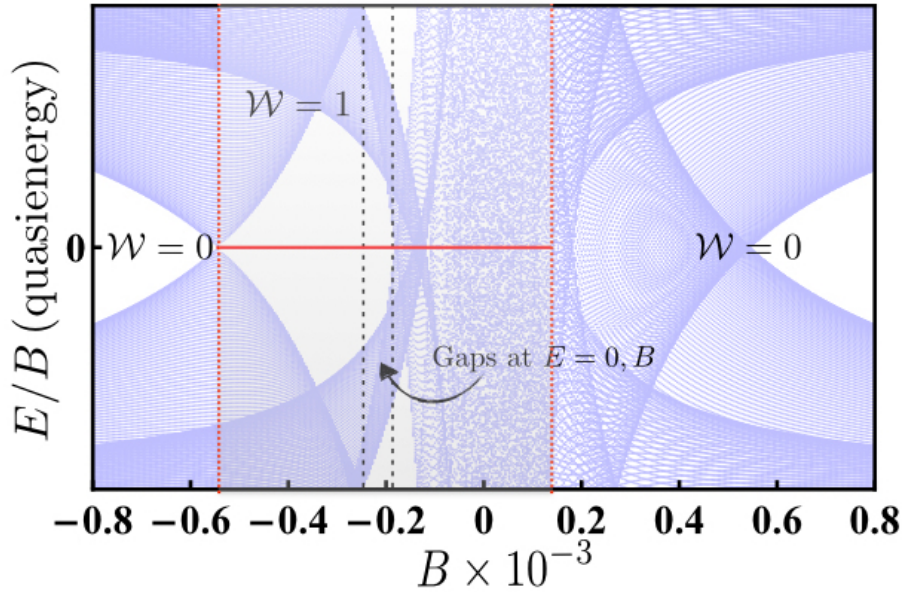


Figure 8.3: The quasi-spectrum (normalised by the driving  $B$ ) for an open Shiba chain, in the regime of small coherence length as function of the driving frequency  $B$ . The horizontal red line stands for the zero quasi-energy Majorana end mode, while  $\mathcal{W}$  defines the bulk winding number (see main text). A region with two gaps, at  $E = 0$  and  $E = B$  exist, but the latter is trivial as we find no Majoranas emerging. We set  $k_F = 159, k_h = \pi/4, v_F = 0.2, \Delta_s = 1, a = 1, \theta = \pi/3, \alpha = 0.9999$ .

setup to be completely isolated, and therefore in a rotating frame the problem would become static, with no subsequent need to perform the Floquet spectrum folding. Second approach would be to couple our driven chain to an external bath (a metallic lead, an STM tip etc.), and thus lose the possibility to get rid of time dependence through RW transformation. In our consideration we chose a third way, i.e. we consider the driven chain to be isolated, however we fold the spectrum of the static problem given by Eq. (8.4). The motivation for it would be the fact that the system in fact is not utterly isolated, and in any realistic experimental setup we would like to probe it.

## 8.4 Detection and physical implementations

The dynamically generated MBS described above could be detected in transport measurements by nearby voltage biased STM tip [171]. Alternatively, one could utilise a recent scheme that relies on the pumped charge by the precessing texture into the STM tip at different position in the chain in the absence of any applied voltage [167, 172]. In order to generate the dynamics, we envision several implementations, depending on the way the magnetic texture emerges in the

first place. In the case of a pre-formed helix, either due to the the RKKY interaction mediated by electrons in the superconductor [128–130], or due to the SOI in the substrate [173], the precession of the helix corresponds simply to global rotations. The traditional way to excite such a mode is by driving the helix with microwaves that excite the ferromagnetic resonance associated with such a rotation mode. However, in recent years there have been tremendous progress in exciting magnetic devices in transport setup by means of the spin Hall effect [174]. Such a setup would allow for an all-electrical implementation of a dynamical magnetic texture – superconductor hybrid, with a controllable frequency (see Appendix D.5 for details on the implementation). Both these methods can give rise to rotations of the helix, but do not result in changes of the pitch. However, when the impurities form a planar ferromagnet (with exchange interaction keeping the spins in a plane), it becomes possible to control the pitch  $k_h$ , the frequency  $\omega$ , and the cone angle  $\theta$  by means of spin biases, as showed recently in several works [175–177]. This goes by the name of spin superfluidity, as there is a direct mapping between a superfluid flow (such as in  $\text{He}_4$ ) and the magnetisation flow in such a planar spin configuration. As detailed in Appendix D.5, such manipulations are possible simply by changing the spin biases induced by the spin Hall effect applied over the planar spin configuration, with a pitch in one-to-one correspondence with the spin super-current flowing through the magnetic system, and an adjustable frequency depending on the relative biases [176, 177].

## 8.5 Discussion

The setup proposed in this work can be generalised to a chain of precessing magnetic impurities deposited on top of a 3D superconductor. Despite a modification in the Shiba wave function coherence length, we expect no qualitative difference in our main argument concerning a controlled topological phase transition. Moreover, a 3D superconductor is expected to reflect the short coherence length regime, whereas a 2D one – the long coherence length regime. As a future extension of this work we propose to consider more complicated networks of driven magnetic impurities, e.g. a 2D array. Also, generalisations to more complicated textures and precessions is in order, as our perfect rotation wave description would break down, and a fully Floquet approach would be required. The same arguments should apply when the substrate (superconductor) posses spin-orbit interaction.

It is worth mentioning that, as expected, all these results are in a perfect qualitative agreement with those presented in Ref. [35], for driving frequency  $B = 0$ . We do not expect any quantitative agreement since we consider a 2D underlying superconductor.

In conclusion, in this Chapter we proposed a way to engineer a controllable topological phase transition by means of magnetisation texture dynamics. We have shown that a chain of precessing classical spins deposited on top of an s-wave superconductor gives rise to a topologically non-trivial Shiba band, and we have demonstrated that topological phase transitions in such a band can be controlled by changing the driving frequency, a tunable parameter in the spin transport experiments.

# Conclusions

# Summary of Thesis Achievements

In Chapter 5 we have analysed the formation of Yu-Shiba-Rusinov states and impurity states in 1D and 2D superconducting and metallic systems with Rashba spin-orbit coupling. In particular, we have studied the Fourier transform of the local density of states of Shiba states in SCs and of the impurity states in metals, both non-polarised and spin-polarised. We have shown that the spin-polarised density of states contains information that allows one to extract experimentally the strength of the SO coupling. Notably, the features observed in the FT of the SP LDOS split with a magnitude proportional to the SO coupling strength. Moreover, the Friedel oscillations in the SP LDOS in the SC regime show a combination of wavelengths, out of which the SO length can be read-off directly and non-ambiguously. We note that these signatures are only visible in the spin-polarised quantities and in the presence of magnetic impurities. For non-spin-polarised measurements, no such splitting is present and the wave vectors observed in the FT of the SP LDOS basically do not depend on the SO coupling.

When comparing the results for the SC Shiba states to the impurity contribution in the metallic state and we find a few interesting differences, such as a broadening of the FT features corresponding to a spatial exponential decay of the Shiba states compared to the non-SC case. Moreover, the FT of the SP LDOS in the SC regime exhibits extra features with a wavelength equal to the SO length which are not present in the non-SC phase. We have checked that up to a rotation in the spin space our results hold also for other types of SO coupling such as e.g. Dresselhaus.

Chapter 6 has been dedicated to studying the formation of Shiba states in 2D superconductors with breaking inversion symmetry admixture of s-wave and p-wave order parameters. We have found that the number, the energy and especially the spin polarisation of the Shiba states depend strongly on the ratio between the values of the s-wave and p-wave coupling. We have

proposed to test experimentally the presence of the p-wave coupling, as well as the direction of the  $\mathbf{d}$ -vector with respect to the sample plane by measuring the spin polarisation and energy of the Shiba bound states via spin-polarised STM or transport. We note that these signatures are only visible in the spin-polarised quantities and in the presence of magnetic impurities. All the results are obtained both numerically and analytically, with full qualitative correspondence between them.

We believe that these results can be used for studying the topological phases of matter that can be engineered with impurities in different types of p-wave superconductors, in particular the exact analytical form of the Shiba wave functions, are useful for computing the Chern numbers in such emergent topological superconductors.

Summarising the results of Chapter 7, we have proposed a method to engineer topological states by scalar impurities deposited on 2D chiral superconductors. In particular, we have presented a microscopic theory of chiral p-wave superconductors with impurity lattices, allowing us to calculate the topological phase diagram for general impurity strengths and hybridisation. Our results have remarkable conceptual and practical consequences: given a 2D chiral superconductor, it is possible to fabricate a large number of non-trivial descendant states by a straightforward procedure. Because scalar-induced subgap states are generic in time-reversal breaking superconductors and superfluids, our results have universal appeal irrespective of the platform and microscopic details of the chiral state.

Experimental extraction of specific value of the Chern number of a superconductor is an unsolved issue at present. However, by fabricating interfaces between lattices of different lattice constants it is possible to compare whether the two adjacent structures belong to the same topological phase. If the structures belong to different phases, there must exist pronounced subgap local density of states at the boundary due to topological edge modes.

And finally, in Chapter 8 we have put forward a way to engineer a controllable topological phase transition by means of magnetisation texture dynamics. We have shown that a chain of precessing classical spins deposited on top of an s-wave superconductor gives rise to a topologically non-trivial Shiba band, and we have demonstrated that topological phase transitions in such a band can be controlled by changing the driving frequency, a tunable parameter in the spin transport experiments. The winding number of the arising Shiba band has been obtained both numerically and analytically, and its value has been shown to be consistent with the number

of Majorana bound states emerging in the topological phase.

# Perspectives

Several possible extensions of this work could be potentially interesting. First of all, it would be beguiling to generalise the results of Chapters 5 and 6 to more realistic calculations which may include some specific lattice characteristics, more realistic material-dependent tight-binding parameters for the band structure and the SO coupling values. Moreover, since the principal testing method proposed in our work is spin-polarised STM, it could be useful to recompute everything, taking into account the tunnelling processes into an STM tip by employing the tunnelling Hamiltonian approach.

In particular, the findings of Chapter 5 could be tested using for example materials such as Pb, Bi, NbSe<sub>2</sub> or InAs and InSb wires, which are known to have a strong SO coupling, using spin-polarised STM which is nowadays becoming more and more available.

Concerning the theoretical predictions of Chapter 6 about superconductors showing a mixed singlet and triplet order parameters, or purely triplet, it would be interesting to recalculate all the studied spin-polarised quantities for the quasi-2D superconductor Sr<sub>2</sub>RuO<sub>4</sub> described by realistic multiband models, as well as for any other candidate for p-wave pairing. Furthermore, it could be compelling to generalise these results for higher order triplet pairing superconductors, such as for example f-wave.

The setup we have proposed in Chapter 8 could be extended to a chain of precessing magnetic moments deposited on top of a 3D superconductor. Despite a modification in the Shiba wave function coherence length, we expect no qualitative difference in our main argument concerning a controlled topological phase transition. Moreover, a 3D superconductor is expected to reflect the short coherence length regime, whereas a 2D one – the long coherence length regime.

Another future extension of this work would be to consider more complicated networks of driven

magnetic impurities, e.g. 2D arrays and lattices, or taking into account spin-orbit coupling in the superconducting substrate. Moreover, it would be enthralling to check that the main conclusions of that Chapter remain the same in the presence of an STM tip, probing the driven chain. Most of the aforementioned generalisations might lead to breakdown of the rotating wave transformation into a static system, thus requiring a full Floquet description.

# Appendixes

# Appendix A

## Analytical calculation of the Shiba states wave functions

We can calculate analytically the non-polarised and the SP LDOS for the Shiba states exploiting the model described by the Hamiltonians in Eqs. (5.1-5.3). All the integrations below are performed using a linearisation around the Fermi energy. The energies of the Shiba states can be found by solving the corresponding eigenvalue equation (see Ref. [35])

$$[\mathbb{I}_4 - G_0(E, \mathbf{r} = \mathbf{0})V] \Phi(\mathbf{0}) = 0 \quad (\text{A.1})$$

where  $G_0(E, \mathbf{r})$  is the retarded Green's function in real space obtained by a Fourier transform from the retarded Green's function in momentum space  $G_0(E, \mathbf{p}) = [(E + i\delta)\mathbb{I}_4 - \mathcal{H}_0(\mathbf{p})]^{-1}$ , where  $\delta$  is the inverse quasiparticle lifetime. In all the calculations below we take the limit of  $\delta \rightarrow +0$ , and we specify  $+i0$  only in the cases when it affects the results. The wave functions of the Shiba states at  $\mathbf{r} = 0$  are given by the eigenfunctions obtained from the equation above. Their spatial dependence is determined using

$$\Phi(\mathbf{r}) = G_0(E, \mathbf{r})V\Phi(\mathbf{0}) \quad (\text{A.2})$$

Consequently, the non-polarised and the SP LDOS are given by Eq. (4.17) and (4.18). Thus, in order to find the energies and the wave functions corresponding to the Shiba states we need to find the real-space Green's function. This is obtained simply by a Fourier transform of the

unperturbed Green's function in momentum space,  $G_0(E, \mathbf{p})$ .

## A.1 s-wave superconductors with Rashba SOC

### 2D case

We start by writing down the unperturbed Green's function in momentum space, which is given by  $G_0(E, \mathbf{p}) = \frac{1}{2} \sum_{\sigma=\pm} G_0^\sigma(E, \mathbf{p})$ , where

$$G_0^\sigma(E, \mathbf{p}) = -\frac{1}{\xi_\sigma^2 + \omega^2} \begin{pmatrix} 1 & i\sigma e^{-i\phi_{\mathbf{p}}} \\ -i\sigma e^{i\phi_{\mathbf{p}}} & 1 \end{pmatrix} \otimes \begin{pmatrix} E + \xi_\sigma & \Delta_s \\ \Delta_s & E - \xi_\sigma \end{pmatrix}, \quad (\text{A.3})$$

where  $\omega = \sqrt{\Delta_s^2 - E^2}$ ,  $\xi_\sigma = \xi_{\mathbf{p}} + \sigma\lambda p$ . To obtain its real-space dependence one needs to perform the Fourier transform (see Eq. (4.4)). We will thus have four types of integrals:

$$X_0^\sigma(\mathbf{r}) = -\int \frac{d\mathbf{p}}{(2\pi)^2} \frac{e^{i\mathbf{p}\mathbf{r}}}{\xi_\sigma^2 + \omega^2} \quad (\text{A.4})$$

$$X_1^\sigma(\mathbf{r}) = -\int \frac{d\mathbf{p}}{(2\pi)^2} \frac{\xi_\sigma e^{i\mathbf{p}\mathbf{r}}}{\xi_\sigma^2 + \omega^2} \quad (\text{A.5})$$

$$X_2^\sigma(s, \mathbf{r}) = -\int \frac{d\mathbf{p}}{(2\pi)^2} \frac{-is\sigma e^{is\phi_{\mathbf{p}}} e^{i\mathbf{p}\mathbf{r}}}{\xi_\sigma^2 + \omega^2} \quad (\text{A.6})$$

$$X_3^\sigma(s, \mathbf{r}) = -\int \frac{d\mathbf{p}}{(2\pi)^2} \frac{-is\sigma e^{is\phi_{\mathbf{p}}} \xi_\sigma e^{i\mathbf{p}\mathbf{r}}}{\xi_\sigma^2 + \omega^2} \quad (\text{A.7})$$

Since the spectrum is split by SO coupling, there will be two Fermi momenta which can be found the following way:

$$\frac{p^2}{2m} + \sigma\lambda p - \varepsilon_F = 0, \quad p_F^\sigma = \frac{-\sigma\lambda + \sqrt{\lambda^2 + 2\varepsilon_F/m}}{1/m}$$

For  $p > 0$  we linearise the spectrum around the Fermi momenta, thus:

$$\xi_\sigma \approx \left( \frac{p_F^\sigma}{m} + \sigma\lambda \right) (p - p_F^\sigma) = \sqrt{\lambda^2 + 2\varepsilon_F/m} (p - p_F^\sigma) \equiv v(p - p_F^\sigma),$$

therefore  $p = p_F + \xi_\sigma/v$ , where  $v = \sqrt{v_F^2 + \lambda^2}$ . We rewrite:

$$\frac{d\mathbf{p}}{(2\pi)^2} = \frac{m}{2\pi} \left[ 1 - \sigma \frac{\lambda}{v} \right] d\xi_\sigma \frac{d\phi}{2\pi} = \nu_\sigma d\xi_\sigma \frac{d\phi}{2\pi},$$

where  $\nu_\sigma = \nu \left[ 1 - \sigma \frac{\lambda}{v} \right]$ , with  $\nu = m/2\pi$ . Due to the symmetry all the integrals are zero at  $\mathbf{r} = \mathbf{0}$  except for the first one, namely,

$$X_0^\sigma(\mathbf{0}) = -\nu_\sigma \frac{\pi}{\omega}. \quad (\text{A.8})$$

All the coordinate dependences can be calculated using the formalism introduced in Ref. [85].

Finally we get:

$$X_0^\sigma(r) = -2\nu_\sigma \cdot \frac{1}{\omega} \cdot \text{Im} K_0[-i(1 + i\Omega_\sigma)p_F^\sigma r] \quad (\text{A.9})$$

$$X_1^\sigma(r) = -2\nu_\sigma \cdot \text{Re} K_0[-i(1 + i\Omega_\sigma)p_F^\sigma r] \quad (\text{A.10})$$

$$X_2^\sigma(s, \mathbf{r}) = 2s\sigma\nu_\sigma \cdot \frac{1}{\omega} \cdot e^{is\phi_r} \cdot \text{Re} K_1[-i(1 + i\Omega_\sigma)p_F^\sigma r] \quad (\text{A.11})$$

$$X_3^\sigma(s, \mathbf{r}) = -2s\sigma\nu_\sigma \cdot e^{is\phi_r} \cdot \text{Im} K_1[-i(1 + i\Omega_\sigma)p_F^\sigma r], \quad (\text{A.12})$$

where  $\Omega_\sigma = \omega/p_F^\sigma v$  defines the inverse superconducting decay length, and  $p_S = \omega/v$ . Therefore, the Green's function can be written as

$$G_0^\sigma(E, \mathbf{r}) = \begin{pmatrix} EX_0^\sigma + X_1^\sigma & EX_2^\sigma(-) + X_3^\sigma(-) & \Delta_s X_0^\sigma & \Delta_s X_2^\sigma(-) \\ EX_2^\sigma(+) + X_3^\sigma(+) & EX_0^\sigma + X_1^\sigma & \Delta_s X_2^\sigma(+) & \Delta_s X_0^\sigma \\ \Delta_s X_0^\sigma & \Delta_s X_2^\sigma(-) & EX_0^\sigma - X_1^\sigma & EX_2^\sigma(-) - X_3^\sigma(-) \\ \Delta_s X_2^\sigma(+) & \Delta_s X_0^\sigma & EX_2^\sigma(+) - X_3^\sigma(+) & EX_0^\sigma - X_1^\sigma \end{pmatrix},$$

where we omitted all the coordinate dependence. Thus at the origin we have:

$$G_0(E, \mathbf{r} = \mathbf{0}) = -\frac{\pi\nu}{\sqrt{\Delta_s^2 - E^2}} \sigma_0 \otimes \begin{pmatrix} E & \Delta_s \\ \Delta_s & E \end{pmatrix}.$$

Using the expression above along with Eq. (4.16) we find the eigenvalues of the problem, i.e. the energies of the Shiba states:

$$E_{1,\bar{1}} = \pm \frac{1 - \alpha^2}{1 + \alpha^2} \Delta_s.$$

In the subsections below we use these energies and Eq. (4.15) to find the wave functions of the Shiba states. This algorithm will be applied in all the cases discussed below.

### **z-impurity**

The coordinate dependence of the eigenfunctions is given by

$$\Phi_{\bar{1}}(\mathbf{r}) = +\frac{J_z}{2} \sum_{\sigma=\pm} \begin{pmatrix} (E_{\bar{1}} - \Delta_s)X_0^\sigma + X_1^\sigma \\ (E_{\bar{1}} - \Delta_s)X_2^\sigma(+) + X_3^\sigma(+) \\ -(E_{\bar{1}} - \Delta_s)X_0^\sigma + X_1^\sigma \\ -(E_{\bar{1}} - \Delta_s)X_2^\sigma(+) + X_3^\sigma(+) \end{pmatrix}, \quad \Phi_1(\mathbf{r}) = -\frac{J_z}{2} \sum_{\sigma=\pm} \begin{pmatrix} (E_1 + \Delta_s)X_2^\sigma(-) + X_3^\sigma(-) \\ (E_1 + \Delta_s)X_0^\sigma + X_1^\sigma \\ (E_1 + \Delta_s)X_2^\sigma(-) - X_3^\sigma(-) \\ (E_1 + \Delta_s)X_0^\sigma - X_1^\sigma \end{pmatrix},$$

where we omit the arguments  $r$  and  $\mathbf{r}$  in the functions given by Eq. (A.9-A.12). Using these expressions we can compute the asymptotic behaviour of the non-polarised and SP LDOS in coordinate space for the state with positive energy (thus we omit index 1 below):

$$\begin{aligned} S_x(\mathbf{r}) &= +J_z^2 \left(1 + \frac{1}{\alpha^2}\right) \left\{ \sum_{\sigma} \sigma \nu_{\sigma}^2 \frac{\cos(2p_F^{\sigma}r - \theta)}{p_F^{\sigma}} + 2\nu^2 \frac{v_F^2}{v^2} \cdot \frac{\sin p_{\lambda}r}{p_F} \right\} \cdot \frac{e^{-2p_s r}}{r} \cos \phi_{\mathbf{r}} \\ S_y(\mathbf{r}) &= +J_z^2 \left(1 + \frac{1}{\alpha^2}\right) \left\{ \sum_{\sigma} \sigma \nu_{\sigma}^2 \frac{\cos(2p_F^{\sigma}r - \theta)}{p_F^{\sigma}} + 2\nu^2 \frac{v_F^2}{v^2} \cdot \frac{\sin p_{\lambda}r}{p_F} \right\} \cdot \frac{e^{-2p_s r}}{r} \sin \phi_{\mathbf{r}} \\ S_z(r) &= -J_z^2 \left(1 + \frac{1}{\alpha^2}\right) \left\{ \sum_{\sigma} \nu_{\sigma}^2 \frac{\sin(2p_F^{\sigma}r - \theta)}{p_F^{\sigma}} - 2\nu^2 \frac{v_F^2}{v^2} \cdot \frac{\cos p_{\lambda}r}{p_F} \right\} \cdot \frac{e^{-2p_s r}}{r} \\ \rho(r) &= +J_z^2 \left(1 + \frac{1}{\alpha^2}\right) \left\{ 2\frac{\nu^2}{mv} + 2\nu^2 \frac{v_F^2}{v^2} \cdot \frac{\sin(2mvr - \theta)}{p_F} \right\} \cdot \frac{e^{-2p_s r}}{r} \end{aligned}$$

with  $\theta = \begin{cases} \arctg \frac{2\alpha}{1-\alpha^2}, & \text{if } \alpha \neq 1 \\ \frac{\pi}{2}, & \text{if } \alpha = 1 \end{cases}$  and  $p_\lambda = 2m\lambda$ . To perform the Fourier transforms in 2D we use the following equations:

$$\begin{aligned} \mathcal{F}[f(r)] &= 2\pi \int_0^{+\infty} r J_0(pr) f(r) dr \\ \mathcal{F}[\cos \phi_r f(r)] &= 2\pi i \cos \phi_{\mathbf{p}} \cdot \int_0^{+\infty} r J_1(pr) f(r) dr, \\ \mathcal{F}[\sin \phi_r f(r)] &= 2\pi i \sin \phi_{\mathbf{p}} \cdot \int_0^{+\infty} r J_1(pr) f(r) dr \\ \mathcal{F}[\cos 2\phi_r f(r)] &= -2\pi \cos 2\phi_{\mathbf{p}} \int_0^{+\infty} r J_2(pr) f(r) dr, \\ \mathcal{F}[\sin 2\phi_r f(r)] &= -2\pi \sin 2\phi_{\mathbf{p}} \int_0^{+\infty} r J_2(pr) f(r) dr, \end{aligned}$$

where  $f(r)$  is a function that is independent of the angle  $\phi_r$ . Thus we can obtain some information about the main features and symmetries that we observe in momentum space:

$$\begin{aligned} S_x(\mathbf{p}) &= +2\pi i J_z^2 \left(1 + \frac{1}{\alpha^2}\right) \cos \phi_{\mathbf{p}} \int_0^{+\infty} dr J_1(pr) \left\{ \sum_{\sigma} \sigma \nu_{\sigma}^2 \frac{\cos(2p_F^{\sigma} r - \theta)}{p_F^{\sigma}} + 2\nu^2 \frac{v_F^2}{v^2} \cdot \frac{\sin p_{\lambda} r}{p_F} \right\} \cdot e^{-2p_s r} \\ S_y(\mathbf{p}) &= +2\pi i J_z^2 \left(1 + \frac{1}{\alpha^2}\right) \sin \phi_{\mathbf{p}} \int_0^{+\infty} dr J_1(pr) \left\{ \sum_{\sigma} \sigma \nu_{\sigma}^2 \frac{\cos(2p_F^{\sigma} r - \theta)}{p_F^{\sigma}} + 2\nu^2 \frac{v_F^2}{v^2} \cdot \frac{\sin p_{\lambda} r}{p_F} \right\} \cdot e^{-2p_s r} \\ S_z(p) &= -2\pi J_z^2 \left(1 + \frac{1}{\alpha^2}\right) \int_0^{+\infty} dr J_0(pr) \left\{ \sum_{\sigma} \nu_{\sigma}^2 \frac{\sin(2p_F^{\sigma} r - \theta)}{p_F^{\sigma}} - 2\nu^2 \frac{v_F^2}{v^2} \cdot \frac{\cos p_{\lambda} r}{p_F} \right\} \cdot e^{-2p_s r} \\ \rho(p) &= +2\pi J_z^2 \left(1 + \frac{1}{\alpha^2}\right) \int_0^{+\infty} dr J_0(pr) \left\{ 2 \frac{\nu^2}{mv} + 2\nu^2 \frac{v_F^2}{v^2} \cdot \frac{\sin(2mvr - \theta)}{p_F} \right\} \cdot e^{-2p_s r} \end{aligned}$$

**x-impurity**

The coordinate dependence of the eigenfunctions is given by

$$\Phi_{\bar{1}}(\mathbf{r}) = +\frac{J_x}{2} \sum_{\sigma=\pm} \begin{pmatrix} +(E_{\bar{1}} - \Delta_s) [X_0^\sigma(r) + X_2^\sigma(-, \mathbf{r})] + X_1^\sigma(r) + X_3^\sigma(-, \mathbf{r}) \\ +(E_{\bar{1}} - \Delta_s) [X_0^\sigma(r) + X_2^\sigma(+, \mathbf{r})] + X_1^\sigma(r) + X_3^\sigma(+, \mathbf{r}) \\ -(E_{\bar{1}} - \Delta_s) [X_0^\sigma(r) + X_2^\sigma(-, \mathbf{r})] + X_1^\sigma(r) + X_3^\sigma(-, \mathbf{r}) \\ -(E_{\bar{1}} - \Delta_s) [X_0^\sigma(r) + X_2^\sigma(+, \mathbf{r})] + X_1^\sigma(r) + X_3^\sigma(+, \mathbf{r}) \end{pmatrix},$$

$$\Phi_1(\mathbf{r}) = -\frac{J_x}{2} \sum_{\sigma=\pm} \begin{pmatrix} +(E_1 + \Delta_s) [X_0^\sigma(r) - X_2^\sigma(-, \mathbf{r})] + X_1^\sigma(r) - X_3^\sigma(-, \mathbf{r}) \\ -(E_1 + \Delta_s) [X_0^\sigma(r) - X_2^\sigma(+, \mathbf{r})] - X_1^\sigma(r) + X_3^\sigma(+, \mathbf{r}) \\ +(E_1 + \Delta_s) [X_0^\sigma(r) - X_2^\sigma(-, \mathbf{r})] - X_1^\sigma(r) + X_3^\sigma(-, \mathbf{r}) \\ -(E_1 + \Delta_s) [X_0^\sigma(r) - X_2^\sigma(+, \mathbf{r})] + X_1^\sigma(r) - X_3^\sigma(+, \mathbf{r}) \end{pmatrix}.$$

For the positive energy state we compute the asymptotic behaviour of the non-polarised and SP LDOS in coordinate space. We write  $S_x(\mathbf{r}) = S_x^s(r) + S_x^a(\mathbf{r})$ :

$$S_x^s(r) = -J_x^2 \left(1 + \frac{1}{\alpha^2}\right) \left\{ \sum_{\sigma} \nu_{\sigma}^2 \frac{1 + \sin(2p_F^{\sigma}r - 2\beta)}{p_F^{\sigma}} + \gamma (\cos p_{\lambda}r + \sin(2mvr - 2\beta)) \right\} \frac{e^{-2p_s r}}{r}$$

$$S_x^a(\mathbf{r}) = J_x^2 \left(1 + \frac{1}{\alpha^2}\right) \left\{ \sum_{\sigma} \nu_{\sigma}^2 \frac{1 - \sin(2p_F^{\sigma}r - 2\beta)}{p_F^{\sigma}} - \gamma (\cos p_{\lambda}r + \sin(2mvr - 2\beta)) \right\} \frac{e^{-2p_s r}}{r} \cos 2\phi_{\mathbf{r}}$$

$$S_y(\mathbf{r}) = J_x^2 \left(1 + \frac{1}{\alpha^2}\right) \left\{ \sum_{\sigma} \nu_{\sigma}^2 \frac{1 - \sin(2p_F^{\sigma}r - 2\beta)}{p_F^{\sigma}} - \gamma (\cos p_{\lambda}r - \sin(2mvr - \theta)) \right\} \frac{e^{-2p_s r}}{r} \sin 2\phi_{\mathbf{r}}$$

$$S_z(\mathbf{r}) = -J_x^2 \left(1 + \frac{1}{\alpha^2}\right) \left\{ 2 \sum_{\sigma} \sigma \nu_{\sigma}^2 \frac{\cos(2p_F^{\sigma}r - \theta)}{p_F^{\sigma}} + 2\gamma \sin p_{\lambda}r \right\} \frac{e^{-2p_s r}}{r} \cos \phi_{\mathbf{r}}$$

$$\rho(r) = J_x^2 \left(1 + \frac{1}{\alpha^2}\right) \left\{ 4 \frac{\nu^2}{mv} + 2\gamma \sin(2mvr - \theta) \right\} \frac{e^{-2p_s r}}{r}$$

with  $\tan \beta = \alpha$  and  $\gamma \equiv 2\nu^2 \frac{v_F^2}{v^2 p_F}$ . Same as before, performing the Fourier transforms of these expressions allows us to obtain information about the most important features and symmetries

we observe in momentum space:

$$\begin{aligned}
S_x^s(\mathbf{p}) &= -2\pi J_x^2 \left(1 + \frac{1}{\alpha^2}\right) \int_0^{+\infty} dr J_0(pr) \left\{ \sum_{\sigma} \nu_{\sigma}^2 \frac{1 + \sin(2p_F^{\sigma}r - 2\beta)}{p_F^{\sigma}} + \right. \\
&\quad \left. + 2\nu^2 \frac{v_F^2}{v^2} \cdot \frac{\cos p_{\lambda}r + \sin(2mvr - 2\beta)}{p_F} \right\} \cdot e^{-2p_s r} \\
S_x^a(\mathbf{p}) &= -2\pi J_x^2 \left(1 + \frac{1}{\alpha^2}\right) \cos 2\phi_{\mathbf{p}} \int_0^{+\infty} dr J_2(pr) \left\{ \sum_{\sigma} \nu_{\sigma}^2 \frac{1 - \sin(2p_F^{\sigma}r - 2\beta)}{p_F^{\sigma}} - \right. \\
&\quad \left. - 2\nu^2 \frac{v_F^2}{v^2} \cdot \frac{\cos p_{\lambda}r + \sin(2mvr - 2\beta)}{p_F} \right\} \cdot e^{-2p_s r} \\
S_y(\mathbf{p}) &= -2\pi J_x^2 \left(1 + \frac{1}{\alpha^2}\right) \sin 2\phi_{\mathbf{p}} \int_0^{+\infty} dr J_2(pr) \left\{ \sum_{\sigma} \nu_{\sigma}^2 \frac{1 - \sin(2p_F^{\sigma}r - 2\beta)}{p_F^{\sigma}} - \right. \\
&\quad \left. - 2\nu^2 \frac{v_F^2}{v^2} \cdot \frac{\cos p_{\lambda}r - \sin(2mvr - \theta)}{p_F} \right\} \cdot e^{-2p_s r} \\
S_z(\mathbf{p}) &= -2\pi i J_x^2 \left(1 + \frac{1}{\alpha^2}\right) \cos \phi_{\mathbf{p}} \int_0^{+\infty} dr J_1(pr) \left\{ 2 \sum_{\sigma} \sigma \nu_{\sigma}^2 \frac{\cos(2p_F^{\sigma}r - \theta)}{p_F^{\sigma}} + 4\nu^2 \frac{v_F^2}{v^2} \cdot \frac{\sin p_{\lambda}r}{p_F} \right\} \cdot e^{-2p_s r} \\
\rho(p) &= +2\pi J_x^2 \left(1 + \frac{1}{\alpha^2}\right) \int_0^{+\infty} dr J_0(pr) \left\{ 4 \frac{\nu^2}{mv} + 4\nu^2 \frac{v_F^2}{v^2} \cdot \frac{\sin(2mvr - \theta)}{p_F} \right\} \cdot e^{-2p_s r}
\end{aligned}$$

## 1D case

The unperturbed Green's function in momentum space is  $G_0(E, p) = \frac{1}{2} \sum_{\sigma=\pm} G_0^{\sigma}(E, p)$ , where

$$G_0^{\sigma}(E, p) = -\frac{1}{\xi_{\sigma}^2 + \Delta_s^2 - E^2} \begin{pmatrix} 1 & i\sigma \\ -i\sigma & 1 \end{pmatrix} \otimes \begin{pmatrix} E + \xi_{\sigma} & \Delta_s \\ \Delta_s & E - \xi_{\sigma} \end{pmatrix}, \quad (\text{A.13})$$

where  $\xi_{\sigma} = \xi_p + \sigma\lambda p$ . To get the coordinate value one needs to perform the Fourier transform:

$G_0^{\sigma}(E, x) = \int \frac{dp}{2\pi} G_0^{\sigma}(E, p) e^{ipx}$ . We will therefore have two types of integrals:

$$X_0^{\sigma}(x) = -\int \frac{dp}{2\pi} \frac{e^{ipx}}{\xi_{\sigma}^2 + \omega^2}, \quad (\text{A.14})$$

$$X_1^{\sigma}(x) = -\int \frac{dp}{2\pi} \frac{\xi_{\sigma} e^{ipx}}{\xi_{\sigma}^2 + \omega^2}, \quad (\text{A.15})$$

where  $\omega^2 \equiv \Delta_s^2 - E^2$ . Since the spectrum is split by SO coupling, there will be two Fermi momenta which can be found the following way:

$$\frac{p^2}{2m} + \sigma\lambda p - \varepsilon_F = 0, \quad p_F^\sigma = \frac{-\sigma\lambda + \sqrt{\lambda^2 + 2\varepsilon_F/m}}{1/m} \equiv m[-\sigma\lambda + v]$$

For  $p > 0$  we linearise the spectrum around Fermi momenta, thus:

$$\xi_\sigma \approx \left( \frac{p_F^\sigma}{m} + \sigma\lambda \right) (p - p_F^\sigma) = \sqrt{\lambda^2 + 2\varepsilon_F/m} (p - p_F^\sigma) \equiv v(p - p_F^\sigma),$$

therefore  $p = p_F^\sigma + \xi_\sigma/v$  and we get:

$$X_0^\sigma(x) = - \int \frac{dp}{2\pi} \frac{e^{ipx}}{\xi_\sigma^2 + \omega^2} = - \left[ \int_0^{+\infty} \frac{dp}{2\pi} \frac{e^{ipx}}{\xi_\sigma^2 + \omega^2} + \int_0^{+\infty} \frac{dp}{2\pi} \frac{e^{-ipx}}{\xi_{-\sigma}^2 + \omega^2} \right] = \clubsuit$$

$$\int_0^{+\infty} \frac{dp}{2\pi} \frac{e^{ipx}}{\xi_\sigma^2 + \omega^2} \approx \frac{1}{2\pi v} e^{ip_F^\sigma x} \int d\xi_\sigma \frac{e^{i\xi_\sigma x/v}}{\xi_\sigma^2 + \omega^2} = \frac{1}{2v\omega} e^{ip_F^\sigma x} e^{-\omega|x|/v}$$

$$\int_0^{+\infty} \frac{dp}{2\pi} \frac{e^{-ipx}}{\xi_{-\sigma}^2 + \omega^2} \approx \frac{1}{2\pi v} e^{-ip_F^{-\sigma} x} \int d\xi_{-\sigma} \frac{e^{-i\xi_{-\sigma} x/v}}{\xi_{-\sigma}^2 + \omega^2} = \frac{1}{2v\omega} e^{-ip_F^{-\sigma} x} e^{-\omega|x|/v}$$

$$\clubsuit = -\frac{1}{2v\omega} [e^{im[-\sigma\lambda+v]x} + e^{-im[\sigma\lambda+v]x}] e^{-\omega|x|/v} = -\frac{1}{v} \cdot \frac{1}{\omega} \cos mvx e^{-i\sigma m\lambda x} e^{-\omega|x|/v}$$

$$X_1^\sigma(x) = - \int \frac{dp}{2\pi} \frac{\xi_\sigma e^{ipx}}{\xi_\sigma^2 + \omega^2} = - \left[ \int_0^{+\infty} \frac{dp}{2\pi} \frac{\xi_\sigma e^{ipx}}{\xi_\sigma^2 + \omega^2} + \int_0^{+\infty} \frac{dp}{2\pi} \frac{\xi_{-\sigma} e^{-ipx}}{\xi_{-\sigma}^2 + \omega^2} \right] = \spadesuit$$

$$\int_0^{+\infty} \frac{dp}{2\pi} \frac{\xi_\sigma e^{ipx}}{\xi_\sigma^2 + \omega^2} \approx \frac{1}{2\pi v} e^{ip_F^\sigma x} \int d\xi_\sigma \frac{\xi_\sigma e^{i\xi_\sigma x/v}}{\xi_\sigma^2 + \omega^2} = \frac{i}{2v} \operatorname{sgn} x e^{ip_F^\sigma x} e^{-\omega|x|/v}$$

$$\int_0^{+\infty} \frac{dp}{2\pi} \frac{\xi_{-\sigma} e^{-ipx}}{\xi_{-\sigma}^2 + \omega^2} \approx \frac{1}{2\pi v} e^{-ip_F^{-\sigma} x} \int d\xi_{-\sigma} \frac{\xi_{-\sigma} e^{-i\xi_{-\sigma} x/v}}{\xi_{-\sigma}^2 + \omega^2} = -\frac{i}{2v} \operatorname{sgn} x e^{-ip_F^{-\sigma} x} e^{-\omega|x|/v}$$

$$\spadesuit = -\frac{i}{2v} \operatorname{sgn} x \left[ e^{im[-\sigma\lambda+v]x} - e^{-im[\sigma\lambda+v]x} \right] e^{-\omega|x|/v} = \frac{1}{v} \cdot \sin mv|x| e^{-i\sigma m\lambda x} e^{-\omega|x|/v}$$

Finally,

$$X_0^\sigma(x) = -\frac{1}{v} \cdot \frac{1}{\omega} \cos mvx e^{-i\sigma m\lambda x} e^{-\omega|x|/v} \quad (\text{A.16})$$

$$X_1^\sigma(x) = +\frac{1}{v} \cdot \sin mv|x| e^{-i\sigma m\lambda x} e^{-\omega|x|/v} \quad (\text{A.17})$$

and

$$G_0(E, x) = \frac{1}{2} \sum_{\sigma=\pm} \begin{pmatrix} 1 & i\sigma \\ -i\sigma & 1 \end{pmatrix} \otimes \begin{pmatrix} EX_0^\sigma(x) + X_1^\sigma(x) & \Delta_s X_0^\sigma(x) \\ \Delta_s X_0^\sigma(x) & EX_0^\sigma(x) - X_1^\sigma(x) \end{pmatrix}, \quad (\text{A.18})$$

where

$$G_0(\epsilon, x=0) = -\frac{1}{v} \frac{1}{\sqrt{1-\epsilon^2}} \sigma_0 \otimes \begin{pmatrix} \epsilon & 1 \\ 1 & \epsilon \end{pmatrix}, \quad \text{where } \epsilon \equiv E/\Delta_s. \quad (\text{A.19})$$

The eigenvalues and eigenfunctions at  $\mathbf{r} = \mathbf{0}$  can be obtained using Eqs. (4.16) and (4.15) correspondingly. The energy levels are

$$E_{1,\bar{1}} = \pm \frac{1-\alpha^2}{1+\alpha^2} \Delta_s, \quad \text{where } \alpha = J/v. \quad (\text{A.20})$$

In case of an impurity along the  $z$ -axis the corresponding eigenvectors at the origin are

$$\Phi_{\bar{1}}(0) = \begin{pmatrix} 1 & 0 & -1 & 0 \end{pmatrix}^T, \quad \Phi_1(0) = \begin{pmatrix} 0 & 1 & 0 & 1 \end{pmatrix}^T \quad (\text{A.21})$$

and in case of an impurity along the  $x$ -axis:

$$\Phi_{\bar{1}}(0) = \begin{pmatrix} 1 & 1 & -1 & -1 \end{pmatrix}^T, \quad \Phi_1(0) = \begin{pmatrix} 1 & -1 & 1 & -1 \end{pmatrix}^T. \quad (\text{A.22})$$

**z-impurity**

$$\Phi_{\bar{1}}(x) = +\frac{J_z}{2} \sum_{\sigma} \begin{pmatrix} +(E_{\bar{1}} - \Delta_s) X_0^{\sigma} + X_1^{\sigma} \\ -i\sigma [(E_{\bar{1}} - \Delta_s) X_0^{\sigma} + X_1^{\sigma}] \\ -(E_{\bar{1}} - \Delta_s) X_0^{\sigma} + X_1^{\sigma} \\ +i\sigma [(E_{\bar{1}} - \Delta_s) X_0^{\sigma} - X_1^{\sigma}] \end{pmatrix}, \quad \Phi_1(x) = -\frac{J_z}{2} \sum_{\sigma} \begin{pmatrix} +i\sigma [(E_1 + \Delta_s) X_0^{\sigma} + X_1^{\sigma}] \\ (E_1 + \Delta_s) X_0^{\sigma} + X_1^{\sigma} \\ +i\sigma [(E_1 + \Delta_s) X_0^{\sigma} - X_1^{\sigma}] \\ (E_1 + \Delta_s) X_0^{\sigma} - X_1^{\sigma} \end{pmatrix}.$$

Using these expressions we can compute the non-polarised and SP LDOS in both coordinate and momentum space for the positive energy state (omitting the index 1):

$$S_x(x) = \frac{1 + \alpha^2}{4} [2 \sin p_{\lambda} x + \sin(2mv|x| + p_{\lambda} x - 2\theta) - \sin(2mv|x| - p_{\lambda} x - 2\theta)] \cdot e^{-2\omega|x|/v}$$

$$S_y(x) = 0$$

$$S_z(x) = -\frac{1 + \alpha^2}{4} [2 \cos p_{\lambda} x + \cos(2mv|x| + p_{\lambda} x - 2\theta) + \cos(2mv|x| - p_{\lambda} x - 2\theta)] \cdot e^{-2\omega|x|/v}$$

$$\rho(x) = \frac{1 + \alpha^2}{2} [1 + \cos(2mv|x| - 2\theta)] \cdot e^{-2\omega|x|/v}$$

where  $\tan \theta = \alpha$ . We perform the Fourier transform to get the momentum space behaviour, exploiting the following 'standard' integrals:

$$\begin{aligned} \int e^{-2\omega|x|/v} e^{-ipx} dx &= 2 \frac{2\omega/v}{p^2 + (2\omega/v)^2} \\ \int \cos p_{\lambda} x \cdot e^{-2\omega|x|/v} e^{-ipx} dx &= \frac{2\omega}{v} \left[ \frac{1}{(p + p_{\lambda})^2 + (2\omega/v)^2} + \frac{1}{(p - p_{\lambda})^2 + (2\omega/v)^2} \right] \\ \int \sin p_{\lambda} x \cdot e^{-2\omega|x|/v} e^{-ipx} dx &= i \frac{2\omega}{v} \left[ \frac{1}{(p + p_{\lambda})^2 + (2\omega/v)^2} - \frac{1}{(p - p_{\lambda})^2 + (2\omega/v)^2} \right] \\ \int \sin 2mv|x| \cdot e^{-2\omega|x|/v} e^{-ipx} dx &= \frac{p + 2mv}{(p + 2mv)^2 + (2\omega/v)^2} - \frac{p - 2mv}{(p - 2mv)^2 + (2\omega/v)^2} \end{aligned}$$

We rewrite these expressions using  $p_F^{\pm}$ , thus we get:

$$\begin{aligned} \int \cos p_{\lambda} x \cdot e^{-2\omega|x|/v} e^{-ipx} dx &= \frac{2\omega}{v} \left\{ \frac{1}{[p + (p_F^- - p_F^+)]^2 + (2\omega/v)^2} + \frac{1}{([p - (p_F^- - p_F^+)]^2 + (2\omega/v)^2)} \right\} \\ \int \sin p_{\lambda} x \cdot e^{-2\omega|x|/v} e^{-ipx} dx &= i \frac{2\omega}{v} \left\{ \frac{1}{[p + (p_F^- - p_F^+)]^2 + (2\omega/v)^2} - \frac{1}{[p - (p_F^- - p_F^+)]^2 + (2\omega/v)^2} \right\} \\ \int \sin 2mv|x| \cdot e^{-2\omega|x|/v} e^{-ipx} dx &= \frac{p + (p_F^- + p_F^+)}{[p + (p_F^- + p_F^+)]^2 + (2\omega/v)^2} - \frac{p - (p_F^- + p_F^+)}{[p - (p_F^- + p_F^+)]^2 + (2\omega/v)^2} \end{aligned}$$

For the last two integrals we introduce symbols  $\sum_{p'}$  and  $\widetilde{\sum}_{p'}$  (wide tilde signify that we take the difference, not sum), where  $p' \in \{p - p_\lambda, p + p_\lambda\}$ . Thus we have

$$\begin{aligned} & \int \cos(2mv|x| - 2\theta) \cos p_\lambda x \cdot e^{-2\omega|x|/v} e^{-ipx} dx = \\ & = \frac{1}{2} \sum_{p'} \left\{ \frac{1 - \alpha^2}{1 + \alpha^2} \cdot \frac{2\omega}{v} \left[ \frac{1}{(p' + 2mv)^2 + (2\omega/v)^2} + \frac{1}{(p' - 2mv)^2 + (2\omega/v)^2} \right] + \right. \\ & \quad \left. + \frac{2\alpha}{1 + \alpha^2} \cdot \left[ \frac{p' + 2mv}{(p' + 2mv)^2 + (2\omega/v)^2} + \frac{p' - 2mv}{(p' - 2mv)^2 + (2\omega/v)^2} \right] \right\} \end{aligned}$$

$$\begin{aligned} & \int \cos(2mv|x| - 2\theta) \sin p_\lambda x \cdot e^{-2\omega|x|/v} e^{-ipx} dx = \\ & = \frac{1}{2i} \widetilde{\sum}_{p'} \left\{ \frac{1 - \alpha^2}{1 + \alpha^2} \cdot \frac{2\omega}{v} \left[ \frac{1}{(p' + 2mv)^2 + (2\omega/v)^2} + \frac{1}{(p' - 2mv)^2 + (2\omega/v)^2} \right] + \right. \\ & \quad \left. + \frac{2\alpha}{1 + \alpha^2} \cdot \left[ \frac{p' + 2mv}{(p' + 2mv)^2 + (2\omega/v)^2} + \frac{p' - 2mv}{(p' - 2mv)^2 + (2\omega/v)^2} \right] \right\} \end{aligned}$$

We rewrite these expressions using  $p_F^\pm$ , thus we get:

$$\begin{aligned} & \int \cos(2mv|x| - 2\theta) \cos p_\lambda x \cdot e^{-2\omega|x|/v} e^{-ipx} dx = \\ & = \frac{1 - \alpha^2}{1 + \alpha^2} \cdot \frac{\omega}{v} \left[ \frac{1}{(p + 2p_F^+)^2 + (2\omega/v)^2} + \frac{1}{(p - 2p_F^-)^2 + (2\omega/v)^2} \right] + \\ & \quad + \frac{\alpha}{1 + \alpha^2} \cdot \left[ \frac{p + 2p_F^+}{(p + 2p_F^+)^2 + (2\omega/v)^2} + \frac{p - 2p_F^-}{(p - 2p_F^-)^2 + (2\omega/v)^2} \right] + \\ & \quad + \frac{1 - \alpha^2}{1 + \alpha^2} \cdot \frac{\omega}{v} \left[ \frac{1}{(p + 2p_F^-)^2 + (2\omega/v)^2} + \frac{1}{(p - 2p_F^+)^2 + (2\omega/v)^2} \right] + \\ & \quad + \frac{\alpha}{1 + \alpha^2} \cdot \left[ \frac{p + 2p_F^-}{(p + 2p_F^-)^2 + (2\omega/v)^2} + \frac{p - 2p_F^+}{(p - 2p_F^+)^2 + (2\omega/v)^2} \right] \end{aligned}$$

$$\begin{aligned} & \int \cos(2mv|x| - 2\theta) \sin p_\lambda x \cdot e^{-2\omega|x|/v} e^{-ipx} dx = \\ & = \frac{1}{i} \left\{ \frac{1 - \alpha^2}{1 + \alpha^2} \cdot \frac{\omega}{v} \left[ \frac{1}{(p + 2p_F^+)^2 + (2\omega/v)^2} + \frac{1}{(p - 2p_F^-)^2 + (2\omega/v)^2} \right] + \right. \\ & \quad \left. + \frac{\alpha}{1 + \alpha^2} \cdot \left[ \frac{p + 2p_F^+}{(p + 2p_F^+)^2 + (2\omega/v)^2} + \frac{p - 2p_F^-}{(p - 2p_F^-)^2 + (2\omega/v)^2} \right] \right\} - \\ & \quad - \frac{1}{i} \left\{ \frac{1 - \alpha^2}{1 + \alpha^2} \cdot \frac{\omega}{v} \left[ \frac{1}{(p + 2p_F^-)^2 + (2\omega/v)^2} + \frac{1}{(p - 2p_F^+)^2 + (2\omega/v)^2} \right] + \right. \\ & \quad \left. + \frac{\alpha}{1 + \alpha^2} \cdot \left[ \frac{p + 2p_F^-}{(p + 2p_F^-)^2 + (2\omega/v)^2} + \frac{p - 2p_F^+}{(p - 2p_F^+)^2 + (2\omega/v)^2} \right] \right\} \end{aligned}$$

Using the formula  $\cos^2 \gamma = (1 + \cos 2\gamma)/2$  we can write the momentum space expressions for the non-polarised and SP LDOS components:

$$\begin{aligned}
S_x(p) = & i(1 + \alpha^2) \frac{\omega}{v} \left\{ \frac{1}{[p + (p_F^- - p_F^+)]^2 + (2\omega/v)^2} - \frac{1}{[p - (p_F^- - p_F^+)]^2 + (2\omega/v)^2} \right\} + \\
& + \frac{1}{i} \left\{ \frac{1 - \alpha^2}{2} \cdot \frac{\omega}{v} \left[ \frac{1}{(p + 2p_F^+)^2 + (2\omega/v)^2} + \frac{1}{(p - 2p_F^-)^2 + (2\omega/v)^2} \right] + \right. \\
& \quad \left. + \frac{\alpha}{2} \cdot \left[ \frac{p + 2p_F^+}{(p + 2p_F^+)^2 + (2\omega/v)^2} + \frac{p - 2p_F^-}{(p - 2p_F^-)^2 + (2\omega/v)^2} \right] \right\} - \\
& \quad - \frac{1}{i} \left\{ \frac{1 - \alpha^2}{2} \cdot \frac{\omega}{v} \left[ \frac{1}{(p + 2p_F^-)^2 + (2\omega/v)^2} + \frac{1}{(p - 2p_F^+)^2 + (2\omega/v)^2} \right] + \right. \\
& \quad \left. + \frac{\alpha}{2} \cdot \left[ \frac{p + 2p_F^-}{(p + 2p_F^-)^2 + (2\omega/v)^2} + \frac{p - 2p_F^+}{(p - 2p_F^+)^2 + (2\omega/v)^2} \right] \right\}
\end{aligned}$$

$$\begin{aligned}
S_z(p) = & -(1 + \alpha^2) \frac{\omega}{v} \left\{ \frac{1}{[p + (p_F^- - p_F^+)]^2 + (2\omega/v)^2} + \frac{1}{[p - (p_F^- - p_F^+)]^2 + (2\omega/v)^2} \right\} - \\
& - \frac{1 - \alpha^2}{2} \cdot \frac{\omega}{v} \left[ \frac{1}{(p + 2p_F^+)^2 + (2\omega/v)^2} + \frac{1}{(p - 2p_F^-)^2 + (2\omega/v)^2} \right] - \\
& - \frac{\alpha}{2} \cdot \left[ \frac{p + 2p_F^+}{(p + 2p_F^+)^2 + (2\omega/v)^2} - \frac{p - 2p_F^-}{(p - 2p_F^-)^2 + (2\omega/v)^2} \right] - \\
& - \frac{1 - \alpha^2}{2} \cdot \frac{\omega}{v} \left[ \frac{1}{(p + 2p_F^-)^2 + (2\omega/v)^2} + \frac{1}{(p - 2p_F^+)^2 + (2\omega/v)^2} \right] - \\
& - \frac{\alpha}{2} \cdot \left[ \frac{p + 2p_F^-}{(p + 2p_F^-)^2 + (2\omega/v)^2} + \frac{p - 2p_F^+}{(p - 2p_F^+)^2 + (2\omega/v)^2} \right]
\end{aligned}$$

$$\begin{aligned}
\rho(p) = & (1 + \alpha^2) \left\{ \frac{2\omega/v}{p^2 + (2\omega/v)^2} + \left[ \frac{\omega/v}{[p + (p_F^- + p_F^+)]^2 + (2\omega/v)^2} + \frac{\omega/v}{([p - (p_F^- + p_F^+)]^2 + (2\omega/v)^2)} \right] \right\} + \\
& + \alpha \left\{ \frac{p + (p_F^- + p_F^+)}{[p + (p_F^- + p_F^+)]^2 + (2\omega/v)^2} - \frac{p - (p_F^- + p_F^+)}{[p - (p_F^- + p_F^+)]^2 + (2\omega/v)^2} \right\}
\end{aligned}$$

**x-impurity**

$$\Phi_{\bar{1}}(x) = +\frac{J_x}{2} \sum_{\sigma} \begin{pmatrix} (1+i\sigma)[(E_{\bar{1}}-\Delta_s)X_0^{\sigma}+X_1^{\sigma}] \\ (1-i\sigma)[(E_{\bar{1}}-\Delta_s)X_0^{\sigma}+X_1^{\sigma}] \\ -(1+i\sigma)[(E_{\bar{1}}-\Delta_s)X_0^{\sigma}-X_1^{\sigma}] \\ -(1-i\sigma)[(E_{\bar{1}}-\Delta_s)X_0^{\sigma}-X_1^{\sigma}] \end{pmatrix},$$

$$\Phi_1(x) = +\frac{J_x}{2} \sum_{\sigma} \begin{pmatrix} -(1-i\sigma)[(E_1+\Delta_s)X_0^{\sigma}+X_1^{\sigma}] \\ (1+i\sigma)[(E_1+\Delta_s)X_0^{\sigma}+X_1^{\sigma}] \\ -(1-i\sigma)[(E_1+\Delta_s)X_0^{\sigma}-X_1^{\sigma}] \\ (1+i\sigma)[(E_1+\Delta_s)X_0^{\sigma}-X_1^{\sigma}] \end{pmatrix}.$$

Using these expressions we can compute the non-polarised and SP LDOS in both coordinate and momentum space. We perform the calculation for the positive-energy state, and we find, omitting index 1:

$$S_x(x) = -\frac{1+\alpha^2}{2} [2\cos p_{\lambda}x + \cos(2mv|x| + p_{\lambda}x - 2\theta) + \cos(2mv|x| - p_{\lambda}x - 2\theta)] \cdot e^{-2\omega|x|/v}$$

$$S_y(x) = 0$$

$$S_z(x) = -\frac{1+\alpha^2}{2} [2\sin p_{\lambda}x + \sin(2mv|x| + p_{\lambda}x - 2\theta) - \sin(2mv|x| - p_{\lambda}x - 2\theta)] \cdot e^{-2\omega|x|/v}$$

$$\rho(x) = (1+\alpha^2)[1 + \cos(2mv|x| - 2\theta)] \cdot e^{-2\omega|x|/v}$$

where  $\tan \theta = \alpha$ . Momentum space dependence can be derived from the *z*-impurity expressions since everything coincides up to coefficients.

**y-impurity**

$$\Phi_{\bar{1}}(x) = +J_y \begin{pmatrix} +[(E_{\bar{1}}-\Delta_s)X_0^{-}+X_1^{-}] \\ i[(E_{\bar{1}}-\Delta_s)X_0^{-}+X_1^{-}] \\ -[(E_{\bar{1}}-\Delta_s)X_0^{-}-X_1^{-}] \\ -i[(E_{\bar{1}}-\Delta_s)X_0^{-}-X_1^{-}] \end{pmatrix}, \Phi_1(x) = +J_y \begin{pmatrix} -[(E_1+\Delta_s)X_0^{+}+X_1^{+}] \\ i[(E_1+\Delta_s)X_0^{+}+X_1^{+}] \\ -[(E_1+\Delta_s)X_0^{+}-X_1^{+}] \\ i[(E_1+\Delta_s)X_0^{+}-X_1^{+}] \end{pmatrix}.$$

Using these expressions we can compute the non-polarised and SP LDOS in coordinate space

$$\begin{aligned}
S_x(x) &= 0, \\
S_y(x) &= -(1 + \alpha^2)[1 + \cos(2mv|x| - 2\theta)] \cdot e^{-2\omega|x|/v}, \\
S_z(x) &= 0, \\
\rho(x) &= +(1 + \alpha^2)[1 + \cos(2mv|x| - 2\theta)] \cdot e^{-2\omega|x|/v}.
\end{aligned}$$

## A.2 p-wave superconductors

### Derivation of the energies and coordinate dependence of the Shiba states

We now exploit the model introduced in Chapter 4 to study a pure p-wave SC for which we take  $\Delta_s = 0$ . We only consider triplet superconductors which are gapped. Similar to our previous numerical analysis [84], we study here different  $\mathbf{d}$  vectors describing the triplet p-wave SCs [105]. We focus on two different types of  $\mathbf{d}$  vectors which are generic enough to describe all 2D unconventional triplet gaped superconductors: an in-plane  $\mathbf{d}$  vector,  $\mathbf{d}_{\parallel}(\mathbf{k}) = (k_y, -k_x, 0)$ , which corresponds to an unconventional time-reversal-invariant SC; and an out-of plane  $\mathbf{d}$  vector,  $\mathbf{d}_{\perp}(\mathbf{k}) = (0, 0, k_x + ik_y)$  which corresponds to a time-reversal symmetry-breaking SC. The latter model has been used to describe the properties of  $\text{Sr}_2\text{RuO}_4$  [55].

Note that for these two  $\mathbf{d}$  vectors, the system is characterised by two conserved quantities which can be written as  $M_{\parallel}^z = L_z + \sigma_z/2$  for  $\mathbf{d}_{\parallel}$ , and  $M_{\perp}^z = L_z - \tau_z/2$  for  $\mathbf{d}_{\perp}$  correspondingly. Here  $\tau_z$  is the Pauli matrix acting in the particle-hole subspace and  $\mathbf{L} = \mathbf{r} \times \mathbf{p}$  is the orbital momentum operator.

The eigenvalues corresponding to the energies of the Shiba states, as well as the Shiba wave functions at  $\mathbf{r} = \mathbf{0}$  are independent of the  $\mathbf{d}$  vector choice, and can be found using the method introduced in [35], summarised in Eq. (4.16). Therefore, the first step is to calculate analytically  $G_0(E, \mathbf{r} = \mathbf{0})$ . For this we note that the spectrum of  $\mathcal{H}_0(\mathbf{k})$  is given by  $\mathcal{E}(\mathbf{k}) = \pm\sqrt{\xi_{\mathbf{k}}^2 + \varkappa^2\mathbf{k}^2}$ , with a triplet gap parameter  $\Delta_t \equiv \frac{\varkappa k_F}{\sqrt{1+\tilde{\varkappa}^2}}$ , where  $\tilde{\varkappa} \equiv \varkappa/v_F$ . We need to perform the following

integrals:

$$\begin{aligned} X_0(\mathbf{0}) &= - \int \frac{d\mathbf{k}}{(2\pi)^2} \frac{1}{\xi_{\mathbf{k}}^2 + \varkappa^2 \mathbf{k}^2 - E^2}, \\ X_1(\mathbf{0}) &= - \text{p.v.} \int \frac{d\mathbf{k}}{(2\pi)^2} \frac{\xi_{\mathbf{k}}}{\xi_{\mathbf{k}}^2 + \varkappa^2 \mathbf{k}^2 - E^2}, \\ X_2^\pm(\mathbf{0}) &= \pm \int \frac{d\mathbf{k}}{(2\pi)^2} \frac{i\varkappa k_\pm}{\xi_{\mathbf{k}}^2 + \varkappa^2 \mathbf{k}^2 - E^2}, \end{aligned}$$

where  $k_\pm = k_x \pm ik_y$  and the symbol 'p.v.' corresponds to the principal value. The last integral is zero due to the angular part. The second integral has a UV divergence thus we need to use a natural cut-off which, in this particular case, is equivalent to computing the principal value of the integral. We linearise  $\xi_p$  around the Fermi level, and using the spherical symmetry of the integrals we change variables  $\xi_{\mathbf{k}} \approx v_F(k - k_F)$ ,  $\int \frac{d\mathbf{k}}{(2\pi)^2} = \nu \int d\xi_{\mathbf{k}}$ , where  $\nu = \frac{m}{2\pi}$ , and finally we obtain:

$$\begin{aligned} X_0(\mathbf{0}) &= - \frac{\pi\nu}{\sqrt{1 + \tilde{\varkappa}^2}} \frac{1}{\sqrt{\Delta_t^2 - E^2}}, \\ X_1(\mathbf{0}) &= \frac{\pi\nu}{\sqrt{1 + \tilde{\varkappa}^2}} \frac{\Delta_t}{\sqrt{\Delta_t^2 - E^2}} \frac{\tilde{\varkappa}}{\sqrt{1 + \tilde{\varkappa}^2}}, \\ X_2^\pm(\mathbf{0}) &= 0. \end{aligned}$$

The Green's function for  $\mathbf{r} = \mathbf{0}$  then takes the form:

$$G_0(E, \mathbf{r} = \mathbf{0}) = - \frac{\pi\nu}{\sqrt{1 + \tilde{\varkappa}^2}} \times \frac{1}{\sqrt{\Delta_t^2 - E^2}} \begin{pmatrix} (E - \gamma\Delta_t) \sigma_0 & 0 \\ 0 & (E + \gamma\Delta_t) \sigma_0 \end{pmatrix},$$

where  $\gamma \equiv \frac{\tilde{\varkappa}}{\sqrt{1 + \tilde{\varkappa}^2}}$ . Using this form for the Green's function and Eq. (4.16) we compute below the eigenvalues and eigenfunctions for  $\mathbf{r} = \mathbf{0}$  for different types of impurities, as in the sections above.

### Scalar impurity

Unlike for pure s-wave SCs, in p-wave SCs a purely scalar impurity ( $\mathbf{J} = \mathbf{0}$ ) creates two pairs of degenerate Shiba states with energies

$$E_{\bar{1},\bar{2}} = -\frac{-\gamma\beta^2 + \sqrt{1 + \beta^2(1 - \gamma^2)}}{1 + \beta^2}\Delta_t, \quad E_{1,2} = +\frac{-\gamma\beta^2 + \sqrt{1 + \beta^2(1 - \gamma^2)}}{1 + \beta^2}\Delta_t,$$

where  $\beta = \frac{\pi\nu U}{\sqrt{1+\tilde{z}^2}}$ , and eigenfunctions at the origin

$$\begin{aligned} \Phi_{\bar{1}}(\mathbf{0}) &= \begin{pmatrix} 0 & 1 & 0 & 0 \end{pmatrix}^\top, \quad \Phi_{\bar{2}}(\mathbf{0}) = \begin{pmatrix} 1 & 0 & 0 & 0 \end{pmatrix}^\top, \\ \Phi_2(\mathbf{0}) &= \begin{pmatrix} 0 & 0 & 0 & 1 \end{pmatrix}^\top, \quad \Phi_1(\mathbf{0}) = \begin{pmatrix} 0 & 0 & 1 & 0 \end{pmatrix}^\top. \end{aligned}$$

A possible explanation of the existence of these states is that a p-wave SC contains Cooper pairs with non-zero angular momentum due to the triplet pairing, and thus there are intrinsic magnetic fields impossible to observe unless one introduces a defect into the system, e.g. an impurity of any type. While in the case of a p-wave SC with a non-magnetic impurity we seem to have two pairs of degenerate states, we can think about this situation as having only two Shiba bound states within the gap mixing particle and hole degrees of freedom. Because the particle and hole components are the parts of the same state, they appear symmetrically in energy relative to the chemical potential, the positive and negative energy counterparts corresponding to the particle and hole component of the same bound state wave function respectively [34, 90, 91, 178].

### Magnetic impurity

Since in the case of a purely magnetic impurity ( $U = 0$ ) two types of coupling between the Cooper pairs and the impurity are possible, there are four Shiba states with energies independent of the impurity spin direction:

$$E_{1,\bar{1}} = \pm \frac{\gamma\alpha^2 + \sqrt{1 + \alpha^2(1 - \gamma^2)}}{1 + \alpha^2}\Delta_t, \quad E_{2,\bar{2}} = \pm \frac{-\gamma\alpha^2 + \sqrt{1 + \alpha^2(1 - \gamma^2)}}{1 + \alpha^2}\Delta_t,$$

where  $\alpha = \frac{\pi\nu J}{\sqrt{1+\tilde{z}^2}}$ . For weak impurities these levels are ordered as follows  $E_{\bar{1}} < E_{\bar{2}} < E_2 < E_1$ , while for a stronger impurities the middle levels exchange places, changing the order to  $E_{\bar{1}} <$

$$E_2 < E_{\bar{2}} < E_1.$$

For an impurity with spin along *z*-axis we have:

$$\begin{aligned}\Phi_{\bar{1}}(\mathbf{0}) &= \begin{pmatrix} 0 & 0 & 1 & 0 \end{pmatrix}^\top, \quad \Phi_{\bar{2}}(\mathbf{0}) = \begin{pmatrix} 1 & 0 & 0 & 0 \end{pmatrix}^\top, \\ \Phi_2(\mathbf{0}) &= \begin{pmatrix} 0 & 0 & 0 & 1 \end{pmatrix}^\top, \quad \Phi_1(\mathbf{0}) = \begin{pmatrix} 0 & 1 & 0 & 0 \end{pmatrix}^\top.\end{aligned}$$

For an impurity with spin along *x*-axis, we have:

$$\begin{aligned}\Phi_{\bar{1}}(\mathbf{0}) &= \begin{pmatrix} 0 & 0 & 1 & 1 \end{pmatrix}^\top, \quad \Phi_{\bar{2}}(\mathbf{0}) = \begin{pmatrix} 1 & 1 & 0 & 0 \end{pmatrix}^\top, \\ \Phi_2(\mathbf{0}) &= \begin{pmatrix} 0 & 0 & 1 & -1 \end{pmatrix}^\top, \quad \Phi_1(\mathbf{0}) = \begin{pmatrix} 1 & -1 & 0 & 0 \end{pmatrix}^\top.\end{aligned}$$

### Coordinate dependence of the Shiba wave functions in the 2D case

To find the spatial dependence of the Shiba states wave functions we use Eq. (4.15). While  $G_0(E, \mathbf{r} = \mathbf{0})$  is independent of the choice of  $\mathbf{d}$ ,  $G_0(E, \mathbf{r} \neq \mathbf{0})$ , and thus the spatial dependence of the eigenfunctions, as well as the spatial dependence of the LDOS and SP LDOS change drastically with the choice of  $\mathbf{d}$ . In what follows for every choice of the  $\mathbf{d}$  vector we construct the retarded Green's function and the corresponding eigenfunctions for different types of impurities, for which we also compute all the polarised and non-polarised components of LDOS. However, we note first that for both choices of  $\mathbf{d}$  vector we need to perform the following integrations:

$$\begin{aligned}X_0(\mathbf{r}) &= - \int \frac{d\mathbf{k}}{(2\pi)^2} \frac{e^{i\mathbf{k}\mathbf{r}}}{\xi_{\mathbf{k}}^2 + \varkappa^2 \mathbf{k}^2 - E^2}, \\ X_1(\mathbf{r}) &= - \int \frac{d\mathbf{k}}{(2\pi)^2} \frac{\xi_{\mathbf{k}} e^{i\mathbf{k}\mathbf{r}}}{\xi_{\mathbf{k}}^2 + \varkappa^2 \mathbf{k}^2 - E^2}, \\ X_2^\pm(\mathbf{r}) &= \pm \int \frac{d\mathbf{k}}{(2\pi)^2} \frac{i\varkappa k_\pm e^{i\mathbf{k}\mathbf{r}}}{\xi_{\mathbf{k}}^2 + \varkappa^2 \mathbf{k}^2 - E^2},\end{aligned}$$

We linearise the spectrum  $\xi_{\mathbf{k}} = v_F(k - k_F)$ , denoting

$$\tilde{\varkappa} = \frac{\varkappa}{v_F}, \quad \gamma = \frac{\tilde{\varkappa}}{\sqrt{1 + \tilde{\varkappa}^2}}, \quad \Delta_t = \frac{\varkappa k_F}{\sqrt{1 + \tilde{\varkappa}^2}}, \quad \omega^2 = \frac{\Delta_t^2 - E^2}{1 + \tilde{\varkappa}^2}, \quad \Omega = \frac{\omega}{v_F k_F},$$

and proceed with the calculation in the following way:

$$\begin{aligned}
X_0(r) &= -\frac{\nu}{1+\tilde{\alpha}^2} \int d\xi_{\mathbf{k}} \int \frac{d\varphi_{\mathbf{k}} e^{i(k_F + \frac{\xi_{\mathbf{k}}}{v_F})r \cos(\varphi_{\mathbf{k}} - \varphi_r)}}{2\pi (\xi_{\mathbf{k}} + \gamma\Delta_t)^2 + \omega^2} = -\frac{\nu}{1+\tilde{\alpha}^2} \int d\xi_{\mathbf{k}} \frac{J_0 \left[ \left(1 + \frac{\xi_{\mathbf{k}}}{v_F k_F}\right) k_F r \right]}{(\xi_{\mathbf{k}} + \gamma\Delta_t)^2 + \omega^2} = \\
&= -\frac{\nu}{1+\tilde{\alpha}^2} \frac{1}{v_F k_F} \int dW \frac{J_0(W k_F r)}{(W + \gamma^2 - 1)^2 + \Omega^2} = \\
&= -\frac{\nu}{1+\tilde{\alpha}^2} \frac{1}{v_F k_F} \frac{2}{\pi} \int_1^{+\infty} \frac{dU}{\sqrt{U^2 - 1}} \int dW \frac{\sin(k_F r U W)}{(W + \gamma^2 - 1)^2 + \Omega^2} = \\
&= -\frac{\nu}{1+\tilde{\alpha}^2} \frac{1}{v_F k_F} \frac{2}{\pi} \operatorname{Im} \int_1^{+\infty} \frac{dU}{\sqrt{U^2 - 1}} \int dW \frac{e^{ik_F r U W}}{(W + \gamma^2 - 1)^2 + \Omega^2} = \\
&= -\frac{2\nu}{1+\tilde{\alpha}^2} \frac{1}{\omega} \operatorname{Im} \int_1^{+\infty} \frac{dU}{\sqrt{U^2 - 1}} e^{ik_F r (1 - \gamma^2 + i\Omega)U} = \\
&= -\frac{2\nu}{1+\tilde{\alpha}^2} \cdot \frac{1}{\omega} \cdot \operatorname{Im} K_0[-i(1 - \gamma^2 + i\Omega)k_F r], \\
X_1(r) &= -\frac{\nu}{1+\tilde{\alpha}^2} \int d\xi_{\mathbf{k}} \int \frac{d\varphi_{\mathbf{k}} \xi_{\mathbf{k}} e^{i(k_F + \frac{\xi_{\mathbf{k}}}{v_F})r \cos(\varphi_{\mathbf{k}} - \varphi_r)}}{2\pi (\xi_{\mathbf{k}} + \gamma\Delta_t)^2 + \omega^2} = -\frac{\nu}{1+\tilde{\alpha}^2} \int d\xi_{\mathbf{k}} \frac{\xi_{\mathbf{k}} J_0 \left[ \left(1 + \frac{\xi_{\mathbf{k}}}{v_F k_F}\right) k_F r \right]}{(\xi_{\mathbf{k}} + \gamma\Delta_t)^2 + \omega^2} = \\
&= -\frac{\nu}{1+\tilde{\alpha}^2} \int dW \frac{(W - 1) J_0(W k_F r)}{(W + \gamma^2 - 1)^2 + \Omega^2} = \\
&= -\frac{\nu}{1+\tilde{\alpha}^2} \frac{2}{\pi} \operatorname{Im} \int_1^{+\infty} \frac{dU}{\sqrt{U^2 - 1}} \int dW \frac{(W - 1) e^{ik_F r U W}}{(W + \gamma^2 - 1)^2 + \Omega^2} = \\
&= -\frac{2\nu}{1+\tilde{\alpha}^2} \operatorname{Im} \int_1^{+\infty} \frac{dU}{\sqrt{U^2 - 1}} \left( i - \frac{\gamma^2}{\Omega} \right) e^{ik_F r (1 - \gamma^2 + i\Omega)U} = \\
&= -\frac{2\nu}{1+\tilde{\alpha}^2} \cdot \operatorname{Im} \left\{ \left( i - \frac{\gamma^2}{\Omega} \right) K_0[-i(1 - \gamma^2 + i\Omega)k_F r] \right\}, \\
X_2^{\pm}(r) &= \pm \frac{i\kappa\nu}{1+\tilde{\alpha}^2} \int k d\xi_{\mathbf{k}} \int \frac{d\varphi_{\mathbf{k}} e^{\pm i\varphi_{\mathbf{k}}} e^{i(k_F + \frac{\xi_{\mathbf{k}}}{v_F})r \cos(\varphi_{\mathbf{k}} - \varphi_r)}}{2\pi (\xi_{\mathbf{k}} + \gamma\Delta_t)^2 + \omega^2} = \\
&= \mp \frac{\kappa k_F \cdot \nu}{1+\tilde{\alpha}^2} \cdot e^{\pm i\varphi_r} \int d\xi_{\mathbf{k}} \frac{\left(1 + \frac{\xi_{\mathbf{k}}}{v_F k_F}\right) J_1 \left[ \left(1 + \frac{\xi_{\mathbf{k}}}{v_F k_F}\right) k_F r \right]}{(\xi_{\mathbf{k}} + \gamma\Delta_t)^2 + \omega^2} = \\
&= \pm \frac{\kappa k_F \cdot \nu}{1+\tilde{\alpha}^2} \cdot e^{\pm i\varphi_r} \cdot \frac{\partial}{\partial(k_F r)} \int d\xi_{\mathbf{k}} \frac{J_0 \left[ \left(1 + \frac{\xi_{\mathbf{k}}}{v_F k_F}\right) k_F r \right]}{(\xi_{\mathbf{k}} + \gamma\Delta_t)^2 + \omega^2} = \\
&= \pm \frac{2\nu}{1+\tilde{\alpha}^2} \cdot \frac{\kappa k_F}{\omega} e^{\pm i\varphi_r} \times \operatorname{Re} \left\{ (1 - \gamma^2 + i\Omega) K_1[-i(1 - \gamma^2 + i\Omega)k_F r] \right\},
\end{aligned}$$

where

$$e^{\pm i\varphi_r} = \frac{x \pm iy}{\sqrt{x^2 + y^2}} = \frac{x \pm iy}{r}.$$

Note that the integrals calculated for the pure *p*-wave case must coincide with the ones for *s*-wave provided  $\Delta_t \rightarrow \Delta_s$  and  $\varkappa = 0$  (and thus  $\gamma = 0$ ). As expected this substitution shows that the results of the integrations are consistent.

Below we summarise the results of the calculations above:

$$\begin{aligned} X_0(r) &= -\frac{2\nu}{1 + \tilde{\varkappa}^2} \cdot \frac{1}{\omega} \cdot \text{Im} K_0 [-i(1 - \gamma^2 + i\Omega)k_F r] \\ X_1(r) &= -\frac{2\nu}{1 + \tilde{\varkappa}^2} \cdot \text{Im} \left\{ \left( i - \frac{\gamma^2}{\Omega} \right) K_0 [-i(1 - \gamma^2 + i\Omega)k_F r] \right\} \\ X_2^\pm(\mathbf{r}) &= \pm \frac{2\nu}{1 + \tilde{\varkappa}^2} \cdot \frac{\varkappa k_F}{\omega} \cdot e^{\pm i\varphi_r} \text{Re} \left\{ (1 - \gamma^2 + i\Omega) K_1 [-i(1 - \gamma^2 + i\Omega)k_F r] \right\}, \end{aligned}$$

where we denote  $\Omega \equiv \frac{\omega}{v_F k_F} = \frac{1}{v_F k_F} \frac{\sqrt{\Delta_t^2 - E^2}}{\sqrt{1 + \tilde{\varkappa}^2}}$ , and  $e^{\pm i\varphi_r} \equiv \frac{x \pm iy}{\sqrt{x^2 + y^2}} = \frac{x \pm iy}{r}$  reflects all the characteristic asymmetry originating from the *p*-wave pairing orbital nature. We use the fact that  $\Omega \ll 1$ , which holds for all subgap energies. We give also the asymptotic behaviour of these integrals (see Appendix E for a full derivation):

$$X_0(r) \sim -\frac{\sqrt{2\pi} \nu}{\sqrt{1 + \tilde{\varkappa}^2}} \cdot \frac{1}{\sqrt{\Delta_t^2 - E^2}} \frac{\sin(k'_F r + \pi/4)}{\sqrt{k'_F r}} e^{-k_S r}, \quad (\text{A.23})$$

$$X_1(r) \sim +\frac{\sqrt{2\pi} \nu}{1 + \tilde{\varkappa}^2} \cdot \tilde{\varkappa} \frac{\Delta_t}{\sqrt{\Delta_t^2 - E^2}} \cdot \frac{\sin(k'_F r + \pi/4)}{\sqrt{k'_F r}} e^{-k_S r}, \quad (\text{A.24})$$

$$X_2^\pm(\mathbf{r}) \sim \pm \frac{\sqrt{2\pi} \nu}{1 + \tilde{\varkappa}^2} \cdot \frac{\Delta_t}{\sqrt{\Delta_t^2 - E^2}} \cdot e^{\pm i\varphi_r} \cdot \frac{\cos(k'_F r + \pi/4)}{\sqrt{k'_F r}} e^{-k_S r}, \quad (\text{A.25})$$

where  $k_S = \Omega k_F = \frac{\sqrt{\Delta_t^2 - E^2}}{v_F \sqrt{1 + \tilde{\varkappa}^2}}$  is the inverse superconducting decay length scale, and  $k'_F = \frac{k_F}{1 + \tilde{\varkappa}^2}$ .

### In-plane $d_{\parallel}$

The retarded Green's function in this case can be written using the integrals given above:

$$G_0(E, \mathbf{r}) = \begin{pmatrix} [EX_0(r) + X_1(r)] \sigma_0 & D_{\parallel}(\mathbf{r}) \\ D_{\parallel}(\mathbf{r}) & [EX_0(r) - X_1(r)] \sigma_0 \end{pmatrix},$$

where we denote:

$$D_{\parallel}(\mathbf{r}) \equiv \begin{pmatrix} 0 & X_2^-(\mathbf{r}) \\ X_2^+(\mathbf{r}) & 0 \end{pmatrix}.$$

The wave functions for the SBS arising for different types of impurities can be calculated subsequently using Eq. (4.15).

*Scalar impurity.* In this case we find

$$\begin{aligned} \Phi_{\bar{1}}(\mathbf{r}) &= +U \begin{pmatrix} 0 \\ E_{\bar{1},\bar{2}}X_0(r) + X_1(r) \\ X_2^-(\mathbf{r}) \\ 0 \end{pmatrix}, \quad \Phi_{\bar{2}}(\mathbf{r}) &= +U \begin{pmatrix} E_{\bar{1},\bar{2}}X_0(r) + X_1(r) \\ 0 \\ 0 \\ X_2^+(\mathbf{r}) \end{pmatrix}, \\ \Phi_2(\mathbf{r}) &= -U \begin{pmatrix} X_2^-(\mathbf{r}) \\ 0 \\ 0 \\ E_{1,2}X_0(r) - X_1(r) \end{pmatrix} \Phi_1(\mathbf{r}) &= -U \begin{pmatrix} 0 \\ X_2^+(\mathbf{r}) \\ E_{1,2}X_0(r) - X_1(r) \\ 0 \end{pmatrix}. \end{aligned}$$

It is worth noting that the Hamiltonian in Eq. (4.1) with a scalar impurity described by Eq. (4.2) with  $\mathbf{J} = \mathbf{0}$  still commutes with  $M_{\parallel}^z$  and therefore the states described above are also the eigenstates of this operator, namely:  $M_{\parallel}^z\Phi_{1,\bar{1}} = +\frac{1}{2}\Phi_{1,\bar{1}}$  and  $M_{\parallel}^z\Phi_{2,\bar{2}} = -\frac{1}{2}\Phi_{2,\bar{2}}$ . Therefore, we expect no explicit symmetry breaking nor any explicit p-wave orbital features to be observed in the full LDOS or in the SP LDOS. Indeed, we find that for all the states we have  $S^x(\mathbf{r}) = S^y(\mathbf{r}) = 0$ . Also, we note that the  $z$ -component of the SP LDOS and the LDOS are radially symmetric:

$$\begin{aligned} S_{\bar{1}}^z(r) &= +\rho_{\bar{1}}(r) = -U^2 X_2^-(\mathbf{r}) X_2^+(\mathbf{r}) \geq 0, \\ S_{\bar{2}}^z(r) &= -\rho_{\bar{2}}(r) = +U^2 X_2^-(\mathbf{r}) X_2^+(\mathbf{r}) \leq 0, \\ S_2^z(r) &= -\rho_2(r) = -U^2 [E_{1,2}X_0(r) - X_1(r)]^2 \leq 0, \\ S_1^z(r) &= +\rho_1(r) = +U^2 [E_{1,2}X_0(r) - X_1(r)]^2 \geq 0. \end{aligned}$$

We can see that the degenerate states have exactly opposite spin, and thus the total SP LDOS corresponding to the SBS energies, which is obtained by summing up over the two states with the same energy, is exactly zero, consistent also with the numerical simulations.

Moreover, when comparing the asymptotic behaviour for the SP LDOS, as derived from the asymptotic expressions in Eqs. (A.23,A.24,A.25), with the one obtained for the pure s-wave SC, we see that we have an additional factor  $k'_F = \frac{k_F}{1+\tilde{z}^2}$  depending on the p-wave parameter

$z$  that renormalises the Fermi momentum and also changes the decay length scale. Such renormalisation, if detected, may serve to measure the triplet pairing parameter by analysing the spatial structure of the SBS using STM.

*Magnetic impurity with spin  $\parallel z$ .* For this type of impurity we find

$$\begin{aligned} \Phi_{\bar{1}}(\mathbf{r}) &= +J_z \begin{pmatrix} 0 \\ X_2^+(\mathbf{r}) \\ E_{\bar{1}}X_0(r) - X_1(r) \\ 0 \end{pmatrix}, \quad \Phi_{\bar{2}}(\mathbf{r}) = +J_z \begin{pmatrix} E_2X_0(r) + X_1(r) \\ 0 \\ 0 \\ X_2^+(\mathbf{r}) \end{pmatrix}, \\ \Phi_2(\mathbf{r}) &= -J_z \begin{pmatrix} X_2^-(\mathbf{r}) \\ 0 \\ 0 \\ E_2X_0(r) - X_1(r) \end{pmatrix}, \quad \Phi_1(\mathbf{r}) = -J_z \begin{pmatrix} 0 \\ E_1X_0(r) + X_1(r) \\ X_2^-(\mathbf{r}) \\ 0 \end{pmatrix}. \end{aligned}$$

Like in the case of a scalar impurity, we note that the Hamiltonian still commutes with  $M_{\parallel}^z$ , and therefore the states found above are also the eigenstates of  $M_{\parallel}^z$ , such that  $M_{\parallel}^z\Phi_{\bar{1},\bar{2}} = +\frac{1}{2}\Phi_{\bar{1},\bar{2}}$ , and  $M_{\parallel}^z\Phi_{1,2} = -\frac{1}{2}\Phi_{1,2}$ . For all the states  $S^x(\mathbf{r}) = S^y(\mathbf{r}) = 0$ . Below we give the expressions for the  $z$ -component of the SP LDOS, and for the non-polarised LDOS, which are fully radially symmetric, same as for a scalar impurity:

$$\begin{aligned} S_{\bar{1}}^z(r) &= +\rho_{\bar{1}}(r) = +J_z^2 (E_{\bar{1}}X_0(r) - X_1(r))^2 \geq 0, \\ S_{\bar{2}}^z(r) &= -\rho_{\bar{2}}(r) = +J_z^2 X_2^-(\mathbf{r})X_2^+(\mathbf{r}) \leq 0, \\ S_2^z(r) &= -\rho_2(r) = -J_z^2 (E_2X_0(r) + X_1(r))^2 \leq 0, \\ S_1^z(r) &= +\rho_1(r) = -J_z^2 X_2^-(\mathbf{r})X_2^+(\mathbf{r}) \geq 0. \end{aligned}$$

We can see from these expressions that the average SPDOS, obtained by integrating these expressions over all space, is positive for the first and fourth states, and negative for the second and third. Thus, the analytical results are perfectly consistent with the numerical simulations given in [84].

*Magnetic impurity with spin  $\parallel x$ .* Unlike the cases of a scalar impurity and of a magnetic impurity along  $z$ , the Hamiltonian describing a magnetic impurity with the spin along  $x$  no longer commutes with  $M_{\parallel}^z$  and therefore the SBS are not the eigenstates of this operator, and

are thus expected to break the rotational symmetry that we have observed in the previous limits. Indeed we obtain:

$$\begin{aligned} \Phi_{\bar{1}}(\mathbf{r}) &= J_x \begin{pmatrix} X_2^-(\mathbf{r}) \\ X_2^+(\mathbf{r}) \\ +E_{\bar{1}}X_0(r) - X_1(r) \\ +E_{\bar{1}}X_0(r) - X_1(r) \end{pmatrix}, \quad \Phi_{\bar{2}}(\mathbf{r}) = J_x \begin{pmatrix} +E_{\bar{2}}X_0(r) + X_1(r) \\ +E_{\bar{2}}X_0(r) + X_1(r) \\ X_2^-(\mathbf{r}) \\ X_2^+(\mathbf{r}) \end{pmatrix}, \\ \Phi_2(\mathbf{r}) &= J_x \begin{pmatrix} X_2^-(\mathbf{r}) \\ -X_2^+(\mathbf{r}) \\ -E_2X_0(r) + X_1(r) \\ +E_2X_0(r) - X_1(r) \end{pmatrix}, \quad \Phi_1(\mathbf{r}) = J_x \begin{pmatrix} -E_1X_0(r) - X_1(r) \\ +E_1X_0(r) + X_1(r) \\ X_2^-(\mathbf{r}) \\ -X_2^+(\mathbf{r}) \end{pmatrix}. \end{aligned}$$

We exploit once more (4.17-4.18) to compute the LDOS and the SP LDOS and we find:

$$\begin{aligned} S_{\bar{1}}^x(r) &= +\rho_{\bar{1}}(r) = +2J_x^2 (E_{\bar{1}}X_0(r) - X_1(r))^2 \geq 0, \\ S_{\bar{1}}^y(\mathbf{r}) &= S_{\bar{1}}^z(\mathbf{r}) = 0, \\ S_{\bar{2}}^x(\mathbf{r}) &= -J_x^2 \left\{ [X_2^+(\mathbf{r})]^2 + [X_2^-(\mathbf{r})]^2 \right\}, \\ S_{\bar{2}}^y(\mathbf{r}) &= +iJ_x^2 \left\{ [X_2^+(\mathbf{r})]^2 - [X_2^-(\mathbf{r})]^2 \right\}, \\ S_{\bar{2}}^z(\mathbf{r}) &= 0, \\ \rho_{\bar{2}}(r) &= -2J_x^2 X_2^-(\mathbf{r})X_2^+(\mathbf{r}), \\ S_2^x(r) &= -\rho_2(r) = -2J_x^2 (E_2X_0(r) - X_1(r))^2 \leq 0, \\ S_2^y(\mathbf{r}) &= S_2^z(\mathbf{r}) = 0, \\ S_1^x(\mathbf{r}) &= +J_x^2 \left\{ [X_2^+(\mathbf{r})]^2 + [X_2^-(\mathbf{r})]^2 \right\}, \\ S_1^y(\mathbf{r}) &= -iJ_x^2 \left\{ [X_2^+(\mathbf{r})]^2 - [X_2^-(\mathbf{r})]^2 \right\}, \\ S_1^z(\mathbf{r}) &= 0, \\ \rho_1(r) &= -2J_x^2 X_2^-(\mathbf{r})X_2^+(\mathbf{r}). \end{aligned}$$

Indeed, we see that the  $x$ -components of the spin of the states  $\bar{1}$  and 2 are opposite in sign, while the rotational symmetry for these states is preserved. However the states  $\bar{2}$  and 1 show peculiar orbital features characteristic for the p-wave, that we show in figure A.1 by plotting the corresponding SP LDOS. The rings of high intensity appearing in these figures correspond

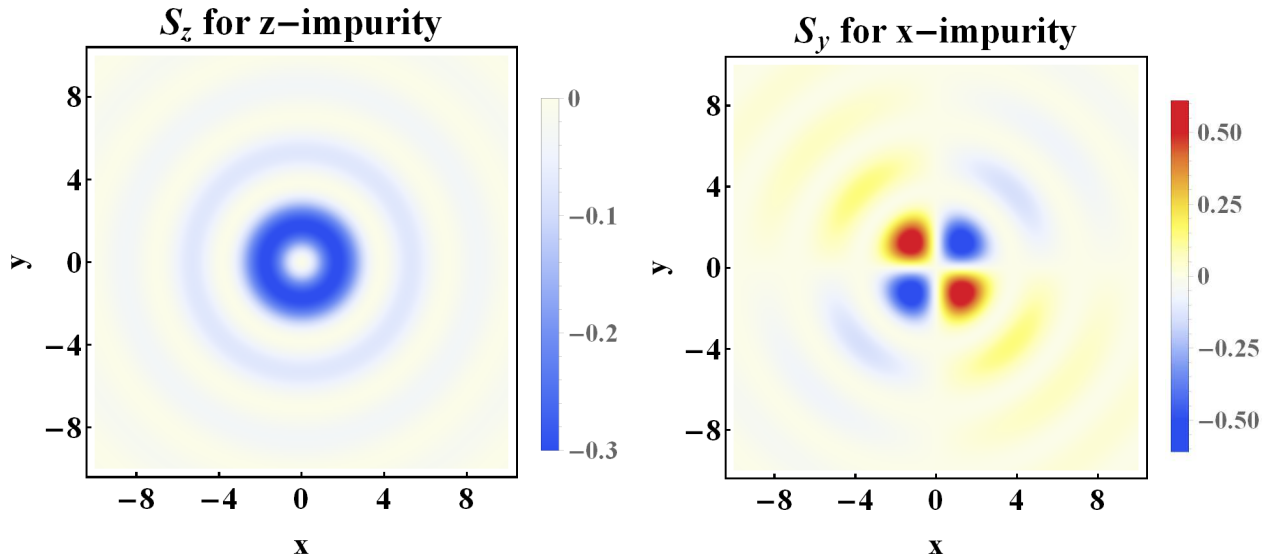


Figure A.1: SP LDOS (in arbitrary units) in coordinate space, for an in-plane  $\mathbf{d}$  vector, and for an energy  $E = E_2$ . We consider a magnetic impurity with spin along  $z$  (upper panel) and along  $y$  (lower panel), with impurity strengths of  $J_z = 2$  and  $J_x = 2$  respectively. The SP LDOS in the upper panel is radially symmetric, whereas in the lower one it reflects the characteristic *p*-wave four-fold symmetry. We set  $\Delta_s = 0$ ,  $\varkappa = 0.2$  and an inverse quasiparticle lifetime  $\delta = 0.01$ .

to Friedel oscillations with the wave vector  $2k'_F$  defined above. The strong radially asymmetric behaviour of the  $S_x$  component for an  $x$ -impurity is consistent with the  $\cos 2\phi_r$  dependence arising in the asymptotic expansion of  $[X_2^+(\mathbf{r})]^2 + [X_2^-(\mathbf{r})]^2$ .

Let us focus on the states  $\bar{2}$  and 1 and particularly on their average spin. Noticing that

$$X_2^\pm(\mathbf{r}) = \pm e^{\pm i\varphi_r} F(r),$$

where  $F(r)$  has no angular dependence, we thus find

$$\int d\mathbf{r} [X_2^\pm(\mathbf{r})]^2 = \int_0^{+\infty} r F^2(r) dr \int_0^{2\pi} e^{\pm 2i\varphi_r} d\varphi_r = 0$$

due to the angular part. Therefore, we find that the average spin for the states  $\bar{2}$  and 1 is exactly zero which is consistent with previous numerical analysis [84]. This result can be directly traced back to the *p*-wave nature of the host superconductor which manifests in some of the Shiba states.

### Out-of-plane $\mathbf{d}_\perp$

Among the unconventional SCs,  $\text{Sr}_2\text{RuO}_4$  is believed to be a p-wave superconductor with an out-of-plane  $\mathbf{d}$  vector [55]. Contrary to the in-plane  $\mathbf{d}$  vector, such p-wave SC breaks time reversal symmetry. It is therefore interesting to analyse and compare it with the case of  $\mathbf{d}_\parallel$ . The retarded Green's function can be written as:

$$G_0(E, \mathbf{r}) = \begin{pmatrix} [EX_0(r) + X_1(r)] \sigma_0 & D_\perp(\mathbf{r}) \\ -D_\perp^*(\mathbf{r}) & [EX_0(r) - X_1(r)] \sigma_0 \end{pmatrix},$$

where we used

$$D_\perp(\mathbf{r}) \equiv \begin{pmatrix} iX_2^+(\mathbf{r}) & 0 \\ 0 & -iX_2^+(\mathbf{r}) \end{pmatrix}.$$

We proceed following the same scheme as for  $\mathbf{d}_\parallel$ .

*Scalar impurity.* For this type of impurity we find

$$\begin{aligned} \Phi_{\bar{1}}(\mathbf{r}) &= +U \begin{pmatrix} 0 \\ E_{\bar{1}}X_0(r) + X_1(r) \\ 0 \\ iX_2^-(\mathbf{r}) \end{pmatrix}, & \Phi_{\bar{2}}(\mathbf{r}) &= +U \begin{pmatrix} E_2X_0(r) + X_1(r) \\ 0 \\ -iX_2^-(\mathbf{r}) \\ 0 \end{pmatrix}, \\ \Phi_2(\mathbf{r}) &= -U \begin{pmatrix} 0 \\ -iX_2^+(\mathbf{r}) \\ 0 \\ E_2X_0(r) - X_1(r) \end{pmatrix}, & \Phi_1(\mathbf{r}) &= -U \begin{pmatrix} iX_2^+(\mathbf{r}) \\ 0 \\ E_1X_0(r) - X_1(r) \\ 0 \end{pmatrix}. \end{aligned}$$

We note that, similar to the case of  $\mathbf{d}_\parallel$ , the Hamiltonian for a scalar impurity commutes with  $M_\perp^z$  and therefore the states found above are also eigenstates of  $M_\perp^z$ , namely:  $M_\perp^z \Phi_{\bar{1},\bar{2}} = -\frac{1}{2} \Phi_{\bar{1},\bar{2}}$

and  $M_{\perp}^z \Phi_{1,2} = +\frac{1}{2} \Phi_{1,2}$ . We thus have  $S^x(\mathbf{r}) = S^y(\mathbf{r}) = 0$ , and:

$$\begin{aligned} S_{\bar{1}}^z(r) &= -\rho_{\bar{1}}(r) = +U^2 X_2^-(\mathbf{r}) X_2^+(\mathbf{r}) \leq 0, \\ S_{\bar{2}}^z(r) &= +\rho_{\bar{2}}(r) = -U^2 X_2^-(\mathbf{r}) X_2^+(\mathbf{r}) \geq 0, \\ S_2^z(r) &= -\rho_2(r) = -U^2 (E_{1,2} X_0(r) - X_1(r))^2 \leq 0, \\ S_1^z(r) &= +\rho_1(r) = +U^2 (E_{1,2} X_0(r) - X_1(r))^2 \geq 0, \end{aligned}$$

once more radially symmetric. Obviously, the total SP LDOS vanishes, as it adds up exactly to zero for both pairs of degenerate states.

*Magnetic impurity with spin  $\parallel z$ .* We find for the SBS eigenstates

$$\begin{aligned} \Phi_{\bar{1}}(\mathbf{r}) &= +J_z \begin{pmatrix} iX_2^+(\mathbf{r}) \\ 0 \\ E_{\bar{1}}X_0(r) - X_1(r) \\ 0 \end{pmatrix}, & \Phi_{\bar{2}}(\mathbf{r}) &= +J_z \begin{pmatrix} E_{\bar{2}}X_0(r) + X_1(r) \\ 0 \\ -iX_2^-(\mathbf{r}) \\ 0 \end{pmatrix}, \\ \Phi_2(\mathbf{r}) &= -J_z \begin{pmatrix} 0 \\ -iX_2^+(\mathbf{r}) \\ 0 \\ E_2X_0(r) - X_1(r) \end{pmatrix}, & \Phi_1(\mathbf{r}) &= -J_z \begin{pmatrix} 0 \\ E_1X_0(r) + X_1(r) \\ 0 \\ iX_2^-(\mathbf{r}) \end{pmatrix}. \end{aligned}$$

Same as before  $M_{\perp}^z \Phi_{\bar{1},2} = +\frac{1}{2} \Phi_{\bar{1},2}$  and  $M_{\perp}^z \Phi_{1,\bar{2}} = -\frac{1}{2} \Phi_{1,\bar{2}}$ . Thus  $S^x(\mathbf{r}) = S^y(\mathbf{r}) = 0$ , and

$$\begin{aligned} S_{\bar{1}}^z(r) &= +\rho_{\bar{1}}(r) = +J_z^2 (E_{\bar{1}}X_0(r) - X_1(r))^2 \geq 0, \\ S_{\bar{2}}^z(r) &= +\rho_{\bar{2}}(r) = -J_z^2 X_2^-(\mathbf{r}) X_2^+(\mathbf{r}) \geq 0, \\ S_2^z(r) &= -\rho_2(r) = -J_z^2 (E_2X_0(r) - X_1(r))^2 \leq 0, \\ S_1^z(r) &= -\rho_1(r) = +J_z^2 X_2^-(\mathbf{r}) X_2^+(\mathbf{r}) \leq 0. \end{aligned}$$

It is easy to see using the definitions of  $X_2^{\pm}(\mathbf{r})$  that all the functions above have no angular dependence, and moreover do not change sign when varying  $r$ . Thus we infer that the spatially-averaged spin is positive for the states  $\bar{1}, \bar{2}$  and negative for the states 1, 2 and thus the inner states have spins of the same sign for  $\mathbf{d}_{\perp}$ , different from what we obtain for  $\mathbf{d}_{\parallel}$ , for which the inner states have opposite signs. This may be used experimentally as one of the distinguishing

features between these two choices of  $\mathbf{d}$  vectors.

*Magnetic impurity with spin  $\parallel x$ .* Unlike for  $\mathbf{d}_{\parallel}$ , for  $\mathbf{d}_{\perp}$  the Hamiltonian of a magnetic impurity with spin along  $x$  commutes with  $M_{\perp}^z$  and, therefore, the SBS are also eigenstates of  $M_{\perp}^z$ :  $M_{\perp}^z \Phi_{\bar{1},2} = +\frac{1}{2} \Phi_{\bar{1},2}$  and  $M_{\perp}^z \Phi_{1,\bar{2}} = -\frac{1}{2} \Phi_{1,\bar{2}}$ . That is why we expect that the SBS preserve the rotational symmetry in this limit, and that no peculiar feature due to the p-wave four-fold symmetry can be observed. Indeed

$$\begin{aligned} \Phi_{\bar{1}}(\mathbf{r}) &= +J_x \begin{pmatrix} iX_2^+(\mathbf{r}) \\ -iX_2^+(\mathbf{r}) \\ E_{\bar{1}}X_0(r) - X_1(r) \\ E_{\bar{1}}X_0(r) - X_1(r) \end{pmatrix}, & \Phi_{\bar{2}}(\mathbf{r}) &= +J_x \begin{pmatrix} E_{\bar{2}}X_0(r) + X_1(r) \\ E_{\bar{2}}X_0(r) + X_1(r) \\ -iX_2^-(\mathbf{r}) \\ iX_2^-(\mathbf{r}) \end{pmatrix}, \\ \Phi_2(\mathbf{r}) &= -J_x \begin{pmatrix} iX_2^+(\mathbf{r}) \\ iX_2^+(\mathbf{r}) \\ E_2X_0(r) - X_1(r) \\ -(E_2X_0(r) - X_1(r)) \end{pmatrix}, & \Phi_1(\mathbf{r}) &= -J_x \begin{pmatrix} E_1X_0(r) + X_1(r) \\ -(E_1X_0(r) + X_1(r)) \\ -iX_2^-(\mathbf{r}) \\ -iX_2^-(\mathbf{r}) \end{pmatrix}, \end{aligned}$$

and for all the states  $S^y(\mathbf{r}) = S^z(\mathbf{r}) = 0$ . The other components are given by

$$\begin{aligned} S_{\bar{1}}^x(r) &= \rho_{\bar{1}}(r) = +2J_z^2 (E_{\bar{1}}X_0(r) - X_1(r))^2 \geq 0, \\ S_{\bar{2}}^x(r) &= -\rho_{\bar{2}}(r) = +2J_z^2 X_2^-(\mathbf{r})X_2^+(\mathbf{r}) \leq 0, \\ S_2^x(r) &= -\rho_2(r) = -2J_z^2 (E_2X_0(r) - X_1(r))^2 \leq 0, \\ S_1^x(r) &= +\rho_1(r) = -2J_z^2 X_2^-(\mathbf{r})X_2^+(\mathbf{r}) \geq 0. \end{aligned}$$

It is easy to see that all the functions above have rotational symmetry and give the same sign for the spatially-averaged spin for the inner states.

## Derivation of the effective gaps for a SC with mixed singlet and triplet pairing

Below we consider a SC with mixed singlet and triplet pairing, defined by an in-plane  $\mathbf{d}$  vector  $\mathbf{d} = \mathbf{d}_{\parallel}$ . Note that in all the further calculations we linearise the dispersion relation around the Fermi energy. All the integrations are performed using this approximation. The unperturbed

Green's function in momentum space can be written as:

$$G_0(E, \mathbf{k}) = \frac{1}{2} \sum_{\sigma=\pm} G_0^\sigma(E, \mathbf{k}),$$

where

$$G_0^\sigma(E, \mathbf{k}) = -\frac{1}{\xi_{\mathbf{k}}^2 + (\Delta_s + \sigma\kappa k)^2 - E^2} \begin{pmatrix} 1 & i\sigma e^{-i\varphi} \\ -i\sigma e^{i\varphi} & 1 \end{pmatrix} \otimes \begin{pmatrix} E + \xi_{\mathbf{k}} & \Delta_s + \sigma\kappa k \\ \Delta_s + \sigma\kappa k & E - \xi_{\mathbf{k}} \end{pmatrix},$$

To get the zero coordinate value we linearise  $\xi_{\mathbf{k}}$  around Fermi level and calculate the following integrals:

$$G_0^\sigma(E, \mathbf{r} = \mathbf{0}) = -\int \frac{d\mathbf{k}}{(2\pi)^2} \frac{1}{\xi_{\mathbf{k}}^2 + (\Delta_s + \sigma\kappa k)^2 - E^2} \begin{pmatrix} 1 & 0 \\ 0 & 1 \end{pmatrix} \otimes \begin{pmatrix} E + \xi_{\mathbf{k}} & \Delta_s + \sigma\kappa k \\ \Delta_s + \sigma\kappa k & E - \xi_{\mathbf{k}} \end{pmatrix},$$

We need to calculate integrals of the form

$$I_n = -\int \frac{d\mathbf{k}}{(2\pi)^2} \frac{A_n}{\xi_{\mathbf{k}}^2 + (\Delta_s + \sigma\kappa k)^2 - E^2},$$

where  $n = 1, 2, 3$  and  $A_1 = E$ ,  $A_2 = \xi_{\mathbf{k}}$ , and  $A_3 = \Delta_s + \sigma\kappa k$ . Using  $k = k_F + \xi_{\mathbf{k}}/v_F$  we get:

$$-\int \frac{d\mathbf{k}}{(2\pi)^2} \frac{A_n}{\xi_{\mathbf{k}}^2 + (\Delta_s + \sigma\kappa k)^2 - E^2} = -\frac{\nu}{1 + \kappa^2} \int d\xi_{\mathbf{k}} \frac{A_n}{(\xi_{\mathbf{k}} + \sigma\gamma\Delta_{eff}^\sigma)^2 + \omega_\sigma^2},$$

where  $\nu \equiv \frac{m}{2\pi}$ ,  $\gamma \equiv \frac{\tilde{\kappa}}{\sqrt{1+\tilde{\kappa}^2}}$ ,  $\omega_\sigma^2 \equiv \frac{(\Delta_{eff}^\sigma)^2 - E^2}{1+\kappa^2}$ ,  $\Delta_{eff}^\sigma \equiv \frac{\Delta_s + \sigma\kappa k_F}{\sqrt{1+\tilde{\kappa}^2}}$ . Performing the integrations we get:

$$\begin{aligned} I_1 &= -\frac{\pi\nu}{\sqrt{1+\tilde{\kappa}^2}} \frac{E}{\sqrt{(\Delta_{eff}^\sigma)^2 - E^2}} \\ I_2 &= +\frac{\pi\nu}{\sqrt{1+\tilde{\kappa}^2}} \frac{\Delta_{eff}^\sigma}{\sqrt{(\Delta_{eff}^\sigma)^2 - E^2}} \sigma\gamma \\ I_3 &= -\frac{\pi\nu}{\sqrt{1+\tilde{\kappa}^2}} \frac{\Delta_{eff}^\sigma}{\sqrt{(\Delta_{eff}^\sigma)^2 - E^2}} \frac{1}{\sqrt{1+\tilde{\kappa}^2}} \end{aligned}$$

The integrals of all off-diagonal components are zeros due to the angular part. Thus we get:

$$G_0^\sigma(E, \mathbf{0}) = -\frac{\pi\nu}{\sqrt{1+\tilde{\kappa}^2}} \frac{1}{\sqrt{(\Delta_{eff}^\sigma)^2 - E^2}} \begin{pmatrix} E - \sigma\gamma\Delta_{eff}^\sigma & 0 & \frac{\Delta_{eff}^\sigma}{\sqrt{1+\tilde{\kappa}^2}} & 0 \\ 0 & E - \sigma\gamma\Delta_{eff}^\sigma & 0 & \frac{\Delta_{eff}^\sigma}{\sqrt{1+\tilde{\kappa}^2}} \\ \frac{\Delta_{eff}^\sigma}{\sqrt{1+\tilde{\kappa}^2}} & 0 & E + \sigma\gamma\Delta_{eff}^\sigma & 0 \\ 0 & \frac{\Delta_{eff}^\sigma}{\sqrt{1+\tilde{\kappa}^2}} & 0 & E + \sigma\gamma\Delta_{eff}^\sigma \end{pmatrix}.$$

It is clear that all the features arising from the bulk of a SC with mixed s-wave and p-wave types of pairing are originating from the expressions for the effective gaps, namely:

$$\Delta_{eff}^\pm = \frac{|\Delta_s \pm \kappa k_F|}{\sqrt{1+\tilde{\kappa}^2}},$$

the smallest of the two being the superconducting gap.

## Variation of the DOS for a mixed impurity in pure p-wave superconductor.

We consider a pure p-wave SC with  $\mathbf{d} = \mathbf{d}_\parallel$ . We plot the energy levels using the numerical calculations performed within the T-matrix approximation and a discretised (tight-binding) Hamiltonian. We plot in Fig. A.2, the density of states (DOS) as a function of energy and  $J_z$ .

### Singlet pairing $\Delta_s$ variation for mixed impurity

In Fig. A.3 we compute numerically the density of states for a mixture of triplet and singlet pairing in the presence of 2% of impurities with both scalar and magnetic components. We consider a discretised (tight-binding model) and we use the T-matrix approximation. We fix the triplet pairing and we vary the singlet pairing such that we move from a p-wave-dominant regime to an s-wave-dominant regime when the two pairing components are equal.

### Spin dependence of the DOS with respect to $\kappa$ for $\mathbf{J}_{z,x} = \mathbf{6}$

We plot in Fig. A.4 the SPDOS as a function of  $\kappa$  for both the in-plane  $\mathbf{d}$  vector (first row) and the perpendicular to the plane  $\mathbf{d}$  vector (second row) for an impurity spin pointing along

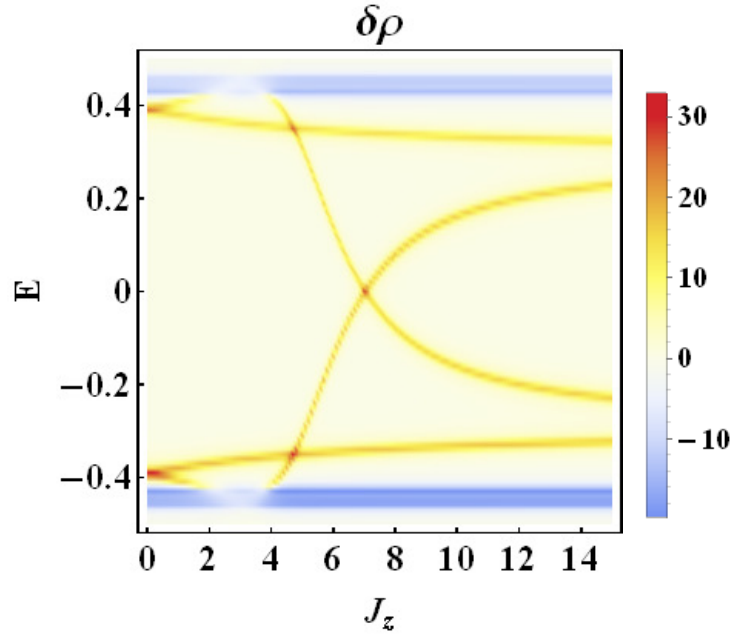


Figure A.2: DOS as a function of energy and  $J_z$  as calculated using the T-matrix approximation and a discretised tight-binding Hamiltonian (see main text). We set  $t = 1, \mu = -3, \varkappa = 0.5, U = 3$ . For small values of  $J_z$  there is also a linear splitting of the bound states levels.

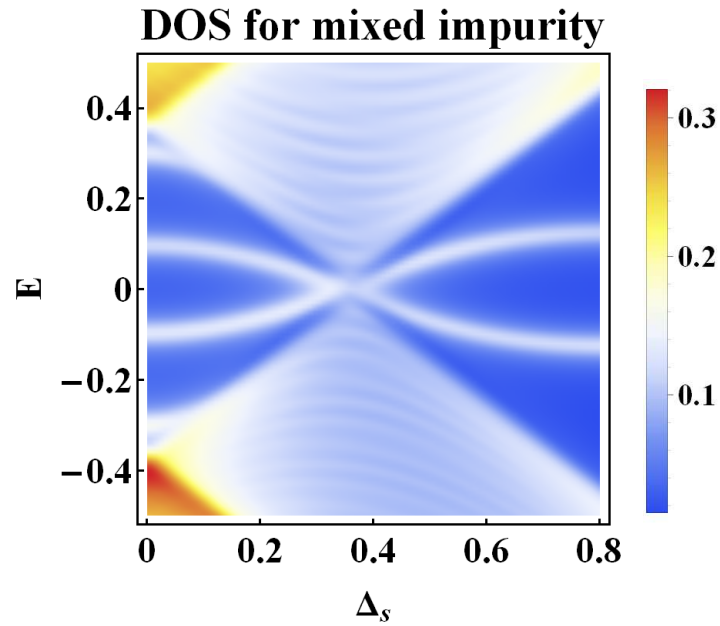


Figure A.3: DOS as a function of energy and the s-wave order parameter. We set  $t = 1, \mu = -3, \varkappa = 0.4, U = 1, J_z = 4$ . For small values of  $\Delta_s$  there are actually two distinct subgap Shiba states, whereas for larger values one of the two states is pushed into the bulk.

the z or x axis.

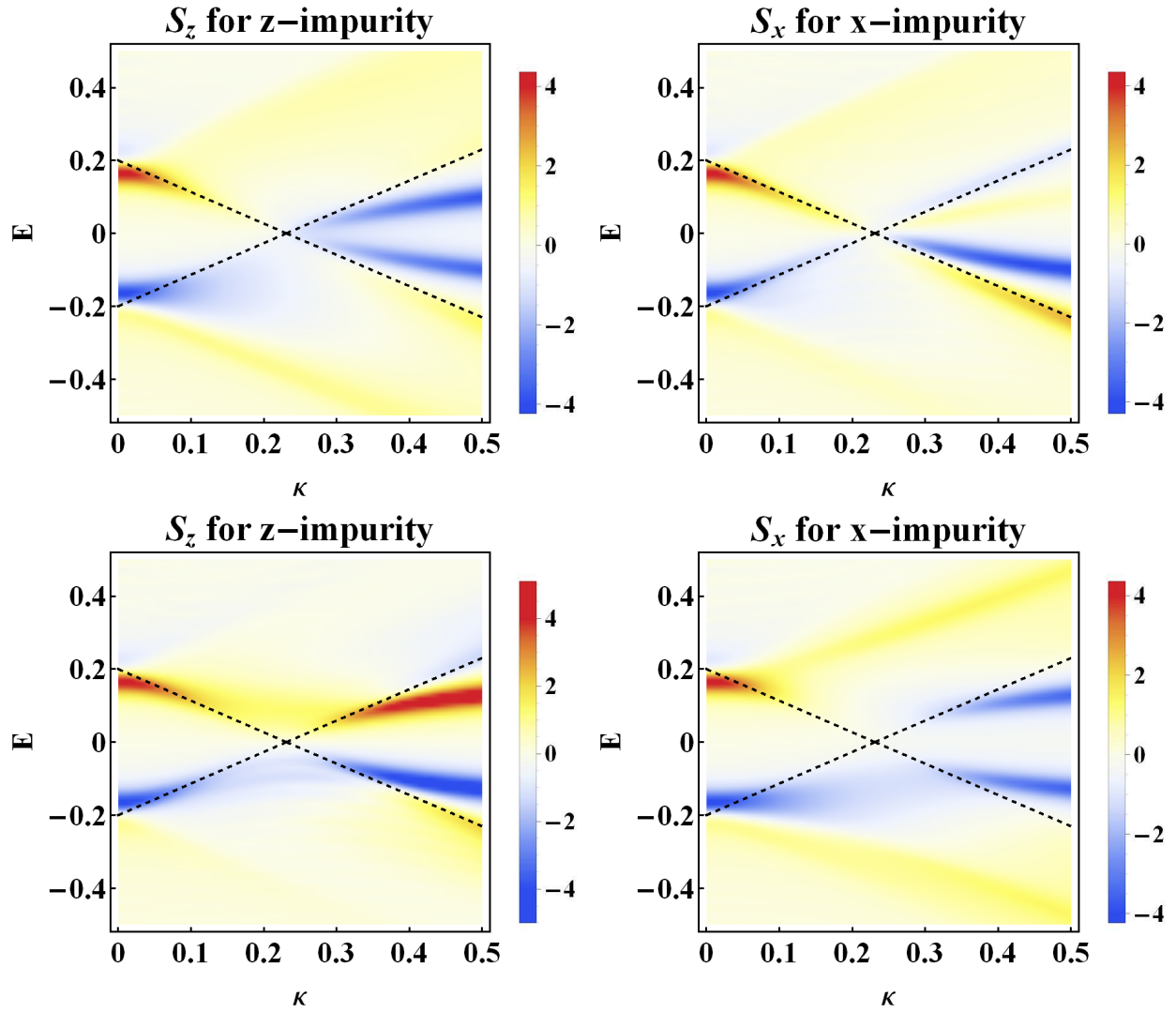


Figure A.4: SPDOS as a function of energy and the p-wave order parameter  $\varkappa$ . The  $\mathbf{d}$  vector is in-plane in the first row and perpendicular to the plane in the second row. We consider magnetic impurities with an impurity strength of  $J_z = 6$  (left column), and with  $J_x = 6$  (right column). We set  $\Delta_s = 0.2$ , and an inverse quasiparticle lifetime of  $\delta = 0.03$ .

## FT of the LDOS and of the SP LDOS for the Shiba states in a SC with mixed s-wave and p-wave pairing

We consider an in-plane  $\mathbf{d}$  vector and both in-plane ( $J_x = 2$ ) and perpendicular to the plane ( $J_z = 2$ ) impurities. We plot in Fig. A.5 and in A.6 the FT of the LDOS as well as of the SP LDOS components for the first positive-energy (respectively negative-energy) Shiba state. Note that for a mixed type of pairing all the spin components are non-zero, while for a pure s-wave or pure p-wave only the component parallel to the impurity spin is non zero. Note also that the spin components non-parallel to the impurity have a characteristic structure breaking

the radial symmetry.

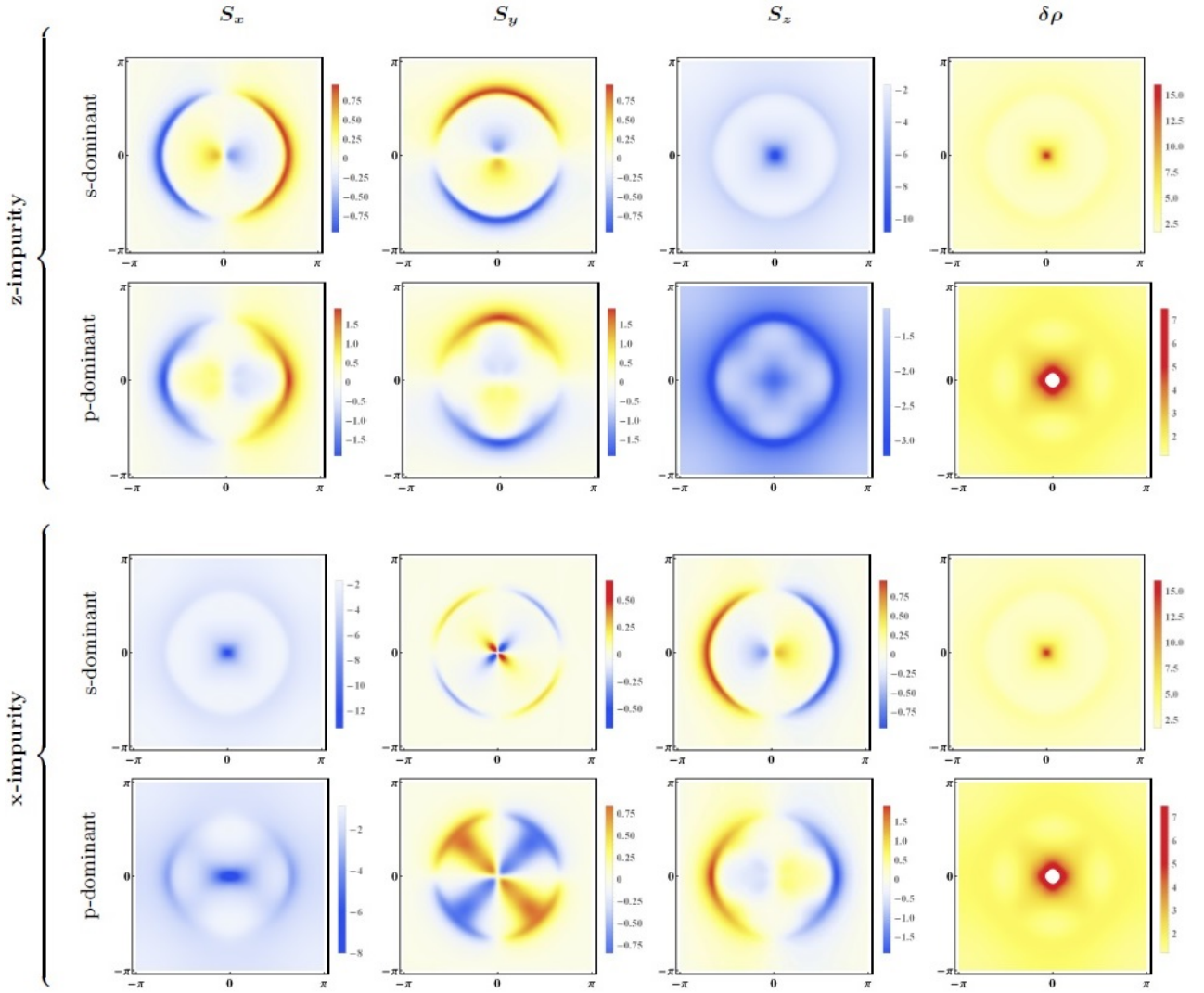


Figure A.5: The FT of the LDOS as well as of the SP LDOS components for the first positive-energy Shiba state as a function of momentum  $(p_x, p_y)$  for a magnetic impurity with  $J_z = 2$  (first two rows) and  $J_x = 2$  (last two rows). We take  $\Delta_s = 0.2$ ,  $\varkappa = 0.1$  for the s-dominant regime (rows 1 and 3), and  $\Delta_s = 0.2$ ,  $\varkappa = 0.5$  for the p-dominant regime (rows 2 and 4).

## Rashba spin-orbit coupling effect

To consider the effect of Rashba spin-orbit (SO) coupling on the results obtained in the main text, we add an additional term to the Hamiltonian:

$$\mathcal{H}_{SO} = \begin{pmatrix} +\lambda \mathbf{d}_{\parallel} \cdot \boldsymbol{\sigma} & 0 \\ 0 & -\lambda \mathbf{d}_{\parallel} \cdot \boldsymbol{\sigma} \end{pmatrix}$$

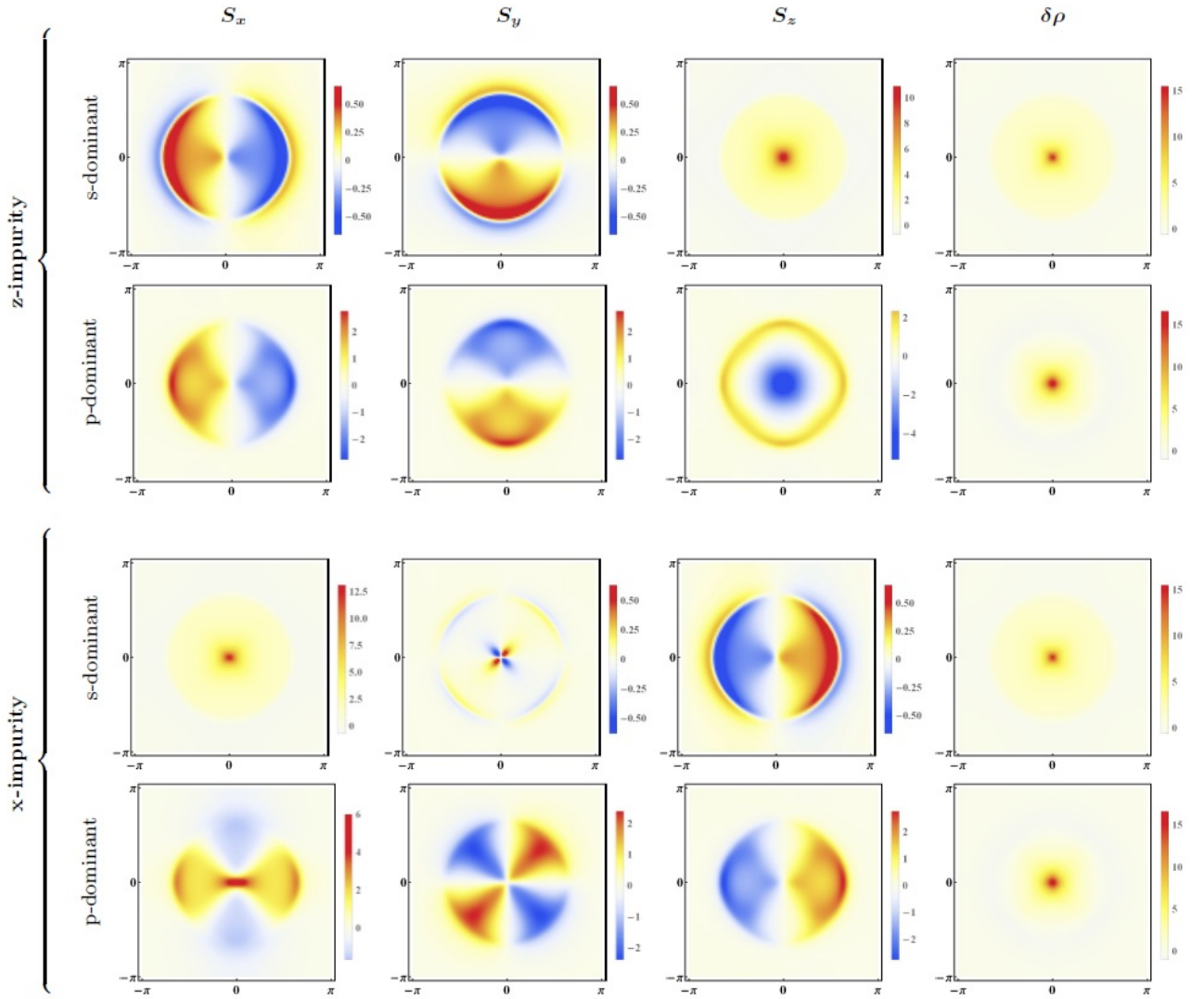


Figure A.6: The FT of the LDOS as well as of the SP LDOS components for the first negative-energy Shiba state as a function of momentum  $(p_x, p_y)$  for a magnetic impurity with  $J_z = 2$  (first two rows) and  $J_x = 2$  (last two rows). We take  $\Delta_s = 0.2$ ,  $\varkappa = 0.1$  for the s-dominant regime (rows 1 and 3), and  $\Delta_s = 0.2$ ,  $\varkappa = 0.5$  for the p-dominant regime (rows 2 and 4).

First of all, we plot the integrated SP LDOS as a function of energy and impurity strength for magnetic impurities with spin along  $z$  (left column) and along  $x$  (right column). As we can see, introducing the SO coupling does not change drastically the results concerning the spin texture of the Shiba states, except for the fact that the accidental cancellation we saw for the upper right panel of the Fig. A.7 is becoming partial, i.e. we can see the other two states as well. This can be explained by plotting the FT of SP LDOS in momentum space for  $\mathbf{d} = \mathbf{d}_{\parallel}$  presented in Fig. A.8. Indeed, the orbital symmetry that we have for the case of pure p-wave in Fig. 6 in the main text is violated in the presence of SO, and thus  $S_x(\mathbf{p} = \mathbf{0}) \neq 0$  any more.

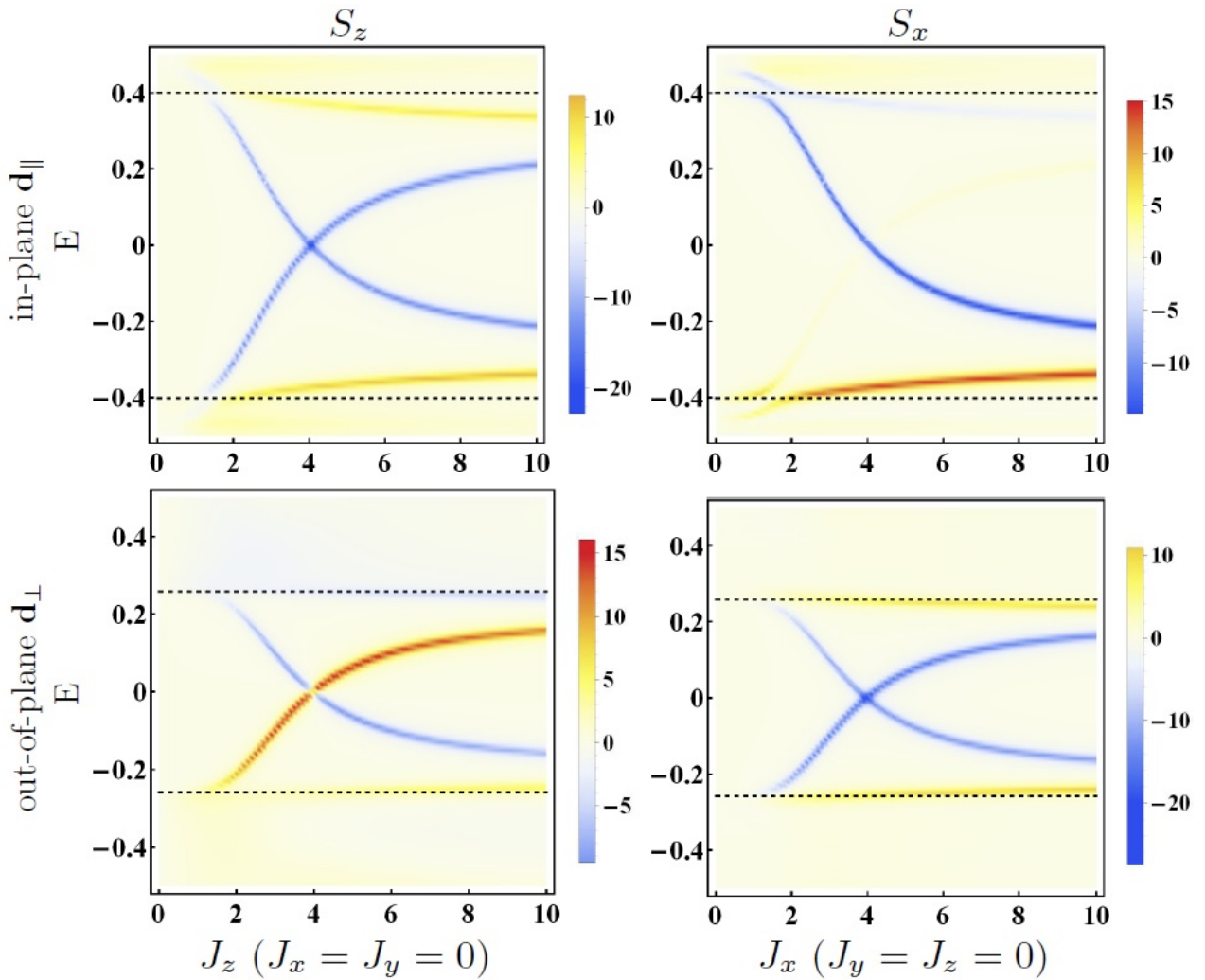


Figure A.7: Average SP LDOS as a function of energy and impurity strength for magnetic impurities with spin along  $z$  (left column) and along  $x$  (right column). We take  $\delta = 0.01$  and we focus on the  $p$ -wave  $\kappa = 0.5$ ,  $\Delta_s = 0$  with spin-orbit coupling  $\lambda = 0.2$  and in-plane  $\mathbf{d}_{\parallel}$  (first row) and out-of-plane  $\mathbf{d}_{\perp}$  (second row).

## Randomly directed impurity

Below we consider a purely  $p$ -wave SC with an in-plane  $\mathbf{d}$  vector and in Fig. A.9 we plot the Fourier transform of the non-polarised and SP LDOS for the Shiba states induced by an impurity with  $\mathbf{J} = (\frac{\sqrt{6}}{2}, \frac{\sqrt{6}}{2}, 1)$  (these values are chosen to have  $|\mathbf{J}| = 2$ ). As pointed out in the main text, this kind of impurity gives rise to all non-zero components of the SP LDOS. The in-plane spin component of the impurity creates four-fold symmetric features similar to those shown in Fig. 8 in the main text, but with an additional rotation in the momentum space, whereas the out-of-plane component induces a feature identical to that on the right panel in Fig. 7 in the main text, thus proving that considering an in-plane and out-of-plane impurities

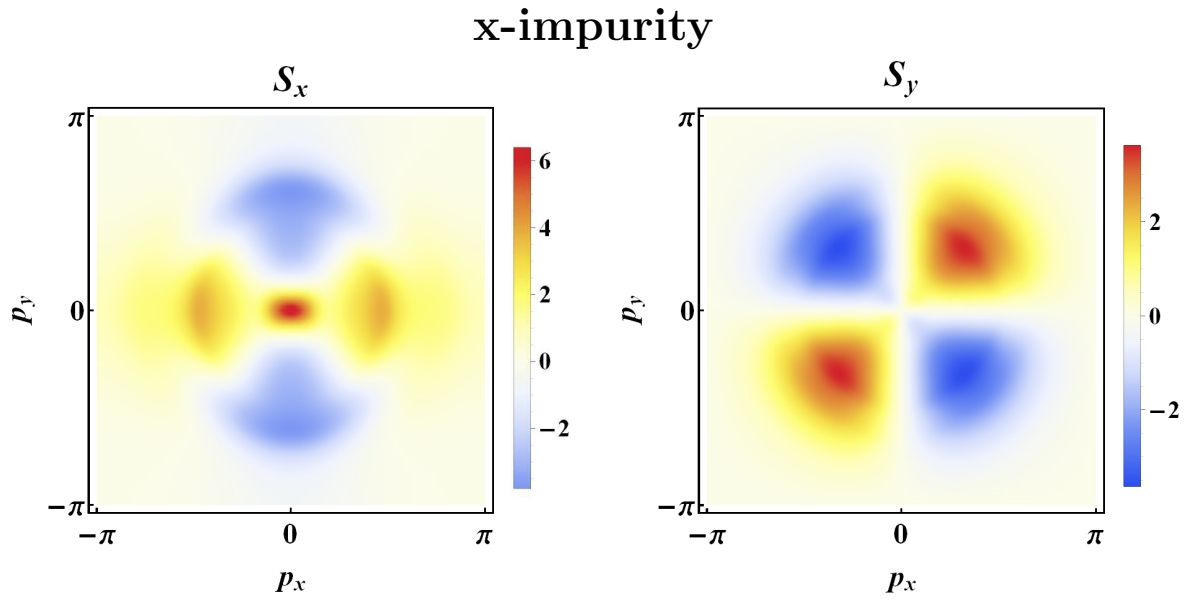


Figure A.8: The real part of the FT of the  $S_x$  and  $S_y$  SP LDOS components in arbitrary units for the hole component of a Shiba state as a function of momentum  $(p_x, p_y)$ , for a magnetic impurity with  $J_x = 2$ . We take p-wave  $\varkappa = 0.5$ ,  $\Delta_s = 0$  with spin-orbit coupling  $\lambda = 0.2$  and in-plane  $\mathbf{d}_{\parallel}$ .

separately is sufficient to capture all the properties of the system.

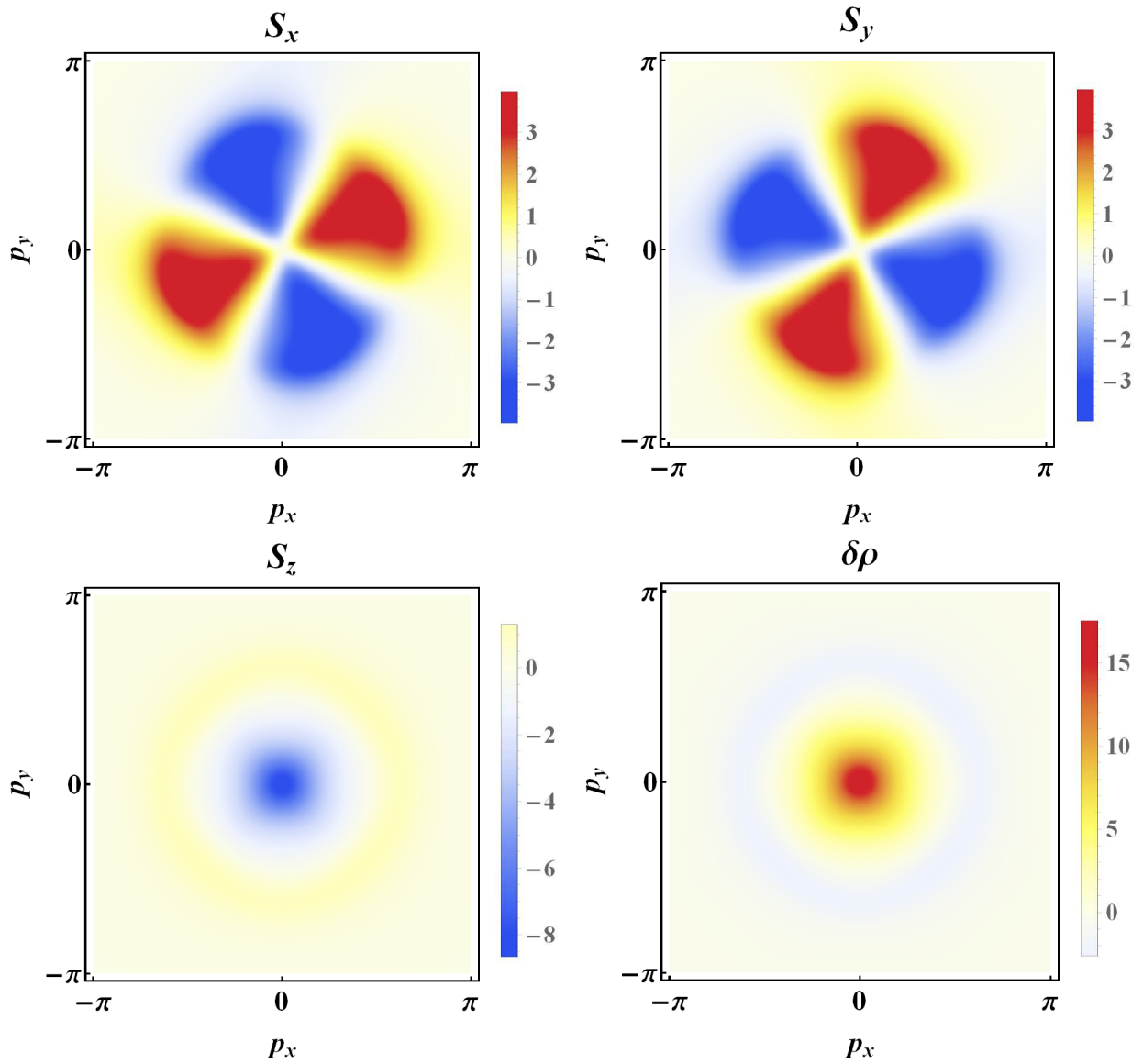


Figure A.9: The FT of the non-polarised LDOS as well as of the SP LDOS components for the first negative-energy Shiba state as a function of momentum  $(p_x, p_y)$  for a magnetic impurity with  $J_x = J_y = \frac{\sqrt{6}}{2}$  and  $J_z = 1$  in a pure *p*-wave with  $\varkappa = 0.5$ .

# Appendix B

## Metallic systems with Rashba SOC in the presence of magnetic impurities

### 2D metallic system

The low-energy Hamiltonian can be written as

$$H_0 = \xi_p \sigma_0 + \lambda(p_y \sigma_x - p_x \sigma_y) = \begin{pmatrix} \xi_p & i\lambda p_- \\ -i\lambda p_+ & \xi_p \end{pmatrix}, \quad (\text{B.1})$$

where  $\xi_p = \frac{p^2}{2m} - \varepsilon_F$ . The corresponding spectrum is given by  $\mathcal{E} = \xi_p \pm \lambda p$ . The retarded Green's function reads

$$G_0(E, \mathbf{p}) = \frac{1}{(E - \xi_p + i0)^2 - \lambda^2 p^2} \begin{pmatrix} E - \xi_p + i0 & i\lambda p_- \\ -i\lambda p_+ & E - \xi_p + i0 \end{pmatrix} \quad (\text{B.2})$$

To compute the eigenvalues for a single localised impurity we calculate

$$G_0(E, \mathbf{r} = \mathbf{0}) = \int \frac{d\mathbf{p}}{(2\pi)^2} \frac{E - \xi_p + i0}{(E - \xi_p + i0)^2 - \lambda^2 p^2} \begin{pmatrix} 1 & 0 \\ 0 & 1 \end{pmatrix} = \frac{1}{2} \sum_{\sigma} \int \frac{d\mathbf{p}}{(2\pi)^2} \frac{1}{E - \xi_{\sigma} + i0} \begin{pmatrix} 1 & 0 \\ 0 & 1 \end{pmatrix}, \quad (\text{B.3})$$

where  $\xi_\sigma = \xi_p + \sigma\lambda p$ . For  $p > 0$  we linearise the spectrum around Fermi momenta, thus:

$$\xi_\sigma \approx \left( \frac{p_F^\sigma}{m} + \sigma\lambda \right) (p - p_F^\sigma) = \sqrt{\lambda^2 + 2\varepsilon_F/m} (p - p_F^\sigma) \equiv v(p - p_F^\sigma),$$

with  $p_F^\sigma = m[-\sigma\lambda + v]$ , and thus we rewrite:

$$\frac{d\mathbf{p}}{(2\pi)^2} = \frac{m}{2\pi} \left[ 1 - \sigma \frac{\lambda}{v} \right] d\xi_\sigma \frac{d\phi}{2\pi} = \nu_\sigma d\xi_\sigma \frac{d\phi}{2\pi},$$

where  $\nu_\sigma = \nu [1 - \sigma \frac{\lambda}{v}]$ , with  $\nu = m/2\pi$ . Thus we get:

$$\int \frac{d\mathbf{p}}{(2\pi)^2} \frac{1}{E - \xi_\sigma + i0} = \nu_\sigma \int d\xi_\sigma \frac{1}{E - \xi_\sigma + i0} = -i\pi\nu_\sigma,$$

and therefore:

$$G_0(E, \mathbf{r} = \mathbf{0}) = \frac{1}{2} \sum_{\sigma} (-i\pi\nu_\sigma) \begin{pmatrix} 1 & 0 \\ 0 & 1 \end{pmatrix} = -i\pi\nu \begin{pmatrix} 1 & 0 \\ 0 & 1 \end{pmatrix} \quad (\text{B.4})$$

Since there is no energy dependence, there will be no impurity-induced states. To find the coordinate dependence of the Green's function we calculate:

$$X_0^\sigma(r) = \int \frac{d\mathbf{p}}{(2\pi)^2} \frac{e^{i\mathbf{p}\mathbf{r}}}{E - \xi_\sigma + i0} \quad (\text{B.5})$$

$$X_1^\sigma(s, \mathbf{r}) = \int \frac{d\mathbf{p}}{(2\pi)^2} \frac{-is e^{is\phi_{\mathbf{p}}} e^{i\mathbf{p}\mathbf{r}}}{E - \xi_\sigma + i0} \quad (\text{B.6})$$

Below we use the Sokhotsky formula:

$$\frac{1}{x + i0} = \mathcal{P} \frac{1}{x} - i\pi\delta(x)$$

$$\begin{aligned} X_0^\sigma(r) &= \int \frac{d\mathbf{p}}{(2\pi)^2} \frac{e^{i\mathbf{p}\mathbf{r}}}{E - \xi_\sigma + i0} = \nu_\sigma \int d\xi_\sigma \int \frac{d\phi_{\mathbf{p}}}{2\pi} \frac{e^{i\mathbf{p}\mathbf{r} \cos(\phi_{\mathbf{p}} - \phi_{\mathbf{r}})}}{E - \xi_\sigma + i0} = \nu_\sigma \int d\xi_\sigma \frac{J_0[(p_F^\sigma + \xi_\sigma/v)r]}{E - \xi_\sigma + i0} = \\ &= \nu_\sigma \left\{ \mathcal{P} \int d\xi_\sigma \frac{J_0[(p_F^\sigma + \xi_\sigma/v)r]}{E - \xi_\sigma} - i\pi \int d\xi_\sigma \delta(E - \xi_\sigma) J_0[(p_F^\sigma + \xi_\sigma/v)r] \right\} = \spadesuit \end{aligned}$$

We calculate separately the first integral:

$$\begin{aligned} \mathcal{P} \int d\xi_\sigma \frac{J_0 [(p_F^\sigma + \xi_\sigma/v) r]}{E - \xi_\sigma} &= \frac{2}{\pi} \int_1^{+\infty} \frac{du}{\sqrt{u^2 - 1}} \mathcal{P} \int d\xi_\sigma \frac{\sin [(p_F^\sigma + \xi_\sigma/v) r]}{E - \xi_\sigma} = \\ &= \frac{2}{\pi} \text{Im} \int_1^{+\infty} \frac{du}{\sqrt{u^2 - 1}} \mathcal{P} \int d\xi_\sigma \frac{e^{i(p_F^\sigma + \xi_\sigma/v)r}}{E - \xi_\sigma} = \frac{2}{\pi} \text{Im} \int_1^{+\infty} \frac{du}{\sqrt{u^2 - 1}} e^{ip_\sigma r u} \cdot \mathcal{P} \int dx \frac{e^{-i\frac{r}{v}x}}{x} = \clubsuit \end{aligned}$$

$$\mathcal{P} \int dx \frac{e^{-i\frac{r}{v}x}}{x} = \mathcal{P} \int \frac{\cos \frac{r}{v}x}{x} dx - i \mathcal{P} \int \frac{\sin \frac{r}{v}x}{x} dx = 0 - i\pi = -i\pi$$

Therefore:

$$\clubsuit = -2 \text{Im} \int_1^{+\infty} \frac{ie^{ip_\sigma r u}}{\sqrt{u^2 - 1}} du = -2 \int_1^{+\infty} \frac{\cos p_\sigma r u}{\sqrt{u^2 - 1}} du = \pi Y_0(p_\sigma r), \quad p_\sigma \neq 0$$

$$\spadesuit = \pi \nu_\sigma [Y_0(p_\sigma r) - iJ_0(p_\sigma r)].$$

The second integral is

$$\begin{aligned} X_1^\sigma(s, \mathbf{r}) &= \int \frac{d\mathbf{p}}{(2\pi)^2} \frac{-ise^{is\phi_{\mathbf{p}}} e^{i\mathbf{p}\mathbf{r}}}{E - \xi_\sigma + i0} = \nu_\sigma \int d\xi_\sigma \int \frac{d\phi_{\mathbf{p}}}{2\pi} \frac{-ise^{is\phi_{\mathbf{p}}} e^{i\mathbf{p}\mathbf{r} \cos(\phi_{\mathbf{p}} - \phi_{\mathbf{r}})}}{E - \xi_\sigma + i0} = \\ &= se^{is\phi_{\mathbf{r}}} \nu_\sigma \int d\xi_\sigma \frac{J_1 [(p_F^\sigma + \xi_\sigma/v) r]}{E - \xi_\sigma + i0} = \\ &= se^{is\phi_{\mathbf{r}}} \cdot \nu_\sigma \left\{ \mathcal{P} \int d\xi_\sigma \frac{J_1 [(p_F^\sigma + \xi_\sigma/v) r]}{E - \xi_\sigma} - i\pi \int d\xi_\sigma \delta(E - \xi_\sigma) J_1 [(p_F^\sigma + \xi_\sigma/v) r] \right\} = \heartsuit \end{aligned}$$

We calculate separately the first integral:

$$\begin{aligned}
\mathcal{P} \int d\xi_\sigma \frac{J_1 [(p_F^\sigma + \xi_\sigma/v) r]}{E - \xi_\sigma} &= \mathcal{P} \int dx \frac{J_1 [(p_\sigma - x/v) r]}{x} = -\frac{\partial}{\partial r} \mathcal{P} \int dx \frac{J_0 [(p_\sigma - x/v) r]}{x(p_\sigma - x/v)} = \\
&= -\frac{\partial}{\partial r} \mathcal{P} \int dy \frac{J_0 [(p_\sigma - y) r]}{y(p_\sigma - y)} = -\frac{\partial}{\partial(p_\sigma r)} \left[ \mathcal{P} \int dy \frac{J_0 [(p_\sigma - y) r]}{y} + \mathcal{P} \int dy \frac{J_0 [(p_\sigma - y) r]}{p_\sigma - y} \right] = \\
&= -\frac{\partial}{\partial(p_\sigma r)} \frac{2}{\pi} \operatorname{Im} \int_1^{+\infty} \frac{du}{\sqrt{u^2 - 1}} \left[ \mathcal{P} \int \frac{e^{i(p_\sigma - y)ru}}{y} dy + \mathcal{P} \int \frac{e^{i(p_\sigma - y)ru}}{p_\sigma - y} dy \right] = \\
&= -2 \frac{\partial}{\partial(p_\sigma r)} \operatorname{Im} \int_1^{+\infty} \frac{idu}{\sqrt{u^2 - 1}} [1 - e^{ip_\sigma ru}] = -2 \int_1^{+\infty} \frac{u \sin p_\sigma ru}{\sqrt{u^2 - 1}} du = 2 \frac{\partial}{\partial(p_\sigma r)} \int_1^{+\infty} \frac{\cos p_\sigma ru}{\sqrt{u^2 - 1}} du = \\
&= -\pi \frac{\partial}{\partial(p_\sigma r)} Y_0(p_\sigma r) = \pi Y_1(p_\sigma r), \quad p_\sigma \neq 0
\end{aligned}$$

Therefore:

$$\heartsuit = \pi \nu_\sigma [Y_1(p_\sigma r) - iJ_1(p_\sigma r)].$$

Finally:

$$X_0^\sigma(r) = \pi \nu_\sigma [Y_0(p_\sigma r) - iJ_0(p_\sigma r)] \quad (\text{B.7})$$

$$X_1^\sigma(s, \mathbf{r}) = se^{is\phi_r} \left\{ \pi \nu_\sigma [Y_1(p_\sigma r) - iJ_1(p_\sigma r)] \right\} \equiv se^{is\phi_r} \tilde{X}_1^\sigma(r), \quad (\text{B.8})$$

where  $p_\sigma = p_F^\sigma + E/v \neq 0$ . Thus the Green's function for  $\mathbf{r} \neq \mathbf{0}$  can be written as:

$$G_0(E, \mathbf{r}) = \frac{1}{2} \sum_\sigma \begin{pmatrix} X_0^\sigma(r) & -\sigma e^{-i\phi_r} \tilde{X}_1^\sigma(r) \\ \sigma e^{i\phi_r} \tilde{X}_1^\sigma(r) & X_0^\sigma(r) \end{pmatrix} \quad (\text{B.9})$$

Below we compute the T-matrix for different types of impurities. Impurity potentials take the following forms:

$$V_z = J_z \begin{pmatrix} 1 & 0 \\ 0 & -1 \end{pmatrix}, \quad V_x = J_x \begin{pmatrix} 0 & 1 \\ 1 & 0 \end{pmatrix}$$

The corresponding T-matrices read

$$T_z = \begin{pmatrix} \frac{J}{1+i\pi\nu J} & 0 \\ 0 & -\frac{J}{1-i\pi\nu J} \end{pmatrix}, \quad T_x = \frac{J}{1+\pi^2\nu^2 J^2} \begin{pmatrix} -i\pi\nu J & 1 \\ 1 & -i\pi\nu J \end{pmatrix}.$$

For each type of impurity we can compute the SP and non-polarised LDOS using Eqs. (4.7-4.10).

### z-impurity

We denote  $\alpha = \pi\nu J$  and write the asymptotic expansions of the non-polarised and SP LDOS components in coordinate space (for details see Appendix E):

$$\begin{aligned} S_x(\mathbf{r}) &\sim +\frac{J}{1+\alpha^2} \frac{\cos\phi_{\mathbf{r}}}{r} \sum_{\sigma} \sigma \frac{\nu_{\sigma}^2}{p_{\sigma}} \sin 2p_{\sigma}r \\ S_y(\mathbf{r}) &\sim +\frac{J}{1+\alpha^2} \frac{\sin\phi_{\mathbf{r}}}{r} \sum_{\sigma} \sigma \frac{\nu_{\sigma}^2}{p_{\sigma}} \sin 2p_{\sigma}r \\ S_z(r) &\sim -\frac{J}{1+\alpha^2} \frac{2}{r} \sum_{\sigma} \frac{\nu_{\sigma}^2}{p_{\sigma}} \cos 2p_{\sigma}r \\ \rho(r) &\sim -\frac{J}{1+\alpha^2} 4\alpha\nu^2 \frac{v_F^2}{v^2} \frac{1}{\sqrt{p_F^2 + 2mE + E^2/v^2}} \cdot \frac{\sin p_{\varepsilon}r}{r}, \end{aligned}$$

where  $p_{\varepsilon} = 2(mv + E/v)$ , and we get for  $p_{\sigma} > 0$ :

$$\begin{aligned} S_x(\mathbf{p}) &\sim +\frac{J}{1+\alpha^2} \cdot 2\pi i \cos\phi_{\mathbf{p}} \int_0^{+\infty} dr J_1(pr) \sum_{\sigma} \sigma \frac{\nu_{\sigma}^2}{p_{\sigma}} \sin 2p_{\sigma}r \\ S_y(\mathbf{p}) &\sim +\frac{J}{1+\alpha^2} \cdot 2\pi i \sin\phi_{\mathbf{p}} \int_0^{+\infty} dr J_1(pr) \sum_{\sigma} \sigma \frac{\nu_{\sigma}^2}{p_{\sigma}} \sin 2p_{\sigma}r \\ S_z(p) &\sim -\frac{J}{1+\alpha^2} \cdot 4\pi \int_0^{+\infty} dr J_0(pr) \sum_{\sigma} \frac{\nu_{\sigma}^2}{p_{\sigma}} \cos 2p_{\sigma}r \\ \rho(p) &\sim -\frac{J}{1+\alpha^2} \cdot 8\pi\alpha\nu^2 \frac{v_F^2}{v^2} \frac{1}{\sqrt{p_F^2 + 2mE + E^2/v^2}} \int_0^{+\infty} dr J_0(pr) \sin p_{\varepsilon}r \end{aligned}$$

### x-impurity

$$\begin{aligned}
S_x(\mathbf{r}) &\sim -\frac{J}{1+\alpha^2} \frac{1}{r} \left\{ 2\nu^2 \frac{v_F^2}{v^2} \frac{\cos p_\varepsilon r}{\sqrt{p_F^2 + 2mE + E^2/v^2}} + \sum_\sigma \frac{\nu_\sigma^2}{p_\sigma} \cos 2p_\sigma r + \right. \\
&\quad \left. + \cos 2\phi_{\mathbf{r}} \left[ -2\nu^2 \frac{v_F^2}{v^2} \frac{\cos p_\varepsilon r}{\sqrt{p_F^2 + 2mE + E^2/v^2}} + \sum_\sigma \frac{\nu_\sigma^2}{p_\sigma} \cos 2p_\sigma r \right] \right\} \\
S_y(\mathbf{r}) &\sim -\frac{J}{1+\alpha^2} \frac{\sin 2\phi_{\mathbf{r}}}{r} \left[ -2\nu^2 \frac{v_F^2}{v^2} \frac{\cos p_\varepsilon r}{\sqrt{p_F^2 + 2mE + E^2/v^2}} + \sum_\sigma \frac{\nu_\sigma^2}{p_\sigma} \cos 2p_\sigma r \right] \\
S_z(\mathbf{r}) &\sim -\frac{J}{1+\alpha^2} \frac{\cos \phi_{\mathbf{r}}}{r} \sum_\sigma \sigma \frac{\nu_\sigma^2}{p_\sigma} \sin 2p_\sigma r \\
\rho(r) &\sim -\frac{J}{1+\alpha^2} \cdot \frac{\alpha}{r} \cdot 4\nu^2 \frac{v_F^2}{v^2} \frac{\sin p_\varepsilon r}{\sqrt{p_F^2 + 2mE + E^2/v^2}}
\end{aligned}$$

With the corresponding Fourier transforms:

$$\begin{aligned}
S_x(\mathbf{p}) &= S_x^{sym}(p) + S_x^{asym}(\mathbf{p}) \sim \\
&\sim -\frac{J}{1+\alpha^2} \cdot 2\pi \int_0^{+\infty} dr J_0(pr) \left[ 2\nu^2 \frac{v_F^2}{v^2} \frac{\cos p_\varepsilon r}{\sqrt{p_F^2 + 2mE + E^2/v^2}} + \sum_\sigma \frac{\nu_\sigma^2}{p_\sigma} \cos 2p_\sigma r \right] - \\
&\quad -\frac{J}{1+\alpha^2} \cdot 2\pi \cos 2\phi_{\mathbf{p}} \int_0^{+\infty} dr J_2(pr) \left[ 2\nu^2 \frac{v_F^2}{v^2} \frac{\cos p_\varepsilon r}{\sqrt{p_F^2 + 2mE + E^2/v^2}} - \sum_\sigma \frac{\nu_\sigma^2}{p_\sigma} \cos 2p_\sigma r \right] \\
S_y(\mathbf{p}) &\sim -\frac{J}{1+\alpha^2} \cdot 2\pi \sin 2\phi_{\mathbf{p}} \int_0^{+\infty} dr J_2(pr) \left[ 2\nu^2 \frac{v_F^2}{v^2} \frac{\cos p_\varepsilon r}{\sqrt{p_F^2 + 2mE + E^2/v^2}} - \sum_\sigma \frac{\nu_\sigma^2}{p_\sigma} \cos 2p_\sigma r \right] \\
S_z(\mathbf{p}) &\sim -\frac{J}{1+\alpha^2} \cdot 2\pi i \cos \phi_{\mathbf{p}} \int_0^{+\infty} dr J_1(pr) \sum_\sigma \sigma \frac{\nu_\sigma^2}{p_\sigma} \sin 2p_\sigma r \\
\rho(p) &\sim -\frac{J}{1+\alpha^2} \cdot 8\pi\alpha\nu^2 \frac{v_F^2}{v^2} \frac{1}{\sqrt{p_F^2 + 2mE + E^2/v^2}} \int_0^{+\infty} dr J_0(pr) \sin p_\varepsilon r
\end{aligned}$$

As a final remark of this section we point out that while finalising this work we became aware of a recent work [179] focusing on the real space Friedel oscillations in the metallic regime.

## 1D metallic system

The low-energy Hamiltonian in the non-SC regime can be written as

$$H_0 = \xi_p \sigma_0 + \lambda(p_y \sigma_x - p_x \sigma_y) = \begin{pmatrix} \xi_p & i\lambda p \\ -i\lambda p & \xi_p \end{pmatrix} \quad (\text{B.10})$$

where  $\xi_p = \frac{p^2}{2m} - \varepsilon_F$ . The corresponding spectrum is given by  $\mathcal{E} = \xi_p \pm \lambda p$  and the retarded Green's function reads

$$G_0(E, \mathbf{p}) = \frac{1}{(E - \xi_p + i0)^2 - \lambda^2 p^2} \begin{pmatrix} E - \xi_p + i0 & i\lambda p \\ -i\lambda p & E - \xi_p + i0 \end{pmatrix}. \quad (\text{B.11})$$

To compute the eigenvalues for a single localised impurity we calculate

$$G_0(E, x=0) = \int \frac{dp}{2\pi} \frac{E - \xi_p + i0}{(E - \xi_p + i0)^2 - \lambda^2 p^2} \begin{pmatrix} 1 & 0 \\ 0 & 1 \end{pmatrix} = \frac{1}{2} \sum_{\sigma} \int \frac{dp}{2\pi} \frac{1}{E - \xi_{\sigma} + i0} \begin{pmatrix} 1 & 0 \\ 0 & 1 \end{pmatrix}, \quad (\text{B.12})$$

where  $\xi_{\sigma} = \xi_p + \sigma \lambda p$ . For  $p > 0$  we linearise the spectrum around the Fermi momenta, thus:

$$\xi_{\sigma} \approx \left( \frac{p_F^{\sigma}}{m} + \sigma \lambda \right) (p - p_F^{\sigma}) = \sqrt{\lambda^2 + 2\varepsilon_F/m} (p - p_F^{\sigma}) \equiv v(p - p_F^{\sigma}),$$

where  $p_F^{\sigma} = m[-\sigma \lambda + v]$ , and thus we get:

$$\int \frac{dp}{2\pi} \frac{1}{E - \xi_{\sigma} + i0} \approx \frac{1}{2\pi v} \left[ \int \frac{d\xi_{\sigma}}{E - \xi_{\sigma} + i0} + \int \frac{d\xi_{-\sigma}}{E - \xi_{-\sigma} + i0} \right] = -\frac{i}{v}$$

This leads to:

$$G_0(E, x=0) = \frac{1}{2} \sum_{\sigma} \begin{pmatrix} -i \\ v \end{pmatrix} \begin{pmatrix} 1 & 0 \\ 0 & 1 \end{pmatrix} = -\frac{i}{v} \begin{pmatrix} 1 & 0 \\ 0 & 1 \end{pmatrix} \quad (\text{B.13})$$

Since there is no energy dependence, there will be no impurity-induced states. The Green's function coordinate dependence is given by the following expression:

$$G_0(E, x) = \frac{1}{2} \sum_{\sigma} \int \frac{dp}{2\pi} \frac{e^{ipx}}{E - \xi_{\sigma} + i0} \begin{pmatrix} 1 & i\sigma \\ -i\sigma & 1 \end{pmatrix} \quad (\text{B.14})$$

To find the coordinate dependence of the Green's function we calculate:

$$X_0^{\sigma}(x) = \int \frac{dp}{2\pi} \frac{e^{ipx}}{E - \xi_{\sigma} + i0} \quad (\text{B.15})$$

To compute this integral below we employ the Sokhotsky formula  $\frac{1}{x+i0} = \mathcal{P}\frac{1}{x} - i\pi\delta(x)$ :

$$X_0^{\sigma}(x) = \int \frac{dp}{2\pi} \frac{e^{ipx}}{E - \xi_{\sigma} + i0} = \frac{1}{2\pi v} \left[ e^{ip_F^{\sigma}x} \int d\xi_{\sigma} \frac{e^{i\xi_{\sigma}x/v}}{E - \xi_{\sigma} + i0} + e^{-ip_F^{-\sigma}x} \int d\xi_{-\sigma} \frac{e^{-i\xi_{-\sigma}x/v}}{E - \xi_{-\sigma} + i0} \right]$$

We compute explicitly only one of the integrals in the brackets since the other one can be computed the same way:

$$\int d\xi_{\sigma} \frac{e^{i\xi_{\sigma}x/v}}{E - \xi_{\sigma} + i0} = \mathcal{P} \int d\xi_{\sigma} \frac{e^{i\xi_{\sigma}x/v}}{E - \xi_{\sigma}} - i\pi \int d\xi_{\sigma} \delta(E - \xi_{\sigma}) e^{i\xi_{\sigma}x/v} = -i\pi (1 + \text{sgn } x) e^{iEx/v}$$

Finally we have:

$$X_0^{\sigma}(x) = -\frac{i}{v} \exp \left[ i \left( mv + \frac{E}{v} \right) |x| \right] e^{-i\sigma m \lambda x}, \quad (\text{B.16})$$

and the Green's function can be written as:

$$G_0(E, x) = \frac{1}{2} \sum_{\sigma} \begin{pmatrix} 1 & i\sigma \\ -i\sigma & 1 \end{pmatrix} X_0^{\sigma}(x). \quad (\text{B.17})$$

Below we compute the T-matrix for different types of impurities. Impurity potentials take the following forms:

$$V_z = J \begin{pmatrix} 1 & 0 \\ 0 & -1 \end{pmatrix}, \quad V_x = J \begin{pmatrix} 0 & 1 \\ 1 & 0 \end{pmatrix}, \quad V_y = J \begin{pmatrix} 0 & -i \\ i & 0 \end{pmatrix}.$$

The corresponding T-matrices are computed using

$$T_z = \begin{pmatrix} \frac{J}{1+iJ/v} & 0 \\ 0 & -\frac{J}{1-iJ/v} \end{pmatrix}, T_x = \frac{J}{1+J^2/v^2} \begin{pmatrix} -iJ/v & 1 \\ 1 & -iJ/v \end{pmatrix}, T_y = \frac{J}{1+J^2/v^2} \begin{pmatrix} -iJ/v & -i \\ i & -iJ/v \end{pmatrix}.$$

For each type of impurity we can compute the non-polarised and SP LDOS using Eqs. (4.7-4.10) where we replace  $\mathbf{r}$  by  $x$ . By taking the Fourier transforms of the expressions above we get the momentum space dependence. Below we denote  $\alpha = J/v$ .

### **z-impurity**

$$\begin{aligned} S_x(x) &= +\frac{\alpha}{1+\alpha^2} \cdot \frac{1}{\pi v} [\cos(p_\varepsilon|x| - p_\lambda x) - \cos(p_\varepsilon|x| + p_\lambda x)] \\ S_y(x) &= 0 \\ S_z(x) &= +\frac{\alpha}{1+\alpha^2} \cdot \frac{1}{\pi v} [\sin(p_\varepsilon|x| - p_\lambda x) + \sin(p_\varepsilon|x| + p_\lambda x)] \\ \rho(x) &= -\frac{2\alpha^2}{1+\alpha^2} \cdot \frac{1}{\pi v} \cos p_\varepsilon x \end{aligned}$$

where we denote  $p_\varepsilon = 2(mv + E/v)$ ,  $p_\lambda = 2m\lambda$ . After taking the Fourier transform we get:

$$\begin{aligned} S_x(p) &= +\frac{\alpha}{1+\alpha^2} \cdot \frac{i}{\pi v} \left[ \frac{1}{p+p_\varepsilon+p_\lambda} - \frac{1}{p+p_\varepsilon-p_\lambda} - \frac{1}{p-p_\varepsilon+p_\lambda} + \frac{1}{p-p_\varepsilon-p_\lambda} \right] \\ S_y(p) &= 0 \\ S_z(p) &= +\frac{\alpha}{1+\alpha^2} \cdot \frac{1}{\pi v} \left[ \frac{1}{p+p_\varepsilon+p_\lambda} + \frac{1}{p+p_\varepsilon-p_\lambda} - \frac{1}{p-p_\varepsilon+p_\lambda} - \frac{1}{p-p_\varepsilon-p_\lambda} \right] \\ \rho(p) &= -\frac{2\alpha^2}{1+\alpha^2} \cdot \frac{1}{v} [\delta(p-p_\varepsilon) + \delta(p+p_\varepsilon)] \end{aligned}$$

**x-impurity**

$$\begin{aligned}
S_x(x) &= +\frac{\alpha}{1+\alpha^2} \cdot \frac{1}{\pi v} [\sin(p_\varepsilon|x| - p_\lambda x) + \sin(p_\varepsilon|x| + p_\lambda x)] \\
S_y(x) &= 0 \\
S_z(x) &= -\frac{\alpha}{1+\alpha^2} \cdot \frac{1}{\pi v} [\cos(p_\varepsilon|x| - p_\lambda x) - \cos(p_\varepsilon|x| + p_\lambda x)] \\
\rho(x) &= -\frac{2\alpha^2}{1+\alpha^2} \cdot \frac{1}{\pi v} \cos p_\varepsilon x
\end{aligned}$$

We do not give the Fourier transform for these expressions since they coincide with the ones for a  $z$ -impurity if we exchange  $S_z$  and  $S_x$  and change the overall sign.

**y-impurity**

$$\begin{aligned}
S_x(x) &= S_z(x) = 0 \\
S_y(x) &= +\frac{2\alpha}{1+\alpha^2} \cdot \frac{1}{\pi v} \sin p_\varepsilon|x| \\
\rho(x) &= -\frac{2\alpha^2}{1+\alpha^2} \cdot \frac{1}{\pi v} \cos p_\varepsilon x
\end{aligned}$$

The corresponding Fourier transform is:

$$S_y(p) = \frac{2\alpha}{1+\alpha^2} \cdot \frac{1}{\pi v} \left[ \frac{1}{p+p_\varepsilon} - \frac{1}{p-p_\varepsilon} \right]$$

# Appendix C

## Engineering with scalar impurities in a p-wave SC

### C.1 Spinless p-wave case

The Bogoliubov-de Gennes Hamiltonian can be separated into a bulk and an impurity term,  $\mathcal{H} = \mathcal{H}^{(\text{bulk})} + \mathcal{H}^{(\text{imp})}$ , where the bulk Hamiltonian,

$$\mathcal{H}_{\mathbf{p}}^{(\text{bulk})} = \xi_{\mathbf{p}}\tau_z + \kappa(p_x\tau_x - p_y\tau_y),$$

in the Nambu basis  $(\psi_{\mathbf{p}}, \psi_{-\mathbf{p}}^\dagger)^\text{T}$ . Here  $\xi_{\mathbf{p}} = \frac{\mathbf{p}^2}{2m} - \epsilon_F$  with the Fermi energy  $\epsilon_F$ , and  $\kappa$  is the superconducting  $p$ -wave pairing amplitude. The Pauli matrices  $\tau_i$  operate in the particle-hole space. The impurity Hamiltonian,

$$\mathcal{H}^{(\text{imp})}(\mathbf{r}) = U\tau_z \sum_n \delta(\mathbf{r} - \mathbf{r}_n)$$

describes an scalar impurity of strength  $U$  located at position  $\mathbf{r}_j$ .

The BdG equation  $\mathcal{H}(\mathbf{r})\Psi(\mathbf{r}) = E\Psi(\mathbf{r})$  yields

$$[E - \mathcal{H}^{(\text{bulk})}(\mathbf{r})]\Psi(\mathbf{r}) = U\tau_z \sum_n \delta(\mathbf{r} - \mathbf{r}_n)\Psi(\mathbf{r}).$$

We change to momentum space using the Fourier transform  $\Psi(\mathbf{r}) = \int \frac{d\mathbf{p}}{(2\pi)^2} e^{i\mathbf{p}\cdot\mathbf{r}} \Psi_{\mathbf{p}}$  and thus obtain

$$[E - \mathcal{H}_{\mathbf{p}}^{(\text{bulk})}] \Psi_{\mathbf{p}} = U \tau_z \sum_j e^{-i\mathbf{p}\cdot\mathbf{r}_j} \Psi(\mathbf{r}_j).$$

Solving for  $\Psi_{\mathbf{p}}$  and going back to real space, we thus find

$$\Psi(\mathbf{r}) = U \sum_j G_0(E, \mathbf{r} - \mathbf{r}_j) \tau_z \Psi(\mathbf{r}_j), \quad (\text{C.1})$$

where  $G_0(E, \mathbf{r}) = \int \frac{d\mathbf{p}}{(2\pi)^2} e^{i\mathbf{p}\cdot\mathbf{r}} [E - \mathcal{H}_{\mathbf{p}}^{(\text{bulk})}]^{-1}$  is the bulk Green function.

## C.2 Single scalar impurity bound states

Let us first consider a single impurity at the origin. We can set  $\mathbf{r} = \mathbf{0}$  in Eq. (C.1) and obtain the following eigenvalue equation for the impurity energies:

$$[\mathbb{I} - U G_0(E, \mathbf{0}) \tau_z] \Psi(\mathbf{0}) = 0.$$

As we are considering only subgap energies, we can evaluate  $G_0(E, \mathbf{0})$  assuming  $|E| < \Delta_t$ , yielding  $G_0(E, \mathbf{0}) = -\frac{\pi\nu}{\sqrt{1+\tilde{\kappa}^2}} \frac{\Delta_t}{\sqrt{\Delta_t^2 - E^2}} [E\mathbb{I} - \gamma\tau_z]$ . Here we have defined quantities  $\gamma = \frac{\tilde{\kappa}}{\sqrt{1+\tilde{\kappa}^2}}$ ,  $\tilde{\kappa} = \frac{\kappa}{v_F}$  and  $\Delta_t = \frac{\kappa k_F}{\sqrt{1+\tilde{\kappa}^2}}$  where  $v_F$  is the Fermi velocity and  $\nu$  the density of states in the bulk. Inserting this result into the single-impurity eigenvalue equation yields

$$\left[ \mathbb{I} + \frac{\beta}{\sqrt{\Delta_t^2 - E^2}} (E\tau_z - \gamma\Delta_t\mathbb{I}) \right] \Psi(\mathbf{0}) = 0, \quad (\text{C.2})$$

where  $\beta = \pi\nu U$  is the dimensionless impurity strength determining the bound state energy. Eq. (C.2) has two solutions for both repulsive  $\beta > 0$  and attractive  $\beta < 0$  impurities. For  $\beta > 0$  the solutions have energies  $E = \epsilon_{\pm} = \pm \frac{\gamma\beta^2 - \sqrt{1+\beta^2(1-\gamma^2)}}{1+\beta^2} \Delta_t$  with eigenstates  $\Psi_+(\mathbf{0}) = (1, 0)^T$  and  $\Psi_-(\mathbf{0}) = (0, 1)^T$ . For  $\beta < 0$  the energies are  $E = \epsilon'_{\pm} = \pm \frac{\gamma\beta^2 + \sqrt{1-\beta^2(1-\gamma^2)}}{1+\beta^2} \Delta_t$ .

### C.3 Lattice of scalar impurities

In case of multiple impurities at positions  $\mathbf{r}_i$ , Eq. (C.1) becomes

$$[\mathbb{I} - UG_0(E, \mathbf{0}) \tau_z] \Psi(\mathbf{r}_i) = U \sum_{j \neq i} G_0(E, \mathbf{r}_i - \mathbf{r}_j) \tau_z \Psi(\mathbf{r}_j). \quad (\text{C.3})$$

To proceed, we need to evaluate  $G_0(E, \mathbf{r})$  for  $|\mathbf{r}| > 0$ . Employing methods outlined in Ref. [85] we obtain

$$G_0(E, \mathbf{r}) = \begin{pmatrix} EX_0(\mathbf{r}) + X_1(\mathbf{r}) & iX_2^+(\mathbf{r}) \\ -iX_2^-(\mathbf{r}) & EX_0(\mathbf{r}) - X_1(\mathbf{r}) \end{pmatrix},$$

where

$$\begin{aligned} X_0(\mathbf{r}) &= - \int \frac{d\mathbf{p}}{(2\pi)^2} \frac{e^{i\mathbf{p}\cdot\mathbf{r}}}{\xi_p^2 + \kappa^2 \mathbf{p}^2 - E^2} = - \frac{2\nu}{\Delta_t \sqrt{1 - (E/\Delta_t)^2}} \text{Im} \left\{ K_0[-i(1 + i\tilde{\kappa})k_F r] \right\}, \\ X_1(\mathbf{r}) &= - \int \frac{d\mathbf{p}}{(2\pi)^2} \frac{\xi_p e^{i\mathbf{p}\cdot\mathbf{r}}}{\xi_p^2 + \kappa^2 \mathbf{p}^2 - E^2} = -2\nu \text{Im} \left\{ \left(1 + i \frac{\tilde{\kappa}}{\sqrt{1 - (E/\Delta_t)^2}}\right) K_0[-i(1 + i\tilde{\kappa})k_F r] \right\}, \\ X_2^\pm(\mathbf{r}) &= \pm \int \frac{d\mathbf{p}}{(2\pi)^2} \frac{i\kappa p_\pm e^{i\mathbf{p}\cdot\mathbf{r}}}{\xi_p^2 + \kappa^2 \mathbf{p}^2 - E^2} \\ &= - \frac{2\nu}{\sqrt{1 - (E/\Delta_t)^2}} \frac{x \pm iy}{r} \text{Re} \left\{ \left(1 + i\tilde{\kappa} \sqrt{1 - (E/\Delta_t)^2}\right) K_1[-i(1 + i\tilde{\kappa})k_F r] \right\}. \end{aligned}$$

In the above expressions the functions  $K_i(x)$  stand for modified Bessel functions of the second kind. These expressions have been obtained by linearising the bulk dispersion and are valid to the order  $\mathcal{O}(\tilde{\kappa}^2)$ . For large arguments the functions satisfy  $X_{0/1}(\mathbf{r}), X_2^\pm(\mathbf{r}) \sim \frac{e^{ik_F r}}{\sqrt{k_F r}} e^{-r/\xi_E}$  which means that hybridisation of adjacent impurity states at mid-gap energies decay slowly for short distances and exponentially at distances longer than the coherence length  $\xi_E^{-1} = \Delta_t \sqrt{1 - (E/\Delta_t)^2} / v_F$ . The spatial structure of the bound state wave functions imply that energy scale controlling the hybridisation between two impurity states at distance  $a$  apart is  $\Delta_t / \sqrt{k_F a}$ .

For each impurity site  $\mathbf{r}_i$ , the relation in Eq. (C.3) is satisfied. Therefore, for  $N$  impurities, these equations form a closed set of equations for  $2N$  subgap eigenvalues  $E$  and eigenvectors  $\Psi(\mathbf{r}_i) = \begin{pmatrix} u(\mathbf{r}_i) & v(\mathbf{r}_i) \end{pmatrix}^T$  at the impurity sites. Instead of seeking an exact solution for the full range of parameters, we consider the eigenvalue equation for deep-lying eigenstates  $|E| \ll \Delta_t$ . As discussed below, this approach will reproduce the exact topological phase diagram since the gap-closing transitions take place at  $E = 0$ . In addition, we obtain the spectrum of the system

in the deep-dilute impurity regime  $\beta \gg 1$ ,  $\sqrt{k_F a} \gg 1$  where the spectrum is confined to the mid gap region. Following Ref. [35], we can linearise the LHS of Eq. (C.3) with respect to  $E$  and evaluate the coupling term on the RHS for  $E = 0$ :

$$\left[ \mathbb{I} + \beta \left( \frac{E}{\Delta_t} \tau_z - \gamma \mathbb{I} \right) \right] \Psi(\mathbf{r}_i) = U \sum_{j \neq i} \lim_{E \rightarrow 0} G_0(E, \mathbf{r}_i - \mathbf{r}_j) \tau_z \Psi(\mathbf{r}_j). \quad (\text{C.4})$$

Multiplying both sides by  $\tau_z \beta^{-1} \Delta_t$  leads to

$$\begin{pmatrix} \Delta_t(\beta^{-1} - \gamma) + E & 0 \\ 0 & -\Delta_t(\beta^{-1} - \gamma) + E \end{pmatrix} \Psi(\mathbf{r}_i) = \frac{\Delta_t}{\pi\nu} \sum_{j \neq i} \lim_{E \rightarrow 0} \begin{pmatrix} X_1(\mathbf{r}_{ij}) & -iX_2^+(\mathbf{r}_{ij}) \\ iX_2^-(\mathbf{r}_{ij}) & -X_1(\mathbf{r}_{ij}) \end{pmatrix} \Psi(\mathbf{r}_j).$$

This equation can be written compactly as  $\sum_j H_{ij} \Psi_j = E \Psi_i$ , where  $\Psi_i \equiv \Psi(\mathbf{r}_i)$  and

$$H_{mn} = \begin{pmatrix} h_{mn} & \Delta_{mn} \\ (\Delta_{mn})^\dagger & -h_{mn}^* \end{pmatrix},$$

with

$$h_{mn} = \begin{cases} \Delta_t(\gamma - \beta^{-1}) & m = n \\ \frac{\Delta_t}{\pi\nu} X_1(\mathbf{r}_{mn})|_{E=0} & m \neq n \end{cases} \quad \Delta_{mn} = \begin{cases} 0 & m = n \\ -i \frac{\Delta_t}{\pi\nu} X_2^+(\mathbf{r}_{mn})|_{E=0} & m \neq n. \end{cases} \quad (\text{C.5})$$

This is equivalent to Eq. (7.2) in the main text.

## C.4 H as a topological Hamiltonian

The effective Hamiltonian (C.5) is obtained through the steps outlined in Pientka *et al.* in the pioneering work [35]. For deep impurities  $\beta \gg 1$  that are weakly coupled  $\sqrt{k_F a} \gg 1$  the bands are lying near the gap centre and the spectrum can be calculated by this approach. However, in the present case the effective Hamiltonian (C.5) has more general utility beyond the low-energy theory. The expression (C.5) can be regarded as a topological Hamiltonian, providing access to the exact phase diagram of the full model (C.3) beyond the deep-dilute impurity limit.

The role of the expression (C.5) as topological Hamiltonian can be understood by the following arguments. The  $E = 0$  eigenstates of the exact problem (C.3) and effective problem  $H\Psi = E\Psi$

coincide *exactly*. This simply follows from the fact that the only approximation in the derivation of (C.5) from Eq. (C.3) involves setting a number of energy arguments to zero, a difference that does not affect the  $E = 0$  solutions in any way. Since the topological phase transitions take place precisely when  $E = 0$  solutions exist, indicating the closing of the energy gap, the phase boundaries of the effective model and the full model necessarily coincide. In addition, in the vicinity of the phase boundaries the energy gap is small and the low-lying solutions of Eq. (C.3) differ very little from the effective model and can be adiabatically deformed to each other effectively. Therefore the Chern numbers calculated from the effective model (C.5) match the Chern numbers of the full model, even in the regime where deep-dilute approximation is not applicable.

Obtaining reliable energy eigenvalues is a different matter- those can be calculated from the model (C.5) only for small energies  $E/\Delta_t \ll 1$  and with the accuracy that depends on the validity of the deep-dilute assumption. The corrections to the spectrum obtained from the effective Hamiltonian will be of the order of  $\mathcal{O}(\frac{\beta^{-1}}{\sqrt{k_F a}})$  which is second order in the small parameters in the deep-dilute regime.

## C.5 Including spin

Here we discuss how our results of topological state engineering apply to the spinful chiral  $p$ -wave state with the  $d$ -vector of the triplet parametrisation perpendicular to the plane. This has been the main candidate to describe superconductivity in strontium ruthenate. In addition to the Nambu matrices we introduce another set of Pauli matrices  $\sigma_i$  and define  $\sigma_0 = \mathbb{I}_{2 \times 2}$ . In absence of scalar impurities, the bulk is described by the  $4 \times 4$  Hamiltonian

$$\mathcal{H}_{\mathbf{p}}^{(\text{bulk})} = \xi_{\mathbf{p}} \tau_z \otimes \sigma_0 + \varkappa (p_x \tau_x - p_y \tau_y) \otimes \sigma_z,$$

which is expressed in the basis  $(\hat{\Psi}_{p\uparrow}, \hat{\Psi}_{p\downarrow}, \hat{\Psi}_{-p\downarrow}^\dagger, -\hat{\Psi}_{-p\uparrow}^\dagger)^\text{T}$ . This state describes pairing of opposite spins in the orbital  $L_z = 1$  channel. The scalar impurity term  $\mathcal{H}^{(\text{imp})}(\mathbf{r}) = U \tau_z \otimes \sigma_0 \sum_n \delta(\mathbf{r} - \mathbf{r}_n)$  also has a diagonal spin structure. Thus by defining two spinors  $\Psi_1 = (\hat{\Psi}_{p\uparrow}, \hat{\Psi}_{-p\downarrow}^\dagger)^\text{T}$ ,  $\Psi_2 = (\hat{\Psi}_{p\downarrow}, \hat{\Psi}_{-p\uparrow}^\dagger)^\text{T}$ , the full  $4 \times 4$  BdG Hamiltonian can be transformed to two decoupled  $2 \times 2$  blocks identical to the spinless model studied above. The impurity problem and topology can be

studied separately for the blocks exactly as for spinless fermions.

## C.6 Effect of a non-localised potential

Below we introduce a non-localised scalar potential to study the effect of other scattering channels than the s one. We make use of the formalism introduced in Ref. [83].

We consider a non-localised single scalar impurity described by  $\mathcal{H}_{imp} = U(\mathbf{r}) \cdot \tau_z$ . For that we decompose in momentum space  $U(\mathbf{p}) = \sum_l U_l(p) e^{il\theta}$ . The unperturbed Green's function in momentum space reads:

$$G(E, \mathbf{p}) = -\frac{1}{\xi_p^2 + \varkappa^2 p^2 - E^2} \begin{pmatrix} E + \xi_p & i\varkappa p_+ \\ -i\varkappa p_- & E - \xi_p \end{pmatrix},$$

Note that we omit the "0" index for the Green's function to stay consistent with Ref. [83]. Rewriting the function above using the harmonic decomposition  $G(E, \mathbf{p}) = \sum_n G_n(E, p) e^{in\theta}$ , where  $p = |\mathbf{p}|$  we get:

$$\begin{aligned} G_0(E, p) &= -\frac{1}{\xi_p^2 + \varkappa^2 p^2 - E^2} \begin{pmatrix} E + \xi_p & 0 \\ 0 & E - \xi_p \end{pmatrix}, \\ G_{-1}(E, p) &= -\frac{1}{\xi_p^2 + \varkappa^2 p^2 - E^2} \begin{pmatrix} 0 & 0 \\ -i\varkappa p & 0 \end{pmatrix}, \\ G_1(E, p) &= -\frac{1}{\xi_p^2 + \varkappa^2 p^2 - E^2} \begin{pmatrix} 0 & i\varkappa p \\ 0 & 0 \end{pmatrix}. \end{aligned}$$

All the higher harmonics corresponding to  $|n| > 1$  are absent in the bare Green's function. For further calculations we need to compute the averaged values of these functions over momenta,

namely  $\overline{G_n(E)} = \int_0^{+\infty} \frac{pdp}{2\pi} G_n(E, p)$ :

$$\begin{aligned}\overline{G_0(E)} &= \begin{pmatrix} EX_0 + X_1 & 0 \\ 0 & EX_0 - X_1 \end{pmatrix}, \\ \overline{G_{-1}(E)} &= \begin{pmatrix} 0 & 0 \\ -i(\kappa p_F X_0 + \tilde{\kappa} X_1) & 0 \end{pmatrix}, \\ \overline{G_1(E)} &= \begin{pmatrix} 0 & i(\kappa p_F X_0 + \tilde{\kappa} X_1) \\ 0 & 0 \end{pmatrix},\end{aligned}$$

with

$$X_0 = -\frac{\pi\nu}{\sqrt{1 + \tilde{\kappa}^2}} \frac{1}{\sqrt{\Delta_t^2 - E^2}}, \quad X_1 = \frac{\pi\nu}{\sqrt{1 + \tilde{\kappa}^2}} \frac{\gamma \Delta_t}{\sqrt{\Delta_t^2 - E^2}}, \quad \gamma = \frac{\tilde{\kappa}}{\sqrt{1 + \tilde{\kappa}^2}}, \quad \Delta_t = \frac{\kappa p_F}{\sqrt{1 + \tilde{\kappa}^2}},$$

which have been calculated explicitly in Ref. [85]. For a bound state solution to exist, the following condition must be satisfied (Eq. (S25) from Ref. [83]):

$$\det \begin{pmatrix} \overline{G_0(E)} U_{-1} \tau_z - \tau_0 & \overline{G_{-1}(E)} U_0 \tau_z & 0 \\ \overline{G_1(E)} U_{-1} \tau_z & \overline{G_0(E)} U_0 \tau_z - \tau_0 & \overline{G_{-1}(E)} U_1 \tau_z \\ 0 & \overline{G_1(E)} U_0 \tau_z & \overline{G_0(E)} U_1 \tau_z - \tau_0 \end{pmatrix} = 0.$$

The equation above yields the energy levels. We next consider only the harmonics  $l = \pm 1$  and  $l = 0$  for the scattering potential. This is enough for our purpose to demonstrate that they lead to Shiba states with energy near the gap edges. Note that the symmetry of the problem requires  $U_{-1} = U_1$ , and thus we get

$$\frac{\beta_1(\epsilon - \gamma)}{\sqrt{1 - \epsilon^2}} = -1, \quad \frac{(\beta_0 - \beta_1)\epsilon - \gamma(\beta_0 + \beta_1)}{\sqrt{1 - \epsilon^2}} = -(1 + \beta_0\beta_1)$$

where we denote  $\beta_{0,1} \equiv \frac{\pi\nu U_{0,1}}{\sqrt{1 + \tilde{\kappa}^2}}$ ,  $\epsilon \equiv \frac{E}{\Delta_t}$ . Note that each of these equations is giving a positive-energy solution, which always has a particle-hole symmetric negative-energy partner as required by particle-hole symmetry. We solve these equations considering  $\beta_0 > \beta_1$ . This is a valid approximation since we expect the scatterings in the other channels than s to be weaker.

Therefore, we obtain:

$$E_1^\pm = \pm \frac{\gamma\beta_1^2 - \sqrt{1 + \beta_1^2(1 - \gamma^2)}}{1 + \beta_1^2} \Delta_t,$$

$$E_2^\pm = \pm \frac{\gamma(\beta_0^2 - \beta_1^2) - (1 + \beta_0\beta_1)\sqrt{1 + \beta_0^2 + \beta_1^2 + \beta_0^2\beta_1^2 - \gamma^2(\beta_0 + \beta_1)^2}}{1 + \beta_0^2 + \beta_1^2 + \beta_0^2\beta_1^2} \Delta_t.$$

For  $\beta_1 \rightarrow 0$  we expect these solutions to coincide with the ones we had before for a delta-like potential (in other words, when we take into account only the  $s$ -scattering channel). Indeed,

$$\lim_{\beta_1 \rightarrow 0} E_1^\pm = \lim_{\beta_1 \rightarrow 0} \left[ \mp \frac{\gamma\beta_1^2 - \sqrt{1 + \beta_1^2(1 - \gamma^2)}}{1 + \beta_1^2} \Delta_t \right] = \pm \Delta_t,$$

and therefore two subgap states merge with the quasiparticle continuum. The other two

$$\begin{aligned} \lim_{\beta_1 \rightarrow 0} E_2^\pm &= \lim_{\beta_1 \rightarrow 0} \left[ \mp \frac{\gamma(\beta_0^2 - \beta_1^2) - (1 + \beta_0\beta_1)\sqrt{1 + \beta_0^2 + \beta_1^2 + \beta_0^2\beta_1^2 - \gamma^2(\beta_0 + \beta_1)^2}}{1 + \beta_0^2 + \beta_1^2 + \beta_0^2\beta_1^2} \Delta_t \right] = \\ &= \mp \frac{\gamma\beta_0^2 - \sqrt{1 + \beta_0^2(1 - \gamma^2)}}{1 + \beta_0^2} \Delta_t \end{aligned}$$

coincide with the ones we obtained previously for a fully localised impurity.

The calculations above show that the states appearing due to other scattering channels are situated very close to the superconducting gap and, therefore, can be disregarded. Therefore in the  $s$ -dominated scattering channel, we can prove that the low-energy Shiba states (which are the ones we keep as a low-energy basis) come from the delta-like potential approximation.

## C.7 Spectrum of an infinite strip

Here we illustrate topological properties of a system with finite width but infinite length. As depicted in Fig. C.1, the chiral edge states are localised near the sample edge. We assume a square lattice geometry with lattice constant  $a$  and Fourier transform the Hamiltonian in  $x$  direction. In Fig. C.2 we have plotted four sample spectra as a function of momentum  $k_x$  corresponding to different Chern numbers. The edge state manifest as states traversing the bulk gap. Both edges support  $|C|$  chiral edge states. Since the edge states plotted in Fig. C.2 have monotonic dispersions, each horizontal line in the bulk gap crosses  $|C|$  states with positive

slope and negative slope in the full Brillouin zone. These states are localised at the opposite edges.

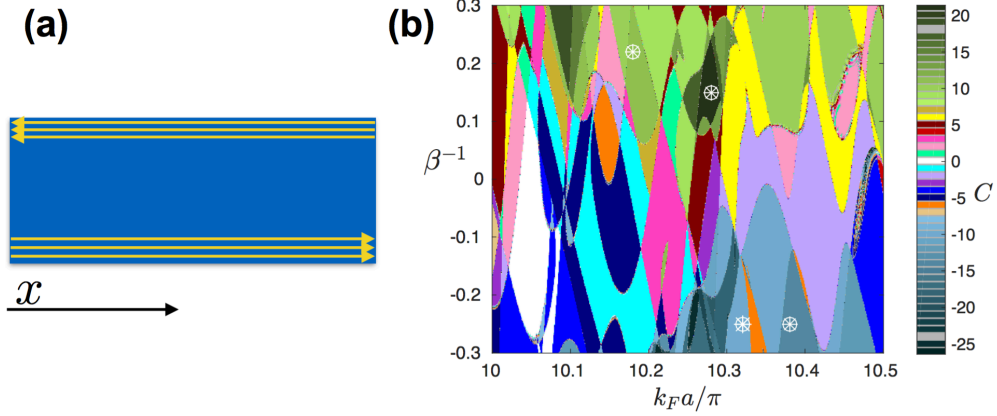


Figure C.1: (a): In the strip geometry the boundaries support chiral edge modes that propagate in the opposite directions. (b): The phase diagram of the infinite square lattice with a lattice constant  $a$  and coherence length  $\xi/a = 5$ . The four points mark the parameter values employed in the Fig. C.2.

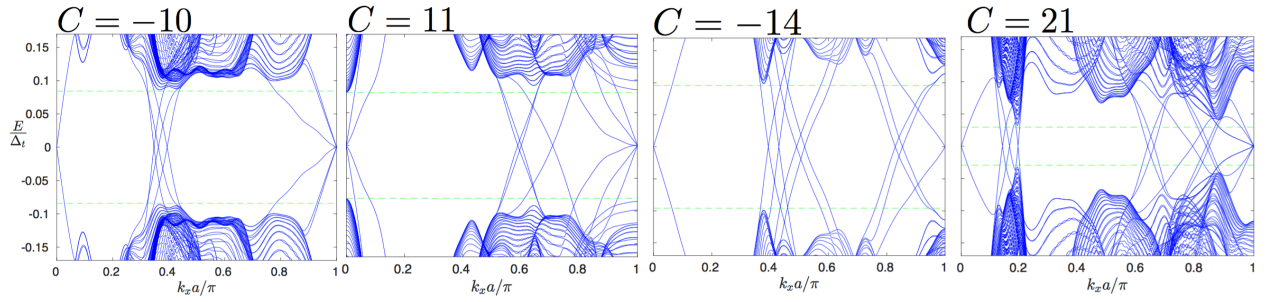


Figure C.2: Spectrum of a strip as a function of momentum in the translation invariant direction in the positive half of the Brillouin zone. The spectra are reflection symmetric  $k_x \rightarrow -k_x$  in the negative half. The different figures correspond to parameters indicated in the Fig. C.1. The horizontal dashed line indicate the position of the bulk gap edge.

# Appendix D

## Dynamical Shiba chain

### D.1 Derivation of the effective two-band model

In this section we show how to derive the effective two-band Hamiltonian given by Eq. (8.7) from the main text. We start by writing the Bogoliubov-de Gennes Hamiltonian for a 2D s-wave superconductor in the Nambu basis  $\Psi_{\mathbf{p}} = (\psi_{\uparrow\mathbf{p}}, \psi_{\downarrow\mathbf{p}}, \psi_{\downarrow-\mathbf{p}}^\dagger, -\psi_{\uparrow-\mathbf{p}}^\dagger)^\top$

$$H_0 = \xi_k \tau_z + \Delta_s \tau_x,$$

with  $\boldsymbol{\tau} = (\tau_x, \tau_y, \tau_z)$  matrices acting in particle-hole subspace. The superconducting order parameter is denoted by  $\Delta_s$ , the spectrum of free electrons is defined as  $\xi_k \equiv \frac{k^2}{2m} - \varepsilon_F$ , where  $\varepsilon_F$  is the Fermi energy. A chain of magnetic impurities with precessing spins deposited on top of the superconductor is given by

$$H_{imp}(t) = \sum_j \mathbf{J}_j(t) \cdot \boldsymbol{\sigma} \delta(\mathbf{r} - \mathbf{r}_j),$$

where  $\boldsymbol{\sigma} = (\sigma_x, \sigma_y, \sigma_z)$  matrices acting in spin subspace. We assume that the impurities are localised at positions  $\mathbf{r}_j$ , and have precessing spins that are defined as

$$\mathbf{J}_j(t) \equiv J [\sin \theta \cos(\omega_0 t + \phi_j), \sin \theta \sin(\omega_0 t + \phi_j), \cos \theta],$$

with precession frequency  $\omega_0$ , polar angle  $\theta$  as shown in Fig. 8.1 in the main text, and equidistant individual phase shifts  $\phi_j \equiv k_h a j$ ,  $j \in \mathbb{Z}$ . In the latter  $a$  denotes the spacing between impurities, and  $k_h$  is the so-called helix step. Thus the full time-dependent Schrödinger equation of the problem reads:

$$i\partial_t \Psi(\mathbf{r}, t) = H_{\text{tot}} \Psi(\mathbf{r}, t), \quad (\text{D.1})$$

where  $H_{\text{tot}}(t) \equiv H_0 + H_{\text{imp}}(t)$ . Since the Hamiltonian is periodic,  $H_{\text{tot}}(t + T) = H_{\text{tot}}(t)$ , with  $T = 2\pi/\omega_0$  we can make use of the Floquet theorem in order to find the resulting (time-dependent) eigenstates and quasi-energy spectrum. However, below we follow a more elegant path employing a rotating wave transformation.

## 1. Rotating wave transformation

The symmetry of the problem allows us to perform a time-dependent unitary transformation that makes the problem fully static. We can write  $\Psi(\mathbf{r}, t) = U(t)\Phi(\mathbf{r})e^{-iEt}$ , with  $U(t) = e^{-i\omega_0 t \sigma_z/2}$  so that we obtain the stationary Schrödinger equation

$$[H_{\text{tot}}(0) - B\sigma_z] \Phi(\mathbf{r}) = E\Phi(\mathbf{r}), \quad (\text{D.2})$$

where the fictitious magnetic field  $B \equiv \omega_0/2$  is perpendicular to the plane of the superconductor, which will be referred to as 'driving frequency' hereinafter, and  $E$  is the quasi-energy defined modulo  $\omega_0$ . Below we rewrite Eq. (D.2) as

$$\Phi(\mathbf{r}) = \sum_j G_0^{eff}(E, \mathbf{r} - \mathbf{r}_j) V_j^{eff} \Phi(\mathbf{r}_j), \quad (\text{D.3})$$

where

$$V_j^{eff} \equiv J \begin{pmatrix} \cos \theta & \sin \theta e^{-i\varphi_j} \\ \sin \theta e^{i\varphi_j} & -\cos \theta \end{pmatrix} \otimes \tau_0$$

and  $G_0^{eff} \equiv [E - \mathcal{H}_0^{eff}]^{-1}$  with  $H_0^{eff} \equiv H_0 - B\sigma_z \otimes \tau_0$ . We write the coordinate dependence of the Green's in the following form:

$$G_0^{eff}(E, \mathbf{r}) = \begin{pmatrix} (E+B)X_0^+ + X_1^+ & 0 & \Delta_s X_0^+ & 0 \\ 0 & (E-B)X_0^- + X_1^- & 0 & \Delta_s X_0^- \\ \Delta_s X_0^+ & 0 & (E+B)X_0^+ - X_1^+ & 0 \\ 0 & \Delta_s X_0^- & 0 & (E-B)X_0^- - X_1^- \end{pmatrix}.$$

Depending on whether  $\mathbf{r} \neq \mathbf{0}$  or  $\mathbf{r} = \mathbf{0}$  we give the expressions for  $X_0^\pm$  below:

$$X_0^\pm(r) = -2\nu \cdot \frac{1}{\omega_\pm} \text{Im} K_0[-i(1+i\Omega_\pm)p_F r], \quad X_0^\pm(\mathbf{0}) = -\pi\nu \frac{1}{\omega_\pm},$$

$$X_1^\pm(r) = -2\nu \cdot \text{Re} K_0[-i(1+i\Omega_\pm)p_F r], \quad X_1^\pm(\mathbf{0}) = 0,$$

where  $\omega_\pm = \Omega_\pm v_F p_F \equiv \sqrt{\Delta_s^2 - (E \pm B)^2}$ .

It is worth noting that the system has two different regimes of driving: gapful when  $B < \Delta_s$  and gapless when  $B > \Delta_s$ . Below we consider the case of a gapful system, and moreover we discuss the case of weak driving  $B \ll \Delta_s$ .

## 2. Effective Hamiltonian for the chain in momentum space

We follow the procedure described in the article by Pientka, Glazman and von Oppen [35] and we start with rewriting Eq. (D.3) for  $\mathbf{r} = \mathbf{r}_i$ , i.e. for the points where the impurities are localised:

$$\left[ \mathbb{I} - G_0^{eff}(E, \mathbf{0}) V_i^{eff} \right] \Phi(\mathbf{r}_i) = \sum_{j \neq i} G_0^{eff}(E, \mathbf{r}_i - \mathbf{r}_j) V_j^{eff} \Phi(\mathbf{r}_j). \quad (\text{D.4})$$

We consider the so-called deep-dilute regime in which the energies of the impurity-induced states are very close to zero. Therefore, we use an approximation for both left and right side of the equation above, leaving in the left side the diagonal term, linear in E. The equation takes form:

$$\left[ \mathbb{I} - \tilde{G}_0^{eff}(E, \mathbf{0}) V_i^{eff} \right] \Phi(\mathbf{r}_i) \approx \sum_{j \neq i} G_0^{eff}(0, \mathbf{r}_i - \mathbf{r}_j) V_j^{eff} \Phi(\mathbf{r}_j), \quad (\text{D.5})$$

where on the left side we make a Taylor expansion up to terms linear in  $E$ :

$$\tilde{G}_0^{eff}(E, \mathbf{0}) = -\frac{\pi\nu}{\omega} \left[ \begin{pmatrix} B & 0 & \Delta_s & 0 \\ 0 & -B & 0 & \Delta_s \\ \Delta_s & 0 & B & 0 \\ 0 & \Delta_s & 0 & -B \end{pmatrix} + \frac{\Delta_s^2}{\omega^2} \begin{pmatrix} E & 0 & \frac{B}{\Delta_s}E & 0 \\ 0 & E & 0 & \frac{B}{\Delta_s}E \\ \frac{B}{\Delta_s}E & 0 & E & 0 \\ 0 & \frac{B}{\Delta_s}E & 0 & E \end{pmatrix} \right] \quad (\text{D.6})$$

with  $\omega \equiv \sqrt{\Delta_s^2 - B^2}$ . Below we will keep only the diagonal terms of the second matrix in Eq. (D.6), since  $B \ll \Delta_s$ . On the right side of Eq. (D.5) we have

$$G_0^{eff}(0, r_{ij}) = \frac{\pi\nu}{\omega} \begin{pmatrix} B\tilde{X}_0 + \omega\tilde{X}_1 & 0 & \Delta_s\tilde{X}_0 & 0 \\ 0 & -B\tilde{X}_0 + \omega\tilde{X}_1 & 0 & \Delta_s\tilde{X}_0 \\ \Delta_s\tilde{X}_0 & 0 & B\tilde{X}_0 - \omega\tilde{X}_1 & 0 \\ 0 & \Delta_s\tilde{X}_0 & 0 & -B\tilde{X}_0 - \omega\tilde{X}_1 \end{pmatrix},$$

where

$$\tilde{X}_0(r_{ij}) = -\frac{2}{\pi} \text{Im} K_0 \left[ -i \left( 1 + i \frac{\omega}{v_F p_F} \right) p_F r_{ij} \right], \quad (\text{D.7})$$

$$\tilde{X}_1(r_{ij}) = -\frac{2}{\pi} \text{Re} K_0 \left[ -i \left( 1 + i \frac{\omega}{v_F p_F} \right) p_F r_{ij} \right], \quad (\text{D.8})$$

and  $r_{ij} \equiv |\mathbf{r}_i - \mathbf{r}_j| = |i - j|a$ . Our goal is to write Eq. (D.5) as a Shrödinger equation, to achieve that we use the following unitary transformation:

$$U_i = \text{diag} \{ e^{i\varphi_i/2}, e^{-i\varphi_i/2}, e^{i\varphi_i/2}, e^{-i\varphi_i/2} \}, \quad \tilde{\Phi}(\mathbf{r}_i) = U_i \Phi(\mathbf{r}_i).$$

Thus we get

$$\left[ \mathbb{I} - \tilde{G}_0^{eff}(E, \mathbf{0}) \cdot V \right] \tilde{\Phi}(\mathbf{r}_i) = \sum_{j \neq i} G_0^{eff}(0, r_{ij}) \cdot \begin{pmatrix} e^{i(\varphi_i - \varphi_j)/2} & 0 \\ 0 & e^{-i(\varphi_i - \varphi_j)/2} \end{pmatrix} \otimes \tau_0 \cdot V \cdot \tilde{\Phi}(\mathbf{r}_j) \quad (\text{D.9})$$

with

$$V \equiv U_i V_i^{eff} U_i^\dagger = J R(\theta), \quad \text{where } R(\theta) = \begin{pmatrix} \cos \theta & \sin \theta \\ \sin \theta & -\cos \theta \end{pmatrix} \otimes \tau_0$$

Eq. (D.9) then takes form:

$$\sum_j H_{ij} \tilde{\Phi}(\mathbf{r}_j) = E \tilde{\Phi}(\mathbf{r}_i), \quad i, j \in \overline{1, N}, \quad \text{with } H_{ij} = \begin{cases} h_0, & j = i \\ h_{ij}, & j \neq i \end{cases}, \quad (\text{D.10})$$

where

$$h_0 = -\frac{\omega^2}{\Delta_s^2} \left[ \frac{\omega}{\alpha} R(\theta) + B R(2\theta) + \Delta_s \sigma_0 \tau_x \right]$$

$$h_{ij} = \frac{\omega^2}{\Delta_s^2} R(\theta) \cdot \left\{ [B \sigma_z \tau_0 + \Delta_s \sigma_0 \tau_x] \tilde{X}_0(r_{ij}) + \omega \sigma_0 \tau_z \tilde{X}_1(r_{ij}) \right\} \cdot \begin{pmatrix} e^{i\Delta\varphi_{ij}/2} & 0 \\ 0 & e^{-i\Delta\varphi_{ij}/2} \end{pmatrix} \otimes \tau_0 \cdot R(\theta),$$

with  $\Delta\varphi_{ij} \equiv \varphi_i - \varphi_j$ , and the phases can be expressed in terms of the helix step  $k_h$  and spacing  $a$ ,  $\varphi_j = k_h x_j = k_h a \cdot j$ . The system described by Eq. (D.10) is translational-invariant and therefore we can perform a FT to obtain the Hamiltonian in the momentum space, namely:

$$\mathcal{H}(k) = \sum_j H_{ij} e^{ikr_{ij}} = h_0 + \sum_{j \neq i} h_{ij} e^{ikr_{ij}} \quad (\text{D.11})$$

The  $4 \times 4$  form of the Hamiltonian (D.11) is not convenient for studying the Shiba band since it takes into account the bands that are very close to the edge of the superconducting gap. Therefore, we perform a unitary transformation

$$\mathcal{U} \equiv \exp \left\{ i \frac{\theta + \alpha \frac{B}{\Delta_s} \sin \theta}{2} \sigma_y \right\} \otimes \exp \left\{ i \frac{\pi}{4} \tau_y \right\}, \quad (\text{D.12})$$

that in the leading order in  $B$  diagonalises  $h_0$ , namely:

$$\begin{aligned} [\mathcal{U} h_0 \mathcal{U}^\dagger]_{11} &= - \left[ \left( 1 + \frac{1}{\alpha} \right) \Delta_s + B \cos \theta \right] \\ [\mathcal{U} h_0 \mathcal{U}^\dagger]_{22} &= - \left[ \left( 1 - \frac{1}{\alpha} \right) \Delta_s - B \cos \theta \right] \\ [\mathcal{U} h_0 \mathcal{U}^\dagger]_{33} &= + \left[ \left( 1 - \frac{1}{\alpha} \right) \Delta_s - B \cos \theta \right] \\ [\mathcal{U} h_0 \mathcal{U}^\dagger]_{44} &= + \left[ \left( 1 + \frac{1}{\alpha} \right) \Delta_s + B \cos \theta \right] \end{aligned}$$

The 22 and 33 elements correspond to the sought-for Shiba band, therefore, we can perform

the same transformation for the  $h_{ij}$  and extract only the terms 22, 23, 32, 33, in other words, project our Hamiltonian. Thus below we deal with effective  $2 \times 2$  Hamiltonians.

Two limiting cases are important for understanding: coherence length  $\xi \equiv v_F/\omega$  must be compared to the impurity spacing  $a$ . The case of  $\xi \ll a$  takes into account only the nearest neighbour hopping, therefore in Eq. (D.11) we consider only  $|j - i| \leq 1$ , whereas in the case of  $\xi \gg a$  we should take into account all the possible hoppings. In both regimes the Hamiltonian is written in the following form

$$\mathcal{H}(k) = d_0(k) + \mathbf{d}(k) \cdot \boldsymbol{\Sigma},$$

where  $\boldsymbol{\Sigma} = (\Sigma_x, \Sigma_y, \Sigma_z)$  are Pauli matrices acting in a mixed space defined by the unitary transformation of the initial Nambu basis (see Eq. (D.12)). The components of the  $\mathbf{d}$ -vector are defined below.

### Short coherence length, $\xi \ll a$

In this regime we keep only the terms responsible for the nearest neighbour hopping, and we get:

$$\begin{aligned} d_0(k) &\equiv \tilde{X}_0(a) [\Delta_s \cos \theta - B(1 - \alpha \sin^2 \theta)] \sin \frac{k_h a}{2} \sin ka \\ d_x(k) &\equiv \tilde{X}_1(a) (\Delta_s - \alpha B \cos \theta) \sin \theta \sin \frac{k_h a}{2} \sin ka \\ d_y(k) &\equiv 0 \\ d_z(k) &\equiv - \left[ \left(1 - \frac{1}{\alpha}\right) \Delta_s - B \cos \theta \right] + \tilde{X}_0(a) (\Delta_s - B \cos \theta) \cos \frac{k_h a}{2} \cos ka \end{aligned}$$

### Long coherence length, $\xi \gg a$

In this case one needs to take into account all the possible hopping terms, therefore we perform the summation in Eq. (D.11) up to infinity:

$$F_{0,1}(k, s) \equiv 2 \sum_{m=1}^{\infty} \cos \left[ \left(k + s \frac{k_h}{2}\right) a \cdot m \right] \tilde{X}_{0,1}(a \cdot m) \quad (\text{D.13})$$

Since it is known that  $k_F a \gg 1$ , we can use the asymptotic form of the modified Bessel function of the second kind and perform the summations to obtain a closed analytical form for the momentum-space Hamiltonian. It is known that

$$\begin{aligned}\tilde{X}_0(a \cdot m) &\sim -\sqrt{\frac{2}{\pi}} \cdot \frac{\sin(k_F a \cdot m + \pi/4)}{\sqrt{k_F a \cdot m}} e^{-k_S a \cdot m} \\ \tilde{X}_1(a \cdot m) &\sim -\sqrt{\frac{2}{\pi}} \cdot \frac{\cos(k_F a \cdot m + \pi/4)}{\sqrt{k_F a \cdot m}} e^{-k_S a \cdot m},\end{aligned}$$

where  $k_S \equiv \omega/v_F$ . We perform the summations in Eq. (D.13) using the asymptotic forms above and we get:

$$F_0(k, s) = +\sqrt{\frac{2}{\pi k_F a}} \operatorname{Im} f(k, s), \quad F_1(k, s) = -\sqrt{\frac{2}{\pi k_F a}} \operatorname{Re} f(k, s),$$

with

$$f(k, s) = e^{-i\frac{\pi}{4}} \left[ \operatorname{Li}_{\frac{1}{2}} \left( e^{-k_S a + i(k + s k_h/2 - k_F) a} \right) + \operatorname{Li}_{\frac{1}{2}} \left( e^{-k_S a - i(k + s k_h/2 + k_F) a} \right) \right],$$

where we define the polylogarithm function in a standard way:  $\operatorname{Li}_n(z) = \sum_{m=1}^{\infty} z^m/m^n$ . Finally, the Hamiltonian in the long coherence length regime is defined by:

$$\begin{aligned}d_0(k) &\equiv [\Delta_s \cos \theta - B(1 - \alpha \sin^2 \theta)] \frac{F_0(k, -) - F_0(k, +)}{2} \\ d_x(k) &\equiv (\Delta_s - \alpha B \cos \theta) \sin \theta \frac{F_1(k, -) - F_1(k, +)}{2} \\ d_y(k) &\equiv 0 \\ d_z(k) &\equiv - \left[ \left( 1 - \frac{1}{\alpha} \right) \Delta_s - B \cos \theta \right] + (\Delta_s - B \cos \theta) \frac{F_0(k, -) + F_0(k, +)}{2}\end{aligned}$$

Note that the coefficients before the combinations of polylogarithm functions are the same as for the short coherence length regime. It is also worth mentioning that in the functions  $F_{0,1}(k, s)$  we can set the factor  $e^{-k_S a}$  to unity since  $\xi \gg a$ .

## D.2 Winding number calculation

The  $d_0$  component of the Hamiltonian does not affect its topological properties. The winding number can be computed analytically employing a standard formula

$$W = \frac{1}{2\pi} \int_{-\pi}^{\pi} dk \frac{d_x(k)d'_z(k) - d'_x(k)d_z(k)}{d_x^2(k) + d_z^2(k)}.$$

We do not provide any analytical expressions since the parameter space is very large, and demonstrating all the cases is too cumbersome even for an Appendix. Instead, we plot the results in Figure D.1 for short and long coherence length regimes as functions of driving  $B$  versus either Fermi momentum  $k_F$  and polar angle  $\theta$ . The black lines defining where the winding number changes were utilised in Fig. 8.2 in the main text to facilitate distinguishing between different phases.

## D.3 Frequency domain description of the Shiba bands

In this section we describe the dynamical situation in the frequency domain, and the resulting Floquet band structure. Given a periodic Hamilton  $H(t + T) = H(t)$ , with some period  $T = 2\pi/\omega_0$ , one can write the time dependent Schroedinger equation:

$$i \frac{\partial \psi(t)}{\partial t} = H(t) \psi(t), \quad (\text{D.14})$$

and one can utilise the Floquet theorem to subsequently write:

$$\psi(t) = e^{-iEt} \sum_{m=-\infty}^{\infty} \phi_m e^{im\omega_0 t}, \quad (\text{D.15})$$

with  $\phi_m$  depending on various system parameters, but not  $t$ . These coefficients (or wave functions) satisfy the following time-independent eigenvalue equation:

$$\sum_{m'} H_{mm'} \phi_{m'} = E \phi_m, \quad (\text{D.16})$$

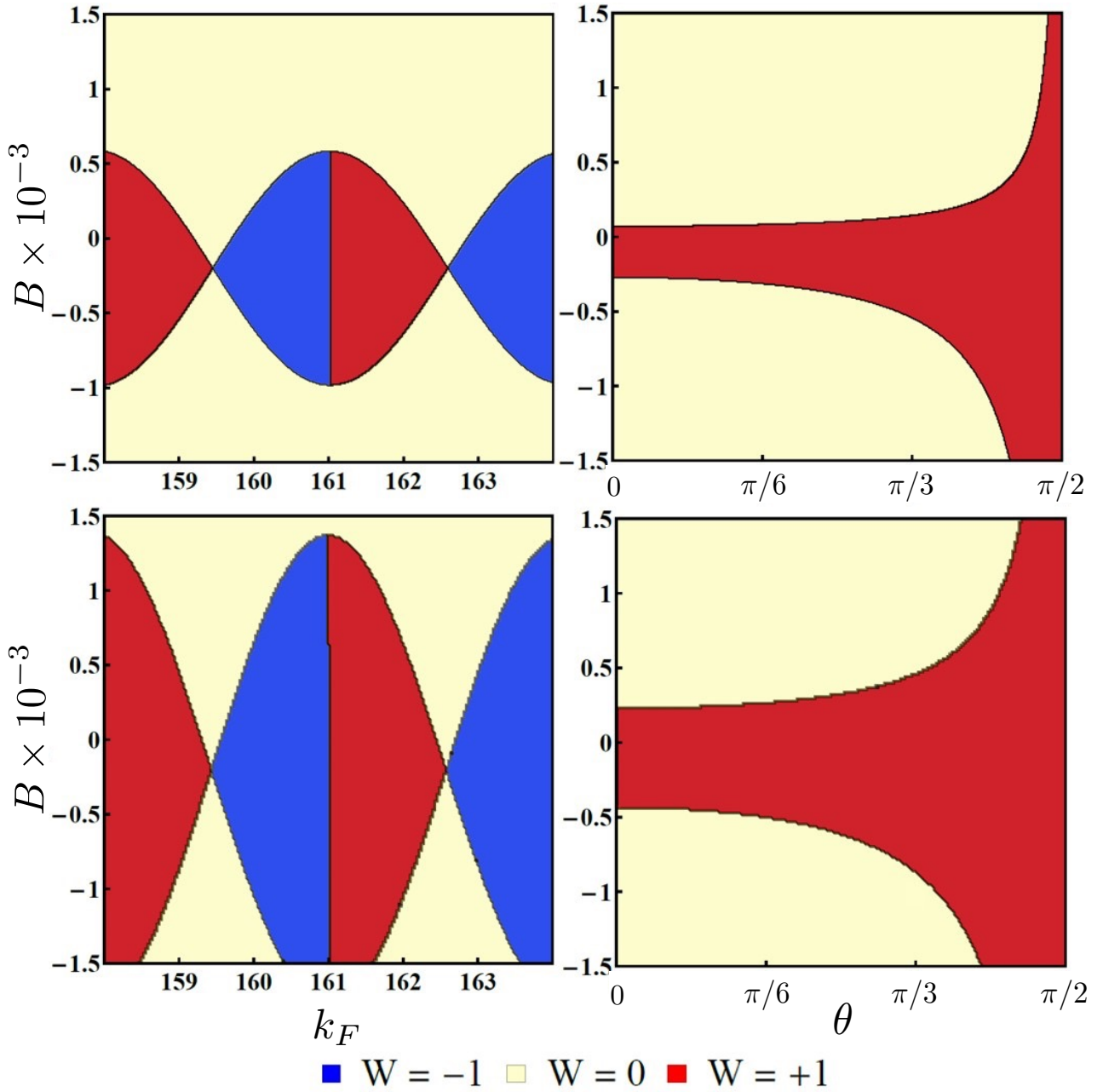


Figure D.1: The winding number of the Shiba band for the small and long coherence length regimes (upper and lower rows correspondingly), plotted as functions of the driving frequency  $B$  (vertical axis) versus the Fermi momentum  $k_F$  (left column,  $\theta = \pi/3$ ) and polar angle  $\theta$  (right column,  $k_F = 159$ ). We set  $k_h = \pi/4, v_F = 0.2, \Delta_s = 1, a = 1, \alpha = 0.9999$ .

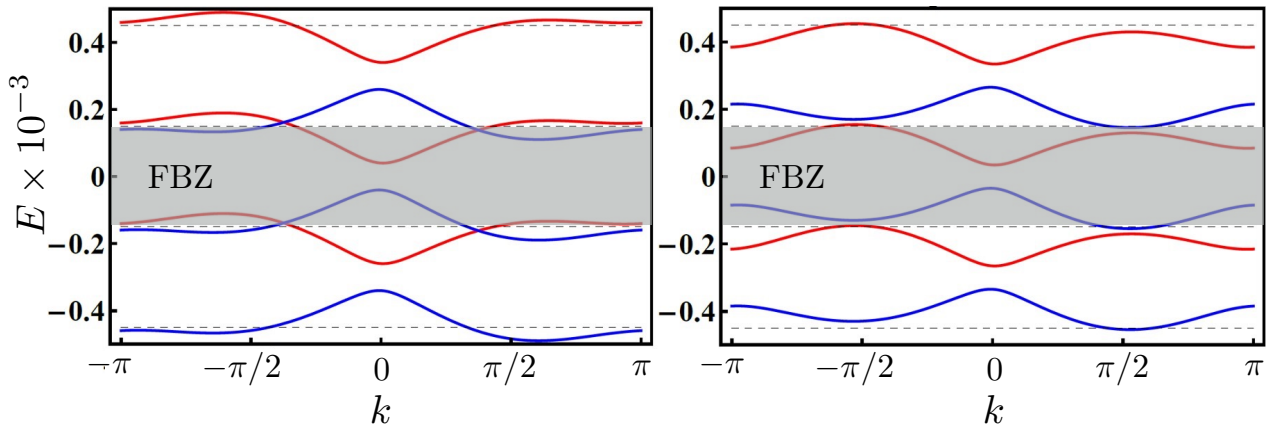


Figure D.2: We plot Shiba bands as functions of energy on the left panel and quasi-energy on the right, versus quasi-momentum in the first Brillouin zone. We set  $\theta = \pi/3$ ,  $k_h = \pi/4$ ,  $k_F = 159.3$ ,  $v_F = 0.2$ ,  $\Delta_s = 1$ ,  $a = 1$ ,  $\alpha = 0.9999$  for both panels. On the left  $B = 0$ , whereas on the right  $B = -0.15 \cdot 10^{-3}$ .

where

$$H_{mm'} = \omega_0 \delta_{mm'} + \frac{1}{T} \int_0^T dt e^{i(m-m')\omega_0 t} H(t). \quad (\text{D.17})$$

We see that the above equation has solutions for  $-\infty < E < \infty$ . However, if  $E$  is an eigenvalue of (D.17) corresponding to the eigenstate  $m$  with amplitudes  $\phi_m$ , then  $\tilde{E} = E + s\omega_0$ , where  $s$  is any integer, is also an eigenvalue corresponding to an  $\tilde{\phi}_{m+s}$  eigenstate with amplitudes given by  $\tilde{\phi}_{m+s} = \phi_m$ . This means that all of these solutions correspond to the same time-dependent solution of the Schrödinger equation. Therefore, the Floquet states are uniquely and completely parametrised by quasi-energies in the "first quasi-energy Brillouin zone",  $-\pi/T < E < \pi/T$ . Eq. (D.17) is the temporal analogue of a "repeated zone" scheme for conventional band structure calculations. Let us consider our model of a driven spin helix coupled to a superconductor. To ease the discussion, it is instructive to write this Hamiltonian as follows:

$$H_{\text{tot}}(t) = H_0 + \sum_{j=1}^N [J_j^z \sigma_z + J_j^+ \sigma_- e^{-i\omega_0 t} + J_j^- \sigma_+ e^{i\omega_0 t}] \delta(\mathbf{r} - \mathbf{r}_j), \quad (\text{D.18})$$

where  $J_j^z = J_0 \cos \theta$ , and  $J_j^\pm = J_0 \sin \theta e^{\pm i\phi_j}$ , and  $H_0$  is the superconducting Hamiltonian that was defined before. Note that  $[H_0, \sigma_z] = 0$ , and that we can identify the  $J_j^{+(-)}$  processes with emission (absorption of a photon, or any bosonic quanta). Note also that the functions  $\phi_m$  depend, among other things, on the spin degree of freedom. With that identification, we immediately can establish that the resulting Hamiltonian in Eq. (D.17) can be decomposed in

blocks of  $2 \times 2$  in the  $\text{spin} \otimes \text{photon}$  space, or  $\{\phi_{m\downarrow}, \phi_{m+1\uparrow}\}$  constitute a closed basis (does not couple to other bands). More specifically, we obtain the following matrix:

$$H_{\text{mm}-1} = \begin{pmatrix} H_0 + m\omega_0 - \sum_j J_j^z \delta(\mathbf{r} - \mathbf{r}_j) & \sum_j J_j^+ \delta(\mathbf{r} - \mathbf{r}_j) \\ \sum_j J_j^- \delta(\mathbf{r} - \mathbf{r}_j) & H_0 + (m-1)\omega_0 + \sum_j J_j^z \delta(\mathbf{r} - \mathbf{r}_j) \end{pmatrix}, \quad (\text{D.19})$$

which can be cast in terms of a "pseudospin"  $\tilde{\sigma}$  as follows:

$$H_{m,\downarrow}^{m-1,\uparrow} = (m + 1/2)\omega_0 + H_0 - (\omega_0/2)\tilde{\sigma}_z + \sum_j \mathbf{J}_j \cdot \tilde{\sigma} \delta(\mathbf{r} - \mathbf{r}_j). \quad (\text{D.20})$$

Note that from the perspective of the superconductor,  $\sigma$  and  $\tilde{\sigma}$  act exactly in the same fashion. We can now easily interpret our results: in the extended zone scheme, the initial bands only couple the same  $m$ 's in the absence of driving. However, once the driving is tuned on, the bands with adjacent  $m$ 's and opposite spins get mixed. Moreover, each pair of such bands are shifted in energy by  $\omega_0(m+1/2)$ . To highlight this behaviour, it worth doing the following comparison: the static spectrum, in the absence of driving, but presented in the extended zone scheme for a given frequency  $\omega_0$  (copies of the spectrum shifted by  $\omega_0(m+1/2)$ , but not interacting with each other for different  $m$ 's), and the Floquet spectrum for the driven system, presented again in the extended zone scheme. We see that indeed, in the driven case, there is level crossing between adjacent  $m$ 's, with a splitting that can be evaluated from solving Eq. (D.19). Since the spectrum is composed of separated blocks that emulate the static Hamiltonian, indifferent of the periodic or open boundary conditions, the entire edge structure and topology is given by these (shifted, but equivalent) blocks.

On the left panel in Figure D.2 we plot the Shiba band energies versus quasi-momentum in the absence of driving, showing also the Floquet-like band structure (bands are replicated artificially, using the value of driving for the right panel, since there is no driving on the left one). When we turn on the driving we see that the crossings of the left panel become the anticrossings on the right panel, where we plot quasi-energies (Floquet bands) of Shiba band versus quasi-momentum. This qualitative analysis is analogous to that carried out by M. Rudner et al. (see Fig. 5 of PRX **3**, 031005), and allows to see how the topological phase transition occurs in this system subject to periodic driving.

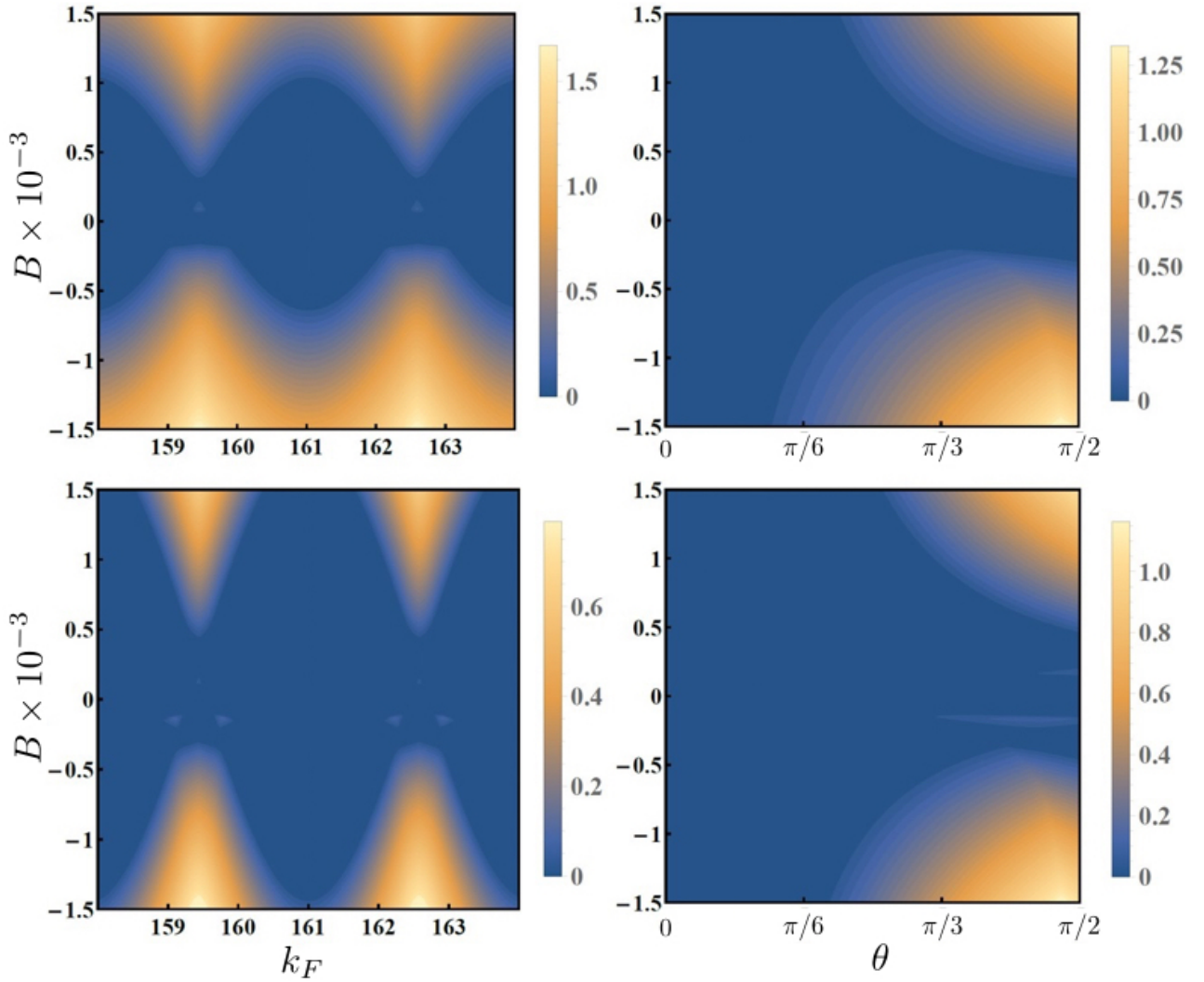


Figure D.3: The gap around quasi-energy  $E = B$  of the Shiba band for the small and large coherence length regimes (first and second rows respectively), plotted as functions of the driving frequency  $B$  and the Fermi momentum  $k_F$  (precession angle  $\theta$ ) in the left (right) column. We set  $k_h = \pi/4, v_F = 0.2, \Delta_s = 1, a = 1, \alpha = 0.9999$ . The Fermi momentum  $k_F = 159$  in the left column and the polar angle  $\theta = \pi/3$  in the right column.

## D.4 Shiba band gap at $E=B$

In Fig.8.2 in the main text we presented only the gap value of the Shiba band taken at quasi-energy  $E = 0$ . For completeness we present also in Figure D.3 the gap at quasi-energy  $E = B$ . As discussed in the main text, no Majorana fermions emerge at the latter quasi-energy value.

## D.5 Circuit implementation of a precessing helical texture

In this section we present a simplified version of the implementation of a controlled dynamical helical texture in a circuit model. In Fig. D.4 we present a sketch of our proposal: a chain of magnetic impurities on top of an  $s$ -wave superconductor forming spin helix (texture) of pitch  $k_h$  and an angle  $\theta$  is being sandwiched between two metallic leads with strong spin-orbit interaction. Passing a charge current  $J_c^L$  through the left metal gives rise to a spin accumulation  $\boldsymbol{\mu}_s^L = \mathbf{e}_z \mu_s^L$  at the edge via the spin Hall effect [174]. This spin bias, being non-collinear with the local magnetisation on the left, gives rise to a local torque that brings the texture into precession. Below we describe a simplified version of the model that describes quantitatively the induced precession of the texture, assuming the texture is rigid and that the entire spin is carried by the texture only. Moreover, for simplicity, we assume no bulk Gilbert damping of the (precessing) magnetic texture, although such a component is easily accommodated in our theory. Our theoretical modelling follows closely the ideas developed in Ref. [177] for describing superfluid spin flow in planar ferromagnets. Following Ref. [180], the spin current exchanged with the lead  $r = L, R$  by the helix can be expressed as:

$$\mathbf{J}_s^r = \frac{1}{4\pi} [\mathcal{R}g_{\uparrow\downarrow}^r \mathbf{m} \times + \mathcal{I}g_{\uparrow\downarrow}^r] (\tilde{\boldsymbol{\mu}}_s^r \times \mathbf{m}), \quad (\text{D.21})$$

where  $g_{\uparrow\downarrow}^r \equiv \mathcal{R}g_{\uparrow\downarrow}^r + i\mathcal{I}g_{\uparrow\downarrow}^r$  is the so called spin mixing conductance, which quantifies the interface  $r = L, R$  and which can be in general complex [181], and  $\mathbf{m} \equiv \mathbf{S}/S_0$ . Also,  $\tilde{\boldsymbol{\mu}}_s^r \equiv \boldsymbol{\mu}_s^r - \hbar \mathbf{m} \times \dot{\mathbf{m}}$ , namely in the dynamical case the applied spin bias (or spin torque) is reduced effectively by the spin pumping contribution [180]. Next we note that the spin texture possesses  $U(1)$  symmetry, namely it is invariant with respect to rotations around the  $z$  axis. That implies that the spin current along this direction is conserved, and thus we focus on the  $z$  component only. Also, we assume that for a rigid texture (helix) the spin precession satisfies:

$$\mathbf{m} \equiv \mathbf{m}(t) = [\cos(\omega_0 t + \phi) \sin \theta, \sin(\omega_0 t + \phi) \sin \theta, \cos \theta], \quad (\text{D.22})$$

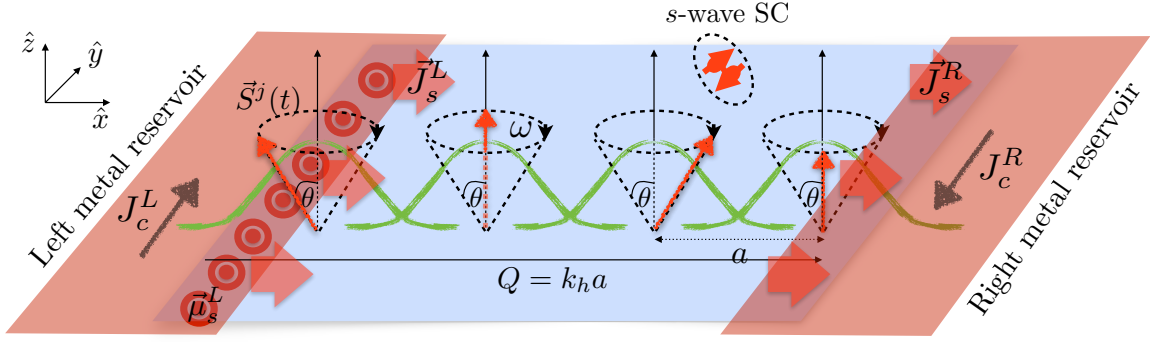


Figure D.4: Normal-metal—Magnetic Texture—normal-metal heterostructure that can be used to excite in a controlled fashion the precession of the chain of magnetic impurities inserted in an  $s$ -wave superconductor. A charge current  $J_c^L$  in the left lead (red) gives rise to a spin accumulation  $\vec{\mu}_s^L \equiv \vec{e}_z \mu_s^L$  at the interface via the spin Hall effect, and the spin current pumped into the right reservoir,  $\vec{J}_s^R$ , generates a transverse charge current  $J_c^R$  through the inverse spin Hall effect. The spin current from the left ( $\vec{J}_s^L$ ) to the right lead ( $\vec{J}_s^R$ ) is established dynamically via the precession of the magnetic (helical) texture.

with  $\phi$  arbitrary. With this, the spin currents along  $z$  at each end (lead) is found as follows:

$$J_{s,z}^{L,R} = \pm \frac{\mathcal{R}g_{\uparrow\downarrow}^{L,R}}{4\pi} (\mu_s^{L,R} - \omega_0) \sin^2 \theta, \quad (\text{D.23})$$

where we used the  $-$  sign for the right spin current to emphasise that this is the current injected into the lead and not the flow into the texture (which is just the opposite). Since we assume no dissipation mechanisms in the bulk we have that  $J_{s,z}^L = J_{s,z}^R$ , which gives for the precession frequency the following expression:

$$\omega_0 = \frac{\mathcal{R}g_{\uparrow\downarrow}^L \mu_s^L + \mathcal{R}g_{\uparrow\downarrow}^R \mu_s^R}{\mathcal{R}g_{\uparrow\downarrow}^L + \mathcal{R}g_{\uparrow\downarrow}^R}. \quad (\text{D.24})$$

We thus see that by controlling the spin biases on the two ends, via the spin Hall, effect the precession frequency can be tuned at will. Moreover, by tuning the biases such that  $\mathcal{R}g_{\uparrow\downarrow}^L \mu_s^L = -\mathcal{R}g_{\uparrow\downarrow}^R \mu_s^R$ , the precession frequency vanishes. More complicated models (including, for example, dissipation, change in the cone angle, electrons, magnons, etc.) will alter this conclusion, but the general picture should still hold true. For completeness, we also provide with the resulting expression for the spin current at either of the ends:

$$J_{s,z}^L = \frac{1}{4\pi} \frac{\mathcal{R}g_{\uparrow\downarrow}^L \mathcal{R}g_{\uparrow\downarrow}^R (\mu_s^L - \mu_s^R)}{\mathcal{R}g_{\uparrow\downarrow}^L + \mathcal{R}g_{\uparrow\downarrow}^R} \sin^2 \theta, \quad (\text{D.25})$$

which vanishes any time one of the leads is disconnected. However, it does not necessary vanish in the case when  $\omega_0$  vanishes (see condition above). We note in passing that relaxing the condition of a rigid texture should allow, as stressed in the main text, to control non only the frequency, but also the pitch  $k_h$ . For example, if the initial impurity spins are lying in-plane, but forming no helix in the absence of the leads, once subjected to spin biases will give rise to a dynamical texture such that the spin current is transported from the left to right lead. In a long wavelength description, the Hamiltonian describing such a setup reads [176, 177]:

$$H_F = \int dx [A(\nabla \mathbf{m}(x))^2 + Km_z^2]/2, \quad (\text{D.26})$$

where  $A$  and  $K$  stand for the exchange stiffness and the anisotropy, respectively, where  $\mathbf{m} = (\sqrt{1 - m_z^2} \cos \phi, \sqrt{1 - m_z^2} \sin \phi, m_z)$ . For  $m_z \ll 1$ , it was shown that the spin current (along  $z$ ) at some position  $x$  in the chain between the two leads reads:

$$J_{s,z}(x) = -A\nabla\phi(x), \quad (\text{D.27})$$

which, in the absence of dissipation, should coincide with the spin currents at the left lead  $J_{s,z}^L$ . In such a case, we can readily see that  $\phi(x, t) = \phi(0, t) - (J_{s,z}^L/A)x$ , with  $\phi(0, t) = \omega_0 t$ . The resulting pitch of the texture (assuming, in the lattice model  $a = 1$ ) can be read as

$$k_h = 2\pi A/J_{s,z}^L. \quad (\text{D.28})$$

By inspecting the above conditions for the precession frequency and for the spin current, we see that by tuning the spin biases we can tune independently the frequency  $\omega_0$  and the pitch  $k_h$  (we can even reduce the chain to the static case). Thus, such an implementation is extremely versatile for implementing our proposed dynamical model.

# Appendix E

## Asymptotic expansions

Since the integrals are expressed in terms of Neumann function and Bessel function of the first kind, we give their asymptotic behaviour for  $x \rightarrow +\infty$ :

### Bessel functions of the first kind

$$J_0(x) \sim +\sqrt{\frac{2}{\pi x}} \cos\left(x - \frac{\pi}{4}\right), \quad J_1(x) \sim -\sqrt{\frac{2}{\pi x}} \cos\left(x + \frac{\pi}{4}\right)$$

### Bessel functions of the second kind

In this appendix we give the asymptotic expansions for the modified Bessel functions of the second kind  $K_0$  and  $K_1$ . It is known that:

$$K_\nu(z) \sim \sqrt{\frac{\pi}{2}} \frac{e^{-z}}{\sqrt{z}} \left[ 1 + O\left(\frac{1}{z}\right) \right] \quad \text{for } |z| \rightarrow \infty$$

Since the asymptotic form is independent of  $\nu$ , we will omit it below. For the case of pure s-wave:

$$K[-i(1+i\Omega)k_F r] \sim \frac{e^{i(1+i\Omega)k_F r}}{\sqrt{-i(1+i\Omega)k_F r}} = \frac{e^{ik_F r}}{\sqrt{\Omega-i}} \frac{e^{-k_S r}}{\sqrt{k_F r}} = *$$

We rewrite  $\sqrt{\Omega-i} = (1+\Omega^2)^{1/4} e^{-i\theta/2}$ , where  $\theta = \arctan \frac{1}{\Omega}$  and we get

$$* = \frac{1}{(1+\Omega^2)^{1/4}} \frac{e^{i(k_F r + \theta/2)}}{\sqrt{k_F r}} e^{-k_S r} \approx \frac{e^{i(k_F r + \pi/4)}}{\sqrt{k_F r}} e^{-k_S r},$$

where  $k_S = \omega/v_F$ . The approximation is valid since for all subgap energies since  $\Omega \ll 1$ . Thus

$$\operatorname{Re} K[-i(1+i\Omega)k_F r] \sim \frac{\cos(k_F r + \pi/4)}{\sqrt{k_F r}} e^{-k_S r}, \quad \operatorname{Im} K[-i(1+i\Omega)k_F r] \sim \frac{\sin(k_F r + \pi/4)}{\sqrt{k_F r}} e^{-k_S r}.$$

Similarly, for the case of pure p-wave we get:

$$\begin{aligned} \operatorname{Re} K[-i(1-\gamma^2+i\Omega)k_F r] &\sim \frac{\cos(k'_F r + \pi/4)}{\sqrt{k'_F r}} e^{-k_S r}, \\ \operatorname{Im} K[-i(1-\gamma^2+i\Omega)k_F r] &\sim \frac{\sin(k'_F r + \pi/4)}{\sqrt{k'_F r}} e^{-k_S r}, \end{aligned}$$

where  $k'_F = k_F(1-\gamma^2) = \frac{k_F}{1+\tilde{z}^2}$  and  $k_S = \omega/v_F$ .

## Neumann functions

$$Y_0(x) \sim -\sqrt{\frac{2}{\pi x}} \cos\left(x + \frac{\pi}{4}\right), \quad Y_1(x) \sim -\sqrt{\frac{2}{\pi x}} \cos\left(x - \frac{\pi}{4}\right)$$

# Annex

# Majorana fermions in finite-size strips with in-plane magnetic fields

In what follows we study the Majorana bound states arising in finite-size strips with Rashba spin-orbit coupling in the presence of an in-plane Zeeman magnetic field. Using two different methods, first, the numerical diagonalisation of the tight-binding Hamiltonian, and second, finding the singular points of the Hamiltonian (see Refs. [182–185]), we obtain the topological phase diagram for these systems as a function of the chemical potential and the magnetic field, and we demonstrate the consistency of these two methods. We note that the ‘singular points technique’ can also be used e.g. to recover the phase diagrams in Chapter 8. By introducing disorder into these systems we confirm that the states with even number of Majorana pairs are not topologically protected. Finally, we show that a calculation of the  $\mathbb{Z}_2$  topological invariants recovers correctly the parity of the number of Majorana bound states pairs, and it is thus fully consistent with the phase diagrams of the disordered systems.

## §.1 Introduction

There has been a lot of progress recently in realising Majorana bound states (MBS) in various low-dimensional systems both theoretically [35, 40, 46, 47, 106, 114, 116, 127, 129, 132, 186–198] and experimentally [50–52, 122, 199]. The key ingredients are a strong Rashba spin-orbit coupling and Zeeman magnetic fields. However, the inevitable orbital effects of the magnetic field drastically modify the topological phase diagram, eventually destroying the MBS [200–203]. One possible way to avoid orbital effects is to use in-plane magnetic fields [204–207].

In Refs. [208–211] various low-dimensional systems, such as infinite ribbons and finite-size strips,

have been studied. These systems respect particle-hole symmetry (PHS), but violate time-reversal symmetry (TRS) due to the presence of a magnetic field. Therefore, the corresponding topological phase diagrams have been obtained by computing the  $\mathbb{Z}_2$  topological invariant (in accordance with the well-known tenfold topological classification [212]), as well as numerical methods. However, only the case of magnetic fields perpendicular to the plane of the system has been considered.

Below we consider the formation of MBS in infinite ribbons and finite-size strips, while focusing on in-plane magnetic fields. We thus show that infinite ribbons can host one or two pairs of chiral Majorana modes in the presence of an in-plane magnetic field perpendicular to the edges, and we calculate the corresponding topological phase diagram. For finite-size strips we first use a numerical diagonalisation of the tight-binding Hamiltonian [213] which allows us to evaluate the Majorana polarisation (MP) [208, 210, 211]. We show that one or multiple MBS pairs can form along the short edges of the system for an in-plane magnetic field parallel to the longer dimension of the finite-size strips, and we calculate the topological phase diagrams of these systems. Second we use the singular points (SP) technique introduced in Refs. [182–185], based on the momentum values where the determinant of the Hamiltonian vanishes, and we show that it yields results consistent with the numerical ones.

We study the stability of the resulting topological states with respect to disorder [209], and we confirm that the states with even numbers of Majorana fermions are not protected, whereas those with odd numbers are. We also perform a calculation of the  $\mathbb{Z}_2$  invariant which should give one access to the parity of the number of Majorana modes. Indeed we find that this calculation predicts correctly a topologically non-trivial character for the phase-space regions shown numerically to have an odd number of MBS pairs and to survive the effects of disorder.

The rest of this Annex is organised as follows: in Section II we introduce the general model and give a concise description of the tight-binding and singular points techniques, as well as of the Majorana polarisation definition. In Section III we present the results for 1D wires and infinite ribbons. In Section IV we present the phase diagrams for finite-size strips of different widths, using the numerical diagonalisation and singular points methods. In Section V we present the effects of disorder and we compare the disordered results with those obtained using a topological-invariant calculation. In Section VI we consider finite-size square systems. Finally, we conclude in Section VII leaving the technical details of topological invariant calculations for

the Supplementary Information.

## §.2 Model and methods

We introduce a model that can describe different 1D and 2D systems with an intrinsic (or proximity-induced) s-wave superconducting pairing  $\Delta$ , longitudinal and transversal Rashba spin-orbit couplings  $\lambda_{x,y}$ , and a Zeeman magnetic field  $\mathbf{B} = (B_x, B_y, B_z)$ . We write the Hamiltonian in the Nambu basis  $\Psi_{\mathbf{r}} = \{c_{\mathbf{r}\uparrow}^\dagger, c_{\mathbf{r}\downarrow}^\dagger, c_{\mathbf{r}\downarrow}, -c_{\mathbf{r}\uparrow}\}$ , where  $c_{\mathbf{r}\sigma}$  ( $c_{\mathbf{r}\sigma}^\dagger$ ) annihilates (creates) a particle of spin  $\sigma$  at site  $\mathbf{r} = (i, j)$  in a square lattice:

$$\begin{aligned}
 H = \sum_{\mathbf{r}} & \left[ \Psi_{\mathbf{r}}^\dagger (-\mu\tau_z + \Delta\tau_x + \mathbf{B} \cdot \boldsymbol{\sigma}) \Psi_{\mathbf{r}} + \right. \\
 & + \Psi_{\mathbf{r}}^\dagger (-t_x - i\lambda_x\sigma_y) \tau_z \Psi_{\mathbf{r}+\mathbf{x}} + \text{H.c.} + \\
 & \left. + \Psi_{\mathbf{r}}^\dagger (-t_y + i\lambda_y\sigma_x) \tau_z \Psi_{\mathbf{r}+\mathbf{y}} + \text{H.c.} \right], \tag{§.1}
 \end{aligned}$$

where  $t$  is the hopping amplitude,  $\mu$  denotes the chemical potential,  $\mathbf{x}, \mathbf{y}$  are unit vectors for the  $x$  and  $y$  directions correspondingly, and the lattice spacing is set to unity.

### §.2.1 Numerical tight-binding techniques and the Majorana polarisation

The eigenstates of the tight-binding Hamiltonian described above can be obtained using a numerical diagonalisation (here performed using the MatQ code [213]). In the Nambu basis, an eigenstate  $j$  of the tight binding Hamiltonian can be written as  $\psi_{\mathbf{r}}^{j\tau} = \{u_{\mathbf{r}\uparrow}^j, u_{\mathbf{r}\downarrow}^j, v_{\mathbf{r}\downarrow}^j, -v_{\mathbf{r}\uparrow}^j\}$ , where  $u$  and  $v$  denote the electron and hole components respectively. The vector of the local Majorana polarisation [208, 210, 211] on each site  $\mathbf{r} = (x, y)$ , for the eigenstate  $j$  is given by:

$$P^j(\mathbf{r}) \equiv \begin{pmatrix} P_x^j(\mathbf{r}) \\ P_y^j(\mathbf{r}) \end{pmatrix} \equiv \begin{pmatrix} -2 \text{Re} [u_{\mathbf{r}\uparrow}^j v_{\mathbf{r}\uparrow}^j + u_{\mathbf{r}\downarrow}^j v_{\mathbf{r}\downarrow}^j] \\ -2 \text{Im} [u_{\mathbf{r}\uparrow}^j v_{\mathbf{r}\uparrow}^j + u_{\mathbf{r}\downarrow}^j v_{\mathbf{r}\downarrow}^j] \end{pmatrix} \tag{§.2}$$

This quantity allows to discriminate locally pure electron (hole) states from Majorana-like states. It is easy to see that for pure electron ( $v_{\mathbf{r}\uparrow} = v_{\mathbf{r}\downarrow} = 0$ ) and pure hole states ( $u_{\mathbf{r}\uparrow} = u_{\mathbf{r}\downarrow} = 0$ ) the local Majorana polarisation equals to zero. For our purposes it is more practical to use

the integral of the MP vector over a spatial region  $\mathcal{R}$  defined as:

$$C_j = \left| \sum_{\mathbf{r} \in \mathcal{R}} [P_x^j(\mathbf{r}) + iP_y^j(\mathbf{r})] \right|^2 \quad (\text{N.3})$$

Note that in Eqs. (N.2,N.3) we assume that the wave function is normalised.

To obtain the topological phase diagram we first find the lowest energy states of the given system. If these states have energies close to zero they may be MBS. We divide our system into two halves (along the shorter length), and we compute the integral of the MP vector in each of these halves defined by  $\mathbf{r} \in \mathcal{R}$  for each 'zero'-energy state. The states that have  $C = 1$  are MBS, and those with  $C = 0$  are regular electron or hole states. Note that we may have only a pair of state with  $C = 1$ , or multiple degenerate zero-energy MBS states with  $C = 1$ . In the results that we present here we sum the MP over all the lowest energy states. Note however that the states with even  $C$  (even number of MBS pairs) are not topologically protected, and thus any small disorder introduced into the system destroys such Majorana states.

### N.2.2 Singular points of the Hamiltonian

To find a MBS in a system described by a PHS Hamiltonian  $H(k)$ , we seek for localised zero-energy solutions of the Schrödinger equation:  $H(k)\Phi = 0$ . In the most general case these solutions are of the form  $e^{ikr}$  that can be rewritten as  $e^{ik_{\parallel}r_{\parallel}} \cdot e^{-zr_{\perp}}$ , where  $k_{\parallel}$  denotes the 'good' quantum number and  $z$  is defined below. We analytically continue  $k$  to the complex plane and we consider the solutions of the following equation

$$\det H(k) = 0, \quad (\text{N.4})$$

defining the so-called singular points  $k_i \equiv k_{\parallel} + iz$  in the complex plane at which the determinant of the Hamiltonian vanishes. By definition  $z$  is given by the imaginary part of the singular point  $k_i$ . The practical use of these complex momentum values is the following: by continuously changing the parameters of our Hamiltonian, we continuously change the corresponding  $k_i$ 's. If we are in a topological phase,  $z$  must be positive (in other words the solution is localised). As soon as  $z$  crosses zero and becomes negative, the solution becomes delocalised, and therefore we enter a non-topological phase. Further details can be found in Refs. [182–184].

We propose the following way of constructing a phase diagram. The parameter space is given by the chemical potential  $\mu$  and the magnetic field  $B = |\mathbf{B}|$ . Firstly, we find all the  $k_i$ 's as a function of the parameters in the Hamiltonian, such that  $k_i = k_i(\mu, B), i \in \overline{1, 2N}$ , where  $2N$  is the total number of  $k_i$  solutions. We then sort them at each point in the parameter space with respect to their imaginary parts as follows:  $\text{Im } k_i < \text{Im } k_{i+1}, i \in \overline{1, 2N-1}$ . Sorting is one way to construct continuous functions  $\text{Im } k_i(\mu, B)$  in the parameter space. Although it is possible to deal with discontinuities analytically [184], in numerical simulations the continuity of  $\text{Im } k_i$ 's becomes crucial since it is hard to discriminate the zeros of  $\text{Im } k_i(\mu, B)$  from its discontinuities. Subsequently we look for the functions  $k_i(\mu, B)$  whose imaginary part crosses zero. This can be done by plotting their imaginary part as a function of the system parameters. Since Eq. (8.4) yields pairs of solutions with opposite imaginary parts, and since these pairs have been sorted according to their imaginary parts, it is therefore sufficient to plot the imaginary part of either the smallest positive root ( $i = N + 1$ ) or of the largest negative root ( $i = N$ ). The set of points  $(\mu_0, B_0)$  where  $\text{Im } k_N(\mu_0, B_0) = 0$  (or equivalently  $\text{Im } k_{N+1}(\mu_0, B_0) = 0$ ) yield thus the phase transition lines between the topological and non-topological regions in the phase diagram.

Note that this technique can in principle used also to count the number of MBS present in a given phase. The corresponding counting formula is extremely simplified when 'Exceptional points' are present [182, 183] for a system with unbroken chiral symmetry. In such a case, the Hamiltonian can be brought to a block off-diagonal form, however, when the chiral symmetry is broken, this block-off diagonal form cannot be achieved in any basis and it becomes cumbersome to isolate two sets of  $N$  continuous solutions  $k_i$  (with opposite imaginary parts) and plug them into the counting formula to get the total number of MBS. Thus we will use the singular points method only to find the phase-transition lines. In order to find the number of MBS pairs in a given phase we will rely on the numerical tight-binding calculations.

## §.3 1D wires and infinite ribbons

### §.3.1 1D wire

We start by describing the well-known phase diagram of a 1D SC wire which we take to be lying along the  $x$ -axis ( $N_y = 1$  and  $N_x \gg 1$ ). In the presence of a magnetic field the time-reversal symmetry (TRS) is broken, and only the particle-hole symmetry (PHS) holds,

therefore the system is in the topological class D described by a  $\mathbb{Z}_2$  invariant [212]. If the applied magnetic field is perpendicular to the spin-orbit direction, i.e. either  $\mathbf{B} = (0, 0, B_z)$  or  $\mathbf{B} = (B_x, 0, 0)$ , the SC wire enters a gapful topological phase as soon as  $B_x$  or  $B_z$  become larger than  $\sqrt{(\mu - 2t_x)^2 + \Delta^2}$ . The corresponding phase diagram is shown in Fig. 8.1. Further details of the  $\mathbb{Z}_2$  invariant calculation can be found in the first subsection of the Supplementary Information.

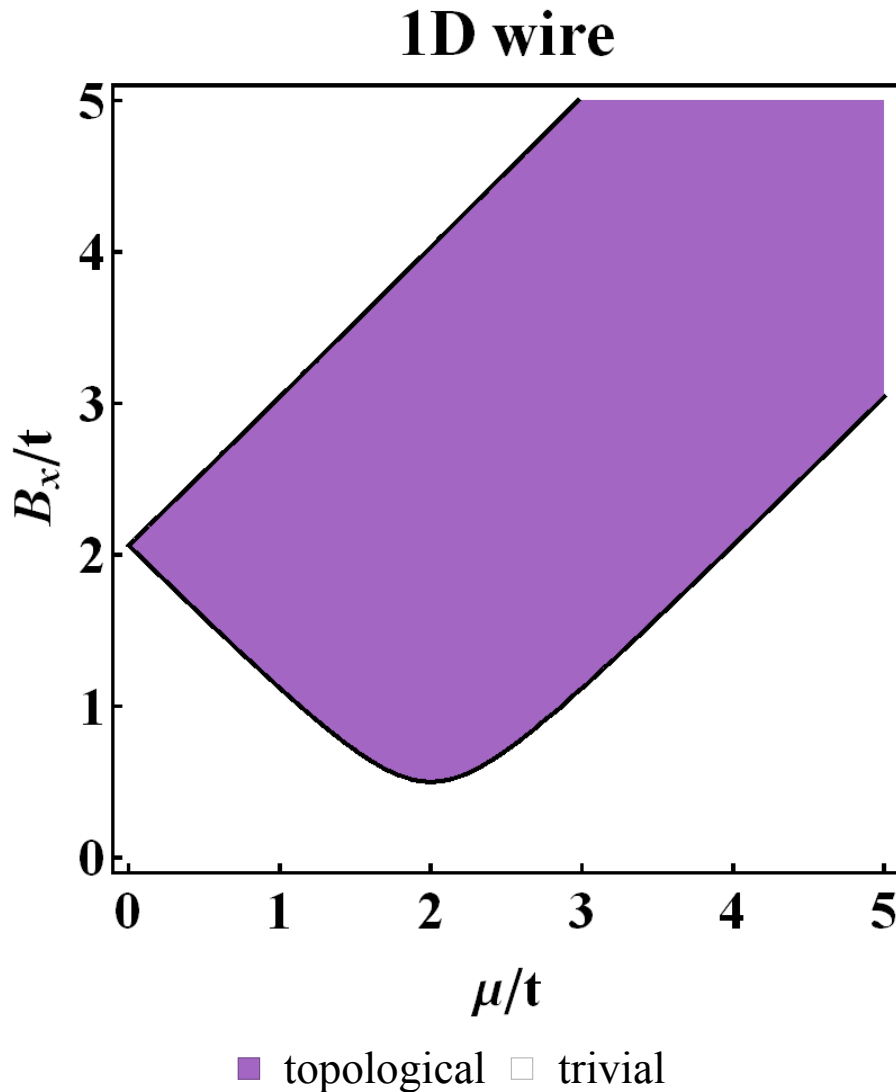


Figure 8.1: The phase diagram of a 1D superconducting nanowire obtained with topological invariant calculation as a function of the chemical potential  $\mu$  and the magnetic field along the wire  $B = B_x$  (the phase diagram remains the same in the case of a magnetic field perpendicular to the wire  $B = B_z$ ). We set  $\Delta = 0.2t$ ,  $\lambda_x = 0.5t$ .

### §.3.2 Infinite ribbon

In this subsection we study a 2D ribbon with a finite but large number of sites in the  $y$ -direction ( $N_y \gg 1$ ), and infinite in the  $x$ -direction  $N_x \rightarrow \infty$  (see Fig. §.2). We set  $\lambda_x = \lambda_y = \lambda$  and  $t_x = t_y = 1$ . We are interested in the zero-energy solutions localised at the edges of the ribbon. In Fig. §.3 we plot the band structure of this system for an in-plane magnetic field  $B_y$  parallel

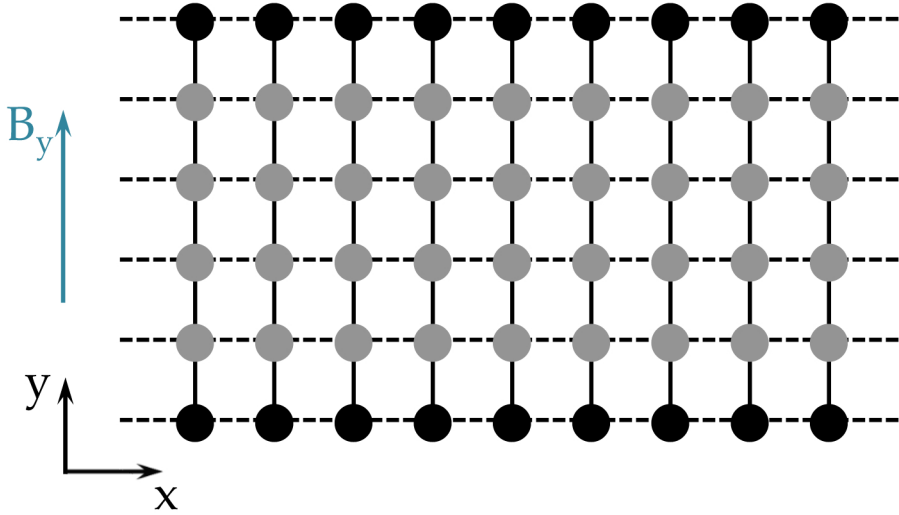


Figure §.2: A sketch of a 2D ribbon along  $x$ -axis with a magnetic field  $B = B_y$  perpendicular to its edges. The black sites denote the edges of the ribbon where the chiral Majorana modes are localised.

to the  $y$ -axis (perpendicular to the ribbon edges), as well as the topological phase diagram of such a ribbon obtained using the tight-binding numerical diagonalisation and the evaluation of the MP as described in Section §.2. First of all, we note that the spectrum is PHS even though the band structure is not. Second, as we can see from the band structure, the system may become gapless, i.e. there are region in the momentum space in which the gap in the spectrum is closing. However, despite the fact that there is no overall gap, chiral MBS do form, and they correspond to values of momenta in which the bulk spectrum remains gapped (e.g.  $k_x a = 0$  and  $k_x a = \pi$ ). Such states are localised and propagate along the edges of the ribbon. We should note that similar situations in which the closing the gap can occur for certain regions in the parameter space have been previously studied, and it has been shown that, despite the absence of an overall gap, the system can still be topological, and support MBS [214–218]. The number of MBS pairs varies from 0 to 2, depending on the parameters of the system (see Fig. §.3). However, the case of two Majorana fermions propagating at the same boundary is not stable, and in the absence of protection by TRS, for example in the presence of small disorder, such

states would combine to form a conventional fermionic state. Thus the system is topologically non-trivial only when the number of MBS pairs is equal to 1. It is also worth mentioning

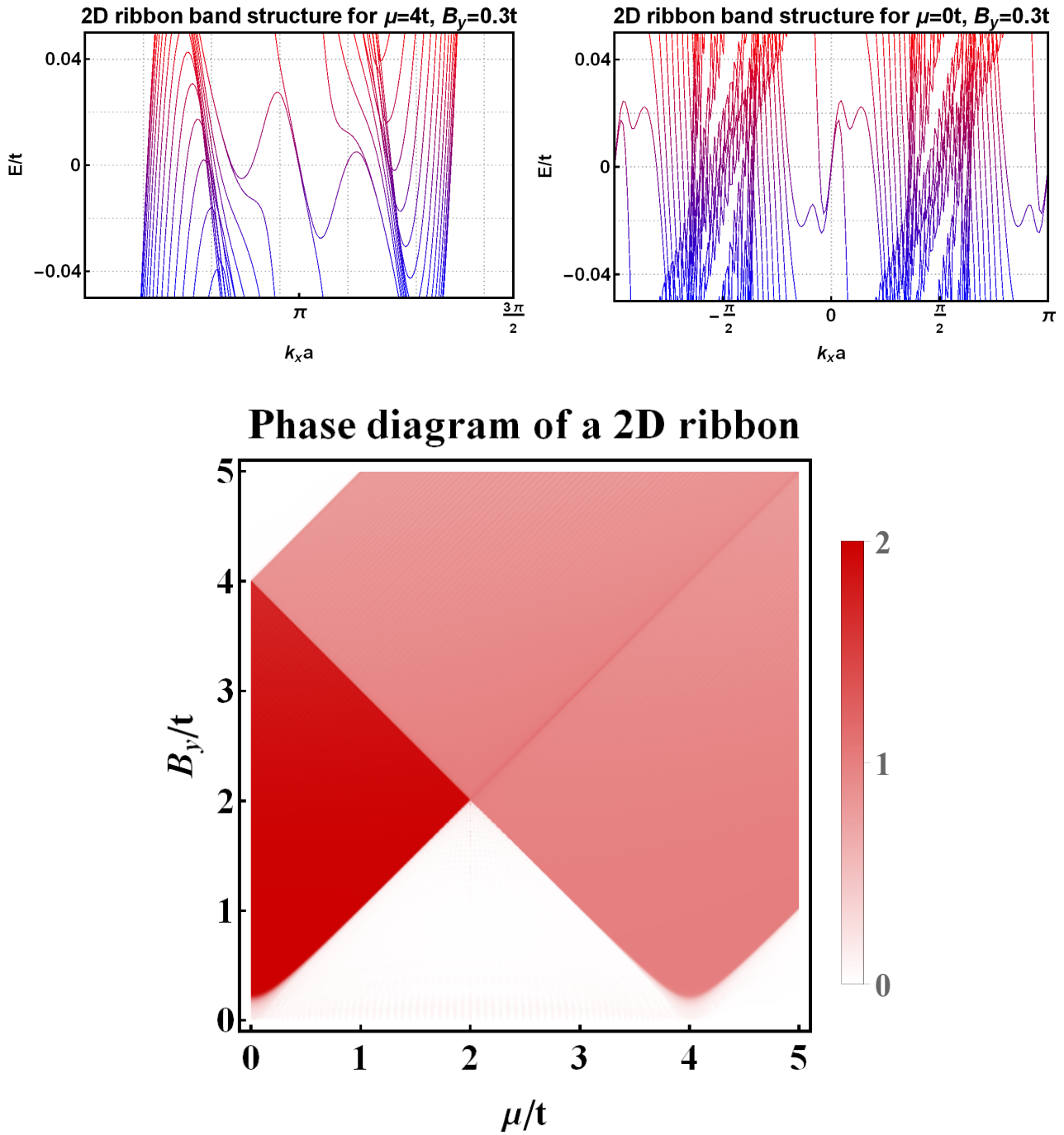


Figure 8.3: Band structure of a 2D ribbon with a magnetic field  $B = B_y$  perpendicular to the edges for  $\mu = 4t, B_y = 0.3t$  (upper left panel) and  $\mu = 0t, B_y = 0.3t$  (upper right panel). Note that the system may host either one or two pairs of chiral Majorana modes. The corresponding topological phase diagram (lower panel) depicts the number of Majorana modes (as evaluated from the total MP) as a function of  $\mu$  and  $B$ . In all the examples we set  $\Delta = 0.2t, \lambda_x = \lambda_y = 0.5t$ .

that the number of sites in the  $y$  direction must be large enough so that the overlap of the

wave functions of the two Majorana states localised on the two opposite edges of the ribbon is exponentially small, and that these states cannot hybridise and acquire a finite energy.

Note that if the magnetic field is applied along the  $x$ -axis the system is also gapless, however, in this case no Majorana modes form, for any region in the parameter space, and the system is fully trivial.

## 8.4 Finite-size strips

In what follows we focus on quasi-1D systems, i.e. systems made-up of  $N_y > 1$  coupled wires each with a finite but large number of sites  $N_x \gg 1$  and  $N_x \gg N_y$ . We consider an in-plane magnetic field  $B_x$  parallel to the long edge of the system (see Fig. 8.4). Note that for a magnetic

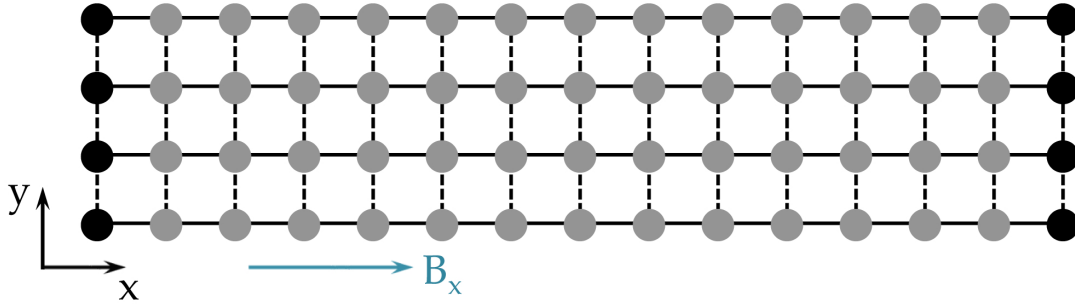


Figure 8.4: A sketch of a quasi-1D wire with a magnetic field  $B = B_x$  along the  $x$ -axis. The black sites denote the short edges of the system where the Majorana modes would be localised. The quasi-1D system can be thought of as a set of 1D wires coupled in  $y$ -direction.

field parallel to the  $y$ -axis, no Majorana states can form, since the magnetic field would in this case be parallel to the direction of the spin-orbit coupling in the wires. A similar system was considered in Ref. [211], but only for magnetic fields perpendicular to the plane of the system.

As described in Section 8.2, we will use two main tools to obtain the phase diagram for these systems. The first is to numerically diagonalise the tight-binding Hamiltonian and employ the integrated MP by plotting its value as a function of the chemical potential and the magnetic field. The second is to assume that the momentum  $k_x$  along  $x$  is a 'good' quantum number, and exploit the SP technique. In Fig. 8.5 we show numerically that the results of the first two methods are fully consistent. Each phase transition boundary defined as a change in the number of MBS pairs obtained via the MP technique corresponds to a line of zeroes in the SP plot. The only apparent exception is the special case of the white lines in the  $N_y = 4$  close to

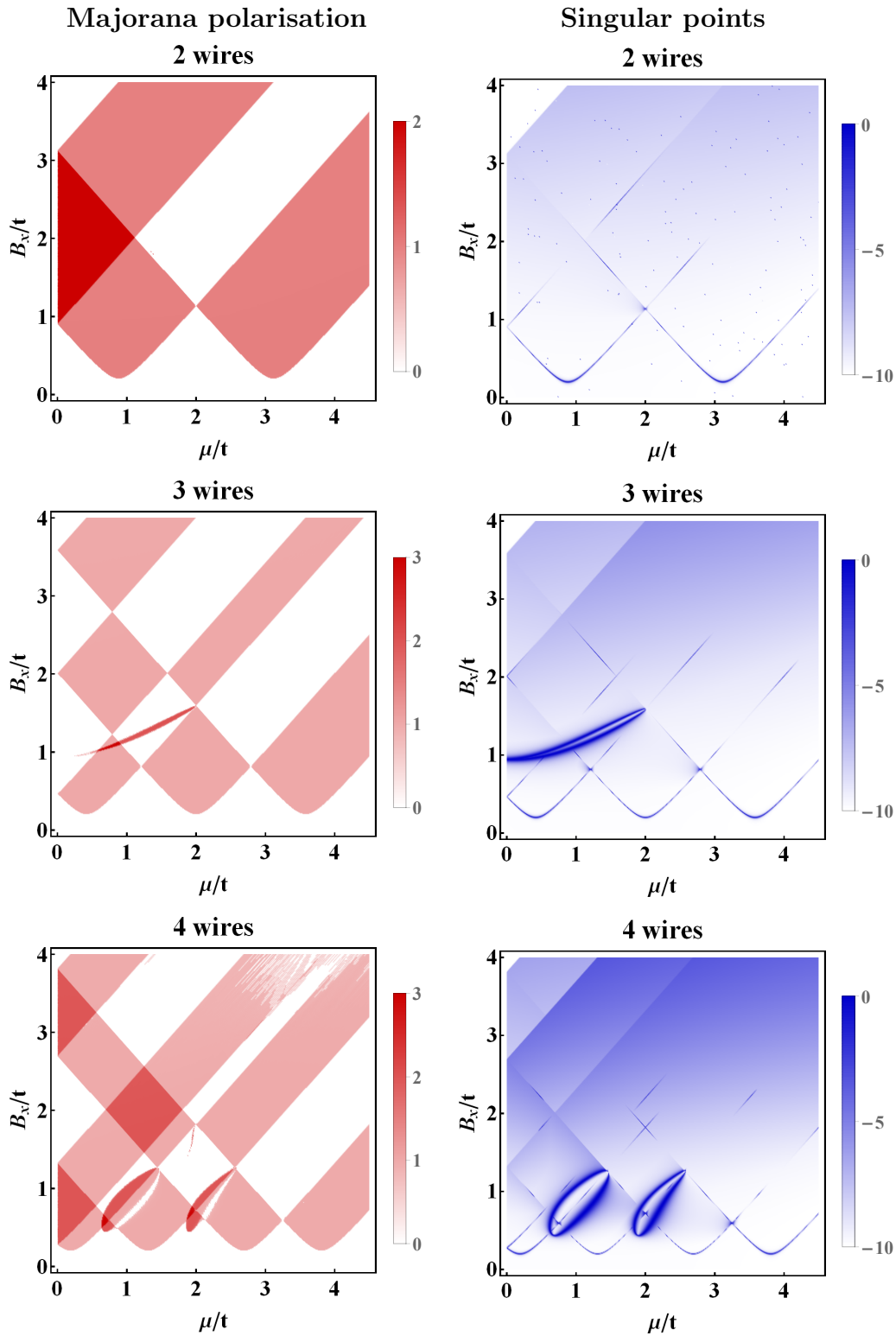


Figure 8.5: Topological phase diagrams in the  $(\mu, B_x)$  plane. In the left column we plot the total MP summed over all the low-energy states with a MP larger than a given cut-off, here taken to be 0.8. The colour scheme indicates the number of MBS pairs. In the right column we plot the results of the SP calculation; the phase transition lines are given by the zeroes of the plot. We consider systems with 2, 3 and 4 coupled wires. The results of these two methods are consistent, and the phase transition lines coincide. We set  $\Delta = 0.2t$ ,  $\lambda_x = \lambda_y = 0.5t$ .

$\mu = t$  and  $\mu = 2.2t$  and  $B = 0.5t$ . They seem to correspond to the special case of a zero-size non-topological line-like region between two topological regions with one pair of MBS. Such situations, i.e. topological regions divided by a line of non-topological points, can arise, and are well captured here by the SP method. The numerical method is a bit less precise for such situations, and the non-topological line acquires a finite width, mostly because of the finite length of the considered systems (in the infinite-length limit the width of these regions should go to zero).

Note that the integrated MP allows not only to show the phase transition boundaries, but also to give access to the number of emerging MBS. Since the chiral symmetry (a combination of the PHS and the TRS) is absent due to the magnetic field which breaks the TRS, we cannot easily use the counting formula introduced in Ref. [184] to obtain the number of Majorana modes using this method. The counting formula is in principle also applicable in the absence of the chiral symmetry, but the broken TRS case is very cumbersome and much harder to implement numerically. Therefore, we use here the SP technique only to obtain the phase transition lines; the actual number of the MBS pairs and the topological character of a given phase space region are obtained numerically via the calculation of the total MP. We should point out that some segments of the phase transition lines in the right column of Fig. §.5 are almost non-visible. This is not due to the failure of the method, but to the numerical grid: the regions in which the zeroes of the determinant occur are very thin and the number of points required in the grid would be too large to capture them entirely. We did check though that the phase transition lines are present everywhere as expected, even if not fully shown in Fig. §.5.

Note also that by increasing the number of wires we can increase the number of MBS. However, as we will show in the next section only the states with an odd number of MBS pairs are topologically protected.

## §.5 Effects of disorder and topological invariant calculations

In what follows we show that a small amount of disorder makes the Majorana modes re-combine and form regular electronic states in all the regions in the parameter space with an even number

of Majorana modes; thus these regions are not topologically protected. However, in all the regions with odd numbers of Majorana modes one MBS pair survives the effects of disorder. In the left column of Fig. 8.7 we show the phase diagrams for finite-size strips in the presence

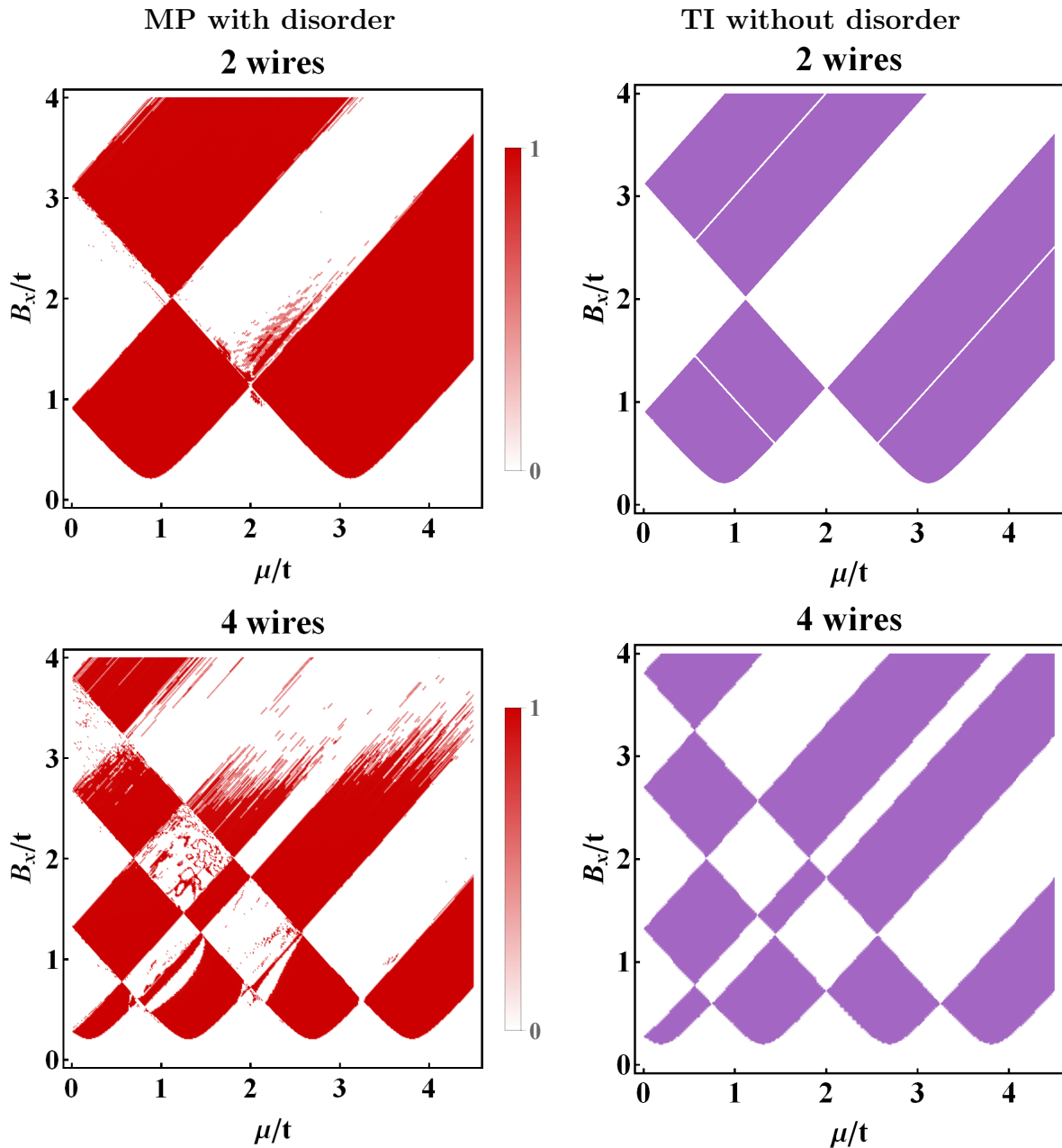


Figure 8.6: Topological phase diagrams in the  $(\mu, B_x)$  plane for 2 and 4 coupled wires. In the left column we depict the MP of the lowest-energy mode for a disordered system. We impose a MP cutoff of 0.95 (the states with MP smaller than 1 cannot be considered actual Majoranas and usually correspond to non-zero energies, even if they remain Majorana-like). In the right column we depict the phase diagram as obtained using the topological invariant calculation (without disorder) (the topological regions are shown in violet). Note that, up to some special-points lines, the TI results are fully consistent with the those for the MP in the disordered system, which is expected since the TI gives access to the parity of the number of the MBS. In all the panels  $\Delta = 0.2t$ ,  $\lambda_x = \lambda_y = 0.5t$ .

of disorder. The disorder considered here is a random variation of the value of the Zeeman magnetic field with an intensity of 5% around its average value. [209] Indeed, we see that in the even-parity regions of the phase space the Majorana modes are destroyed, confirming their non-topological character.

We also present the corresponding phase diagrams computed using the topological invariant (TI) (for the details of the derivations see the Supplementary Information, as well as Ref. [211]). In Fig. §.7 we compare the phase diagrams showing the topological regions surviving the effects of disorder (left column) and those obtained using the topological invariant (right column). Indeed, up to some sets of lines of special points, the topological regions, as predicted by the topological invariant, coincide with the regions in the phase diagram shown numerically to exhibit an odd-parity of MBS pairs and to survive the presence of disorder.

It is also worth discussing how the value of the topological gap protecting the zero-energy states changes in the presence of disorder. In Fig. §.8 we plot the energy spectra of a 4-wire finite-size strip for a fixed value of the chemical potential as a function of an in-plane magnetic field  $B_x$ , both in the absence and in the presence of disorder. This corresponds to taking vertical cuts of the lower left panels of Figs. §.5 and §.7. Without disorder, in full accordance with Fig. §.5, we have MBS for magnetic fields  $B_x$  from  $\sim 0.45t$  to  $\sim 0.73t$  and  $\sim 0.92t$  to  $\sim 1.25t$ . It is worth mentioning that certain regions contain more than one pair of MBS. The number of pairs is shown above the corresponding Majorana zero energy lines, highlighted in red. First, we note that, consistent with the phase diagrams presented in Figs. §.5 and §.7, all the regions with odd numbers of MBS are protected against disorder, exhibiting one stable zero-energy mode (*cf.* regions from  $\sim 0.55t$  to  $\sim 0.64t$  and  $\sim 0.92t$  to  $\sim 1.25t$  respectively), whereas in the regions with even numbers these states acquire a finite energy in the presence of disorder, confirming that these regions in the phase diagram are not topologically protected. Moreover we see that the gap protecting these zero-energy states is affected slightly by disorder, more significantly for the states with even numbers of Majoranas, consistent with the lack of topological protection for these states.

## §.6 Finite-size squares

If both  $N_{x,y} \gg 1$  and are comparable in size then we are dealing with an open 2D system. In

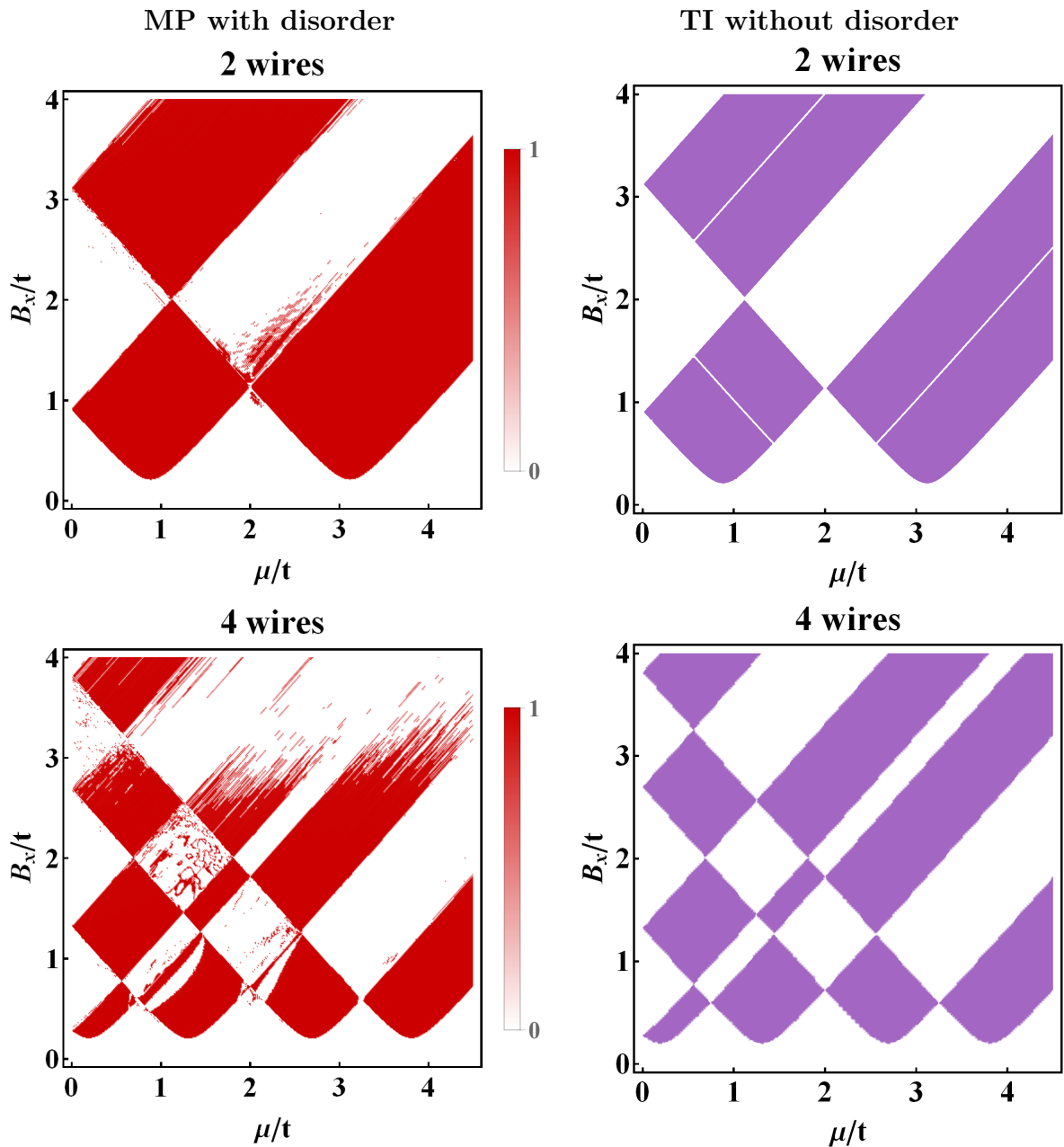


Figure 8.7: Topological phase diagrams in the  $(\mu, B_x)$  plane for 2 and 4 coupled wires. In the left column we depict the MP of the lowest-energy mode for a disordered system. We impose a MP cutoff of 0.95 (the states with MP smaller than 1 cannot be considered actual Majoranas and usually correspond to non-zero energies, even if they remain Majorana-like). In the right column we depict the phase diagram as obtained using the topological invariant calculation (without disorder) (the topological regions are shown in violet). Note that, up to some special-points lines, the TI results are fully consistent with the those for the MP in the disordered system, which is expected since the TI gives access to the parity of the number of the MBS. In all the panels  $\Delta = 0.2t$ ,  $\lambda_x = \lambda_y = 0.5t$ .

Ref. [211] it has been shown that for perpendicular Zeeman magnetic fields finite-energy quasi-Majorana-like states ( $C = \sqrt{2}/2$ ) may form, localised mostly in the corners of these square flakes, for a set of parameters inside the 2D bulk topological phase. However, for in-plane

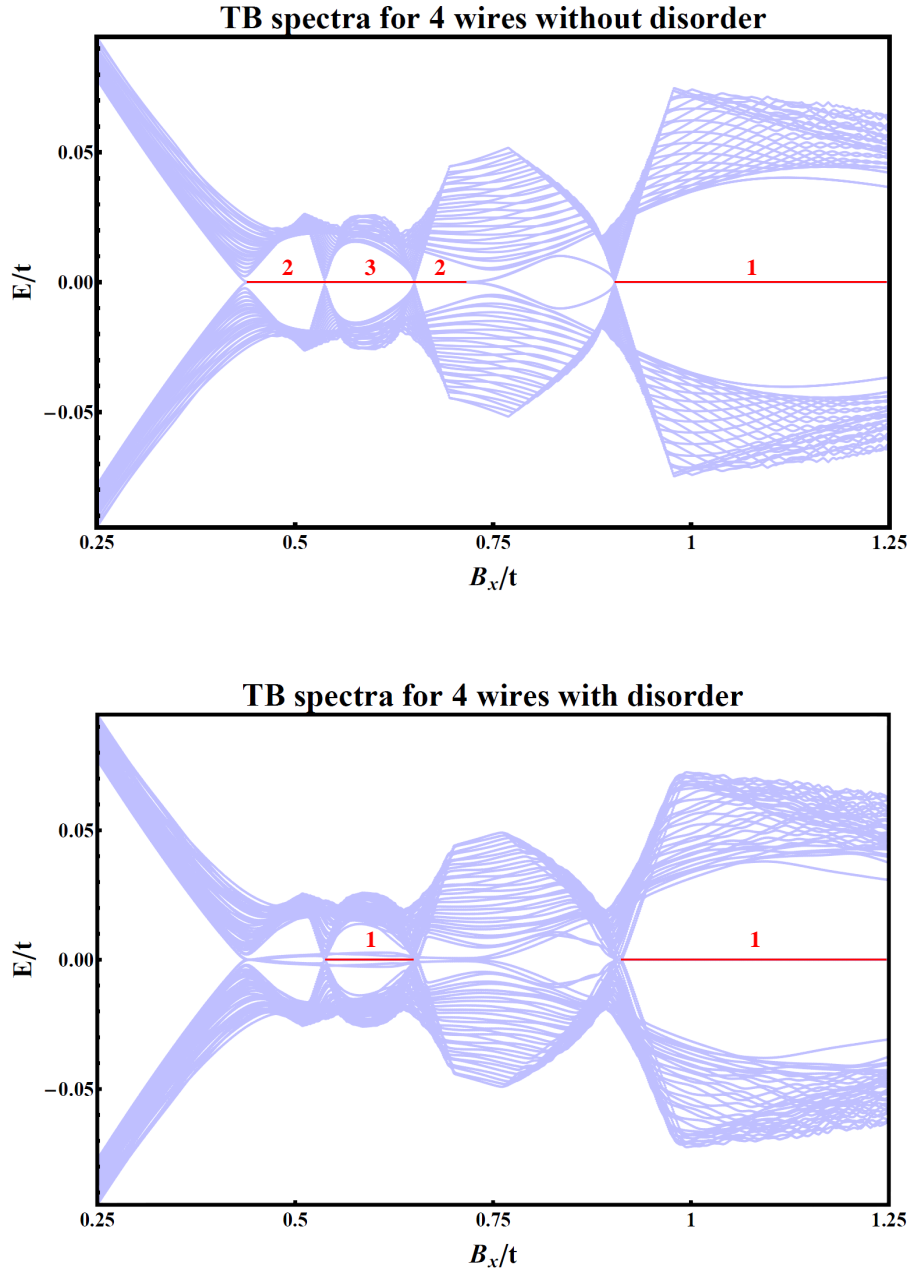


Figure 8.8: Energy spectra for 4-wires finite-size strips with and without disorder (lower and upper panel respectively) as a function of an in-plane magnetic field  $B_x$ , varying from  $0.25t$  to  $1.25t$ . We restrict ourselves to plotting only the lowest 60 energy levels and we set  $\Delta = 0.2t$ ,  $\lambda_x = \lambda_y = 0.5t$ , and  $\mu = 0.69t$ . These panels correspond to vertical cuts of lower left panels in Fig. 8.5 and 8.7 respectively. The number of pairs is shown above the corresponding Majorana zero energy lines, highlighted in red.

magnetic fields (e.g. along  $x$ -axis) the situation is very different since the rotation symmetry is broken and we always have an in-plane special direction, and we can no longer expect quasi-Majorana states with rotationally symmetric MP.

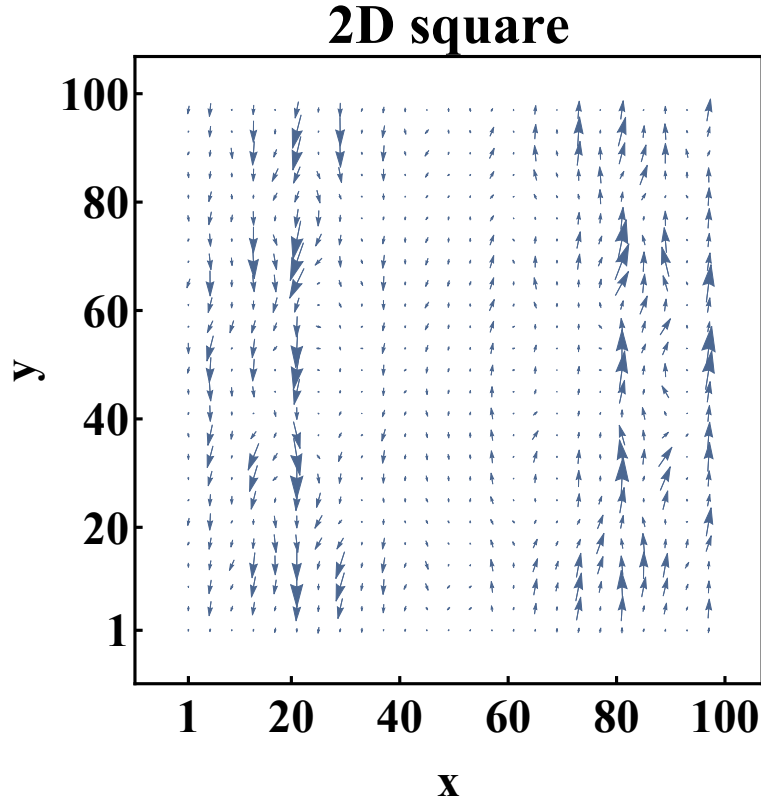


Figure 8.9: The MP vector for a square system consisting of  $100 \times 100$  sites in a magnetic field along the  $x$ -axis. We choose a set of parameters  $\mu = 4t$ ,  $B_x = 0.28t$ ,  $\Delta = 0.2t$ ,  $\lambda_x = \lambda_y = 0.5t$ .

By analysing the MP of these systems we note that the generic situation that emerges is that depicted in Fig. 8.9: quasi-disordered edge states localised on the edges of the system perpendicular to the magnetic field. Such states have also a quasi-disordered MP, and the integral of the MP over one of these edges states is finite (for the case in Fig. 8.9 this is of the order of 0.9).

This tendency to form a Majorana state is larger for values of the magnetic field close to the transition, and for systems with a very large  $N_x$  we can actually recover actual Majorana states in these systems on the edges perpendicular to the magnetic field. The systems required to recover a full Majorana are too large for our numerical abilities, but even for smaller systems we have managed to tune up the parameters to get a MP up to 0.9, and increasing the size will improve this value. This is important from an experimental perspective, since it indicates that for in-plane fields actual Majorana states can form even in wide square systems, while for perpendicular fields this can never be the case unless one dimension is much larger than the

other one.

## §.7 Conclusions

We have studied the formation of Majorana bound states in infinite ribbons, finite-size strips and squares with Rashba spin-orbit coupling and an in-plane magnetic field. We have shown that in infinite ribbons chiral Majorana fermions may form when the magnetic field is perpendicular to the edges of the ribbon. Furthermore, we have studied finite-size strips exploiting a numerical diagonalisation technique and the Majorana polarisation, as well as the singular points technique, and we have proven the qualitative equivalence of these two methods in constructing the phase diagrams of these systems. We have also evaluated the topological invariant for the quasi-1D systems and we have shown that its usage allows one to obtain the correct phase diagrams for the parity of the number of MBS pairs. Moreover, we have confirmed numerically that the phases with even number of MBS pairs are not stable in the presence of disorder, and are thus topologically trivial, while the phases with an odd number of MBS preserve their topological character.

## §.8 Supplementary Information: TI calculation

In what follows we compute topological invariants for several systems discussed above. We write the Bogoliubov-de Gennes Hamiltonian on a square lattice in the Nambu basis  $\{\psi_\uparrow, \psi_\downarrow, \psi_\downarrow^\dagger, -\psi_\uparrow^\dagger\}$  as:

$$\mathcal{H}(k) = \begin{pmatrix} f(k) & \mathcal{L}(k) & \Delta & 0 \\ \mathcal{L}^*(k) & f(k) & 0 & \Delta \\ \Delta & 0 & -f(k) & \mathcal{L}^*(-k) \\ 0 & \Delta & \mathcal{L}(-k) & -f(k) \end{pmatrix} + \begin{pmatrix} B_z & B_- & 0 & 0 \\ B_+ & -B_z & 0 & 0 \\ 0 & 0 & B_z & B_- \\ 0 & 0 & B_+ & -B_z \end{pmatrix} \quad (\text{§.5})$$

where  $\mathbf{B} = (B_x, B_y, B_z)$  is the magnetic field,  $B_\pm \equiv B_x \pm iB_y$ ,  $f(k)$  is the dimension-dependent dispersion for electrons on the lattice with a chemical potential  $\mu$  and a hopping parameter  $t$ , while  $\mathcal{L}(k)$  is the Rashba spin-orbit coupling term, which also depends on the dimensionality of the lattice. We disregard the orbital effects of the magnetic field. The Hamiltonian given by

Eq. (8.5) is particle-hole symmetric, i.e.

$$\Xi \mathcal{H}(k) \Xi^{-1} = -\mathcal{H}(-k), \quad \Xi \equiv \sigma_y \otimes \tau_y \mathcal{K}, \quad (8.6)$$

where  $\mathcal{K}$  is the complex conjugate operator, and we set  $\Lambda \equiv \sigma_y \otimes \tau_y$ .

### 8.8.1 1D wires

We consider a 1D superconducting nanowire with Rashba spin-orbit coupling and with an arbitrary direction of the magnetic field. We thus have  $f(k) \equiv -2t \cos k - \mu$  and  $\mathcal{L}(k) \equiv i\lambda \sin k$ . As long as the magnetic field is not collinear with the spin-orbit coupling ( $B_z$  or  $B_x$ , but not

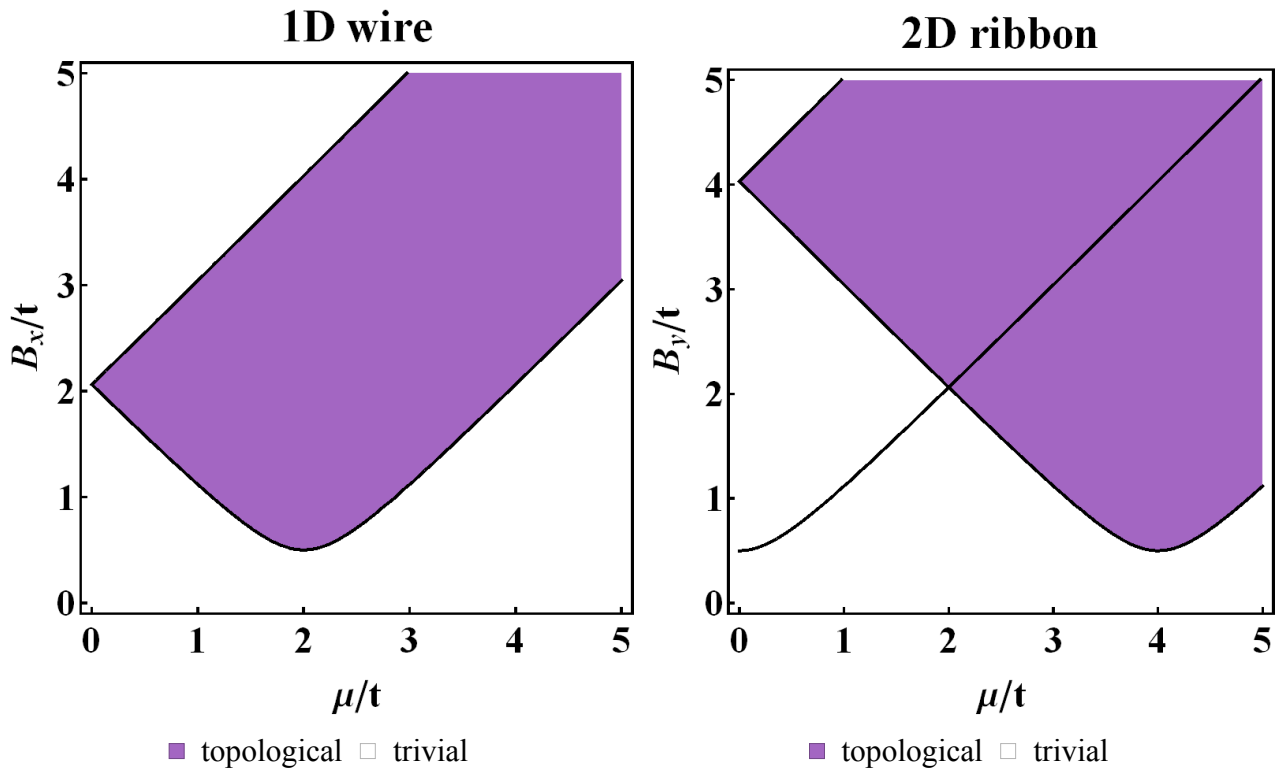


Figure 8.10: The phase diagram of a 1D nanowire (left panel) and of a 2D ribbon (right panel) as a function of the chemical potential  $\mu$  and the magnetic field  $B$ , obtained using a topological invariant calculation. In the case of a wire the magnetic field is either along the wire  $B = B_x$  or perpendicular to the wire  $B = B_z$ , whereas in the case of a 2D ribbon it is perpendicular to the edge of the ribbon, i.e.  $B = B_y$ . The black lines correspond to the values for which the topological invariant  $\delta = 0$ . The topological regions are coloured in violet. We set  $\Delta = 0.2t, \lambda_x = 0.5t, \lambda_y = 0t$  for the left panel and  $\Delta = 0.2t, \lambda_x = \lambda_y = 0.5t$  for the right one.

$B_y$ ), the system stays gapful and thus topological invariants are well-defined. Time-reversal

symmetry is broken in the presence of a magnetic field, therefore we expect to have a  $\mathbb{Z}_2$  topological invariant in accordance with the classification in Ref. [212]. On the contrary, if we consider the case of a non-zero  $B_y$  along the y-axis, we end up having a gapless trivial phase. Thus, below we set  $B_y = 0$ .

To compute the topological invariant we seek the Gamma-points of the Hamiltonian (8.5), i.e. the points for which  $\mathcal{L}(k) = 0$ . It is easy to see that within the first Brillouin zone we have two such points:  $\Gamma_1 = 0$ ,  $\Gamma_2 = \pi$ . At each of these points one can define a skew-symmetric matrix  $W(k = \Gamma_i) = \mathcal{H}(k = \Gamma_i)\Lambda$  with an associated Pfaffian. The topological invariant is given by

$$\delta = \prod_{k=\Gamma_i} \frac{\sqrt{\det [W(k)]}}{\text{Pf} [W(k)]}. \quad (8.7)$$

This expression can be simplified using the identity  $(\text{Pf} A)^2 = \det A$ , thus yielding:

$$\delta = \prod_{k=\Gamma_i} \text{sgn Pf} [W(k)] = \text{sgn Pf} [W(0)] \text{sgn Pf} [W(\pi)]. \quad (8.8)$$

We compute the corresponding Pfaffians

$$\text{Pf} [W(0)] = B^2 - \Delta^2 - (\mu + 2t)^2, \quad \text{Pf} [W(\pi)] = B^2 - \Delta^2 - (\mu - 2t)^2,$$

where  $B^2 \equiv |\mathbf{B}|^2 = B_x^2 + B_z^2$ . Therefore, the topological invariant is given by:

$$\delta = \text{sgn} \left[ (B^2 - \Delta^2 - (\mu + 2t)^2)(B^2 - \Delta^2 - (\mu - 2t)^2) \right]. \quad (8.9)$$

The corresponding phase diagram is given in Fig. 8.1 as well as on the left panel of Fig. 8.10.

### 8.8.2 2D systems

For this system  $f(\mathbf{k}) \equiv -2t(\cos k_x + \cos k_y) - \mu$  and  $\mathcal{L}(\mathbf{k}) \equiv i\lambda(\sin k_x - i \sin k_y)$  is the Rashba spin-orbit coupling term. Despite the fact that in parallel magnetic fields the system can become gapless for certain regions in the parameter space, below we compute *formally* a  $\mathbb{Z}_2$  topological invariant. This invariant should indicate the parity of the number of Majorana modes arising at the edges introduced into the system. To compute the topological invariant we find the Gamma-points of the Hamiltonian (8.5), i.e. the points where  $\mathcal{L}(\mathbf{k}) = 0$ . Within the first

Brillouin zone there are four such points:  $\Gamma_1 = (0, 0)$ ,  $\Gamma_2 = (\pi, 0)$ ,  $\Gamma_3 = (0, \pi)$ ,  $\Gamma_4 = (\pi, \pi)$ . At each of these points one can define a skew-symmetric matrix  $W(\mathbf{k} = \Gamma_i) = \mathcal{H}(\mathbf{k} = \Gamma_i)\Lambda$  with an associated Pfaffian. Exactly as in the previous subsection the topological invariant is given by

$$\delta = \prod_{\mathbf{k}=\Gamma_i} \text{sgn Pf}[W(\mathbf{k})]. \quad (\aleph.10)$$

Computing the corresponding Pfaffians we get:

$$\begin{aligned} \text{Pf}[W(\Gamma_1)] &= B^2 - \Delta_s^2 - (\mu + 4t)^2, \quad \text{Pf}[W(\Gamma_4)] = B^2 - \Delta^2 - (\mu - 4t)^2, \\ \text{Pf}[W(\Gamma_2)] &= \text{Pf}[W(\Gamma_3)] = B^2 - \Delta^2 - \mu^2, \end{aligned}$$

where  $B^2 \equiv |\mathbf{B}|^2 = B_x^2 + B_y^2 + B_z^2$ . Therefore, the topological invariant is given by:

$$\delta = (B^2 - \Delta^2 - \mu^2)^2 \text{sgn} \left[ (B^2 - \Delta^2 - (\mu + 4t)^2)(B^2 - \Delta^2 - (\mu - 4t)^2) \right]. \quad (\aleph.11)$$

A corresponding phase diagram is given in the right panel of the Fig.  $\aleph.10$ . It is clear that there is no difference between the cases of a magnetic field perpendicular to the plane and an in-plane magnetic field perpendicular to the edges of the ribbon (note however that an in-plane magnetic field parallel to the edges of the ribbon does not give rise to a topological phase for any region in the parameter space). Despite the closing of the gap, this calculation yields the correct result for the parity of the number of Majorana modes (compare with the results of the numerical simulations presented in Fig.  $\aleph.3$ ).

### $\aleph.8.3$ Infinite ribbons and finite-size strips

We follow the section about finite-size strips in Ref. [211], but instead of considering a magnetic field perpendicular to the plane of the system, we consider also non-zero in-plane components of the magnetic field,  $B_x$  and  $B_y$ . The Fourier-transformed Hamiltonian of this system in the case of  $N_y$  coupled wires can be written in the Nambu basis  $\{\psi_\uparrow, \psi_\downarrow, \psi_\downarrow^\dagger, -\psi_\uparrow^\dagger\}^T$  in the following

manner:

$$\begin{aligned}
 \mathcal{H}(k) &= \\
 &= \begin{pmatrix} f(k)\mathbb{I}_{N_y} - tM_{1N_y} & \mathcal{L}(k)\mathbb{I}_{N_y} + i\lambda M_{2N_y} & \Delta\mathbb{I}_{N_y} & \hat{0} \\ [-\mathcal{L}(k)\mathbb{I}_{N_y} - i\lambda M_{2N_y}]^T & f(k)\mathbb{I}_{N_y} - tM_{1N_y} & \hat{0} & \Delta\mathbb{I}_{N_y} \\ \Delta\mathbb{I}_{N_y} & \hat{0} & -f(k)\mathbb{I}_{N_y} + tM_{1N_y} & [\mathcal{L}(-k)\mathbb{I}_{N_y} + i\lambda M_{2N_y}]^T \\ \hat{0} & \Delta\mathbb{I}_{N_y} & -\mathcal{L}(-k)\mathbb{I}_{N_y} - i\lambda M_{2N_y} & -f(k)\mathbb{I}_{N_y} + tM_{1N_y} \end{pmatrix} \\
 &+ \begin{pmatrix} B_z\mathbb{I}_{N_y} & (B_x - iB_y)\mathbb{I}_{N_y} & \hat{0} & \hat{0} \\ (B_x + iB_y)\mathbb{I}_{N_y} & -B_z\mathbb{I}_{N_y} & \hat{0} & \hat{0} \\ \hat{0} & \hat{0} & B_z\mathbb{I}_{N_y} & (B_x - iB_y)\mathbb{I}_{N_y} \\ \hat{0} & \hat{0} & (B_x + iB_y)\mathbb{I}_{N_y} & -B_z\mathbb{I}_{N_y} \end{pmatrix}, \tag{8.12}
 \end{aligned}$$

where the  $N_y \times N_y$  square matrices  $\mathbb{I}_{N_y}$ ,  $M_{1N_y}$ ,  $M_{2N_y}$  act in the sublattice space and are defined as follows:

$$[\mathbb{I}_{N_y}]_{ij} = \delta_{ij}, \quad [M_{1N_y}]_{ij} = \delta_{i,j-1} + \delta_{i-1,j}, \quad [M_{2N_y}]_{ij} = -\delta_{i,j-1} + \delta_{i-1,j}, \quad \forall i, j \in \overline{1, N_y},$$

with  $\delta$  denoting the Kronecker delta. We define also the spectrum of the free electrons  $f(k) = -2t \cos k - \mu$ , and the spin-orbit coupling term  $\mathcal{L}(k) = -2i\lambda \sin k$ . In this system the PHS operator can be written as follows:

$$\Xi \equiv \Lambda \mathcal{K} \equiv \begin{pmatrix} \hat{0} & \hat{0} & \hat{0} & -\mathbb{I}_{N_y} \\ \hat{0} & \hat{0} & \mathbb{I}_{N_y} & \hat{0} \\ \hat{0} & \mathbb{I}_{N_y} & \hat{0} & \hat{0} \\ -\mathbb{I}_{N_y} & \hat{0} & \hat{0} & \hat{0} \end{pmatrix} \mathcal{K}, \tag{8.13}$$

where  $\mathcal{K}$  is the complex conjugation operator. We take the same path as in the previous subsections: firstly, we find the Gamma-points of the Hamiltonian (8.12), i.e. the points where  $\mathcal{L}(k) = 0$ . We find only two such points in the first Brillouin zone:  $\Gamma_1 = 0$ ,  $\Gamma_2 = \pi$ . A skew-symmetric matrix  $W(k = \Gamma_i) \equiv \mathcal{H}(k = \Gamma_i)\Lambda$  is defined at each of those points along with an

associated Pfaffian. Exactly as before, the topological invariant is given by

$$\delta = \text{sgn Pf} [W(0)] \text{sgn Pf} [W(\pi)] \quad (\aleph.14)$$

We do not give here the analytical expressions for  $\delta$  since they are quite cumbersome. To obtain the topological phase diagram we plot in the right column of Fig. [\aleph.7](#) the topological invariant as given by Eq. [\(\aleph.14\)](#), as a function of an in-plane magnetic field  $B_x$  and the chemical potential  $\mu$ .

# Bibliography

- [1] D. van Delft and P. Kes, “The discovery of superconductivity,” *Physics Today*, vol. 63, no. 9, 2010.
- [2] W. Meissner and R. Ochsenfeld, “Ein neuer Effekt bei Eintritt der Supraleitfähigkeit,” *Die Naturwissenschaften*, vol. 21, no. 44, 1933.
- [3] E. Maxwell, “Isotope effect in the superconductivity of mercury,” *Phys. Rev.*, vol. 78, 1950.
- [4] C. A. Reynolds, B. Serin, W. H. Wright, and L. B. Nesbitt, “Superconductivity of isotopes of mercury,” *Phys. Rev.*, vol. 78, 1950.
- [5] V. L. Ginzburg and L. D. Landau, “On the theory of superconductivity,” *Zh. Eksp. Teor. Fiz.*, vol. 20, 1950.
- [6] J. Bardeen, L. N. Cooper, and J. R. Schrieffer, “Microscopic theory of superconductivity,” *Phys. Rev.*, vol. 106, 1957.
- [7] L. P. Gor’kov, “Microscopic derivation of the Ginzburg-Landau equations in the theory of superconductivity,” *Zh. Eksp. Teor. Fiz.*, vol. 36, 1959.
- [8] R. Balian and N. R. Werthamer, “Superconductivity with pairs in a relative  $p$ -wave,” *Phys. Rev.*, vol. 131, 1963.
- [9] J. Friedel, “Metallic alloys,” *Il Nuovo Cimento*, vol. 7, no. S2, 1958.
- [10] Y. Hasegawa and P. Avouris, “Direct observation of standing wave formation at surface steps using scanning tunneling spectroscopy,” *Phys. Rev. Lett.*, vol. 71, 1993.

- [11] M. F. Crommie, C. P. Lutz, and D. M. Eigler, “Imaging standing waves in a two-dimensional electron gas,” *Nature*, vol. 363, 1993.
- [12] K. Kanisawa, M. J. Butcher, H. Yamaguchi, and Y. Hirayama, “Imaging of Friedel oscillation patterns of two-dimensionally accumulated electrons at epitaxially grown InAs(111) *A* surfaces,” *Phys. Rev. Lett.*, vol. 86, 2001.
- [13] C. Bena, “Effect of a single localized impurity on the local density of states in monolayer and bilayer graphene,” *Phys. Rev. Lett.*, vol. 100, 2008.
- [14] S. N. Artemenko, G. Xianlong, and W. Wonneberger, “Friedel oscillations in a gas of interacting one-dimensional fermionic atoms confined in a harmonic trap,” *Journal of Physics B: Atomic, Molecular and Optical Physics*, vol. 37, no. 7, 2004.
- [15] S. N. Artemenko, S. V. Remizov, and D. S. Shapiro, “Impurity-induced coherent current oscillations in one-dimensional conductors,” *JETP Letters*, vol. 87, no. 12, 2008.
- [16] A. Virosztek and Á. Bácsi, “Friedel oscillations around a short range scatterer: The case of graphene,” *Journal of Superconductivity and Novel Magnetism*, vol. 25, no. 3, 2012.
- [17] J.-W. Rhim and Y. B. Kim, “Anisotropic density fluctuations, plasmons, and Friedel oscillations in nodal line semimetal,” *New Journal of Physics*, vol. 18, no. 4, 2016.
- [18] F. Vonau, D. Aubel, G. Gewinner, C. Pirri, J. C. Peruchetti, D. Bolmont, and L. Simon, “Fermi contour imaging of the two-dimensional semimetal ErSi<sub>2</sub> by Fourier-transform scanning tunneling spectroscopy,” *Phys. Rev. B*, vol. 69, 2004.
- [19] F. Vonau, D. Aubel, G. Gewinner, S. Zabrocki, J. C. Peruchetti, D. Bolmont, and L. Simon, “Evidence of hole-electron quasiparticle interference in ErSi<sub>2</sub> semimetal by Fourier-transform scanning tunneling spectroscopy,” *Phys. Rev. Lett.*, vol. 95, 2005.
- [20] L. Simon, C. Bena, F. Vonau, M. Cranney, and D. Aubel, “Fourier-transform scanning tunnelling spectroscopy: the possibility to obtain constant-energy maps and band dispersion using a local measurement,” *Journal of Physics D: Applied Physics*, vol. 44, no. 46, 2011.
- [21] P. Anderson, “Theory of dirty superconductors,” *Journal of Physics and Chemistry of Solids*, vol. 11, no. 1-2, 1959.

- [22] B. T. Matthias, H. Suhl, and E. Corenzwit, “Spin exchange in superconductors,” *Phys. Rev. Lett.*, vol. 1, 1958.
- [23] L. Yu, “Bound state in superconductors with paramagnetic impurities,” *Acta Physica Sinica*, vol. 21, no. 1, 1965.
- [24] H. Shiba, “Classical spins in superconductors,” *Progress of Theoretical Physics*, vol. 40, no. 3, 1968.
- [25] A. I. Rusinov, “Superconductivity near a paramagnetic impurity,” *Soviet Journal of Experimental and Theoretical Physics Letters*, vol. 9, 1969.
- [26] A. Yazdani, B. A. Jones, C. P. Lutz, M. F. Crommie, and D. M. Eigler, “Probing the local effects of magnetic impurities on superconductivity,” *Science*, vol. 275, 1997.
- [27] G. Ménard and *et al.*, “Coherent long-range magnetic bound states in a superconductor,” *Nature Physics*, vol. 11, 2015.
- [28] T. Meng, J. Klinovaja, S. Hoffman, P. Simon, and D. Loss, “Superconducting gap renormalization around two magnetic impurities: From Shiba to Andreev bound states,” *Phys. Rev. B*, vol. 92, 2015.
- [29] W. Gerlach and O. Stern, “Der experimentelle Nachweis des magnetischen Moments des Silberatoms,” *Zeitschrift für Physik*, vol. 8, no. 1, 1922.
- [30] W. Gerlach and O. Stern, “Der experimentelle Nachweis der Richtungsquantelung im Magnetfeld,” *Zeitschrift für Physik*, vol. 9, no. 1, 1922.
- [31] W. Gerlach and O. Stern, “Das magnetische Moment des Silberatoms,” *Zeitschrift für Physik*, vol. 9, no. 1, 1922.
- [32] R. Wiesendanger, “Spin mapping at the nanoscale and atomic scale,” *Rev. Mod. Phys.*, vol. 81, 2009.
- [33] C. Moca, E. Demler, B. Jankó, and G. Zaránd, “Spin-resolved spectra of Shiba multiplets from Mn impurities in MgB<sub>2</sub>,” *Phys. Rev. B*, vol. 77, 2008.
- [34] A. V. Balatsky, I. Vekhter, and J.-X. Zhu, “Impurity-induced states in conventional and unconventional superconductors,” *Rev. Mod. Phys.*, vol. 78, 2006.

- [35] F. Pientka, L. I. Glazman, and F. von Oppen, “Topological superconducting phase in helical Shiba chains,” *Phys. Rev. B*, vol. 88, 2013.
- [36] L. H. Thomas, “The motion of the spinning electron,” *Nature (London)*, vol. 117, p. 514, 1926.
- [37] Y. A. Bychkov and E. I. Rashba, “Properties of a 2D electron gas with lifted spectral degeneracy,” *JETP Letters*, vol. 39, 1984.
- [38] A. Manchon, A. H. C. Koo, J. Nitta, S. M. Frolov, and R. A. Duine, “New perspectives for Rashba spin-orbit coupling,” *Nature Materials*, vol. 14, 2015.
- [39] M. Z. Hasan and C. L. Kane, “Colloquium: Topological insulators,” *Rev. Mod. Phys.*, vol. 82, 2010.
- [40] X.-L. Qi and S.-C. Zhang, “Topological insulators and superconductors,” *Rev. Mod. Phys.*, vol. 83, 2011.
- [41] C. L. Kane and E. J. Mele, “Quantum spin Hall effect in graphene,” *Phys. Rev. Lett.*, vol. 95, 2005.
- [42] M. König, S. Wiedmann, C. Brüne, A. Roth, H. Buhmann, L. W. Molenkamp, X.-L. Qi, and S.-C. Zhang, “Quantum spin Hall effect and topological phase transition in HgTe quantum wells,” *Science*, vol. 318, 2007.
- [43] B. A. Bernevig, T. L. Hughes, and S.-C. Zhang, “Quantum spin Hall effect and topological phase transition in HgTe quantum wells,” *Science*, vol. 314, 2006.
- [44] D. Hsieh, Y. Xia, D. Qian, L. Wray, F. Meier, J. H. Dil, J. Osterwalder, L. Patthey, A. V. Fedorov, H. Lin, A. Bansil, D. Grauer, Y. S. Hor, R. J. Cava, and M. Z. Hasan, “Observation of time-reversal-protected single-Dirac-cone topological-insulator states in  $\text{Bi}_2\text{Te}_3$  and  $\text{Sb}_2\text{Te}_3$ ,” *Phys. Rev. Lett.*, vol. 103, 2009.
- [45] D. Hsieh, , Y. Xia, D. Qian, L. Wray, J. H. Dil, F. Meier, J. Osterwalder, L. Patthey, J. G. Checkelsky, N. P. Ong, A. V. Fedorov, H. Lin, A. Bansil, D. Grauer, Y. S. Hor, R. J. Cava, and M. Z. Hasan, “A tunable topological insulator in the spin helical Dirac transport regime,” *Nature*, vol. 460, 2009.

- [46] Y. Oreg, G. Refael, and F. von Oppen, “Helical liquids and Majorana bound states in quantum wires,” *Phys. Rev. Lett.*, vol. 105, 2010.
- [47] R. M. Lutchyn, J. D. Sau, and S. Das Sarma, “Majorana fermions and a topological phase transition in semiconductor-superconductor heterostructures,” *Phys. Rev. Lett.*, vol. 105, 2010.
- [48] J. D. Sau, R. M. Lutchyn, S. Tewari, and S. Das Sarma, “Generic new platform for topological quantum computation using semiconductor heterostructures,” *Phys. Rev. Lett.*, vol. 104, 2010.
- [49] J. Alicea, “Majorana fermions in a tunable semiconductor device,” *Phys. Rev. B*, vol. 81, 2010.
- [50] V. Mourik, K. Zuo, S. M. Frolov, P. S. M., E. P. A. M. Bakkers, and L. P. Kouwenhoven, “Signatures of Majorana fermions in hybrid superconductor-semiconductor nanowire devices,” *Science*, vol. 336, 2012.
- [51] M. T. Deng, C. L. Yu, G. Y. Huang, M. Larsson, P. Caroff, and H. Q. Xu, “Anomalous zero-bias conductance peak in a Nb-insb nanowire-Nb hybrid device,” *Nano lett.*, vol. 12, 2012.
- [52] A. Das, Y. Ronen, Y. Most, Y. Oreg, M. Heiblum, and H. Shtrikman, “Zero-bias peaks and splitting in an Al-InAs nanowire topological superconductor as a signature of Majorana fermions,” *Nature Physics*, vol. 8, 2012.
- [53] H. O. H. Churchill, V. Fatemi, K. Grove-Rasmussen, M. T. Deng, P. Caroff, H. Q. Xu, and C. M. Marcus, “Superconductor-nanowire devices from tunneling to the multichannel regime: Zero-bias oscillations and magnetoconductance crossover,” *Phys. Rev. B*, vol. 87, no. 24, 2013.
- [54] S. M. Albrecht, A. P. Higginbotham, M. Madsen, F. Kuemmeth, T. S. Jespersen, J. Nygard, P. Krogstrup, and C. M. Marcus, “Exponential protection of zero modes in Majorana islands,” *Nature*, vol. 531, 2016.
- [55] A. P. Mackenzie and Y. Maeno, “The superconductivity of  $\text{Sr}_2\text{RuO}_4$  and the physics of spin-triplet pairing,” *Rev. Mod. Phys.*, vol. 75, 2003.

- [56] R. Joynt and L. Taillefer, “The superconducting phases of  $\text{UPt}_3$ ,” *Rev. Mod. Phys.*, vol. 74, 2002.
- [57] S. Sasaki, M. Kriener, K. Segawa, K. Yada, Y. Tanaka, M. Sato, and Y. Ando, “Topological superconductivity in  $\text{Cu}_x\text{Bi}_2\text{Se}_3$ ,” *Phys. Rev. Lett.*, vol. 107, 2011.
- [58] J. Sinova, S. O. Valenzuela, J. Wunderlich, C. H. Back, and T. Jungwirth, “Spin Hall effects,” *Rev. Mod. Phys.*, vol. 87, 2015.
- [59] I. Žutić, J. Fabian, and S. Das Sarma, “Spintronics: Fundamentals and applications,” *Rev. Mod. Phys.*, vol. 76, 2004.
- [60] S. LaShell, B. A. McDougall, and E. Jensen, “Spin splitting of an  $\text{Au}(111)$  surface state band observed with angle resolved photoelectron spectroscopy,” *Phys. Rev. Lett.*, vol. 77, no. 16, 1996.
- [61] C. R. Ast, J. Henk, A. Ernst, L. Moreschini, M. C. Falub, D. Pacilé, P. Bruno, K. Kern, and M. Grioni, “Giant spin splitting through surface alloying,” *Phys. Rev. Lett.*, vol. 98, no. 18, 2007.
- [62] A. Varykhalov, D. Marchenko, M. R. Scholz, E. D. L. Rienks, T. K. Kim, G. Bihlmayer, J. Sánchez-Barriga, and O. Rader, “ $\text{Ir}(111)$  surface state with giant Rashba splitting persists under graphene in air,” *Phys. Rev. Lett.*, vol. 108, no. 6, 2012.
- [63] M. Hoesch, T. Greber, V. Petrov, M. Muntwiler, M. Hengsberger, W. Auwärter, and J. Osterwalder, “Spin-polarized Fermi surface mapping,” *Journal of Electron Spectroscopy and Related Phenomena*, vol. 124, no. 2-3, 2002.
- [64] M. Hochstrasser, J. G. Tobin, E. Rotenberg, and S. D. Kevan, “Spin-resolved photoemission of surface states of  $\text{W}(110)-(1 \times 1)\text{H}$ ,” *Phys. Rev. Lett.*, vol. 89, no. 21, 2002.
- [65] M. Hoesch, M. Muntwiler, V. N. Petrov, M. Hengsberger, L. Patthey, M. Shi, M. Falub, T. Greber, and J. Osterwalder, “Spin structure of the Shockley surface state on  $\text{Au}(111)$ ,” *Phys. Rev. B*, vol. 69, no. 24, 2004.
- [66] T. Hirahara, K. Miyamoto, I. Matsuda, T. Kadono, A. Kimura, T. Nagao, G. Bihlmayer, E. V. Chulkov, S. Qiao, K. Shimada, H. Namatame, M. Taniguchi, and S. Hasegawa,

- “Direct observation of spin splitting in bismuth surface states,” *Phys. Rev. B*, vol. 76, no. 15, 2007.
- [67] D. Hsieh, Y. Xia, L. Wray, D. Qian, A. Pal, J. H. Dil, J. Osterwalder, F. Meier, G. Bihlmayer, C. L. Kane, Y. S. Hor, R. J. Cava, and M. Z. Hasan, “Observation of unconventional quantum spin textures in topological insulators,” *Science*, vol. 323, no. 5916, 2009.
- [68] K. Yaji, Y. Ohtsubo, S. Hatta, H. Okuyama, K. Miyamoto, T. Okuda, A. Kimura, H. Namatame, M. Taniguchi, and T. Aruga, “Large Rashba spin splitting of a metallic surface-state band on a semiconductor surface,” *Nature Communications*, vol. 1, no. 2, 2010.
- [69] C. Jozwiak, Y. L. Chen, A. V. Fedorov, J. G. Analytis, C. R. Rotundu, A. K. Schmid, J. D. Denlinger, Y.-D. Chuang, D.-H. Lee, I. R. Fisher, R. J. Birgeneau, Z.-X. Shen, Z. Hussain, and A. Lanzara, “Widespread spin polarization effects in photoemission from topological insulators,” *Phys. Rev. B*, vol. 84, no. 16, 2011.
- [70] F. Kuemmeth, S. Ilani, D. C. Ralph, and P. L. McEuen, “Coupling of spin and orbital motion of electrons in carbon nanotubes,” *Nature*, vol. 452, 2004.
- [71] C. Fasth, A. Fuhrer, L. Samuelson, V. N. Golovach, and D. Loss, “Direct measurement of the spin-orbit interaction in a two-electron InAs nanowire quantum dot,” *Phys. Rev. Lett.*, vol. 98, 2007.
- [72] P. T. Sprunger, L. Petersen, E. W. Plummer, E. Lægsgaard, and F. Besenbacher, “Giant Friedel oscillations on the Beryllium(0001) surface,” *Science*, vol. 275, no. 5307, 1997.
- [73] L. Petersen, P. Hofmann, E. Plummer, and F. Besenbacher, “Fourier transform-STM: determining the surface Fermi contour,” *Journal of Electron Spectroscopy and Related Phenomena*, vol. 109, no. 12, 2000.
- [74] P. Hofmann, B. G. Briner, M. Doering, H.-P. Rust, E. W. Plummer, and A. M. Bradshaw, “Anisotropic two-dimensional Friedel oscillations,” *Phys. Rev. Lett.*, vol. 79, 1997.
- [75] J. I. Pascual, G. Bihlmayer, Y. M. Koroteev, H.-P. Rust, G. Ceballos, M. Hansmann, K. Horn, E. V. Chulkov, S. Blügel, P. M. Echenique, and P. Hofmann, “Role of spin in quasiparticle interference,” *Phys. Rev. Lett.*, vol. 93, 2004.

- [76] J. E. Hoffman, K. McElroy, D.-H. Lee, K. M. Lang, H. Eisaki, S. Uchida, and J. C. Davis, “Imaging quasiparticle interference in  $\text{Bi}_2\text{Sr}_2\text{CaCu}_2\text{O}_{8+\delta}$ ,” *Science*, vol. 297, no. 5584, 2002.
- [77] K. McElroy, R. W. Simmonds, J. E. Hoffman, D.-H. Lee, J. Orenstein, H. Eisaki, S. Uchida, and J. C. Davis, “Relating atomic-scale electronic phenomena to wave-like quasiparticle states in superconducting  $\text{Bi}_2\text{Sr}_2\text{CaCu}_2\text{O}_{8+\delta}$ ,” *Nature*, vol. 422, 2003.
- [78] M. Vershinin, S. Misra, S. Ono, Y. Abe, Y. Ando, and A. Yazdani, “Local ordering in the pseudogap state of the high- $T_c$  superconductor  $\text{Bi}_2\text{Sr}_2\text{CaCu}_2\text{O}_{8+\delta}$ ,” *Science*, vol. 303, no. 5666, 2004.
- [79] S.-H. Ji, T. Zhang, Y.-S. Fu, X. Chen, X.-C. Ma, J. Li, W.-H. Duan, J.-F. Jia, and Q.-K. Xue, “High-resolution scanning tunneling spectroscopy of magnetic impurity induced bound states in the superconducting gap of Pb thin films,” *Phys. Rev. Lett.*, vol. 100, 2008.
- [80] N. Hatter, B. W. Heinrich, M. Ruby, J. I. Pascual, and K. J. Franke, “Magnetic anisotropy in Shiba bound states across a quantum phase transition,” *Nature Communications*, vol. 6, 2015. Article.
- [81] M. M. Ugeda, A. J. Bradley, Y. Zhang, S. Onishi, Y. Chen, W. Ruan, C. Ojeda-Aristizabal, H. Ryu, M. T. Edmonds, H.-Z. Tsai, A. Riss, S.-K. Mo, D. Lee, A. Zettl, Z. Hussain, Z.-X. Shen, and M. F. Crommie, “Characterization of collective ground states in single-layer  $\text{NbSe}_2$ ,” *Nature Physics*, vol. 12, no. 1, 2015.
- [82] P. M. R. Brydon, S. Das Sarma, H.-Y. Hui, and J. D. Sau, “Topological Yu-Shiba-Rusinov chain from spin-orbit coupling,” *Phys. Rev. B*, vol. 91, 2015.
- [83] Y. Kim, J. Zhang, E. Rossi, and R. M. Lutchyn, “Impurity-induced bound states in superconductors with spin-orbit coupling,” *Phys. Rev. Lett.*, vol. 114, 2015.
- [84] V. Kaladzhyan, C. Bena, and P. Simon, “Characterizing  $p$ -wave superconductivity using the spin structure of Shiba states,” *Phys. Rev. B*, vol. 93, 2016.
- [85] V. Kaladzhyan, C. Bena, and P. Simon, “Asymptotic behavior of impurity-induced bound states in low-dimensional topological superconductors,” *Journal of Physics: Condensed Matter*, vol. 28, no. 48, 2016.

- [86] C. Brun and et al., “Remarkable effects of disorder on superconductivity of single atomic layers of lead on silicon,” *Nature Physics*, vol. 10, 2014.
- [87] L. Petersen, L. Bürgi, H. Brune, F. Besenbacher, and K. Kern, “Comment on ”observation of two-dimensional fermi contour of a reconstructed Au(111) surface using fourier transform scanning tunneling microscopy”,” *Surface Science*, vol. 443, no. 12, 1999.
- [88] G. Mahan, *Many-Particle Physics*. Physics of Solids and Liquids, Springer, 2000.
- [89] H. Bruus and K. Flensberg, *Many-Body Quantum Theory in Condensed Matter Physics: An Introduction*. Oxford Graduate Texts, OUP Oxford, 2004.
- [90] A. Sakurai, “Comments on superconductors with magnetic impurities,” *Progress of Theoretical Physics*, vol. 44, no. 6, 1970.
- [91] M. I. Salkola, A. V. Balatsky, and J. R. Schrieffer, “Spectral properties of quasiparticle excitations induced by magnetic moments in superconductors,” *Phys. Rev. B*, vol. 55, 1997.
- [92] G. Dresselhaus, “Spin-orbit coupling effects in zinc blende structures,” *Phys. Rev.*, vol. 100, 1955.
- [93] F. Steglich, J. Aarts, C. D. Bredl, W. Lieke, D. Meschede, W. Franz, and H. Schäfer, “Superconductivity in the presence of strong Pauli paramagnetism:  $\text{CeCu}_2\text{Si}_2$ ,” *Phys. Rev. Lett.*, vol. 43, 1979.
- [94] S. Kittaka, Y. Aoki, Y. Shimura, T. Sakakibara, S. Seiro, C. Geibel, F. Steglich, H. Ikeda, and K. Machida, “Multiband superconductivity with unexpected deficiency of nodal quasiparticles in  $\text{CeCu}_2\text{Si}_2$ ,” *Phys. Rev. Lett.*, vol. 112, 2014.
- [95] A. J. Leggett, “A theoretical description of the new phases of liquid  $^3\text{He}$ ,” *Rev. Mod. Phys.*, vol. 47, 1975.
- [96] J. C. Wheatley, “Experimental properties of superfluid  $^3\text{He}$ ,” *Rev. Mod. Phys.*, vol. 47, 1975.
- [97] D. Jérôme, A. Mazaud, M. Ribault, and K. Bechgaard, “Superconductivity in a synthetic organic conductor  $(\text{TMTSF})_2\text{PF}_6$ ,” *Journal de Physique Lettres*, vol. 41, no. 4, 1980.

- [98] J. G. Bednorz and K. A. Müller, “Possible high- $T_c$  superconductivity in the Ba-La-Cu-O system,” *Zeitschrift für Physik B Condensed Matter*, vol. 64, no. 2, 1986.
- [99] Y. Maeno, H. Hashimoto, K. Yoshida, S. Nishizaki, T. Fujita, J. G. Bednorz, and F. Lichtenberg, “Superconductivity in a layered perovskite without copper,” *Nature*, vol. 372, no. 6506, 1994.
- [100] Y. Maeno, S. Kittaka, T. Nomura, S. Yonezawa, and K. Ishida, “Evaluation of spin-triplet superconductivity in  $\text{Sr}_2\text{RuO}_4$ ,” *Journal of the Physical Society of Japan*, vol. 81, no. 1, 2012.
- [101] V. Mineev and K. Samokhin, *Introduction to Unconventional Superconductivity*. Gordon and Breach Science, 1999.
- [102] M. Sigrist, “Introduction to unconventional superconductivity in non-centrosymmetric metals,” *AIP Conf. Proc.*, vol. 1162, 2009.
- [103] L. P. Gor’kov and E. I. Rashba, “Superconducting 2D system with lifted spin degeneracy: Mixed singlet-triplet state,” *Phys. Rev. Lett.*, vol. 87, 2001.
- [104] P. A. Frigeri, D. F. Agterberg, A. Koga, and M. Sigrist, “Superconductivity without inversion symmetry: MnSi versus  $\text{CePt}_3\text{Si}$ ,” *Phys. Rev. Lett.*, vol. 92, 2004.
- [105] E. Bauer and M. Sigrist, *Non-Centrosymmetric Superconductors*. Springer-Verlag, Berlin, 2012.
- [106] L. Fu and C. L. Kane, “Superconducting proximity effect and Majorana fermions at the surface of a topological insulator,” *Phys. Rev. Lett.*, vol. 100, 2008.
- [107] J. M. Lu, O. Zheliuk, I. Leermakers, N. F. Q. Yuan, U. Zeitler, K. T. Law, and J. T. et Ye, “Evidence for two-dimensional ising superconductivity in gated  $\text{MoS}_2$ ,” *Science*, 2015.
- [108] X. Xi and et al., “Ising pairing in superconducting  $\text{NbSe}_2$  atomic layers,” *Nature Physics*, 2015.
- [109] A. B. Vorontsov, I. Vekhter, and M. Eschrig, “Surface bound states and spin currents in noncentrosymmetric superconductors,” *Phys. Rev. Lett.*, vol. 101, 2008.

- [110] Y. Tanaka, T. Yokoyama, A. V. Balatsky, and N. Nagaosa, “Theory of topological spin current in noncentrosymmetric superconductors,” *Phys. Rev. B*, vol. 79, 2009.
- [111] Q.-H. Wang and Z. D. Wang, “Impurity and interface bound states in  $d_{x^2-y^2}+id_{xy}$  and  $p_x+ip_y$  superconductors,” *Phys. Rev. B*, vol. 69, 2004.
- [112] B. Liu and I. Eremin, “Impurity resonance states in noncentrosymmetric superconductor CePt<sub>3</sub>Si: A probe for Cooper-pairing symmetry,” *Phys. Rev. B*, vol. 78, 2008.
- [113] Y. Nagai, Y. Ota, and M. Machida, “Nonmagnetic impurity effects in a three-dimensional topological superconductor: From  $p$ - to  $s$ -wave behaviors,” *Phys. Rev. B*, vol. 89, 2014.
- [114] M. Sato and S. Fujimoto, “Topological phases of noncentrosymmetric superconductors: Edge states, Majorana fermions, and non-Abelian statistics,” *Phys. Rev. B*, vol. 79, 2009.
- [115] P. Burset, F. Keidel, Y. Tanaka, N. Nagaosa, and B. Trauzettel, “Transport signatures of superconducting hybrids with mixed singlet and chiral triplet states,” *Phys. Rev. B*, vol. 90, 2014.
- [116] J. D. Sau and E. Demler, “Bound states at impurities as a probe of topological superconductivity in nanowires,” *Phys. Rev. B*, vol. 88, 2013.
- [117] I. A. Firmo, S. Lederer, C. Lupien, A. P. Mackenzie, J. C. Davis, and S. A. Kivelson, “Evidence from tunneling spectroscopy for a quasi-one-dimensional origin of superconductivity in Sr<sub>2</sub>RuO<sub>4</sub>,” *Phys. Rev. B*, vol. 88, 2013.
- [118] T. Scaffidi, J. C. Romers, and S. H. Simon, “Pairing symmetry and dominant band in Sr<sub>2</sub>RuO<sub>4</sub>,” *Phys. Rev. B*, vol. 89, 2014.
- [119] T. Scaffidi and S. H. Simon, “Large Chern number and edge currents in Sr<sub>2</sub>RuO<sub>4</sub>,” *Phys. Rev. Lett.*, vol. 115, 2015.
- [120] Z. Wang and et al., “Quasiparticle interference and strong electron-mode coupling in the quasi-one-dimensional bands of Sr<sub>2</sub>RuO<sub>4</sub>,” *arXiv:1701.02773*, 2017.
- [121] D. M. Eigler and E. K. Schweizer, “Positioning single atoms with a scanning tunnelling microscope,” *Nature*, vol. 344, no. 6266, 1990.

- [122] S. Nadj-Perge, I. K. Drozdov, J. Li, H. Chen, S. Jeon, J. Seo, A. H. MacDonald, B. A. Bernevig, and A. Yazdani, “Observation of Majorana fermions in ferromagnetic atomic chains on a superconductor,” *Science*, vol. 346, no. 6209, 2014.
- [123] C. Nayak, S. H. Simon, A. Stern, M. Freedman, and S. Das Sarma, “Non-Abelian anyons and topological quantum computation,” *Rev. Mod. Phys.*, vol. 80, 2008.
- [124] R. Pawlak, M. Kisiel, J. Klinovaja, T. Meier, S. Kawai, T. Glatzel, D. Loss, and E. Meyer, “Probing atomic structure and Majorana wavefunctions in mono-atomic Fe chains on superconducting Pb surface,” *Npj Quantum Information*, vol. 2, 2016. Article.
- [125] M. Ruby, F. Pientka, Y. Peng, F. von Oppen, B. W. Heinrich, and K. J. Franke, “End states and subgap structure in proximity-coupled chains of magnetic adatoms,” *Phys. Rev. Lett.*, vol. 115, 2015.
- [126] T.-P. Choy, J. M. Edge, A. R. Akhmerov, and C. W. J. Beenakker, “Majorana fermions emerging from magnetic nanoparticles on a superconductor without spin-orbit coupling,” *Phys. Rev. B*, vol. 84, 2011.
- [127] S. Nadj-Perge, I. K. Drozdov, B. A. Bernevig, and A. Yazdani, “Proposal for realizing Majorana fermions in chains of magnetic atoms on a superconductor,” *Phys. Rev. B*, vol. 88, 2013.
- [128] B. Braunecker and P. Simon, “Interplay between classical magnetic moments and superconductivity in quantum one-dimensional conductors: Toward a self-sustained topological Majorana phase,” *Phys. Rev. Lett.*, vol. 111, 2013.
- [129] J. Klinovaja, P. Stano, A. Yazdani, and D. Loss, “Topological superconductivity and Majorana fermions in RKKY systems,” *Phys. Rev. Lett.*, vol. 111, 2013.
- [130] M. M. Vazifeh and M. Franz, “Self-organized topological state with Majorana fermions,” *Phys. Rev. Lett.*, vol. 111, 2013.
- [131] F. Pientka, L. I. Glazman, and F. von Oppen, “Unconventional topological phase transitions in helical Shiba chains,” *Phys. Rev. B*, vol. 89, 2014.
- [132] K. Pöyhönen, A. Westström, J. Röntynen, and T. Ojanen, “Majorana states in helical Shiba chains and ladders,” *Phys. Rev. B*, vol. 89, 2014.

- [133] J. Röntynen and T. Ojanen, “Tuning topological superconductivity in helical Shiba chains by supercurrent,” *Phys. Rev. B*, vol. 90, 2014.
- [134] A. Heimes, P. Kotetes, and G. Schön, “Majorana fermions from Shiba states in an anti-ferromagnetic chain on top of a superconductor,” *Phys. Rev. B*, vol. 90, 2014.
- [135] I. Reis, D. J. J. Marchand, and M. Franz, “Self-organized topological state in a magnetic chain on the surface of a superconductor,” *Phys. Rev. B*, vol. 90, 2014.
- [136] A. Heimes, D. Mendler, and P. Kotetes, “Interplay of topological phases in magnetic adatom-chains on top of a Rashba superconducting surface,” *New Journal of Physics*, vol. 17, 2015.
- [137] A. Westström, K. Pöyhönen, and T. Ojanen, “Topological properties of helical Shiba chains with general impurity strength and hybridization,” *Phys. Rev. B*, vol. 91, 2015.
- [138] B. Braunecker and P. Simon, “Self-stabilizing temperature-driven crossover between topological and nontopological ordered phases in one-dimensional conductors,” *Phys. Rev. B*, vol. 92, 2015.
- [139] K. Pöyhönen, A. Westström, and T. Ojanen, “Topological superconductivity in ferromagnetic atom chains beyond the deep-impurity regime,” *Phys. Rev. B*, vol. 93, 2016.
- [140] J. Röntynen and T. Ojanen, “Topological superconductivity and high Chern numbers in 2D ferromagnetic Shiba lattices,” *Phys. Rev. Lett.*, vol. 114, 2015.
- [141] J. Röntynen and T. Ojanen, “Chern mosaic: Topology of chiral superconductivity on ferromagnetic adatom lattices,” *Phys. Rev. B*, vol. 93, 2016.
- [142] J. Li, T. Neupert, Z. Wang, A. H. MacDonald, A. Yazdani, and B. A. Bernevig, “Two-dimensional chiral topological superconductivity in Shiba lattices,” *Nature Communications*, vol. 7, 2016. Article.
- [143] S. Nakosai, Y. Tanaka, and N. Nagaosa, “Two-dimensional  $p$ -wave superconducting states with magnetic moments on a conventional  $s$ -wave superconductor,” *Phys. Rev. B*, vol. 88, 2013.

- [144] M. Schechter, K. Flensberg, M. H. Christensen, B. M. Andersen, and J. Paaske, “Self-organized topological superconductivity in a Yu-Shiba-Rusinov chain,” *Phys. Rev. B*, vol. 93, 2016.
- [145] T. Neupert, A. Yazdani, and B. A. Bernevig, “Shiba chains of scalar impurities on unconventional superconductors,” *Phys. Rev. B*, vol. 93, 2016.
- [146] L. Kimme and T. Hyart, “Existence of zero-energy impurity states in different classes of topological insulators and superconductors and their relation to topological phase transitions,” *Phys. Rev. B*, vol. 93, 2016.
- [147] A. P. Schnyder, S. Ryu, A. Furusaki, and A. W. W. Ludwig, “Classification of topological insulators and superconductors in three spatial dimensions,” *Phys. Rev. B*, vol. 78, 2008.
- [148] S. Ryu, A. P. Schnyder, A. Furusaki, and A. W. W. Ludwig, “Topological insulators and superconductors: tenfold way and dimensional hierarchy,” *New Journal of Physics*, vol. 12, 2010.
- [149] S. D. Sarma, M. Freedman, and C. Nayak, “Majorana zero modes and topological quantum computation,” *Npj Quantum Information*, vol. 1, 2015. Review Article.
- [150] A. Kitaev, “Fault-tolerant quantum computation by anyons,” *Annals of Physics*, vol. 303, no. 1, 2003.
- [151] Y. Peng, F. Pientka, L. I. Glazman, and F. von Oppen, “Strong localization of Majorana end states in chains of magnetic adatoms,” *Phys. Rev. Lett.*, vol. 114, 2015.
- [152] J. Zhang, Y. Kim, E. Rossi, and R. M. Lutchyn, “Topological superconductivity in a multichannel Yu-Shiba-Rusinov chain,” *Phys. Rev. B*, vol. 93, 2016.
- [153] S. Hoffman, J. Klinovaja, and D. Loss, “Topological phases of inhomogeneous superconductivity,” *Phys. Rev. B*, vol. 93, 2016.
- [154] V. Kaladzhyan, J. Röntynen, P. Simon, and T. Ojanen, “Topological state engineering by potential impurities on chiral superconductors,” *Phys. Rev. B*, vol. 94, 2016.
- [155] M. H. Christensen, M. Schechter, K. Flensberg, B. M. Andersen, and J. Paaske, “Spiral magnetic order and topological superconductivity in a chain of magnetic adatoms on a two-dimensional superconductor,” *Phys. Rev. B*, vol. 94, 2016.

- [156] B. E. Feldman *et al.*, “High-resolution studies of the Majorana atomic chain platform,” *Nat. Phys.*, vol. 13, 2017.
- [157] T. Kitagawa, E. Berg, M. Rudner, and E. Demler, “Topological characterization of periodically driven quantum systems,” *Phys. Rev. B*, vol. 82, 2010.
- [158] N. H. Lindner, G. Refael, and V. Galitski, “Floquet topological insulator in semiconductor quantum wells,” *Nat Phys*, vol. 7, no. 6, 2011.
- [159] L. Jiang, T. Kitagawa, J. Alicea, A. R. Akhmerov, D. Pekker, G. Refael, J. I. Cirac, E. Demler, M. D. Lukin, and P. Zoller, “Majorana fermions in equilibrium and in driven cold-atom quantum wires,” *Phys. Rev. Lett.*, vol. 106, 2011.
- [160] M. Trif and Y. Tserkovnyak, “Resonantly tunable Majorana polariton in a microwave cavity,” *Phys. Rev. Lett.*, vol. 109, 2012.
- [161] Q.-J. Tong, J.-H. An, J. Gong, H.-G. Luo, and C. H. Oh, “Generating many Majorana modes via periodic driving: A superconductor model,” *Phys. Rev. B*, vol. 87, 2013.
- [162] M. Thakurathi, A. A. Patel, D. Sen, and A. Dutta, “Floquet generation of Majorana end modes and topological invariants,” *Phys. Rev. B*, vol. 88, 2013.
- [163] A. Gómez-León and G. Platero, “Floquet-Bloch theory and topology in periodically driven lattices,” *Phys. Rev. Lett.*, vol. 110, 2013.
- [164] D. E. Liu, A. Levchenko, and H. U. Baranger, “Floquet Majorana fermions for topological qubits in superconducting devices and cold-atom systems,” *Phys. Rev. Lett.*, vol. 111, 2013.
- [165] A. Poudel, G. Ortiz, and L. Viola, “Dynamical generation of Floquet Majorana flat bands in *s*-wave superconductors,” *EPL*, vol. 110, no. 1, 2015.
- [166] J. Klinovaja, P. Stano, and D. Loss, “Topological Floquet phases in driven coupled Rashba nanowires,” *Phys. Rev. Lett.*, vol. 116, 2016.
- [167] V. Kaladzhyan, S. Hoffman, and M. Trif, “Dynamical Shiba states from precessing magnetic moments in an *s*-wave superconductor,” *Phys. Rev. B*, vol. 95, 2017.

- [168] A. P. Schnyder, S. Ryu, A. Furusaki, and A. W. W. Ludwig, “Classification of topological insulators and superconductors in three spatial dimensions,” *Phys. Rev. B*, vol. 78, 2008.
- [169] S. Tewari and J. D. Sau, “Topological invariants for spin-orbit coupled superconductor nanowires,” *Phys. Rev. Lett.*, vol. 109, 2012.
- [170] V. Kaladzhyan, J. Despres, I. Mandal, and C. Bena, “Majorana fermions in finite-size strips with in-plane magnetic fields,” 2016.
- [171] A. Kundu and B. Seradjeh, “Transport signatures of Floquet Majorana fermions in driven topological superconductors,” *Phys. Rev. Lett.*, vol. 111, 2013.
- [172] M. Trif, V. Kaladzhyan, and P. Simon, “Charge pumping into an STM tip by a precessing texture in an *s*-wave superconductor,” (*unpublished*).
- [173] J. Li, T. Neupert, B. A. Bernevig, and A. Yazdani, “Manipulating Majorana zero modes on atomic rings with an external magnetic field,” *Nature Communications*, vol. 7, 2016.
- [174] J. Sinova, S. O. Valenzuela, J. Wunderlich, C. H. Back, and T. Jungwirth, “Spin Hall effects,” *Rev. Mod. Phys.*, vol. 87, 2015.
- [175] J. König, M. C. Bønsager, and A. H. MacDonald, “Dissipationless spin transport in thin film ferromagnets,” *Phys. Rev. Lett.*, vol. 87, 2001.
- [176] E. Sonin, “Spin currents and spin superfluidity,” *Advances in Physics*, vol. 59, no. 3, 2010.
- [177] S. Takei and Y. Tserkovnyak, “Superfluid spin transport through easy-plane ferromagnetic insulators,” *Phys. Rev. Lett.*, vol. 112, 2014.
- [178] R. Žitko, J. S. Lim, R. López, and R. Aguado, “Shiba states and zero-bias anomalies in the hybrid normal-superconductor Anderson model,” *Phys. Rev. B*, vol. 91, 2015.
- [179] N. Khotkevych, Y. Kolesnichenko, and J. van Ruitenbeek, “Quantum interference patterns around magnetic impurities in a 2D electron gas with strong Rashba spin-orbit interaction,” *arXiv:1601.03154v1*, 2016.
- [180] Y. Tserkovnyak, A. Brataas, and G. E. W. Bauer, “Enhanced Gilbert damping in thin ferromagnetic films,” *Phys. Rev. Lett.*, vol. 88, 2002.

- [181] Y. Tserkovnyak, A. Brataas, G. E. W. Bauer, and B. I. Halperin, “Nonlocal magnetization dynamics in ferromagnetic heterostructures,” *Rev. Mod. Phys.*, vol. 77, 2005.
- [182] I. Mandal, “Exceptional points for chiral Majorana fermions in arbitrary dimensions,” *Europhysics Letters*, vol. 110, no. 6, p. 67005, 2015.
- [183] I. Mandal and S. Tewari, “Exceptional point description of one-dimensional chiral topological superconductors/superfluids in BDI class,” *Physica E*, vol. 79, pp. 180 – 187, 2016.
- [184] I. Mandal, “Counting Majorana bound states using complex momenta,” *Condensed Matter Physics*, vol. 19, no. 3, p. 33703, 2016.
- [185] P. San-Jose, E. Prada, and R. Aguado, “Majorana bound states from exceptional points in non-topological superconductors,” *Scientific Reports*, vol. 6, p. 21427, 2016.
- [186] A. Y. Kitaev, “Unpaired Majorana fermions in quantum wires,” *Physics-Uspekhi*, vol. 44, no. 10S, p. 131, 2001.
- [187] L. Fu and C. L. Kane, “Probing neutral Majorana fermion edge modes with charge transport,” *Phys. Rev. Lett.*, vol. 102, p. 216403, May 2009.
- [188] A. C. Potter and P. A. Lee, “Multichannel generalization of Kitaev’s Majorana end states and a practical route to realize them in thin films,” *Phys. Rev. Lett.*, vol. 105, p. 227003, Nov 2010.
- [189] I. Martin and A. F. Morpurgo, “Majorana fermions in superconducting helical magnets,” *Phys. Rev. B*, vol. 85, p. 144505, 2012.
- [190] S. Tewari and J. D. Sau, “Topological invariants for spin-orbit coupled superconductor nanowires,” *Phys. Rev. Lett.*, vol. 109, p. 150408, 2012.
- [191] J. Klinovaja and D. Loss, “Composite Majorana fermion wave functions in nanowires,” *Phys. Rev. B*, vol. 86, p. 085408, 2012.
- [192] T. Mizushima and M. Sato, “Topological phases of quasi-one-dimensional fermionic atoms with a synthetic gauge field,” *New Journal of Physics*, vol. 15, no. 7, p. 075010, 2013.

- [193] D. Wang, Z. Huang, and C. Wu, “Fate and remnants of Majorana zero modes in a quantum wire array,” *Phys. Rev. B*, vol. 89, p. 174510, May 2014.
- [194] I. Seroussi, E. Berg, and Y. Oreg, “Topological superconducting phases of weakly coupled quantum wires,” *Phys. Rev. B*, vol. 89, p. 104523, Mar 2014.
- [195] R. Wakatsuki, M. Ezawa, and N. Nagaosa, “Majorana fermions and multiple topological phase transition in Kitaev ladder topological superconductors,” *Phys. Rev. B*, vol. 89, p. 174514, May 2014.
- [196] P. San-Jose, E. Prada, and R. Aguado, “Mapping the topological phase diagram of multi-band semiconductors with supercurrents,” *Phys. Rev. Lett.*, vol. 112, p. 137001, 2014.
- [197] N. Mohanta and A. Taraphder, “Topological superconductivity and Majorana bound states at the  $\text{LaAlO}_3/\text{SrTiO}_3$  interface,” *EPL (Europhysics Letters)*, vol. 108, no. 6, p. 60001, 2014.
- [198] G. Ben-Shach, A. Haim, I. Appelbaum, Y. Oreg, A. Yacoby, and B. I. Halperin, “Detecting Majorana modes in one-dimensional wires by charge sensing,” *Phys. Rev. B*, vol. 91, p. 045403, Jan 2015.
- [199] E. J. H. Lee, X. Jiang, M. Houzet, R. Aguado, C. M. Lieber, and S. De Franceschi, “Spin-resolved Andreev levels and parity crossings in hybrid superconductor-semiconductor nanostructures,” *Nat Nano*, vol. 9, no. 1, 2014.
- [200] J. S. Lim, L. Serra, R. López, and R. Aguado, “Magnetic-field instability of Majorana modes in multiband semiconductor wires,” *Phys. Rev. B*, vol. 86, p. 121103, Sep 2012.
- [201] J. S. Lim, R. López, and L. Serra, “Emergence of Majorana modes in cylindrical nanowires,” *Europhysics Letters*, vol. 103, no. 3, p. 37004, 2013.
- [202] J. Osea and L. Serra, “Majorana states and magnetic orbital motion in planar hybrid nanowires,” *Phys. Rev. B*, vol. 91, p. 235417, Jun 2015.
- [203] B. Nijholt and A. R. Akhmerov, “Orbital effect of magnetic field on the Majorana phase diagram,” *Phys. Rev. B*, vol. 93, p. 235434, Jun 2016.
- [204] M. Kjaergaard, K. Wölms, and K. Flensberg, “Majorana fermions in superconducting nanowires without spin-orbit coupling,” *Phys. Rev. B*, vol. 85, p. 020503, Jan 2012.

- [205] F. Loder, A. P. Kampf, and T. Kopp, “Route to topological superconductivity via magnetic field rotation,” *Scientific Reports*, vol. 5, p. 15302, Oct 2015.
- [206] S. M. Albrecht, A. P. Higginbotham, M. Madsen, F. Kuemmeth, T. S. Jespersen, J. Nygård, P. Krogstrup, and C. M. Marcus, “Exponential protection of zero modes in Majorana islands,” *Nature*, vol. 531, pp. 206–209, Mar 2016. Letter.
- [207] J. Li, T. Neupert, B. A. Bernevig, and A. Yazdani, “Manipulating Majorana zero modes on atomic rings with an external magnetic field,” *Nature Communications*, vol. 7, 2016.
- [208] D. Sticlet, C. Bena, and P. Simon, “Spin and Majorana polarization in topological superconducting wires,” *Phys. Rev. Lett.*, vol. 108, p. 096802, Mar 2012.
- [209] N. Sedlmayr, J. M. Aguiar-Hualde, and C. Bena, “Flat Majorana bands in two-dimensional lattices with inhomogeneous magnetic fields: Topology and stability,” *Phys. Rev. B*, vol. 91, p. 115415, Mar 2015.
- [210] N. Sedlmayr and C. Bena, “Visualizing Majorana bound states in one and two dimensions using the generalized Majorana polarization,” *Phys. Rev. B*, vol. 92, p. 115115, Sep 2015.
- [211] N. Sedlmayr, J. M. Aguiar-Hualde, and C. Bena, “Majorana bound states in open quasi-one-dimensional and two-dimensional systems with transverse Rashba coupling,” *Phys. Rev. B*, vol. 93, p. 155425, Apr 2016.
- [212] A. Altland and M. R. Zirnbauer, “Nonstandard symmetry classes in mesoscopic normal-superconducting hybrid structures,” *Phys. Rev. B*, vol. 55, pp. 1142–1161, Jan 1997.
- [213] *MatQ*. <http://www.icmm.csic.es/sanjose/MathQ/MathQ.html>.
- [214] J. C. Y. Teo and C. L. Kane, “Topological defects and gapless modes in insulators and superconductors,” *Phys. Rev. B*, vol. 82, p. 115120, Sep 2010.
- [215] S. Matsuura, P.-Y. Chang, A. P. Schnyder, and S. Ryu, “Protected boundary states in gapless topological phases,” *New Journal of Physics*, vol. 15, no. 6, p. 065001, 2013.
- [216] S. Deng, G. Ortiz, A. Poudel, and L. Viola, “Majorana flat bands in s-wave gapless topological superconductors,” *Phys. Rev. B*, vol. 89, p. 140507, Apr 2014.

- [217] Y. Baum, T. Posske, I. C. Fulga, B. Trauzettel, and A. Stern, “Coexisting edge states and gapless bulk in topological states of matter,” *Phys. Rev. Lett.*, vol. 114, p. 136801, Mar 2015.
- [218] Y. Baum, T. Posske, I. C. Fulga, B. Trauzettel, and A. Stern, “Gapless topological superconductors: Model Hamiltonian and realization,” *Phys. Rev. B*, vol. 92, p. 045128, Jul 2015.

---

# List of Publications

## Publications used in the thesis

1. VK, P. Simon, M. Trif, '*Controlling topological superconductivity by magnetization dynamics*', Phys. Rev. B **96**, 020507(R) (2017)
2. VK, S. Hoffman, M. Trif, '*Dynamical Shiba states by precessing magnetic moments in an s-wave superconductor*', Phys. Rev. B **95**, 195403 (2017)
3. VK, J. Despres, I. Mandal, and C. Bena, '*Majorana fermions in finite-size strips with in-plane magnetic fields*', arXiv: 1611.09367 (2016) (accepted to EPJ B)
4. VK, C. Bena, and P. Simon, '*Asymptotic behavior of impurity-induced bound states in low-dimensional topological superconductors*', JP: Condensed Matter **28**, 485701 (2016)
5. VK, P. Simon, and C. Bena, '*Determining the spin-orbit coupling via spin-polarized spectroscopy of magnetic impurities*', Phys. Rev. B **94**, 134511 (2016) (editor's choice)
6. VK, J. Röntynen, P. Simon, and T. Ojanen, '*Topological state engineering by potential impurities on chiral superconductors*', Phys. Rev. B **94**, 060505(R) (2016)
7. VK, C. Bena, and P. Simon, '*Characterizing p-wave superconductivity using the spin structure of Shiba states*', Phys. Rev. B **93**, 214514 (2016)

## Other publications

1. VK and C. Bena, '*Formation of Majorana fermions in finite-size graphene strips*', SciPost Phys. 3, 002 (2017)
2. VK, P. P. Aseev, and S. N. Artemenko, '*Photogalvanic effect in the HgTe/CdTe topological insulator due to edge-bulk optical transitions*', Phys. Rev. B **92**, 155424 (2015)
3. S. N. Artemenko, VK, '*Photogalvanic effects in topological insulators*', JETP Letters, **97**:2 (2013)